Jagiellonian University

Faculty of Physics, Astronomy and Applied Computer Science

Joanna Kozakiewicz

Investigation of the Martian subsurface by analysis of the Schumann resonance parameters

A dissertation submitted to the Jagiellonian University

for the degree of Doctor of Philosophy

PhD Advisor:

Prof. Katarzyna Otmianowska-Mazur

Krakow 2015

Abstract

Two electrically conductive planetary spheres, the ionosphere and the ground, form a spherical waveguide. Within such a planetary cavity a phenomenon called Schumann resonance (SR) can occur. It is a resonance of extremely low frequency (ELF) electromagnetic waves. The resonance parameters are strongly related to the electromagnetic properties of the cavity. On Mars, a low-conductivity ground significantly influences ELF wave propagation. For that reason, a newly developed analytical method, which enables to estimate the Schumann resonance parameters and explicate their dependence of the ground properties, is introduced. The obtained results indicate that the influence of the Martian ground on the SR parameters is important. As a result, Schumann resonance can be used as a tool to study, not only the properties of the Martian atmosphere, but also the properties of the subsurface layers. Schumann resonance may be especially useful in groundwater exploration.

Key words:
Schumann resonance
radio waves
subsurface of Mars

Abstrakt

Dwie elektrycznie przewodzące sfery planetarne, jonosfera i grunt, tworzą kulisty falowód. W takiej wnęce planetarnej może wystąpić zjawisko zwane rezonansem Schumanna (SR). Jest to rezonans fal elektromagnetycznych o bardzo niskich częstotliwościach (ELF), którego parametry są ściśle związane z właściwościami elektromagnetycznymi wnęki. Na Marsie, słabo przewodzący grunt znacząco wpływa na propagację fal ELF. Z tego powodu wprowadzona została metoda analityczna, pozwalająca na oszacowanie parametrów rezonansu Schumanna i ich zależności od właściwości gruntu. Uzyskane wyniki wskazują, że wpływ gruntu marsjańskiego na parametry SR jest ważny. Dzięki temu rezonans Schumanna może być zastosowany jako narzędzie do badania, nie tylko właściwości marsjańskiej atmosfery, ale także warstw podpowierzchniowych. Rezonans Schumanna może być szczególnie przydatny w poszukiwaniu wody pod powierzchnią Marsa.

Słowa kluczowe:
rezonans Schumanna
fale radiowe
podpowierzchnia Marsa

Acknowledgments

This work would not have been finished without help of many people. I am especially grateful to PhD Andrzej Kułak for the opportunity to study this interesting subject of the Schumann resonance phenomenon and for his help and support during my research. I wish to express my gratitude to my PhD advisor Prof. Katrzyna Otmianowska-Mazur and my supervisor Prof. Bogusław Kamys for the possibility to develop my interest in planetary science. I am also grateful to PhD Ewa Malata for creating the opportunity to study geology. I would like to thank Krzysztof Zietara for the discussion and remarks connected to the ELF station design and for the 3D visualization of the Martian platform. I wish to thank PhD Earle R. Williams for useful guidelines and to PhD Marian Soida for his helpful comments on the text of my PhD thesis. I wish to express my gratitude to two people: Anna Stec and Marta Sieprawska-Winkel without whose administrative support I would not be able to begin and complete my work.

This work was supported in part by the Polish Ministry of Science and Higher Education under subsidy for research and development of young researchers and PhD students, and in part by the Polish National Center for Research and Development Grants: NCN-2013/09/N/ST9/02200.

Table of Contents

Introduction

Mars is a cold desert planet, yet the most similar to Earth of all the worlds found in the Solar System. Its proximity and similarity to our planet has resulted in Mars becoming the best-known extraterrestrial planet and the primary object of space missions. The exploration of Mars is being conducted using Earth-based telescopes, remote-sensing orbiters and *in situ* measurements with rovers and landers.

Although many elements of the Martian environment have been well established, the subsurface of the planet is still poorly understood. The previous missions, exploring the Martian ground, were focused mainly on issues related to mineral and chemical composition, surface morphology, and allowed studying near-surface layers on local scales. Such a situation was well recapitulated by *Taylor and McLennan* [2009]:

> "Because efforts at Mars exploration have given priority to finding evidence for life, the curious situation has arisen where sub-millimeter-scale rock textures can be evaluated routinely on the surface but the internal structure of the planet, measured on scales of tens to thousands of kilometers is largely unknown".

The Martian subsurface is an important goal for the future exploration related to the detection of groundwater, life or resources. The present lack of data on this vast region of Mars may be supplemented using a very inexpensive and simple method based on the propagation of electromagnetic (EM) radio waves in the Extremely Low Frequency range (ELF, 3Hz-3kHz). The electromagnetic exploration is planned for the future missions, and the method developed in this project will help to predict the results and interpret the measured data.

ELF radio waves are very weakly attenuated in planetary environments; therefore, they can propagate on very long distances, many times around the globe. They also have a larger skin depth as compared to waves in higher frequency ranges, and hence can penetrate deeper into media. On Mars, as well as on Earth, ELF wave propagation can occur within a ground-ionosphere waveguide, made of two electrically conductive spheres: the ground and the ionosphere. These two spherical layers create a planetary cavity. When this cavity is excited by a source of ELF waves, a resonance phenomenon arises, owing to a rapid increase of the field amplitude at the natural frequencies of the cavity. This resonance was analytically predicted by *Schumann* [1952] and detected, in the terrestrial cavity, few years later [*Balser and Wagner*, 1960]. The Schumann resonance parameters are strongly related to the electromagnetic properties of the cavity, and as a result they carry important information on ELF sources and the waveguide. The planetary ground-ionosphere waveguide is formed of non-ideal conductors, and losses due to a finite ionospheric and ground conductivity lead to lower resonant frequencies and ELF field amplitudes. By studying ELF waves propagation within the waveguide, it is possible to examine the properties of the subsurface, the lower layers of the ionosphere, and to identify ELF waves sources.

ELF methods are particularly predisposed to examine the subsurface layers of Mars, due to the low-conductivity surface, which allows for deep penetration into the Martian ground. The advantages of ELF methods compared to high-frequency (e.g. radar) techniques include greater sensitivity and simpler interpretation of the results [*Grimm*, 2002]. The disadvantages are mainly associated with poorer resolution as they typically give only globally averaged results.

Modeling of the Schumann resonance parameters is possible using analytical and numerical methods. The numerical modeling enables including detailed conductivity profiles, but does not provide relationships between the environmental properties, such as conductivity or permittivity, and the propagation parameters [*Mushtak and Williams*, 2002]. The analytical approach does not have this shortcoming, however up till now, it was limited to studying Schumann resonance solely in relation to the ionosphere. Such an approximation is appropriate on Earth, where the conductivity of the ground is many times higher than the ionospheric conductivity, and the ground can be treated as a perfect conductor. However, on Mars, such an approach is inapplicable. Therefore, an analytical method, which allow including electrical properties of the ground, has been developed [*Kulak et al.*, 2013]. This method enables testing many scenarios difficult to perform by numerical methods, due to time needed to accomplish satisfactory simulations [*Kozakiewicz et al.*, 2015]. In addition the analytical method does not require a significant employment of hardware and software resources and can be widely used. This technique allows also for the development and evaluation of scientific equipment for ELF field measurements on Mars. Such a lightweight ELF apparatus, characterized by extremely low power consumption, is an ideal tool for planetary studies. Furthermore, because of the global nature of the phenomenon, one measuring station is enough to perform some basic research.

The purpose of this work is to determine the possibility of using Schumann resonance measurements on Mars in order to study the subsurface structure of the planet. This task will be carried out in five chapters. The first chapter presents the theoretical and historical background of the Schumann resonance and ELF propagation modeling. In Chapter 2, the properties of the

Martian environment, important for the purpose of this study, are presented. In Chapter 3, the Martian ground models are proposed, taking into consideration the analysis of data from the Martian missions, rocks' conductivity theories, and information on the terrestrial subsurface. On the basis of those models, the Martian ground-ionosphere waveguides are constructed. Subsequently, the analytical method of ELF wave propagation is developed to determine the Schumann resonance and ELF parameters for the given waveguide. The results of this method are presented in Chapter 4. This includes the response of a layered medium to ELF waves, especially the dependence of the layers' thickness, composition, porosity, and temperature upon the propagation parameters. The final point of this chapter is related to the discussion of the results, and establishing the relationship between the ground properties, e.g. the thickness and composition of the layers and the Schumann resonance parameters, i.e. the resonant frequencies, or the quality factors (Q factors). In addition, the attenuation and the phase velocity of ELF waves are calculated for the waveguides as well as the Schumann resonance spectra. In the last chapter, the feasibility of the measurements of the magnetic and electric components of ELF fields at the Martian surface is presented. The limits of such measurements are assessed and the parameters of the measuring equipment, which are crucial for efficient use, are determined.

1 Schumann resonance and ELF propagation in a planetary cavity

1.1 Historical background

Historically, the existence of Schumann resonance, the planetary cavity, and the global atmospheric electric circuit, in view of the fact that all of them are related with the electromagnetic properties and phenomena of the planet, were simultaneously discovered and their discovery was based on several, often reciprocal concepts.

The atmospheric electricity studies began in 1839, when Carl Friedrich Gauss put forward an idea that a conducting layer exists in the atmosphere. Later, from the measurements of the atmospheric electric field in fair weather regions (areas of the atmosphere located away from storms center), Lord Kelvin (William Thompson) concluded that electrification was an atmosphere property. In 1893, although the existence of the ground-ionosphere waveguide on Earth was at that time only suspected, George F. Fitzgerald considered a resonance of electromagnetic waves in the terrestrial cavity and presented its vibration period. A year later, Joseph Larmor derived a theoretical relation for the free periods in a uniform spherical capacitor, which turned out to be the same as the calculated many years later by Schumann [*Besser*, 2007]. Almost at the same time, in 1899, Sydney Chapman established the ground electrical conductivity and stated that it was “similar to that of the moist earth” [*Aplin et al.*, 2008]. Practical evidence, in favor of the existence of the planetary waveguide, was added by Guglielmo Marconi, who, in 1901, sent short radio wave signals across the Atlantic. In the next year, Arthur E. Kennelly and Oliver Heaviside correctly explicated that achievement in terms of the existence of a high-conductivity layer in the atmosphere. The origin of this layer was explained by Victor F. Hess’s discovery of the atmospheric ionization by cosmic rays in 1912. In 1925, Edward Victor Appleton verified the presence of the ionosphere [*Appleton and Barnett*, 1925]. Also in 1920s, C.T.R. Wilson proposed that a global atmospheric circuit must exist to sustain the observed atmospheric electrification [*Wilson*, 1929]. He concluded that this circuit results from a flow of electric currents between the ionized atmosphere and the ground, and is generated by thunderstorms and rain clouds. This theory was tested by measurements of the atmospheric potential gradient during cruises of a geophysical research ship "Carnagie". Even though the properties of the planetary cavity were well characterized at that time, the formal clarification of its resonance phenomena was presented in 1952, when Winfried Otto Schumann calculated the theoretical values of these natural resonant frequencies. Few years later, a Schumann's student, Herbert L. Konig, published some experimental data indicating the existence of this planetary resonance [*Konig,* 1959]. However, for the complete experimental confirmation of the Schumann theory, it was necessary to wait till 1960, when Martin Balser and Charles A. Wagner measured global resonance frequencies. The term ''Schumann resonances'' first appeared in 1965 in the historical review by Theodore R. Madden and W. J. Thompson [*Besser*, 2007].

Presently, with the Schumann resonance measurements on Earth, it is possible to:

- track changes in the average temperature of the tropical regions [*Williams*, 1992];
- study atmosphere-hydrosphere oscillations in the tropical regions [*Satori et al.*, 2009];
- examine the distribution of storm centers [*Dyrda et al.*, 2014];
- determine the impact of solar activity on the lower layers of the Earth's ionosphere [*Schlegel and Fullekrug*, 1999];
- investigate individual discharges connected to lightning activity [*Cummer*, 2000] along with transient luminous events [*Price et al.*, 2001].

Schumann resonance has been proposed as a tool for studying electromagnetic environments in the Solar System [*Simoes et al.,* 2008a] and also for measuring water content in the ice planets: Neptune and Uranus [*Simoes et al.*, 2012], which can be very important for establishing the model of the Solar System's evolution.

1.2 Theoretical background

In this work, the theoretical and observational development of our knowledge on ELF propagation and Schumann resonance is limited only to the most relevant information since even in the robust work of *Nickolaenko and Hayakawa* [2002] authors state:

> "There are a great number of publications on the [Schumann] resonance and on ELF radio propagation. […] It is quite impossible to include this colossal amount of information into a book of limited size."

EM waves of various frequencies can propagate in a planetary waveguide. In frequency domain, EM field can be described by independent structures – modes. The modes in spherical resonators are characterized by their cutoff frequency and divided naturally, due to boundary conditions (see below), on the transverse magnetic TM ($B_r = 0$), and the transverse electric TE ($E_r = 0$) [*Jackson*, 1999]. At frequencies below the cutoff frequency, the given mode does not contribute to propagating EM field. The lower limit for a frequency that can propagate, as well as the spectrum of EM waves (Figure 1), is determined by the conductivity profiles of the waveguide boundaries. The dominant mode in a spherical waveguide is the transverse electromagnetic mode TEM (the TM mode of the zeroth order). This mode has no cutoff frequency.

Propagating waves in a planetary cavity cause a resonance phenomenon. There are two possible resonances: longitudinal and transverse. The lowest resonant frequency in longitudinal direction is related to the planetary radius R. It can be approximated by: $f_l \sim c/(2\pi R)\cdot n$, where $n = 1,2,...$, is the mode of the wave, c – is the speed of light in vacuum. The lowest transverse resonant frequency, associated with the distance between the waveguide boundaries h, can be given by: $f_t \sim c/(2h)\cdot n$ [*Nickolaenko and Hayakawa*, 2002]. This is also the cutoff frequency for the TE modes. These two types of the resonant frequencies differ by the factor: $h/(\pi R)$. The longitudinal resonance, called Schumann resonance, is of the global nature, and is described in point 1.2.1. The transverse resonance is related to a local source, and is not presented in this study.

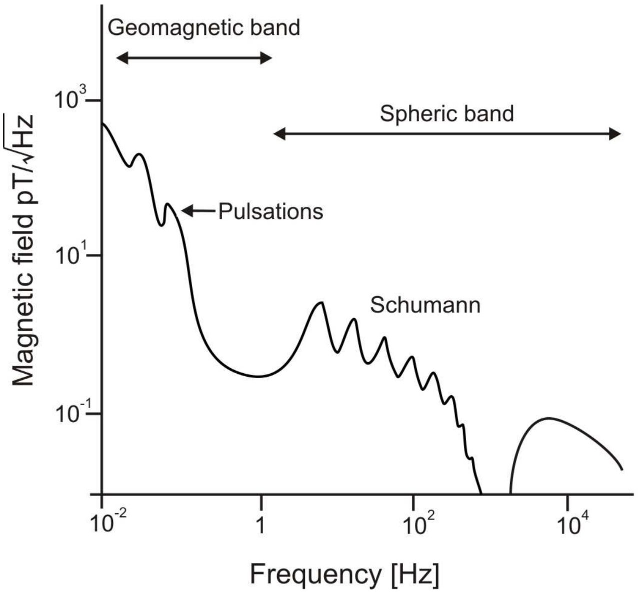

Figure 1. Schematic terrestrial low-frequency EM spectrum. Phenomena that take place in the ionosphere and the magnetosphere are the sources of natural signals in the geomagnetic band. Electrical discharges in the atmosphere, i.e. lightning activity, are the natural sources in the spheric band. The break at 2 kHz is related to the cutoff frequency for the TE mode, while the minimum at 1 Hz is due to the limit frequency of Schumann resonance.

Adapted from *Grimm* [2002].

As there is no cutoff frequency for the TEM mode, there is no lower frequency limit for the cavity. As frequencies approach zero, the waveguide parameters are related to a current flow in the global electric circuit, described in point 1.2.4.

1.2.1 Schumann resonance

To calculate resonance frequencies, Schumann assumed several approximations. He adopted that the ionosphere and the lithosphere are ideal conductors, and between them there is free space. In general, the Maxwell equations can be given as [*Jackson*, 1999]:

$$\nabla \cdot \mathbf{D} = \rho \,, \tag{1.1}$$

$$\nabla \cdot \mathbf{B} = 0 \,, \tag{1.2}$$

$$\nabla \times \mathbf{E} = -\frac{\partial \mathbf{B}}{\partial t} \,, \tag{1.3}$$

$$\nabla \times \mathbf{H} = \mathbf{J} + \frac{\partial \mathbf{D}}{\partial t} \,, \tag{1.4}$$

where: $\mathbf{D} = \varepsilon\mathbf{E}$, $\mathbf{B} = \mu\mathbf{H}$, ε and μ are the permittivity and permeability of the medium, respectively. In the situation considered by Schumann: $\rho = 0$, $\mathbf{J} = 0$, $\mu = \mu_0$, $\varepsilon = \varepsilon_0$, where ε_0 is the permittivity of free space ($8.85\cdot 10^{-12}$ F/m), and μ_0 is the permeability of free space, ($4\pi\cdot 10^{-7}$ H/m). With the time dependence given as $e^{-i\omega t}$, we find from (1.3) and (1.4) that:

$$\nabla\times\mathbf{E} = i\omega\mathbf{B}\,, \tag{1.5}$$

$$\nabla\times\mathbf{B} = -i\omega\varepsilon_0\mu_0\mathbf{E}\,. \tag{1.6}$$

Using these equations, we get:

$$\nabla\times\nabla\times\mathbf{B} = \omega^2\varepsilon_0\mu_0\mathbf{B}\,. \tag{1.7}$$

The left side of (1.7) can be modified using the vector formula: $\nabla\times\nabla\times\mathbf{B} = \nabla\cdot(\nabla\cdot\mathbf{B}) - \nabla^2\mathbf{B}$. As the divergence of the magnetic field is zero, then we obtain the Helmholtz equation:

$$\left(k_0^2+\nabla^2\right)\mathbf{B} = 0\,,\ k_0^2 = \omega^2\varepsilon_0\mu_0 = \omega^2/c^2\,, \tag{1.8}$$

where: k_0 – is the wave number of free space, and $c^2 = 1/\varepsilon_0\mu_0$.

Since the ground and atmosphere are co-centered and spherical layers, it is convenient to use the spherical coordinate system ($r,\ \theta,\ \varphi$) with the center located in the center of the planet.

For the field components the vectorial equation (1.5) and (1.6) in the spherical coordinate system are:

$$\frac{1}{r\sin\theta}\left(\frac{\partial}{\partial\theta}\sin\theta E_\varphi - \frac{\partial}{\partial\varphi}E_\theta\right) = i\omega B_r\,, \tag{1.9a}$$

$$\frac{1}{r\sin\theta}\left(\frac{\partial}{\partial\varphi}E_r - \frac{\partial}{\partial r}r\sin\theta E_\varphi\right) = i\omega B_\theta\,, \tag{1.9b}$$

$$\frac{1}{r}\left(\frac{\partial}{\partial r}rE_\theta - \frac{\partial}{\partial\theta}E_r\right) = i\omega B_\varphi\,, \tag{1.9c}$$

$$-\frac{1}{r\sin\theta}\left(\frac{\partial}{\partial\theta}\sin\theta B_\varphi - \frac{\partial}{\partial\varphi}B_\theta\right) = i\omega\varepsilon_0\mu_0 E_r\,, \tag{1.9d}$$

$$-\frac{1}{r\sin\theta}\left(\frac{\partial}{\partial\varphi}B_r - \frac{\partial}{\partial r}r\sin\theta B_\varphi\right) = i\omega\varepsilon_0\mu_0 E_\theta\,, \tag{1.9e}$$

$$-\frac{1}{r}\left(\frac{\partial}{\partial r}rB_\theta - \frac{\partial}{\partial\theta}B_r\right) = i\omega\varepsilon_0\mu_0 E_\varphi\,. \tag{1.9f}$$

The Laplacian operator of a magnetic field component in this system is:

$$\nabla^2 B = \frac{1}{r}\frac{\partial^2}{\partial r^2}(rB) + \frac{1}{r^2\sin\theta}\frac{\partial}{\partial\theta}\left(\sin\theta\frac{\partial B}{\partial\theta}\right) + \frac{1}{r^2\sin^2\theta}\frac{\partial^2 B}{\partial\varphi^2}\,, \tag{1.10}$$

and inserting (1.10) into (1.8), we get:

$$\frac{\omega^2}{c^2}B + \frac{1}{r}\frac{\partial^2}{\partial r^2}(rB) + \frac{1}{r^2\sin\theta}\frac{\partial}{\partial\theta}\left(\sin\theta\frac{\partial B}{\partial\theta}\right) + \frac{1}{r^2\sin^2\theta}\frac{\partial^2 B}{\partial\varphi^2} = 0\,. \tag{1.11}$$

To solve this equation, we separate the variables for the radial and transverse part:

$$B(r,\theta,\varphi)=\mathrm{R}(r)\mathrm{Y}(\theta,\varphi)=\mathrm{R}(r)\Theta(\theta)\Phi(\varphi) \tag{1.12}$$

Hence from (1.11), we obtain:

$$\frac{\omega^2}{c^2}\mathrm{R}\Theta\Phi+\Theta\Phi\frac{\partial^2}{\partial r^2}(r\mathrm{R})+\frac{\mathrm{R}\Phi}{r^2\sin\theta}\frac{\partial}{\partial\theta}\left(\sin\theta\frac{\partial\Theta}{\partial\theta}\right)+\frac{\mathrm{R}\Theta}{r^2\sin^2\theta}\frac{\partial^2\Phi}{\partial\varphi^2}=0\,.$$

Dividing by $\mathrm{R}\,\Theta\Phi$ and multiplying by r^2, finally we find:

$$r^2\frac{\omega^2}{c^2}+r\frac{1}{\mathrm{R}}\frac{\partial^2}{\partial r^2}(r\mathrm{R})+\frac{1}{\Theta}\frac{1}{\sin\theta}\frac{\partial}{\partial\theta}\left(\sin\theta\frac{\partial\Theta}{\partial\theta}\right)+\frac{1}{\Phi}\frac{1}{\sin^2\theta}\frac{\partial^2\Phi}{\partial\varphi^2}=0\,. \tag{1.13}$$

Equation (1.13) can be separated into three independent parts: radial, azimuthal and zonal. The relation is correct when the sum of the azimuthal and the zonal part is equal to some constant value – the separation constant. Assuming that this value is a, the radial part of (1.13) is:

$$r^2\frac{\omega^2}{c^2}+r\frac{1}{\mathrm{R}}\frac{d^2}{dr^2}(r\mathrm{R})=a\,, \tag{1.14}$$

and then:

$$\frac{1}{\Theta\sin\theta}\frac{d}{d\theta}\left(\sin\theta\frac{d\Theta}{d\theta}\right)+\frac{1}{\Phi\sin^2\theta}\frac{d^2\Phi}{d\varphi^2}=-a\,. \tag{1.15}$$

Again using the separation of the variables in (1.15), we have:

$$\frac{1}{\Phi}\frac{d^2\Phi}{d\varphi^2}=-m^2\,. \tag{1.16}$$

As $\Phi(\varphi)$ must be a periodic function with the period ~2π, the azimuthal part has two solutions: $\Phi(\varphi)\sim e^{\pm im\varphi}$, where m is an integer, and by analogy is called the azimuthal wavenumber. Inserting (1.16) into (1.15), with $x=\cos\theta$, $dx=d(\cos\theta)$, $a=n(n+1)$, we obtain the Legendre equation:

$$\frac{d}{dx}\left[\left(1-x^2\right)\frac{d\Theta}{dx}\right]+\left[n(n+1)-\frac{m^2}{1-x^2}\right]\Theta=0\,, \tag{1.17}$$

which solutions are the associated Legendre polynomials $P_n^m(x)$. Finally, replacing $r\mathrm{R}(r)$ by $A(r)$, in (1.14), we get:

$$\frac{d^2A(r)}{dr^2}-\left[\frac{n(n+1)}{r^2}-\frac{\omega^2}{c^2}\right]A(r)=0\,. \tag{1.18}$$

The solutions of this expression are the spherical Bessel functions. The constant n = 1,2,..., describes the angular dependence of modes, and the azimuthal wave number is in the range of $-n\le m\le n$; therefore, for each m there are $2n+1$ solutions. The analysis of wave propagation in such a case is complicated. However, if we are solely interested in the resonance of the system, we can consider waves of very low frequencies. As it was aforementioned, we are interested in the TM modes. Additionally, we can assume, due to symmetry of the case, that the considered EM field does not depend on the azimuthal component *φ*, thus $\frac{\partial}{\partial\varphi} = m = 0$. From (1.2), written in the spherical coordinates:

$$\nabla\cdot\mathbf{B} = \frac{1}{r^2}\frac{\partial}{\partial r}\left(r^2 B_r\right) + \frac{1}{r\sin\theta}\frac{\partial}{\partial\theta}\left(\sin\theta B_\theta\right) + \frac{1}{r\sin\theta}\frac{\partial}{\partial\varphi}B_\varphi = 0\,, \tag{1.19}$$

we can see that if $B_r = 0$, and $\frac{\partial}{\partial\varphi} = 0$, then the second component of (1.19) must be 0, and $B_\theta = 0$. Only nonzero component of the magnetic field is B_φ, and from (1.9) the nonzero electric component are: E_θ and E_r. Finally, from (1.12), the magnetic field can be given by:

$$B_\varphi(r,\theta) = \frac{A(r)}{r}P_n(\cos\theta)\,. \tag{1.20}$$

In this way, with (1.9d), (1.9c), (1.17), and (1.20), we obtain:

$$E_r = \frac{ic^2}{\omega}\frac{1}{r\sin\theta}\frac{\partial}{\partial\theta}\left(\sin\theta B_\varphi\right) = -\frac{ic^2}{\omega}\frac{A(r)}{r^2}n(n+1)P_n\left(\cos\theta\right), \tag{1.21}$$

$$E_\theta = -\frac{ic^2}{\omega}\frac{1}{r}\frac{\partial}{\partial r}\left(rB_\varphi\right) = -\frac{ic^2}{\omega}\frac{\partial A(r)}{\partial r}P_n\left(\cos\theta\right). \tag{1.22}$$

As *R* >> *h*, we can simplify the term standing in the square bracket in expression (1.18) by a constant $\tilde{q}^2$, in which *r* = *R* [*Jackson*, 1999]. Then (1.18) becomes:

$$\frac{d^2A(r)}{dr^2} - \left[\frac{n(n+1)}{R^2} - \frac{\omega^2}{c^2}\right]A(r) \cong 0\,. \tag{1.23}$$

Hence, it is a simple differential equation, and its solution is:

$$A(r) \cong \tilde{C}\cos(\tilde{q}r) + \tilde{D}\sin(\tilde{q}r)\,. \tag{1.24}$$

From the boundary conditions for the perfect conductor, E_θ is zero for *r* = *R* and *r* = *R* + *h*. Putting on the abovementioned conditions, we obtain from (1.22):

$$\frac{dA(r)}{dr}\Big|_{r=R,R+h} = 0\,. \tag{1.25}$$

Therefore, from (1.25) and replacing *A*(*r*) with (1.24), we get a system of two equations:

$$\frac{dA(r)}{dr}\Big|_{r=R} = -\tilde{C}\tilde{q}\sin(\tilde{q}R) + \tilde{D}\tilde{q}\cos(\tilde{q}R) = 0\,, \tag{1.26a}$$

$$\frac{dA(r)}{dr}\Big|_{r=R+h} = -\tilde{C}\tilde{q}\sin(\tilde{q}R+\tilde{q}h) + \tilde{D}\tilde{q}\cos(\tilde{q}R+\tilde{q}h) = 0\,, \tag{1.26b}$$

from (1.26a), we have $\tilde{C} = \cos(\tilde{q}R)$, $\tilde{D} = \sin(\tilde{q}R)$, and so that: $A(r) \cong \cos\left[\tilde{q}(r-R)\right]$. Additionally, from (1.26b), we obtain that: $\sin(\tilde{q}h) = 0$, that is: $\tilde{q} = \tilde{n}\pi/h$, where $\tilde{n} = 0,1,2,...,$. In turn, $\tilde{q}$, as can be seen from (1.23) is proportional to *ω/c*. Since on Earth and on Mars, the distance between the waveguide boundaries is of the order of 100 km, we find, for $\tilde{n} = 1$, a circular frequency $\omega \sim 10^4$ Hz. It is a TE mode. Low frequencies occur only for $\tilde{n} = 0$, which implies $\tilde{q} = 0$, and hence $A(r) = const$. From (1.23), we find that:

$$\frac{n(n+1)}{R^2} - \frac{\omega^2}{c^2} = 0 \,. \tag{1.27}$$

Inserting the relation: $\omega = 2\pi f$ into (1.27), we get the final solution for the natural frequencies of the resonant cavity – the Schumann formula [*Schumann*, 1952]:

$$f_n = \sqrt{n(n+1)}\frac{c}{2\pi R} \,. \tag{1.28}$$

Using (1.20)-(1.22), we can establish the field components: $E_r \sim 1/r^2 \cdot P_n(\cos\theta)$, $E_\theta = 0$, and $B_\varphi \sim 1/\mathrm{r} \cdot P_n(\cos\theta)$. This is a TEM mode, with nonzero components orthogonal to the direction of the propagation and to each other [*Nickolaenko and Hayakawa*, 2002].

Since SR frequencies are normal modes of the cavity, they are dominant in the noise power spectrum of ELF waves. If the planetary cavities were made of perfect conductors, SR would be visible as peaks at the natural frequencies given by (1.28). However, in real situations, with the boundaries of finite conductivity, this is not true. We can study this problem by taking as an example the terrestrial cavity. Substituting the radius of Earth $R = 6370$ km, from (1.28) we get the values of the resonant frequencies equal to those obtained by Schumann (Table 1). The consecutive resonance frequencies are connected by the relationship: $f_n = 7.5\sqrt{n(n+1)}$. These values are higher by more than 20% as compared to the observed [*Balser and Wagner*, 1960] (Table 1).

Table 1. The Schumann resonance frequencies on Earth.

	***n* = 1**	***n* = 2**	***n* = 3**	***n* = 4**	***n* = 5**
1. The theoretical f using (1.28) [Hz]	10.6	18.3	25.9	33.5	41.0
2. The observed f [Hz]	7.8	14.1	20.3	26.4	32.5
The difference between 1 and 2 [%]	26.0	23.0	22.0	21.0	21.0
The observed $f/\sqrt{n(n+1)}$ [Hz]	5.5	5.8	5.9	5.9	5.9
3. The theoretical f using (1.29) [Hz]	10.5	18.2	25.8	33.3	40.7
4. The theoretical f using (1.30) [Hz]	7.7	13.9	20.1	26.3	32.6
The difference between 2 and 4 [%]	1.3	1.4	1.0	0.4	0.3

This is due Schumann's idealization of the cavity. The final outcome is affected by several issues. The exact modeling should take into account the fact that neither of the boundaries is spherical, but is a more or less deformed triaxial ellipsoid. From the above discussion, we can see that the term $\sqrt{n(n+1)}$ is related to the geometry of the cavity. The difference between the theoretical and observed values allows establishing the shape of the cavity [*Nickolaenko and Hayakawa*, 2002]. From the observation, we can find easily the relationship between consecutive frequencies: $f_n = 5.8\sqrt{n(n+1)}$. The differences between these values and the theoretical ones display that the influence of the Earth shape on the SR parameters does not exceed 5% (Table 1). Therefore, we may assume that the ionosphere and ground are almost spherical. The main problem is then related to the constant term in (1.28). The first problem is connected to using the radius value in (1.23) as the only parameter. A more exact formula, which takes into consideration the distance between the boundaries, is [*Bliokh et al.*, 1980]:

$$f_n = \sqrt{n(n+1)\left(1-\frac{h}{R}\right)}\frac{c}{2\pi R}\ . \tag{1.29}$$

As presented in Table 1, the differences between the results obtained from (1.28) and (1.29) are very small, and thus this is not the main factor responsible for the observed discrepancy. The last issue is connected with the speed of light utilized as the wave phase velocity. The finite conductivity boundaries influence wave propagation. Waves are not reflected without loss, and the speed of light is not a proper value. Then the Schumann resonance frequencies can be given by:

$$f_n = \frac{v_{ph}}{c} f_{0n}, \quad f_{0n} = \frac{c}{2\pi R}\sqrt{n(n+1)}\ , \tag{1.30a,b}$$

where: v_{ph} – the phase velocity of ELF waves. Due to this relation, we are able to estimate the conductivity of the ionosphere and ground by comparing the measured and calculated values of ELF wave phase velocities (Table 1). The wave phase velocity in a given cavity can be easily determined using the analytical modeling introduced in the course of this chapter and presented in detail in Chapter 3.

Other important parameters, which describe the resonator, are the Q factors. The Q factor (quality factor) measures the response sharpness of the cavity to excitations, and is defined as 2π times the ratio of the time-averaged energy stored in the cavity to the energy loss per cycle. The Q factor can be defined as the ratio between the resonant frequency and the half power bandwidth of the resonant peak [*Jackson*, 1999]. The Q factor is also inversely proportional to the relative error of the resonant frequency estimation [*Jackson*, 1999; *Nickolaenko and Hayakawa*, 2002]:

$$Q_n = \frac{f_n}{\Delta f_n} \ ,$$

where: Δf_n – the half power bandwidth. The Q factor for the values presented in Table 1 is of the order of 4, and also indicates that the terrestrial cavity is a damped waveguide. The more damped the cavity, the smaller the Q factor.

1.2.2 Introduction to ELF propagation modeling

Point 1.2.1 displays that the ratio between the speed of light and the phase velocity is very important for ELF propagation in the waveguides made of partially conducting media. The phase velocity in such media is equal to the velocity of light in free space divided by the refractive index η, which is in turn related to the EM properties of the waveguide boundaries.

The EM properties of the ionosphere and the ground can be characterized by the complex conductivity:

$$\bar{\sigma}(z) = \sigma(z) - i\omega\varepsilon(z) \, , \qquad (1.31)$$

associated with the conduction and displacement current:

$$\mathbf{J} + \frac{\partial \mathbf{D}}{\partial t} = \sigma\mathbf{E} - i\omega\varepsilon\mathbf{E} = \bar{\sigma}\mathbf{E} \, ,$$

the complex permittivity, $\bar{\varepsilon} = \frac{i\bar{\sigma}}{\omega}$, and the magnetic permeability, $\bar{\mu} = \mu$ (we can assume that there is no magnetic loss). From (1.3) and (1.4), we can get the Helmholtz wave equation, using a similar transformation as in (1.7):

$$\left(\bar{k}^2 + \nabla^2\right)\mathbf{B} = 0 \, , \; \bar{k}^2 = \omega^2\varepsilon\mu + i\mu\sigma\omega = i\mu\bar{\sigma}\omega \, . \qquad (1.32a,b)$$

The wave number is a complex number:

$$\bar{k} = k_1 + ik_2 = \omega / v_{ph} - i\alpha \, , \qquad (1.33)$$

where its imaginary part describes the wave attenuation, given by the attenuation coefficient α, and the real part the frequency, the phase velocity, and the refractive index. As the wave number $\bar{k} \neq k_0$, the refractive index, $\eta = c/v_{ph} = c\bar{k}/\omega$, is not equal 1. As seen from (1.32b), the wave number, and at the same time the refractive index, depends on the conductivity of the boundaries.

The first term in (1.32b) is related to the energy storage, the second to its dissipation. To describe the medium, we use commonly the loss factor, which is the ratio between these two terms: $\sigma/(\varepsilon\omega)$, or the loss tangent, $\tan\xi = \sigma/(\varepsilon\omega)$. EM field propagate by radiation for high frequencies ($\sigma < \varepsilon\omega$), and by diffusion for low frequencies ($\sigma > \varepsilon\omega$). The boundary condition takes place at $\tan\xi = 1$. In the ELF range, the waves propagate in the diffusive regime, controlled by the conductivity, not by the permittivity of the medium, as it is in the radar range.

As for almost all planetary media $\mu = \mu_0$, we find that:

$$\bar{k}^2 = \omega^2\bar{\varepsilon}\mu = k_0^2c^2\bar{\varepsilon}\mu = k_0^2\bar{\eta}^2 \,,\ \bar{\eta}^2 = \bar{\varepsilon}\mu/\varepsilon_0\mu_0 = \varepsilon_r + \left(\frac{i\sigma}{\varepsilon_0\omega}\right), \tag{1.34a,b}$$

where: ε_r – is the relative permittivity. The medium is regarded as a conductor, when $\sigma/\varepsilon_0\omega >> 1$, and as an insulator if $\sigma/\varepsilon_0\omega << 1$. At a 10 Hz frequency ($\omega$ ~60 Hz), this boundary value is $\sigma = 5\cdot10^{-10}$ S/m [*Rycroft et al.*, 2008].

The amplitude of an electromagnetic wave, during its propagation into a medium, decreases exponentially with distance. The scale length for this penetration is given by the skin depth δ, the depth at which the wave amplitude decreases e-times. From the wave number (1.32b), we see that:

$$\bar{k} = \sqrt{i\mu\bar{\sigma}\omega} = (1+i)\sqrt{\frac{\mu\omega\bar{\sigma}}{2}} = \frac{1}{\delta} + \frac{i}{\delta} \,,\ \delta = \sqrt{\frac{2}{\mu\omega\bar{\sigma}}} \,. \tag{1.35a,b}$$

The skin depth increases as σ decreases. For the boundary value of the conductivity ($5\cdot10^{-10}$ S/m), we find that the skin depth is very large, δ ~7000 km.

The ionosphere and the ground are not made of one layer of constant conductivity. The conductivity of the atmosphere increases with altitude, due to cosmic and solar radiation. Also, as shown in point 1.2.3, it becomes a tensor under the influence of magnetic field. The ground is a mixture of many different rocks, ices, ores, and waters. In addition, its conductivity changes with depth since it is related to temperature. In ELF wave propagation modeling, it is important to estimate the conductivity profiles of the boundaries.

On Earth, liquid water exists at the planetary surface in the form of oceans and seas, but it is also present almost everywhere in rocks. Using the skin depth approach, it is easy to prove that the terrestrial ground is indeed a good conductor at 10 Hz. The average value of the continental surface conductivity is ca. 10^{-2} S/m [*Lowrie*, 2007], and the averaged ocean water conductivity is

3.2 S/m [*Olsen and Kuvshinov*, 2004]. It leads to the skin depth ~1.6 km for the continental crust, and ~100 m for the oceans, giving on average a value of hundreds of meters. Thus, the ground is not a factor influencing the wave phase velocity, and thereby the SR parameters. For that reason, in the history of SR studies, which were carried out in relation to the terrestrial waveguide, the exact influence of the ground on ELF propagation was not established.

Propagating waves in the terrestrial cavity are reflected and transmitted into the ionosphere [*Wait*, 1970]. The reflection coefficients depend on the atmospheric conductivity profile, which varies between daytime and nighttime, the local ambient magnetic field, and the direction of incidence. Modeling of ELF propagation in a planetary waveguide made of the non-uniform and partially conducting ionosphere is possible using numerical and analytical methods. The numerical modeling allows including detailed conductivity profiles, but owing to the time needed to conduct satisfactory simulations, does not provide relationships between the conductivity and propagation parameters. On the contrary, analytical methods allow studying these relationships easily and in a wide range.

The first models were very simple, with the ionosphere made of one uniform layer of finite conductivity [*Wait*, 1962], but they allowed constructing better techniques. Later, the ionosphere was approximated with a few homogenous layers [*Chapman and Jones*, 1964]. The more sophisticated numerical techniques allowed studying multi-layer models with thin uniform layers [*Galejs*, 1965] as well as using direct full-wave integration of the complex differential equations [*Pappert and Moler*, 1974]. However, the limitation of numerical methods forced researchers to use less complex three-layer models of the conductivity profiles in order to study the relationship between the ionospheric conductivity and the SR parameters [*Tran and Polk*, 1979; *Mushtak and Williams*, 2002]. The full-wave approach revealed that only two characteristic layers of the ionosphere influence the behavior of the field components, and all the properties of the ionosphere not associated with these two layers are unimportant for the ELF propagation parameters [*Madden and Thompson*, 1965; *Cole*, 1965]. Basing on these findings, *Greifinger and Greifinger* [1978] proposed the analytical method that allowed studying firstly isotropic, and next anisotropic waveguides [*Greifinger and Greifinger*, 1986].

Presently, analytical as well as numerical techniques are applied to study wave propagation. Three numerical techniques are utilized most frequently. The finite-difference time-domain (FDTD) technique, a grid-based method was used for simulations of the terrestrial and the Martian cavity [*Soriano et al*., 2005; 2007; *Yang et al*. 2006]. Also, the finite element method (FEM) was applied to solve the partial differential equations for complex domains by employing unstructured meshes [*Simoes et al*. 2008a,b]. Besides these two techniques, the transmission line method (TLM), employing a circuit-like approach with resistor and capacitor networks, was employed for SR modeling [*Morente et al*. 2003, *Molina-Cuberos et al*., 2006]. The most popular analytical model is the isotropic Greifingers' approach [*Mushtak and Williams*, 2002], in which the conductivity profiles are approximated by exponential functions. These approximated profiles can be easily integrated in order to obtain the propagation parameters. Firstly, this method was used with two-exponential profiles, however as they do not represent a knee-like change in the ionosphere conductivity, the knee-models were developed, and are used to study planetary cavities [*Mushtak and Williams*, 2002; *Pechony and Price*, 2004]. Such a model is also employed in this work, and is fully described in Chapter 3.

1.2.3 Analytical modeling of ELF propagation

To analyze ELF propagation in a planetary cavity, we use the Maxwell equations (1.1)-(1.4) with the appropriate boundary conditions and Ohm's law.

Ohm's law is a constitutive equation relating current density with electric field: $\mathbf{J} = \sigma \mathbf{E}$. As **E** and **J** are vectors, then σ must be a tensor in general. In isotropic medium, it is in fact a scalar, and **E** and **J** have the same direction. In anisotropic mediums σ is a tensor. Linearity of conductivity is almost always true, but sometimes, it is a function of **E**. Current flow in the atmosphere is one of such examples as the electric breakdown takes place when $E > E_{critical}$ [*Zhdanov and Keller*, 1994].

As in the planetary cavity $R >> h$, we can assume that propagating ELF waves are plane waves, and to study such a situation we can use the Cartesian coordinate system. The boundary conditions that represent situation in which plane EM waves penetrate into a finite conductive medium were presented in the work of *Jackson* [1999]. Inside perfect conductors charges and currents vanish. The boundary condition on the normal magnetic component is related to (1.2):

$$\mathbf{n} \cdot \mathbf{B} = \mathbf{n} \cdot \mathbf{B}_c$$

where: the subscript c denotes the interior of the conductor, **n** – is the unit normal vector. As there is a very thin surface of the conductor where currents can flow, the magnetic flux disappears, and the boundary condition on the tangential electric component from (1.3) is:

$$\mathbf{n} \times \mathbf{E} = \mathbf{n} \times \mathbf{E}_c$$

Consequently, only the normal electric and the tangential magnetic components are different from zero and fall instantly to zero inside the conductor. With a finite conductivity medium, the fields should act in a similar way, but they disappear in a thin layer below the surface, given by the skin depth. Similarly to the surface current density, a current flows inside the conductor and opposes the field penetration in to the medium. In a medium of finite conductivity and described by Ohm's law, there is no surface current density as it would require infinite **E** at the boundary [*Griffiths*, 2005]. As a result, from (1.4), we get the boundary condition:

$$\mathbf{n}\times\mathbf{H}=\mathbf{n}\times\mathbf{H}_c\,. \tag{1.36}$$

For a TEM wave that can be described by $e^{i(kx-\omega t)}$, and which propagates along the x-axis parallel to the surface ($z = 0$), the electric component of ELF field is directed along the z-axis and the magnetic component along the y-axis. If the boundaries were of infinite conductivity, E_z and H_y would be the only components, however due to their finite conductivity, the magnetic component penetrates into the boundary to the penetration depth given by δ and generates an additional electric component E_x. From equations (1.3), (1.4), and (1.31), we obtain:

$$\left(\nabla\times E\right)_y=\left(\frac{\partial E_x}{\partial z}-\frac{\partial E_z}{\partial x}\right)=i\mu\omega H_y\,, \tag{1.37a}$$

$$\left(\nabla\times H\right)_x=-\frac{\partial H_y}{\partial z}=\left(\sigma-i\varepsilon\omega\right)E_x=\bar{\sigma}E_x\,, \tag{1.37b}$$

$$\left(\nabla\times H\right)_z=\frac{\partial H_y}{\partial x}=\left(\sigma-i\varepsilon\omega\right)E_z=\bar{\sigma}E_z\,. \tag{1.37c}$$

The main complication stems from the fact that the boundaries are not sharp, and their conductivity changes with altitude.

Modeling of ELF propagation is convenient to conduct using the complex propagation parameter $\bar{S}$ [*Galejs*, 1972]:

$$\bar{S}\equiv\bar{k}/k_0\,. \tag{1.38}$$

Employing the complex wave number given by (1.33), we can write the propagation parameter as: $\bar{S}=c/v_{ph}-i\alpha c/\omega$. This parameter fully describes the propagation properties of a ground-ionosphere waveguide: the phase velocity v_{ph}, the attenuation coefficient α, as well as the quality factor Q [*Galejs*, 1972]:

$$v_{ph}=c/\mathrm{Re}\,\bar{S}(f)\,,\ \alpha=2\pi f\left|\mathrm{Im}\,\bar{S}(f)\right|/c\,,\ Q=\frac{\mathrm{Re}\,\bar{S}}{2\mathrm{Im}\left|\bar{S}\right|} \tag{1.39a,b,c}$$

Analytical modeling of ELF propagation in planetary cavities can be performed using some simplifications. The first simplification is related to the work of *Greifinger and Greifinger* [1978], in which the authors established that ELF propagation in the planetary cavity is significantly influenced only in the limited altitude range. The lower altitude limit, $\bar{h}_0$, is the altitude at which displacement current is equal to conduction current: $\sigma = \varepsilon_0\omega$. It describes the height at which the electric component starts to be strongly attenuated, and its real part can be roughly described as the ionospheric height. The upper altitude, $\bar{h}_1$, is the altitude at which $\omega\tau_D = 1$, where τ_D – is the magnetic diffusion time through a conductivity scale height. It shows where the magnetic component becomes strongly attenuated and represents the upper boundary of the waveguide. It is the height at which the character of the propagation changes from wave-like to diffusion-like. *Greifinger and Greifinger* [1978] found that those characteristic altitudes are related to the propagation parameter:

$$\bar{S}^2 = \bar{h}_1 / \bar{h}_0 . \tag{1.40}$$

The second simplification is a 2D formalism that can be employed as the distance between the boundaries of the cavity is very small in comparison to the length of ELF waves. Therefore, the waveguide can be treated as a transmission line. As a result, the relationship between the both transverse components of ELF field propagating in the waveguide is the same as the relationship between voltage and current in a transmission line [*Madden and Thompson*, 1965]. Although the previous works applied this technique only to the terrestrial waveguide, it may be used to study properties of any cavity. We can compare the waveguide to a transmission line of a unit length and width, which is described by the resistance and inductance related with the resistance of the ground (R_G) and atmosphere (R_A) as well as with currents flowing through these media (Figure 2). The transmission line is characterized by its elementary components: resistance $\tilde{R}$, conductance G, inductance L, and capacitance C [*Krakowski*, 1995].

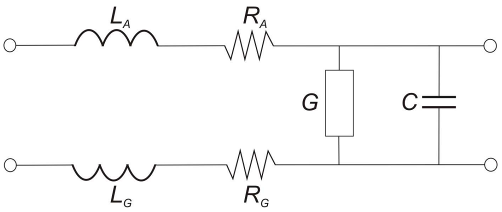

Figure 2. Scheme of the transmission line as a substitute of a planetary waveguide.

In the proposed elementary transmission line, we have the series inductors and resistors, and we can write that $L = L_G + L_A$, and $\tilde{R} = R_G + R_A$,.

Using a 2D formalism, we can employ the two-dimensional telegraph equation (TDTE) technique [*Madden and Thompson*, 1965]. We see that if $I(x,t)$ and $U(x,t)$ is a current and a voltage in the transmission line at given time t and at position x, then the voltage U at the resistor is $I\tilde{R}$ and at the coil $L\,\partial I/\partial t$. The charge on the capacitor is: $q = UC$. We get a decrease in the voltage and the current across the circuit. Using Kirchhoff's Laws in the limit as $\Delta x \to 0$, we have:

$$\frac{\partial}{\partial x}U = -L\frac{\partial}{\partial t}I - \tilde{R}I\,, \tag{1.41a}$$

$$\frac{\partial}{\partial x}I = -C\frac{\partial}{\partial t}U - GU\,. \tag{1.41b}$$

Performing differentiation over x in (1.41a) and substituting the calculated terms by (1.41b), we get a partially differential equation, the telegraph equation [*Jeffrey*, 2003]:

$$\frac{\partial^2}{\partial x^2}U = LC\frac{\partial^2}{\partial t^2}U + \left(LG + \tilde{R}C\right)\frac{\partial}{\partial t}U + G\tilde{R}U\,. \tag{1.42}$$

As the conductance of the ionosphere changes gradually, the distance between the plates is not easy to determine. To solve this problem *Kirillov* [1996] proposed an approach based on the complex values of the capacitance and inductance. From (1.42), we obtain:

$$\frac{\partial^2}{\partial x^2}\overline{U} = -\left(LC\omega^2 - \left(\tilde{R}C + LG\right)i\omega - G\tilde{R}\right)\overline{U} = -\overline{L}\,\overline{C}\,\overline{U}\,, \tag{1.43}$$

where: $\overline{C} = C - iG/\omega$ and $\overline{L} = L - i\tilde{R}/\omega$ are the complex capacitance and conductance, respectively. These values can be given by [*Kirillov*, 1993; *Kirillov et al.*, 1997]:

$$\overline{L} = \mu\overline{h}_m\,,\ \overline{C} = \varepsilon/\overline{h}_e\,. \tag{1.44}$$

Therefore, such a 2D transmission line can be characterized, instead of four parameters, by two complex numbers: $\overline{h}_e$ and $\overline{h}_m$, called the electric and the magnetic altitude, respectively. The electric altitude is responsible for the behavior of the vertical electric component and the magnetic altitude, for the horizontal magnetic component of propagating waves. The electric altitude is much smaller than the magnetic altitude, related with the induction currents. From (1.43), we see that the phase velocity in a transmission line is given by $1/\sqrt{\overline{L}\,\overline{C}}$ and the wave number is: $\overline{k} = \omega\sqrt{\overline{L}\,\overline{C}}$, then from (1.38) and (1.44):

$$\overline{S}^2 = c^2\overline{L}\,\overline{C} = \overline{h}_m/\overline{h}_e\,. \tag{1.45}$$

As (1.40) and (1.45) are very similar to each other, they are used as equal [*Greifinger et al.*, 2007]. Therefore, to solve the problem of ELF propagation in a waveguide, we need to determine these characteristic altitudes.

To obtain those altitudes, we can use the boundary conditions at the surface ($z = 0$), at which: $\overline{L} = \overline{\Phi}/\overline{I}(0)$ and $\overline{C} = \overline{q}(0)/\overline{U}$. The charge collected at the surface is equal to $\overline{q}(0) = \varepsilon E_z(0) = \varepsilon E_{0z}$, and the current which flows at the surface is $\overline{I}(0) = H_y(0) = H_{0y}$ [*Kirillov et al.,* 1997]. From the definition:

$$\overline{U} = -\int_0^\infty E_z(z)dz, \quad \overline{\Phi} = \mu\int_0^\infty H_y(z)dz \tag{1.46a,b}$$

From relations (1.44) and (1.46), we have [*Kulak et al.*, 2013]:

$$\overline{h}_e = -\frac{1}{E_{0z}}\int_0^\infty E_z(z)dz, \; \overline{h}_m = \frac{1}{H_{0y}}\int_0^\infty H_y(z)dz, \tag{1.47a,b}$$

where: $E_z(z)$ and $H_y(z)$ are the vertical electric and horizontal magnetic field distributions and E_{0z} and H_{0y} are their amplitudes at the surface. The distributions are calculated by solving Maxwell's equations in a medium characterized by a complex conductivity. In planetary cavities, the electric altitude is equal to the sum of the electric altitude of the ionosphere $\overline{h}_{ei}$ and the ground $\overline{h}_{eg}$. Similarly, the magnetic altitude is $\overline{h}_m = \overline{h}_{mi} + \overline{h}_{mg}$ [*Kulak et al.*, 2013]. The real parts of the magnetic and electric altitudes are presented in Figure 3. Their imaginary parts are related to wave attenuation. An analytical approach that allows calculating those altitudes with a multi-layer boundary is presented in Chapter 3.

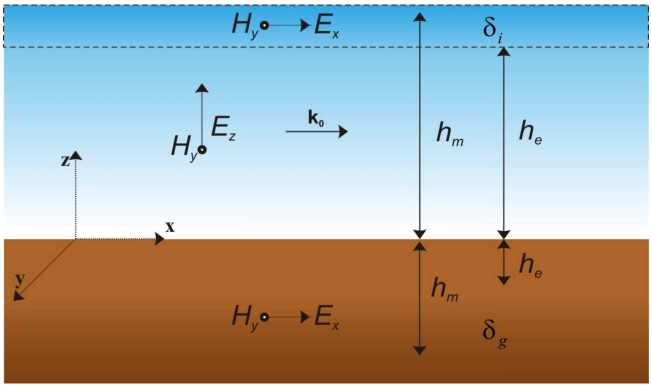

Figure 3. ELF wave penetration into the ground. Due to finite conductivities of the boundaries the magnetic component H_y penetrates the boundary to the depth given by δ and generates an additional electric component E_x. $h_{eg,i}$ and $h_{mg,i}$ are the real parts of the electric and magnetic altitudes of the ground and the ionosphere, respectively. The dashed line indicates the ionosphere boundary.

The conductivity of the ionosphere varies not only with altitude but also with longitude and latitude. The most important variation occurs at the terminator since the conductivity profiles for the nighttime and daytime ionosphere are different. As the scale of ionospheric irregularities is small compared with the ELF wavelengths, propagation is rather stable in the waveguide. However most common disturbances, such as those related to the solar cycle can influence the Schumann resonance parameters [*Satori et al.,* 2005; *Nickolaenko et al.*, 2015]. Also other factors are important, e.g. showers of meteoroids, which increase the conductivity of the lower layers of the ionosphere [*Molina-Cuberos et al.*, 2008]. Therefore, in order to get an accurate description of the ELF propagation, it is necessary to recognize all elements influencing the electrical properties of the cavity. They are described in general situation in the next point, and are presented in detail with reference to the Martian environment in Chapter 2.

1.2.4 Properties of a planetary cavity

As the planetary cavity and the global electric circuit are related to each other, we can describe the planetary cavity by describing the elements of the circuit [*Feynman et al.*, 2005].

In a terrestrial-type planetary environment, several factors allow for existence of the global atmospheric electric circuit. They are related to the presence of [*Aplin*, 2006]:

- two conducting layers;
- charge separation mechanisms to form a dipole structure in the atmosphere;
- electric discharges or precipitation to recharge the circuit;
- current flow related to mobile charged particles to discharge the circuit.

The atmosphere is normally a relatively good insulator (dielectric medium), however, due to ionization by e.g. galactic cosmic rays (GCR), above some altitude its conductivity increases so much that we can treat it like a conductor. This part of the atmosphere, called the ionosphere, forms the upper of the two conducting layers. The lower boundary is the conductive layer of the planetary ground. Rocks are generally insulators. Their higher conductivity can be related to the presence of some conducting medium, e.g. saline water, or high temperatures. Therefore, a ground conductive layer is present at the surface or within the subsurface of the planet. The ionosphere and the ground, between which there is an insulating medium, create a capacitor. In the atmosphere, the presence of phenomena associated with charge separation, leads to electric discharges or precipitation of charged particles. This can be described as a circuit battery and results in arising of the electric field potential difference between the ionosphere and the ground. In such electric field, mobile, charged particles move, resulting in a current flow and discharging of the circuit (Figure 4).

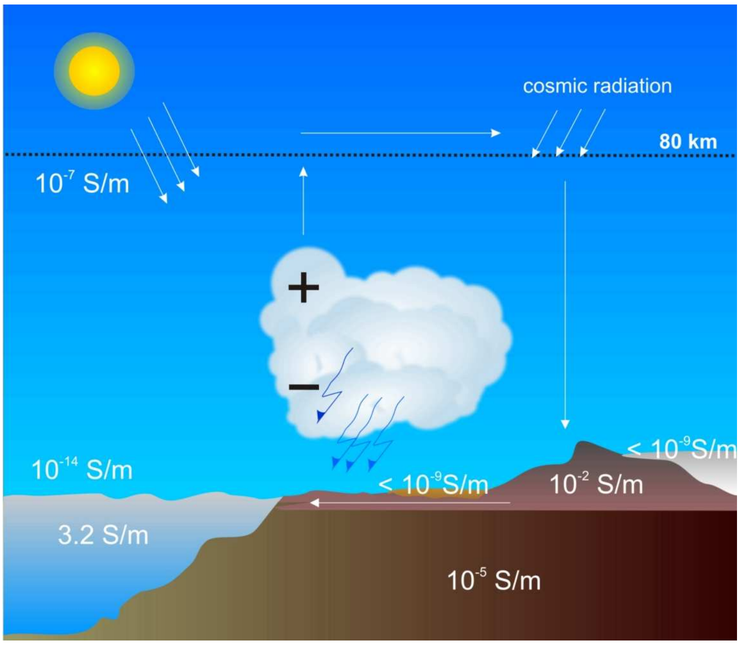

Figure 4. Terrestrial global electric circuit. The dashed line indicates the ionosphere boundary.

The AC (alternating current) component of the global electric circuit is associated with EM sources and can be studied by the Schumann resonance phenomenon. As the DC (direct current) component may respond to both precipitation and electrical discharges, and the AC component only to discharges, current estimated from those two components may be different. As a result, Schumann resonance only indicates the existence of the AC atmospheric electrical circuit, and for the DC circuit additional evidence of current flow is required. As opposite to the DC component, the AC component is unaffected by local conditions. Also, seasonal variations in the AC and DC components may not be linked directly [*Harrison*, 2005].

The resistance of the atmosphere (R_A) and ground (R_G) can be given by [*Harrison*, 2005]:

$$R_A = \frac{1}{4\pi R^2}\int_0^{z_1}\frac{dz}{\sigma_i(z)},\quad R_G = \frac{1}{4\pi R^2}\int_{z_2}^{0}\frac{dz}{\sigma_g(z)}. \qquad (1.48a,b)$$

The total global electrical resistance, R_T, can be found by: $R_T = R_G + R_A$. The capacitance of the global capacitor is given by: $C = 4\pi\varepsilon_0 R^2/H$, where H is the atmospheric scale height. The relaxation time constant for the global electric circuit, τ_c, is given by $\tau_c = CR_T$. In the terrestrial case, we have: $R_T = R_A$, R_A is ca. 250 Ω [*Volland*, 1984], and since the scale height is ca. 8 km, C is ca. 1 F; therefore, τ ~5 min. It is also convenient to introduce the electric relaxation time define as:

$$\tau_e = \varepsilon_0/\sigma_i. \qquad (1.49)$$

It is the time needed by the electric current to adjust to 1/e of its final value after some electric field is applied [*Roble and Tzur*, 1986]. This value increases with decreasing altitude, along with the conductivity. For the terrestrial atmosphere, its maximum value (ca. 40 min) is reached near the planetary surface, and it is a characteristic time of discharging of the global electric circuit after cessation of all electric discharges [*Roble and Tzur*, 1986; *Rycroft et al*., 2000].

On Earth, the surface of the planet is negatively charged, and the ionosphere positively due to the character of sources (see below). The ionospheric potential is ca. +250 kV with respect to the ground. It produces electrical field with an averaged strength of 130 V/m at the planetary surface. Lightning is a battery, which maintains global electric circuit [*Rycroft et al*., 2000]. *Price et al*. [2011] computed that there are 750 thunderstorms at any given moment, and *Christian et al*. [2003] found that a lightning flash rate is ca. 45 per second. Ions in the atmosphere generate electrical fair weather current of the 2 pA/m^2 density, which leads to discharging of the capacitor. The electric current flows downwards through the atmosphere to the ground (positive ions move downwards and negative ones upwards) [*Aplin*, 2008]. The atmospheric conductivity depends on geomagnetic location, aerosol pollution, and increases with height from ~10^{-14} S/m at the surface to 10^{-7} S/m in the ionosphere, at ~80 km altitude [*Rycroft et al*., 2008]. However, the ionosphere is not equipotential. Differences arise from interactions with the solar wind, the intrinsic magnetic field, auroral phenomena or ionospheric dynamo [*Rycroft et al*., 2000]. The electric field in the atmosphere shows a characteristic Universal Time (UT) diurnal variation. It was first detected on the Carnegie ship. The Carnegie variation has a broad peak in the late afternoon when the African thunderstorm center dominates and in the early evening when there is the thunderstorm maximum in the Americas [*Aplin*, 2006]. The African center is stronger then the American one by a factor of 2.8 [*Williams and Satori*, 2004]. The Carnegie variation minimum is in the morning. We know that there are also other temporal variations, e.g. seasonal (related to solar radiation and rotation), decadal (solar cycle effects), and probably of even longer periods [*Harrison*, 2005].

1.2.4.1 Low-frequency EM sources

The main source of ELF waves on Earth is lightning activity, even though a lightning discharge peak is located in the very low frequency range (VLF, 3-30kHz). Within a cumulonimbus cloud (*Cb*) charge exchange arises from particle interactions mainly between ice crystals and soft hail. Ice crystals more often become positively charged and soft hail negatively. This process is followed by charge separation from gravitational settling of hail, which results in forming a dipole within the cloud [*Saunders*, 2008]. When the electric field exceeds the breakdown voltage of the air, or the cloud, an electric discharge takes place. Most lightning events are intra-clouds and only small amount are cloud-to-ground events CG. Most of them, called GC$^-$, carry a negative charge to the ground. Globally lightning activity passes positive charge to the upper and negative charge to the lower conducting layer. Lightning phenomena also take place above clouds, at altitudes 45-95 km above the surface, in a form of transient luminous events (TLE), such as: sprites, elves, blue jets [*Yair*, 2012]. These phenomena have a direct, but a hard to measure impact on the electric circuit [*Rycroft et al.*, 2000]. Large CG^+ discharges (carrying positive charges to the ground) are known to cause sprites, and to be the source of the so-called Q bursts, strong radio signals in the ELF range, propagating around the planet [*Rakov and Uman*, 2006; *Ondraskova et al.*, 2008]. With intra-clouds discharges are related gamma-ray flashes (GRF), which are short burst of gamma-ray photons, produced shortly after the lightning. They are probably generated due to acceleration of ambient electrons to relativistic energies by the strong electric fields in thunderstorms. These relativistic electrons are responsible for production of runaway avalanches (relativistic runaway electron avalanche process, RREA). Natural charging processes do not generate fields to the breakdown level, but only to a few percent of this value [*Farrell and Desch*, 2001]. According to *Gurevich et al*. [2004, 2005] runaway electrons initiate lightning phenomena. However, to trigger the entire process some very energetic particles are necessary, and it is assumed that this role is played by cosmic radiation [*Yair*, 2012].

Thunderstorms are not the only source of electric discharges. They are also related with volcanic activity, which generates discharges during the ejection of pyroclastic materials, as well as to forest fires and large dusty phenomena, such as dust storms [*Rycroft et al.*, 2000]. Lightning activity is not the only mean to transfer charges in the electric circuit. Coronal point discharges known as St. Elma fires as well as convection may play an important role [*Rycroft et al.*, 2000]. Also precipitation from electrified clouds is very essential, transferring negatively charge water droplets [*Aplin et al.*, 2008].

Geomagnetic pulsations, visible on the schematic diagram presented in Figure 1, are generated by the solar wind–magnetosphere coupling. They cover the ultra-low frequency (ULF) range (ca. 1 mHz to ca. 1 Hz) and have periods smaller than few minutes [*Saito*, 1969]. They can be divided into two groups: continuous Pc and irregular Pi [*Alperovich and Fedorov*, 2007]. They are related to various electromagnetic phenomena associated with hydromagnetic waves. The short-period pulsation may display aurora variations, ionospheric current changes, and can be associated with the ionospheric Alfven resonator. The ionospheric Alfven resonator results from shear Alfven waves trapped in the vertical direction between the ionosphere and the magnetosphere [*Belyaev et al.*, 1990; *Lysak*, 1993]. The resonator is excited by lightning generated emission, similarly as Schumann resonance. The long-period pulsations are related to resonant phenomenon of the magnetosphere [*Campbell*, 2003]. On Earth, geomagnetic pulsations are observed from space and from the planetary surface [*Mursula et al.*, 2001].

Another source of oscillation in the terrestrial cavity is related to thermal and gravitational tides. These tides move the atmospheric plasma in the planetary magnetic field, which leads to generation of electric fields and currents in the ionospheric dynamo region (see below). These oscillations are not related directly to solar activity, and therefore, they are called the solar quiet (Sq) variations. They have spectral peaks that occur with periods: 24, 12, 8 and 6 h. The Sq variations affect the planetary mantle to the depth of 400-600 km, inducing currents in these regions [*Campbell*, 2003]. This effect can be used in magneto-telluric sounding since it allows studying deep structure of the planet.

Detail information on the low-frequency sources connected to the Martian environment and important to this study is presented in points 2.3 and 2.4.3.

1.2.4.2 Electrical properties of the atmosphere

Typically the electrical properties of the atmosphere can be characterized by several parameters: the electron, ion and neutral particles density, the effective collision frequency between those atmospheric species, the electron and ion gyrofrequnecy, and the plasma frequency. These parameters are related to the atmospheric composition, its density, and temperature. From them, we can determine the profiles of electrical conductivity.

The plasma frequency matches up with the oscillation frequency for a given species of charged particles under a small charge separation. For electrons, it is given by [*Jackson*, 1999]:

$$\omega_p^2 = \frac{n_e e^2}{m_e \varepsilon_0}, \tag{1.50}$$

where: n_e is the electron density, e is the charge of the electron ($1.60 \cdot 10^{-19}$ C), and m_e is its mass ($9.11 \cdot 10^{-31}$ kg). The ion plasma frequency, ω_{pi}, is much smaller as the ion mass, m_i, is always larger than m_e and [*Treumann et al.*, 2008]:

$$\omega_{pi} = Z \frac{m_e}{m_i} \omega_p \ ,$$

where: Z is the ionic charge number. The interaction between radio waves and the ionosphere depends on the plasma frequency, which for electrons, after inserting the constant values in (1.50), can be given as: $f_p = 8979\sqrt{n_e}$, where f_p is in Hz and n_e in el/cm^3 [*Withers*, 2009]. Radio waves of frequency f propagate through the medium for which $f_p < f$ and are reflected from the medium for which $f_p \geq f$ [*Gurnett et al.*, 2008]. For example, the terrestrial ionosphere is a leaky dielectric for VLF waves, and for higher frequency waves, but a conductor for ELF waves.

The gyrofrequnecy (cyclotron frequency) is a rotation frequency of a charged particle in a magnetic field. For an electron and ion it is, correspondingly [*Jackson*, 1999]:

$$\omega_{be} = eB/m_e, \qquad \omega_{bi} = q_i B/m_i, \tag{1.51a,b}$$

where: q_i – is the ion charge.

The collision frequency measures the frequency of collisions between a given charged species and neutral particles or other charged species. In case of collisions with neutrals, it depends on neutrals density n_n, the neutral molecule or atom cross-section ς, and the average velocity of the charged particles $\langle v \rangle$ [*Goebel and Katz*, 2008]:

$$\nu = n_n \varsigma \langle v \rangle . \tag{1.52}$$

The atmospheric conductivity results from ions and electrons concentrations. The contribution of positive charged particles with charge number larger than 1 is negligible [*Frank-Kamieniecki*, 1968]. As a result, we can adopt that an ion charge is: $q_i = e$. The total atmospheric conductivity is defined by the sum of the ions and electrons conductivity and is given by [*Michael et al.*, 2008]:

$$\sigma_t = e(\mu_+ n_+ + \mu_- n_- + n_e \mu_e), \tag{1.53}$$

where $n_\pm$ and n_e are the densities of ions and electrons, respectively, and $\mu_\pm$ and μ_e are the ion and electron mobilities. The mobility is a velocity acquired by an ion or electron in a unit electric field.

The ion and electron mobilities are functions of their collision frequency. Electrons, due to their small mass, have very high mobility, which is given by:

$$\mu_e = e/(m_e \nu_e), \tag{1.54}$$

where: ν_e is the electron-neutral collision frequency. Using (1.50), (1.53), and (1.54) the ionospheric conductivity solely related to electrons can be described as:

$$\sigma = \frac{e^2 n_e}{m_e \nu_e} = \frac{\varepsilon_0 \omega_p{}^2}{\nu_e} . \tag{1.55}$$

In the ionosphere, the density of neutral gas exceeds the density of plasma; therefore this region is a weakly ionized medium. Fully ionized medium is only expected in the planetary magnetosphere. In partly ionized medium charged particles move under the influence of electric fields, ambient planetary magnetic field, as well as by neutral gas motions. The equation of motion for electrons and ions can be written as [*Melnik and Parrot*, 1999]:

$$\frac{\partial \mathbf{v_e}}{\partial t} = \frac{e}{m_e}(\mathbf{E} + \mathbf{v_e} \times \mathbf{B}) - \nu_e \mathbf{v_e} - \nu_{ei}(\mathbf{v_e} - \mathbf{v_i}), \tag{1.56a}$$

$$\frac{\partial \mathbf{v_i}}{\partial t} = \frac{e}{m_i}(\mathbf{E} + \mathbf{v_i} \times \mathbf{B}) - \nu_i \mathbf{v_i} - \nu_{ie}(\mathbf{v_i} - \mathbf{v_e}), \tag{1.56b}$$

where: $\mathbf{v_{e,i}}$ are the velocities of electrons and ions, ν_{ie}, ν_{ei} are the collision frequencies between charged particles, and ν_i is the ion-neutral collision frequency.

Under the influence of magnetic fields, charged particles do not move along the field lines, but due to the Lorentz force they can move also perpendicular to the field. The ability of ionospheric currents to flow perpendicular depends on the magnetic field magnitude, which change with altitude. The field-aligned conductivity, σ_0, takes place when the magnetic field is weak in comparison to the forces related to the collisions with neutrals (see (1.56)). This happens in the neutral atmosphere, where particles move parallel to **E** and **B**. This conductivity is greater than the perpendicular conductivities, and can be given by (see (1.55)):

$$\sigma_0 = e^2 n_e \left(\frac{1}{m_e \nu_e} + \frac{1}{m_i \nu_i} \right), \tag{1.57}$$

where: ν_i is the ion-neutral collisions frequency. When the magnetic effects are stronger, the perpendicular conductivities are nonzero [*Baker and Martyn*, 1953]. Particles can move parallel to **E** and perpendicular to **B**, which quantitatively can be described by the Pedersen conductivity, obtained from solving the equations of motion (1.56) with the cyclotron frequencies (1.51) [*Opgenoorth et al.*, 2010]:

$$\sigma_P = e^2 n_e \left(\frac{\nu_e}{m_e(\omega_{be}^2 + \nu_e^2)} + \frac{\nu_i}{m_i(\omega_{bi}^2 + \nu_i^2)} \right), \tag{1.58}$$

or orthogonal to **E** and **B,** which is given by the Hall conductivity [*Opgenoorth et al.*, 2010]:

$$\sigma_H = e^2 n_e \left(\frac{\omega_{be}}{m_e(\omega_{be}^2 + \nu_e^2)} - \frac{\omega_{bi}}{m_i(\omega_{bi}^2 + \nu_i^2)} \right). \tag{1.59}$$

From expressions (1.57)-(1.59), we see that when ν given by (1.52) is much larger than ω_b given by (1.51), then σ_P is equal to σ_0, and σ_H << 1. Collisions prevent ions and electrons from movements influenced by the magnetic field. Charged particles are trapped in the neutral medium and are subjected to processes related to this medium. On the other hand, when $\nu \sim \omega_b$, then $\sigma_H = \sigma_P = 0.5\sigma_0$, particles can drift perpendicular to the electric and magnetic field. The different physical properties of ions and electrons lead to different profiles of the collision frequencies and gyrofrequencies of these two species. Above some altitude electrons, which collision frequency is lower than this of ions, are influenced by the magnetic field, while ions still move in accordance with the neutral atmosphere corresponding to winds related with pressure gradients. This process leads to charge separation and creation of the so-called ionospheric dynamo region [*Fillingim et al*., 2010].

The perpendicular conductivities are not only related to strong intrinsic planetary magnetic fields but also to induced ones. *Rosenqvist et al*. [2009] studied the perpendicular conductivities existing in the weak induced magnetosphere around Titan. They have found that the Hall and Pedersen conductivities in such weak draped magnetic fields can be much stronger than those observed on Earth.

In the atmosphere, charged particles are generated *via* various processes, but they are also lost due to recombination with or attachment to other particles. Their concentration is determined by the charged particle balance equation, which describes the relationship between their production rate and loss rate, given by the recombination and attachment. For electrons, the balance equation in a steady state is [*Michael et al*., 2008]:

$$\frac{dn_e}{dt} = q_e - \tilde{\alpha} n_+ n_e - \sum_k n_e \beta_k n_k = 0 \tag{1.60}$$

where: q_e is the production per unit volume, $\tilde{\alpha}$ is the ion-electron recombination coefficient, β_k are the electron-aerosol attachment coefficients, and n_k is the aerosol particles concentration of a given charge k [*Michael et al*., 2008]. Free electrons are unstable in the Earth lower atmosphere, due to their rapid attachment to electrophilic species and formation of negative ions. However, as shown in Chapter 2, they are very common in the atmosphere of Mars.

The major sources of ionization in the atmosphere are solar and cosmic radiation. Solar EUV (extreme ultraviolet), and gamma radiation are responsible for the generation of the planetary main ionospheric layers, located in the upper atmosphere. The lower atmosphere cannot be so easily ionized by the solar radiation, as solar high-energy photons are absorbed in the upper atmosphere and low-energy ones have too small energies. The major contributors to the ionization of the lower layers are galactic cosmic rays (GCR), extremely energetic charged particles from the outside of the heliosphere. GCR are particles comprising protons (up to 90%), α particles (up to 10%), electrons ~1%, and ~1% of heavier nuclei. They also may generate secondary particles in the atmosphere, which can reach even the planetary surface [*Bazilevskaya et al.*, 2008; *Hassler et al.*, 2014]. Their flux is anticorrelated with solar activity. Another source of ionization are solar energetic particles (SEP), which can be impulsive and electron rich, or gradual and proton rich. The first type is related with flares, the second with coronal mass ejections (CME). Their flux is of higher probability during periods of high solar activity. At solar maximum ca. 1000 events of the first type and 10 events of the second type happen a year [*Campbell*, 2003]. Magnetospheric precipitating electrons also have some contribution. Even if they are absorbed in the upper atmosphere, X-rays generated by them can penetrate to lower altitudes [*Bazilevskaya et al*., 2008].

Important information associated with (1.60) is the fact that in an aerosol-polluted atmosphere its conductivity is considerably reduced by ion-aerosol attachments. The maximum aerosol concentration is in the planetary boundary layer (PBL, a part of the troposphere in which motions are directly influence by the presence of the planetary surface), and decreases with altitude. On the other hand, although in the PBL ionization related to radioactive isotopes in the planetary crust takes place, the ionization rate dominates above the PBL [*Harrison*, 2005]. Therefore, the major contribution to the atmospheric resistance is associated with the PBL [*Rycroft et al*., 2008].

Any planetary ionosphere can be divided into several regions, which are generated due to different processes and have different properties. As the main source of ionization is only present during the day, the daytime and nighttime ionospheres are different.

On Earth, the ionosphere consists of four distinct regions (Figure 5). The lowest region is called the D region. Its peak density, ca. 10^3 el/cm^3, is located at ca. 60-90 km altitude. Above it, there is the E region with a peak ca. 10^5 el/cm^3 at 90-120 km altitude. The last region, the F region, at ca. 120-600 km with the electron density ca. 10^6 el/cm^3, is divided into two layers: F1 and F2 with peaks at ca. 200 km and 300 km, respectively. The ionized gases above the F region decrease exponentially. This is the topside ionosphere (600 km). The F region is formed by EUV and precipitation of energetic particles, the E region by soft X-ray. The D region is generated by Lyman α ionization of NO, solar hard X-ray, and GCR [*Witasse et al*., 2008; *Haider et al*., 2009]. The D and F1 regions are present only during daytime. Also the meteoric layer generated by ablation of continuous flux of extraterrestrial dust, consisting of neutral and ionized metal atoms, is present at the altitude ca. 80-110 km with a 10^3–10^4 cm^{-3} electron density peak [*Kopp*, 1997]. The relative abundance of metal species in this layer is similar to carbonaceous chondrites. Meteor showers can increase the concentrations of metal during short periods of time by a factor of 2-3, and sometimes even up to 10 [*Molina-Cuberos et al*., 2008].

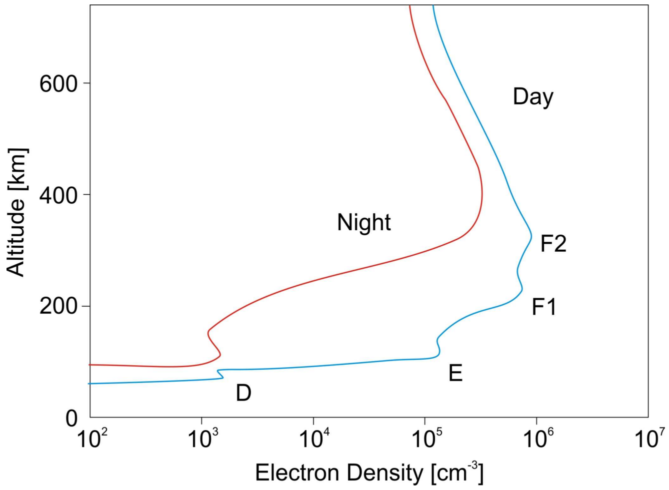

Figure 5. Schematic profiles of the daytime and nighttime electron densities in the terrestrial atmosphere.

The upper ionosphere, in which electrons and ions play an important role, is commonly divided into two regions: lower controlled by photoionization, and upper controlled by dynamical processes. At lower altitudes, the plasma transport timescale, given by: H^2/D_f, where: H – the scale height of the neutral atmosphere, and D_f – the plasma diffusion coefficient (proportional to the sum of the electron temperature T_e, and the ion temperature T_i) is much longer than the photochemical one, given by: $1/(\tilde{\alpha}\, n_e)$, where $\tilde{\alpha}$ is the dissociative recombination coefficient. At higher altitudes, the transport timescale becomes shorter than the photochemical one, and transport processes become important and eventually control the topside of the dayside ionosphere [*Withers*, 2009]. These processes are associated with plasma flow, and can be studied in the kinetically or fluid approach [*Witasse et al.*, 2008]. In the photochemical region, on the other hand, the electron density can be calculated using solely the Chapman theory, in which electrons are only produced by photoionization and lost by electron-ion recombination. In the terrestrial ionosphere, the Chapman theory characterizes very well the E region. In the F region the transport process becomes important, and in the D region cosmic radiation play an important role.

The production of electrons correlates with the solar zenith angle χ. It is the angle from the zenith to the location of the Sun. For $\chi = 0$ (at the zenith), the production rate is equal to q_e, and under the horizon ($\chi < 90°$), it is 0 [*Campbell*, 2003]. It is a quasi-steady state condition, because χ varies slowly. In the Chapman layer, we can also assume that: $n_i = n_e$. From (1.60), we see that ionization changes as $\sqrt{\cos\chi}$:

$$q_e \cos\chi - \tilde{\alpha}_{ie} n_e^2 = 0, \quad n_e = \sqrt{q_e / \alpha_{ie}}\sqrt{\cos\chi} \,. \qquad (1.61a,b)$$

The Chapman theory presents the relationship between the electron density, atmospheric altitude, depicted in the scale height units, and the solar flux [*Withers*, 2009]:

$$n_e(z) = n_{e0} \exp\left[\frac{1}{2}\left(1 - \frac{z - z_0}{H} - Ch \exp\left(-\frac{z - z_0}{H}\right)\right)\right], \qquad (1.62)$$

where: H is the scale height of the atmosphere, n_{e0} is the peak electron density given by (1.61b) for the subpolar point, z_0 is the peak altitude, Ch is a dimensionless factor which for small χ equals to $\sec(\chi)$.

1.2.4.3 Electrical properties of the ground

The planetary surface and subsurface is composed of various rocks, ices and waters. Those materials have different electrical properties (Figure 6). As many common rock-forming minerals are of low conductivity, most dry rocks have conductivities lower than 10^{-8} S/m [*Schon*, 2004]. However, rock conductivity increases with increasing water content and temperature. The accessory minerals within rocks, such as graphite or ores, can also increase this value. The relative permittivity of dry rocks is typically between 3-5 [*Schon*, 2004]. The relative permittivity of ice is ca. 100 at 260 K. For water at 300K, it is ca. 80 [*Petrenko*, 1993].

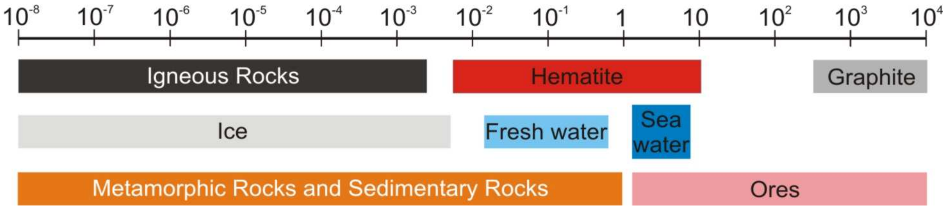

Figure 6. Conductivity of various materials composing planetary surface in S/m.

On Earth, the conductivity of upper part of the ground (from hundreds of meters up to few kilometers) is very high (Figure 7), due to oceans and high water content in rocks and soils. Beneath the surface, however, this value is lower as water content becomes lesser and temperature is not high enough [*Zhdanov and Keller*, 1994]. Yet, that zone of the ground is screened by the high-conductivity one and does not influence ELF propagation.

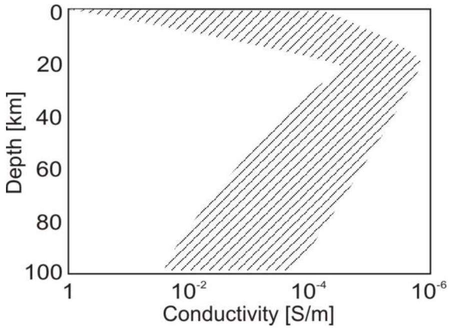

Figure 7. Schematic range of electrical resistivity through the terrestrial crust and upper mantle

Adapted from: *Zhdanov and Keller* [1994].

Nevertheless, *Kamra and Ravichandran* [1993] indicated that the terrestrial surface could not be universally considered as a perfect conductor, particularly in hot, dry areas and at the poles, where its conductivity is lower than 10^{-9} S/m. This is also valid for other bodies in the Solar System, which do not have liquid water at the surface or are not characterized by high near-surface temperatures. The theoretical issues associated with electrical properties of rocks are presented in Chapter 3.

Knowing the properties of a planetary cavity, it is easy to define and determine the important factors influencing ELF wave propagation. In case of Mars, not all of those properties are known, as discussed in Chapter 2. Therefore, in Chapter 2 and 3, some theoretical studies are considered to establish the most probable models of the Martian waveguide.

2 Martian Environment

2.1 Mars exploration

Since ancient times, Mars has been a goal of investigation, and since Galileo Galilei, it has been explored using telescope. But a true revolution in Mars studies is related to space missions. So far, there have been 42 Martian missions, from which only 21 were successful (Table 2). The data acquired during those programs, significant for this study, is presented in the course of this chapter. Although the number of the missions is not small, especially in comparison to the number of those investigating other astronomical objects, three more Mars missions are presently in preparation: the InSight mission by NASA, and two ExoMars missions by ESA and Ruscosmos. Furthermore, there are some projects in the design phase, such as the Mars 2020 mission, which comprises another rover.

Table 2. Missions to Mars.

Launch Date	Name	Country	Type	Result	Information
1960	Marsnik 1	USSR	Flyby	Failure	Did not reach Earth orbit
1960	Marsnik 2	USSR	Flyby	Failure	Did not reach Earth orbit
1962	Sputnik 22	USSR	Flyby	Failure	Earth orbit only
1962	Mars 1	USSR	Flyby	Failure	Radio Failed
1962	Sputnik 24	USSR	Flyby	Failure	Earth orbit only
1964	Zond 2	USSR	Flyby	Failure	Passed Mars, but radio failed
1964	Mariner 3	US	Flyby	Failure	Shroud failed to jettison
1964	Mariner 4	US	Flyby	Success	Flew by 1965
1969	Mars 1969A	USSR	Orbiter	Failure	Launch vehicle failure
1969	Mars 1969B	USSR	Orbiter	Failure	Launch vehicle failure
1969	Mariner 6	US	Flyby	Success	Flew by 1969
1969	Mariner 7	US	Flyby	Success	Flew by 1969
1971	Mariner 8	US	Orbiter	Failure	Launch failure
1971	Kosmos 419	USSR	Lander	Failure	Earth orbit only

1971	Mars 2	USSR	Orbiter/Lander	Failure	Orbiter arrived, but no useful data, lander failed
1971	Mars 3	USSR	Orbiter/Lander	Success	Arrived in 1971, some data
1971	Mariner 9	US	Orbiter	Success	In orbit 1971-72
1973	Mars 4	USSR	Orbiter	Failure	Flew past Mars
1973	Mars 5	USSR	Orbiter	Success	Arrived 1974; lasted a few days
1973	Mars 6	USSR	Orbiter/Lander	Success/Failure	Arrived 1974; contact was lost with lander; little data return
1973	Mars 7	USSR	Orbiter/Lander	Success/Failure	Arrived 1974; lander failure little data return
1975	Viking 1	US	Orbiter/Lander	Success	Arrived 1976; lander operated till 1982
1975	Viking 2	US	Orbiter/Lander	Success	Arrived 1976; lander operated till 1980
1988	Phobos 1	USSR	Orbiter/Lander	Failure	Lost en route to Mars
1988	Phobos 2	USSR	Orbiter/Lander	Failure	Lost near Phobos
1992	Mars Observer	US	Orbiter	Failure	Lost prior to Mars arrival
1996	Mars Global Surveyor	US	Orbiter	Success	Operated 1997-2006
1996	Mars 96	Russia	Orbiter/Lander	Failure	Launch vehicle failure
1996	Mars Pathfinder	US	Lander/Rover	Success	Operated in 1997
1998	Nozomi	Japan	Orbiter	Failure	In heliocentric orbit
1998	Mars Climate Orbiter	US	Orbiter	Failure	Lost on arrival
1999	Mars Polar Lander	US	Lander	Failure	Lost on arrival
2001	Mars Odyssey	US	Orbiter	Success	Arrived in 2001, still operating
2003	Mars Express	ESA	Orbiter/Lander	Success/Failure	Arrived in 2003; lander lost on arrival; still operating
2003	Mars Exploration Rover – Spirit	US	Rover	Success	Operated 2003-2010
2003	Mars Exploration Rover – Opportunity	US	Rover	Success	Arrived in 2004; still operating
2005	Mars Reconnaissance Orbiter	US	Orbiter	Success	Arrived in 2006; still operating
2007	Phoenix Mars Lander	US	Lander	Success	Operated in 2008
2011	Phobos-Grunt/Yinghuo-1	Russia/Chine	Lander/Orbiter	Failure	Stranded in Earth orbit
2011	Mars Science Laboratory	US	Rover	Success	Arrived in 2012; still operating
2013	Mars Atmosphere and Volatile Evolution	US	Orbiter	Success	Arrived in 2014; still operating
2013	Mars Orbiter	India	Orbiter	Success	Arrived in 2014; still operating

On the basis of *Barlow* [2008] and NASA NSSDC: http://nssdc.gsfc.nasa.gov/nmc/ (retrived 30th Sep 2014).

The InSight (Interior Exploration using Seismic Investigations, Geodesy and Heat Transport) is a NASA Discovery Program mission to place a single geophysical lander on Mars. Its payload is equipped with a seismic sensor and a heat probe. Its main objectives are: the investigation of the size and physical state of the core, and determination of the thickness and structure of the crust and the mantle. Its launch is planned in 2016. Also, in the same year the first of the ExoMars (Exobiology on Mars) missions is designed. This program is to investigate the evidence of methane and other trace atmospheric gases that could be signatures of active biological or geological processes. The 2018 ExoMars mission consists of a European rover and a Russian lander. Its main objective is to search life signs.

In 2016, for the first time in the Martian exploration history, it will be possible to investigate electromagnetic field at the planetary surface, as the ExoMars module and the InSight lander payloads contain such sensors. On the lander of the ExoMars 2016 program, called Schiaparelli, the scientific payload DREAMS (Dust characterization, Risk assessment and Environment Analyzer on the Martian Surface) is equipped with an electric field sensor called MicroARES, which is dedicated to measure atmospheric electricity during few days of entry, descent and landing. This instrument is described in more detail in Chapter 5. The InSigth mission includes a magnetometer, which is planned to use as a support for a seismometer in order to reduce magnetic noise.

2.2 Orbital and global parameters

The Martian environment is not a closed system. It has a changeable character and depends on many exogenic and endogenic processes. The most important exogenic factors are related to solar activity.

Mars in many aspects is similar to Earth (Table 3). However, it is located farther from the Sun and receives less energy. The solar constant on Mars is 0.43 of the terrestrial value. Mars and Earth were formed 4.6 Gya from the same matter, gas and dust. Yet, Mars composition is somewhat different from that of Earth. Its average density is 0.71 of the terrestrial density, and its average radius is only 0.53 Earth's radius. These two factors mean that the mass of Mars is 0.11 the mass of Earth, and the gravitational acceleration is only 0.38 of the mean terrestrial value.

The shape of Mars is a triaxial ellipsoid. Mars rotates and revolves counter-clockwise. A day on Mars lasts 1.03 Earth’s day and is called a sol. A Martian year lasts 1.88 Earth’s year, which corresponds to 669 sols. Mars has only two small satellites: Phobos (radius ca. 11 km) and Deimos (radius ca. 6 km).

Table 3. Martian and terrestrial parameters.

Parameter	Mars	Earth
Distance to Sun	1.52 AU	1.00 AU
Perihelion	1.38 AU	0.98 AU
Aphelion	1.67 AU	1.02 AU
Eccentricity	0.0935	0.0167
Obliquity	25.19°	23.44°
Orbit period	686.98 d	365.26 d
Length of day	$24^h39^m35^s$	24^h
Mass	$6.417 \cdot 10^{23}$ kg	$5.973 \cdot 10^{24}$ kg
Mean radius	3390 km	6371 km
Equatorial radius	3396 km	6378 km
Polar radius	3376 km	6357 km
Surface gravity	3.71 m/s^2	9.80 m/s^2
Solar irradiance	589 W/m^2	1368 W/m^2
Mean density	3933 kg/m^3	5514 kg/m^3
Flattening	0.00589	0.00335

On the basis of NASA Planetary Fact Sheet: http://nssdc.gsfc.nasa.gov/planetary/factsheet/ (retrived 30th Sep 2014).

The orbital parameters cannot be ignored in the discussion on the Martian environment. They significantly affect atmospheric circulation and cause climate change as presented in the Milankovitch theory [*Milankovitch*, 1930]. The Mars axis of rotation is inclined to the ecliptic plane, and as a result there are seasons on Mars. The higher the value of the obliquity θ, the greater is the difference in insolation at various latitudes, and greater the difference between summer and winter. Changes in obliquity particularly affect the polar and subpolar regions' insolation. How this factor is important may be illustrated by the fact that when θ exceeds 54°, the annual average solar flux is greater in the polar than in the equatorial regions [*Carr*, 2008]. On Earth, obliquity undergoes cyclical changes lasting about 41,000 years. During this period, it changes in the range between 21.58° and 24.36° [*Kozuchowski*, 2004]. On Mars, these changes are much greater. It is assumed that in the last 5 million years, they ranged from 15° to 35° [*Laskar et al.*, 2002]. Such significant changes in the axis tilt of Mars are due to weaker interaction of tidal forces from the Sun and the lack of a suitably massive natural satellite. Currently, the planet is in a transition period from higher to lower values of obliquity [*Barlow*, 2008]. It is believed that for small θ, Mars has well-developed, massive polar caps in both hemispheres and a thin and transparent atmosphere. For high values of that angle, it is expected that seasonal ice caps are thinner and the planet has dustier atmosphere [*Read and Lewis*, 2004]. Another significant factor influencing the climate of a planet is the eccentricity of its orbit. In the case of Earth, there is a nearly circular orbit, which changes only slightly in a cycle lasting about 92,000 years [*Kozuchowski*, 2004]. These changes, between 0.01-0.05, cause a lengthening or shortening of seasons (presently on Earth the spring-summer period in the northern hemisphere is a few days longer than the fall-winter one). Mars has a more elliptical orbit than Earth. Its eccentricity changes within the range from 0 to 0.12 [*Laskar et al.*, 2002], and may even reach 0.15 [*Carr*, 2008]. The duration of each season on Mars is very uneven with a predominance of tens of days for the spring-summer period in the northern hemisphere [*Barlow*, 2008]. Another important factor is the precession of the equinox point. Currently, Earth and Mars are at perihelion during the fall-winter period on their northern hemispheres.

On Mars, time during the year is measured using the solar longitude Ls, defined as the angle on the planetary orbit between the Mars-Sun position and the vernal equinox point for the northern hemisphere. Spring begins when the solar longitude is 0°. Next seasons are determined by the equinox and solstices: summer is when Ls = 90°, fall for 180°, and winter for Ls = 270°. Mars perihelion is at Ls = 250°.

In studies regarding Mars, the aerographic coordinates system is used. The aerographic latitude is defined similarly to the geographic latitude. In this work, the aerographic longitude is measured eastward from the prime meridian, which passes through the region called Meridiani Planum (Figure 8).

Figure 8. The map of Mars.

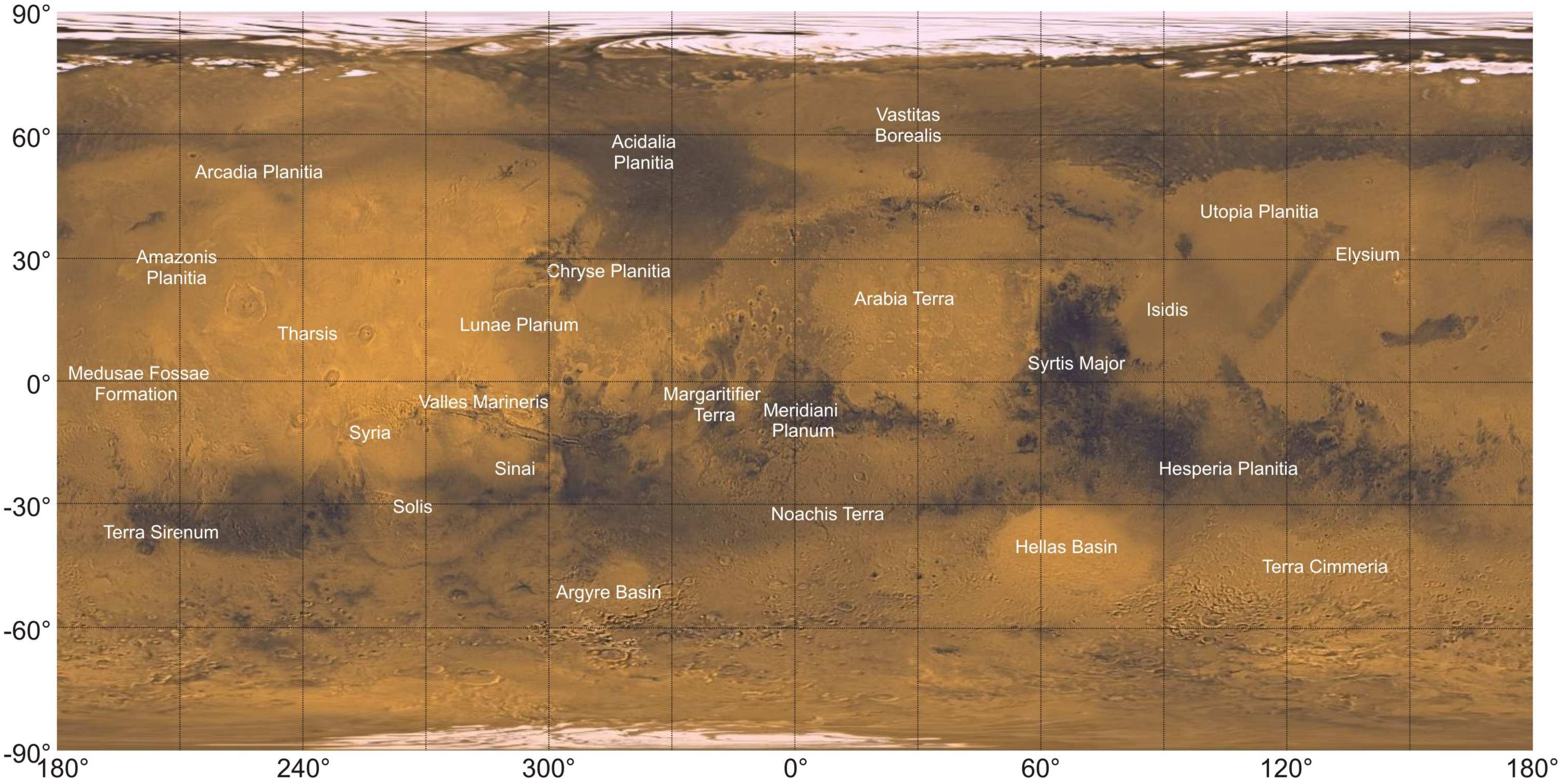

2.3 Magnetosphere

Magnetic field observations on Mars have been made by Mars 3, Phobos 2, and the Global Mars Surveyor (MGS) mission [*Connerney et al.*, 2001; *Brain et al.*, 2003; *Nagy et al.*, 2004]. New information will be acquired by a magnetometer on board the Mars Atmosphere and Volatile EvolutioN (MAVEN) orbiter.

The present Mars does not possess an intrinsic magnetic field, although strong crustal magnetization implies that a Martian dynamo existed in the past [*Acuna et al.*, 1999; *Connerney et al.*, 2004], and ceased some 4 Gya [*Arkani-Hamed and Olson*, 2010]. The nowadays limit for the equatorial field of a Mars dipole is ca. 0.5 nT [*Acuna et al.*, 2001]. For comparison, on Earth, this value is ca. 30 μT [*Campbell*, 2003].

Solar radiation, by ionization of the neutral atmosphere of Mars, creates a daytime ionosphere. The solar wind is shocked and diverted around it. The interplanetary magnetic field (IMF), carried with the solar wind, is draped around this conducting medium as well and creates an induced magnetosphere (Figure 9) [*Nagy et al.*, 2004; *Brain et al.*, 2007]. This magnetosphere is associated with interactions between the solar wind, frozen-in interplanetary magnetic field, and Martian ionosphere and atmosphere.

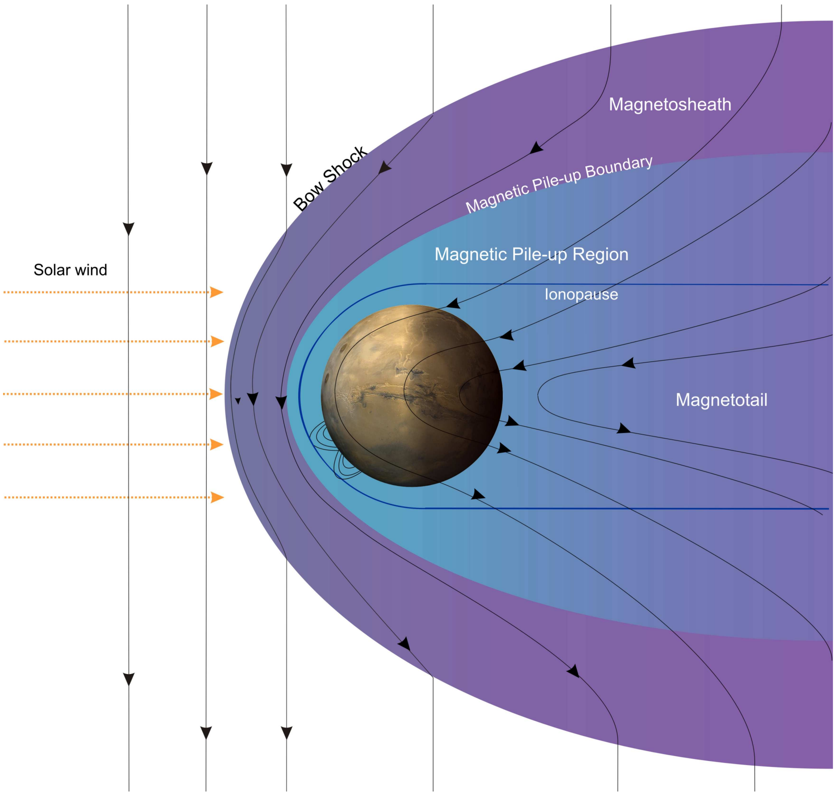

Figure 9. Martian induced magnetosphere. Mini-magnetospheres are marked over the southern hemisphere (see text).

In addition, this situation is yet more complicated, as beside the induced magnetosphere, Mars possesses magnetic anomalies related to remanent magnetization of the crust. This magnetic field, which is often stronger than the induced magnetic field, influences the ionosphere and magnetosphere [*Withers et al*., 2005; *Brain et al*., 2006] (Figure 10).

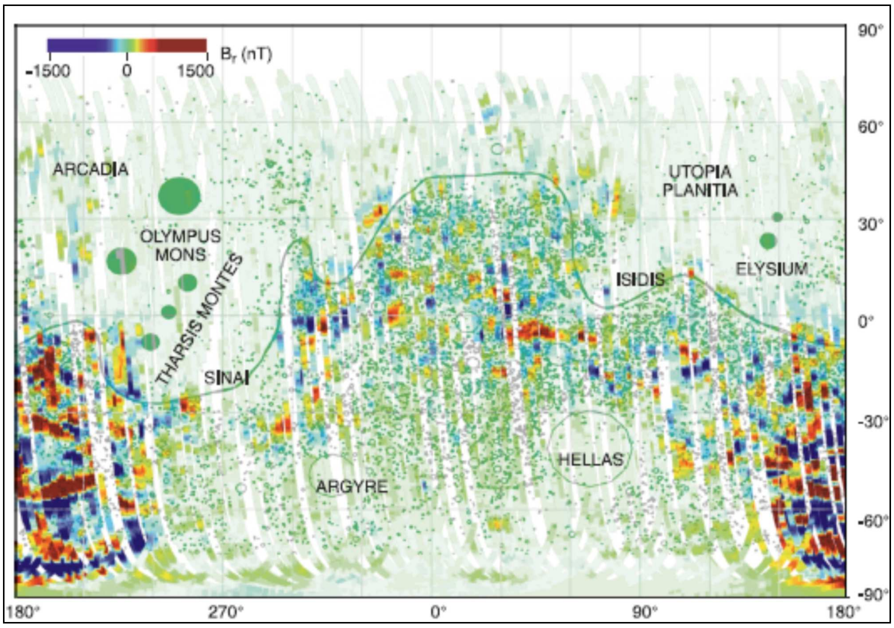

Figure 10. The map of crustal magnetic anomalies measured at ~100-200 km altitude. The green line depicts the dichotomy boundary (see point 2.5).

Source: *Acuna et al.* [1999].

The induced magnetosphere occurs due to solar wind plasma interactions with nonmagnetic celestial bodies. Its existence depends on currents induced within a conducting ionosphere by temporal changes of external magnetic fields in timescales short as compared to the field diffusion into the conductor. The magnetic fields related to these induced currents generally exclude the external field from the conductor, protecting the regions below the ionosphere from the interplanetary magnetic field. The strength of the horizontal induced magnetic field varies in the ionosphere. It is tens of nT on the dayside and only few nT on the nightside [*Brain et al.*, 2003]. The magnetic field morphology on Mars, just like on Venus [*Russell and Vaisberg*, 1983], Titan [*Ness et al.*, 1982], and comets, is dominated by the draping of the IMF lines around the planet [*Luhmann et al.*, 2004; *Nagy et al.*, 2004]. This produces a bow shock (Figure 9). The obstacle at which the IMF is piled up in front of the ionosphere is called the magnetic pile-up boundary (MPB). Between the bow shock and the magnetic pile-up boundary is placed the magnetosheath. The magnetosheath is characterized by turbulent low-amplitude magnetic fields. An extension of the magnetosheath into the wake, stretching far behind the planet, is a comet-like magnetotail [*Luhmann et al.*, 2004]. The observations of Phobos 2 and MGS showed that the magnetotail of Mars consists of two lobes of sunward and antisunward fields. Beneath the magnetosheath, the magnetic pile-up region (MPR) is located. This region is limited by the topside ionosphere on the dayside, and the magnetotail on the nightside. At the MPB, there is a drop in the magnetic field fluctuations, a sharp increase in the field magnitude, as well as a drastic change in ion composition. The solar particles density decreases, commensurate with an increase of planetary ions density [*Nagy et al.*, 2004]. The layer where the pressure of the solar wind is balanced by the thermal pressure of the ionosphere is called the ionopause, which can be locally deformed by the crustal anomalies and in some places can extend outside the MPB [*Opgenoorth et al*., 2010]. The ionopause is the boundary between the cold planetary plasma and the post-shocked hot solar wind plasma. It is an upper limit of the ionosphere [*Nagy et al*., 2004; *Bougher et al.,* 2014; *Haider and Mahajan*, 2014]. Although on Mars this transition is not as sharp as on Venus, in terms of simplicity the word 'ionopause' is used in this work. At the subpolar region of Mars, the typical value of the bow shock boundary is ca. 2000 km above the planet. The magnetic pile-up boundary is located ca. 850 km, and the upper boundary of the ionosphere (the ionopause) ca. 400 km above the surface [*Mitchell et al.*, 2001; *Duru et al.*, 2009].

The remanent crustal magnetization influences the induced magnetosphere, resulting in the complex topology of the Martian magnetic environment. This crustal magnetization is not evenly distributed across the planet. The most intensive magnetic regions are located in the southern highlands, with maximum radial fields exceeding 1500 nT, as it was determined from the MGS observations at ca. 100 km altitude. However, in the majority of regions the field is very weak or absent (Figure 10). Over the strong crustal anomalies, magnetic field lines can change from horizontal to vertical and back again. These features are called mini-magnetospheres, and can isolate the ionosphere from the solar wind plasma. They are also related to cusp-like structures, which allow for downward flow of the solar wind and upward flow of the ionospheric plasma [*Withers*, 2011]. The outermost lines of the crustal magnetic field should be able to reconnect with the IMF lines draped around the mini-magnetospheres. Open field lines connect the Martian surface and the solar wind. Therefore, charged particles can penetrate into the ionosphere resulting in heating and ionization of the neutral atmosphere. In the nighttime ionosphere, patchy structures, which can be similar to the Venusian ionospheric holes, have been found. Neither precipitating electrons nor plasma flow from the dayside ionosphere can repopulate the nightside ionosphere over the intense crustal magnetic field areas, apart from the cusp regions. This means that the ionospheric plasma can be denser outside the mini-magnetospheres than inside them. *Mitchell et al*., [2001] detected plasma voids at around 400 km on the nightside, over regions of crustal magnetization. Particles accelerating along magnetic field lines, result in auroras, observed on the nightside [*Bertaux et al*., 2005] at 50-80 km altitudes [*Lundin et al*., 2006].

The induced magnetic field strength decreases with decreasing altitude, and the magnetic field related to the crustal anomalies decreases with increasing altitude. Commonly the crustal component of the magnetic field dominates over the induced component at altitudes lower than few hundreds kilometers, although the strongest crustal sources are observed up to 1300–1400 km above the surface [*Brain et al.*, 2003].

Sources of a magnetospheric origin that allow for the subsurface exploration on Mars cannot be identified by any simple and direct analogy with the terrestrial phenomena due to the complex nature of the magnetosphere of Mars. The most probable and continual sources of magnetic origin are probably related to Sq current system and magnetic pulsations [*Grimm*, 2002; *Fillingim et al*., 2010]. However, only the latter would be able to generate signals in the ULF-ELF range. Time-varying solar wind perturbations of the mini-magnetospheres, changeable ionospheric currents, and auroras might produce useful signals. However, our insufficient knowledge of electromagnetic processes in the Martian ionosphere and magnetosphere, does not allow precise determination of their properties and possibility of their measurements from the planetary surface.

2.4 Atmosphere

The Martian *in situ* measurements of atmospheric temperature, pressure, wind velocity, and its direction were conducted by the Viking landers [*Seiff and Kirk*, 1977], the Mars Pathfinder rover [*Schofield et al*., 1997], as well as the Mars Curiosity rover [*Harri et al*., 2014]. The Viking landers measured the atmospheric chemical composition during minimum solar activity.

The atmosphere of Mars is very thin as compared to the terrestrial one and it is composed mainly of CO_2. At altitudes above 200 km, atomic oxygen is predicted to be more abundant than CO_2 [*Bougher et al*., 1999]. The average pressure at the surface is ca. 636 Pa (6.36 mbar). The pressure changes with altitude and season. At the summit of Olympus Mons, it is 20 times smaller than at the deepest region of Hellas Basin [*Carr*, 2008]. The season cycle is associated with deposition and sublimation of the polar caps, which leads to changes in the atmospheric pressure up to 20% [*Leovy*, 2001]. The average temperature in the equatorial regions is ca. -55°C (218 K), but at the poles temperature during the night can drop to –140°C (133 K). Yet in the equatorial regions during the summer, the daily maximum reaches 20°C (293 K). The temperature depends on the latitude, time of year, and thermal inertia, which is closely related to the thermal conductivity of the ground. The wind velocity measured by the Viking Landers near the surface in calm season was few m/s and during dust storms 15-30 m/s. In the past, the atmosphere of Mars might be denser, wetter and also different in terms of composition. A thicker, warmer atmosphere in the

Noachain times (see point 2.5) could allow for the presence of liquid water and rainfall [*Barlow*, 2008]. The atmosphere due to low gravity, strong solar wind interactions after the cessation of the magnetic dynamo, and heavy bombardment by impactors had been reduced to its present form. The recent MAVEN UV spectrograph data shows Mars losing atmospheric species to space.

The current composition of the Martian atmosphere is presented in Table 4. The concentration of CO_2 at the surface is ca. $10^{17}/cm^3$. The most interesting trace compound in the atmosphere is methane (CH_4). Methane on Mars was observed from Earth [*Krasnopolsky et al.*, 2004], the Martian orbit [*Formisano et al.*, 2004], and finally *in situ* by the Curiosity rover [*Webster et al.*, 2015]. On Earth, there are two sources of that gas: biological or geological. Its detection in the Mars atmosphere in the concentrations of ca. 10 ppb (on Earth, it is ca. 1800 ppb) was quite unexpected as Martian geological activity is very low (see point 2.5). Yet, these findings on methane on Mars still need to be verified.

Table 4. The major constituents of the Martian atmosphere.

Constituent	Amount [%]
Carbon Dioxide (CO_2)	95.3
Nitrogen (N_2)	2.7
Argon (Ar)	1.6
Oxygen (O_2)	0.13
Carbon Monoxide (CO)	0.08
Water (H_2O)	0.02

Source: http://nssdc.gsfc.nasa.gov/planetary/factsheet/marsfact.html (retrieved 30th Sep 2014).

On the basis of composition, temperature, density and pressure, three layers of the Martian atmosphere have been determined: a lower (troposphere), a middle (mesosphere), and an upper (thermosphere). The scale height of the atmosphere is ca. 11 km [*Petrosyan et al.*, 2011]. During daytime, due to heat exchange with the ground, convection occurs up to about 10 km [*Leovy*, 2001], wherein at night there is a strong temperature inversion at the surface [*Barlow*, 2008]. The temperature decreases with altitude up to about 40 km. On Mars, there is no equivalence for the Earth's stratosphere since ozone (O_3) is present solely in small amounts. Its concentration varies spatially and seasonally [*Blamont and Chassefiere*, 1993]. Larger quantities of ozone have been found only in winter over the poles [*Montmessin and Lefèvre*, 2013]. From 45 km altitude to 100 km, the mesosphere stretches. Here, the temperature continues to drop with altitude, but at the same time there are large fluctuations in the temperature values associated with processes of absorption and reemission of radiation by CO_2 molecules. Above the mesopause, at an altitude of 110 km [*Barlow*, 2008], the thermosphere begins; here the temperature increases with height. The properties of the upper atmosphere depend on solar activity. The ionosphere is located between ca. 100 and 400 km altitude. The exosphere, in which particles escape from the influence of gravitational forces and leave the planet, starts at ca. 250 km [*Chassefiere and Leblanc*, 2004].

CO_2 affects the warming of the lower atmosphere, as it prevents heat escaping from the planet. Also dust particles, always present in the troposphere, influence its temperature. During daytime, dust lowers the temperature in the troposphere, and increases in the upper part of the atmosphere. During nighttime, in turn, it prevents heat loss from the lower atmosphere [*Read and Lewis*, 2004]. The dust mass loading is subjected to seasonal fluctuations. The most effective sources of dust in the atmosphere are dust devils and dust storms. Those phenomena are described in detail in points: 2.4.3.4 and 2.4.3.5.

Uneven solar insolation causes global atmospheric circulation. The Martian atmospheric circulation system is very similar to the terrestrial one, with three cells for each hemisphere. Hadley cell circulation generates eastern winds in the equatorial zone (0-30°), and western winds in the mid-latitudes. In addition, there are planetary waves (Rossby waves), propagating to the east, migrating and non-migrating thermal tides, and condensation flows. Non-migrating tides are not related to the solar radiation but to variations in topography, surface thermal inertia, dust activity, and water ice concentrations. They can propagate westward or eastward [*Guzewich et al.*, 2012]. The thermal continents (see point 2.5) affect circulation of the atmosphere, and are especially important for non-migrating thermal tides. The most important atmospheric cyclic phenomena are diurnal migrating thermal tides and seasonal condensation flows. Diurnal variations are associated with insolation. Mars experiences very large fluctuations in the temperature amplitude during a sol. As the atmosphere cannot maintain the solar heat after sunset, temperature drops quickly, leading to large temperature and pressure differences. This results in migrating thermal tides, moving in a westerly direction. They occur mainly in the equatorial regions at altitudes above 75 km [*Cahoy et al.*, 2006; *Guzewich et al.*, 2012]. Seasonal changes are mainly associated with sublimation and deposition of CO_2 and H_2O exchange between the atmosphere, the lithosphere and the hydrosphere (regolith, polar caps ice, and the subsurface cryosphere). In long-time scales the atmospheric circulation is subjected to changes in the orbital parameters, as discussed in point 2.2.

Beside dust storms and dust devils, other cloudy phenomena are observed frequently in the Martian atmosphere (Figure 11). Thin ice clouds can be visible *in situ*, from the orbit, and even from Earth. Water ice clouds can be found in the evening, at nighttime, in the morning, and above elevated regions such as Olympus Mons or Tharsis [*Hinson and Wilson*, 2004]. The equatorial clouds are made of water ice and are often orogenic. Clouds over winter poles are built mainly of CO_2 [*Read and Lewis*, 2004]. Clouds usually occur at altitudes of 10-20 km, but CO_2 clouds were observed in the mesosphere, even at the altitude about 80 km [*Montmessin et al.*, 2006; 2007]. Although layered clouds, such as *Cs,* dominate, *Cu* clouds associated with convection are sometimes observed. Moreover, there are front-like clouds as well as storm systems. The latter, in a form of a spiral structure, often occur near the polar caps, and are partly responsible for the introduction of dust into the atmosphere. Precipitation can occur only in the form of ice.

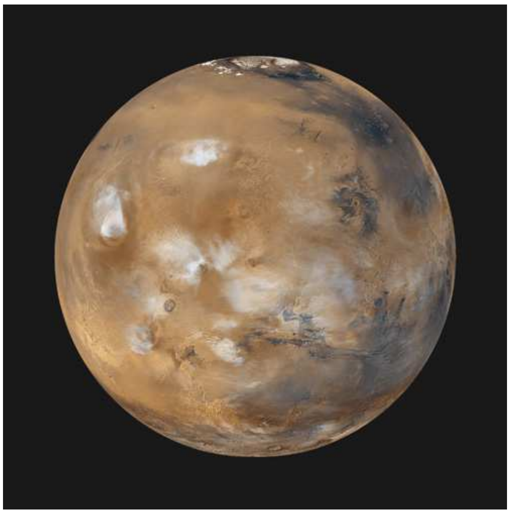

Figure 11. Clouds on Mars as seen by the Mars Global Surveyor.

Source: NASA/Mars Global Surveyor.

2.4.1 Ionosphere

The ionosphere of Mars was investigated by the Mariner [*Kliore et al.*, 1972], Mars [*Vasilev et al.*, 1975], and Viking missions [*Zhang et al.*, 1990], the Mars Global Surveyor [*Rishbeth and Mendillo*, 2004; *Opgenoorth et al.*, 2010], the Mars Express [*Patzold et al.*, 2005; *Morgan et al.*, 2008; *Gurnett et al.*, 2008; *Nemec et al.*, 2011; *Withers et al.*, 2012a], and presently is being studied by the MAVEN [*Bougher et al.*, 2014].

The Martian ionosphere is variable, and this variability is related to many different factors, among them solar activity, meteoroid flux, thermal tides in the neutral atmosphere, and dust storms. The ionosphere is under the influence of the solar wind magnetic field, which varies in time and space, and the crustal magnetic field, which varies in space [*Withers*, 2011]. It also shows asymmetry. In daytime, solar radiation is the main source of ionization above the 80 km altitude, and below it, GCRs dominate. At night, ionization is weaker, and it is mainly produced by GCR, meteoroids, and precipitation from the tail of the Martian magnetosphere.

Because $F_{10.7}$ (solar flux at 10.7 cm = 2800 MHz) is sampled from the Earth orbit, it is necessary to correct it for Mars. Two corrections are needed: to the relative orbital position, and to the distance from the Sun [*Morgan et al.*, 2008]. The solar flux varies by tens of percent from perihelion to aphelion [*Bougher et al.*, 2014] and is smaller than the terrestrial one by a factor of 2.25. The GCR flux on the Martian orbit can be assumed to be similar to the terrestrial value [*Bazilevskaya et al.*, 2008] and it does not change during a sol.

The electron densities profiles of the Martian ionosphere were obtained by direct measurements, radio occultation method, and radar sounding. The direct profiles were measured by two Viking landers in 1976 [*Hanson et al.*, 1977]. These measurements showed that a peak electron density reaches $10^5/\mathrm{cm}^3$ and is placed at ca. 125-135 km altitude. The radio occultation method, which is based on sending radio signals (in the GHz frequency range) from a satellite, passing behind the disk of Mars, to Earth, gives good results for altitudes above ca. 70 km. Mariner 4 spacecraft conducted the first experiment of this type in 1964. Because of the geometry of the planetary orbits, occultations are only possible for solar zenith angles χ between 44 and 136° [*Withers et al.*, 2012a,b]. The radar sounding is associated with the MARSIS (Mars Advanced Radar for Subsurface and Ionosphere Sounding) instrument on Mars Express and SHARAD (SHAllow RADar) on Mars Reconnaissance Orbiter. These instruments transmit radio waves in the MHz range, which are reflected from the ionosphere and planetary surface, and recorded on board. The atmospheric profiles obtained by this method do not reach beyond the main ionospheric layers [*Gurnett et al.*, 2008]. The nightside ionosphere has been measured by fewer instruments and less frequently than the dayside ionosphere; therefore, for this part of the ionosphere the measurement uncertainty is much larger.

The ionosphere is strongly influenced by the chemical composition of the neutral atmosphere. The Viking landers acquired vertical profiles of many species. The most abundant ion in the ionosphere below 300 km is O_2^+. It is produced by photoionization of CO_2 molecules by solar radiation. This leads to production of CO_2^+ ions, which react fast with O, resulting in production of

CO and O_2^+. Slow dissociative recombination of O_2^+: $O_2^+ + e^- \rightarrow O + O$, may explain its abundance [*Withers*, 2009]. Although this dissociative recombination is slow, due to long dynamical timescales in the main ionospheric region, it is the most important loss process removing ions and electrons.

The photochemical region of the ionosphere is located between 80 and 200 km and the transport region at altitudes >200 km. In the daytime ionosphere (Figure 12), the main ionospheric layer, called the M2 layer, is located at the altitude ca. 120-140 km and produced by EUV radiation (ca. 10-100 nm). Its electron density peak is $10^5/\mathrm{cm}^3$. Below this layer, at the altitude ca. 100-120 km (20 km below the M2 layer) is located the so-called M1 layer, produced by solar soft X-ray radiation (ca. 1-10 nm) and subsequent electro-impact ionization [*Rishbeth and Mendillo*, 2004; *Withers*, 2009]. The M1 and M2 layers can be compared with the E and F1 layers of the terrestrial ionosphere, respectively [*Rishbeth and Mendillo*, 2004]. Sometimes, it is possible to observe the meteoric layer, called in this work M3, at ca. 85 km altitude with a peak electron density ca. $10^4/\mathrm{cm}^3$ [*Patzold et al.*, 2005; *Molina-Cuberos et al.*, 2003; *Withers*, 2011]. There is also a lower layer, called the D layer by comparison to the terrestrial ionosphere. It has a peak electron density ~$10^2/\mathrm{cm}^3$ at ca. 35 km altitude, and it is produced by GCR (1-1000 GeV). The D layer is described in detail in point 2.4.2.

The total electron content (TEC) of the ionosphere is ca. $10^{15}/\mathrm{m}^2$ for χ = 0° [*Lillis et al.*, 2010; *Withers*, 2011] and increases during SEP events [*Sheel et al.*, 2012]. During nighttime, the TEC value was calculated to be ~$10^{14}/\mathrm{m}^2$ [*Fillingim et al.*, 2010]. Below the 115 km altitude, the electron temperature, T_e, is equal to the neutral atmosphere temperature [*Molina-Cuberos et al.*, 2002]. It is ca. 200 K at 100 km, and increases to 3000 K at about 250 km [*Opgenoorth et al.*, 2010]. The atmosphere near magnetic anomalies is additionally heated by the solar wind [*Krymskii et al.*, 2002].

Above the M2 layer, the electron density decreases exponentially. In some observations anomalous features are visible above 150 km altitude. They can be described as bulges in the electron density profiles [*Withers*, 2009] (Figure 12). The explanation of their origin is still undetermined. The top of the ionosphere is not fixed due to solar activity and magnetic anomalies, but it is typically 400 km above the surface [*Withers et al.*, 2012a].

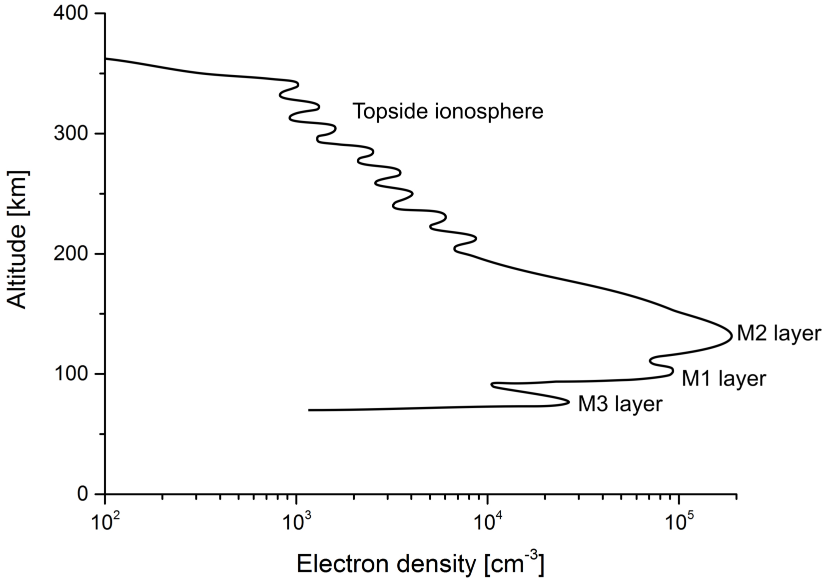

Figure 12. Schematic electron density profile of the dayside ionosphere of Mars.

On the basis of *Withers* [2011].

The M2 layer can be described by the Chapman theory the most easily from all the ionospheric layers. The best-fit parameters from (1.62) for the M2 layer are: $n_{e0} = 1.3 \cdot 10^5/\text{cm}^3$, $z_0 = 107$ km, and $H = 15.2$ km [*Gurnett et al.*, 2008]. The photochemical lifetime at this altitude is of the order of minutes [*Withers*, 2011].

The M1 layer is sometimes very well visible in the electron density profiles, and sometimes, it is only a part of the M2 layer. The M1 layer is under greater influence of the SEP events than the M2 layer as they are associated with shorter wavelengths of the solar spectrum. After a solar flare, enhancement in this region is the largest and the longest [*Mendillo et al.*, 2006; *Withers*, 2011]. Similarly to terrestrial cases, it is observed that during the solar flare the most prominent peak is shifted form the M2 to the M1 region [*Lollo et al.*, 2012].

The region below the M1 layer is affected by many processes not included in the Chapman theory. The presence of the sporadic M3 layer has been predicted by theoretical models [*Pesnell and Grabovsky*, 2000; *Molina-Cuberos et al.*, 2003] and was observed by Mariner 4 during daytime, and few years later by Mars 4 and Mars 5 during nighttime [*Molina-Cuberos et al.*, 2008]. The Mars Express mission confirmed its existence [*Patzold et al.*, 2005]. Meteoroids, consisting of interplanetary dust and fragments of meteorites, are the source of ionospheric ions of Mg^+ and

Fe^+ [*Molina-Cuberos et al.*, 2008]. They are produced from neutral metal atoms by the impact ionization, photoionization, and charge exchange with ions. The latter process is responsible for 99% of their production [*Molina-Cuberos et al.*, 2003]. Characteristics of the meteoric layer, such as width or altitude are positively correlated with each other and negatively correlated with solar radiation or the atmosphere scale height [*Withers*, 2009]. Recent data from a mass spectrometer on the MAVEN orbiter identified metal ions added to the Martian atmosphere by comet C/2013 A1 Siding, which passed close to Mars in October 2014. The detection of eight different metal ions Na, Mg, K, Cr, Mn, Fe, Ni, Zn was conducted. There was similar pattern in the timeline of the detection for all these ions. There was no detection in a period preceding the comet flyby, a sharp peak right away after the flyby, and then a quick return to the previous values [http://lasp.colorado.edu/home/maven]. This layer is expected to be capable of the absorption of radio waves [*Nielsen et al.*, 2007a] as well as the D layer described in the next point.

The nighttime ionosphere (Figure 13) can be defined for χ larger than 105°. It is a place, where space particles are transferred to the atmosphere and planetary volatile species escape to space. In the twilight ionosphere ($90° < \chi < 105°$) during some observations electron densities increase above a predicted from the Chapman theory value, possibly due to irregular structure of the ionosphere, transport from the dayside ionosphere, and precipitating electrons [*Gurnett et al.*, 2008]. Most of the observed profiles are related to the twilight ionosphere, but some information on the nighttime ionosphere has been acquired by Viking Orbiter 1, Mars 4, and Mars 5. The peak altitude is located at ca. 120-150 km with the electron density ca. $5 \cdot 10^3/cm^3$ [*Savich and Samovol*, 1976; *Zhang et al.*, 1990; *Withers et al.*, 2012b]. The results of theoretical calculations displayed that the M2 layer is present during nighttime at altitudes ~125-140 km and has densities ca. 10^3–$10^4/cm^3$ [*Withers et al.*, 2012b]. The nighttime M2 region cannot be related to a decay of the dayside ionosphere as its time constant, given by $1/\tilde{\alpha}\, n_e$ (see point 1.2.4) with the recombination coefficient: $2.55 \cdot 10^{-7}/cm^3/s$ and the electron density ~$10^4/cm^3$, is ca. 400 s [*Haider et al.*, 2007]. The most important sources of the nighttime ionosphere are cosmic radiation, transport from the daytime ionosphere, and precipitating electrons. The plasma flows across the terminator, however, the nightside ionosphere is not well supplied from the dayside [*Nagy et al.*, 2004] (see point 2.3). On the other hand, due to the complex topology of mini-magnetospheres, it is possible for solar wind electron precipitation to the nighttime hemisphere. The influence of the daytime ionosphere due to plasma transport takes place for $\chi \leq 115°$, whereas for larger χ electron precipitation from the magnetosphere is a dominant source.

In the work of *Withers et al*. [2012b], many profiles of the nighttime ionosphere were presented. They are based on the radio occultation technique, and were measured by the Mars Express Radio Science Experiment (MaRS). These results indicate that nightside ionosphere is irregular, variable in time and space. Nightside electron densities are less stable than dayside densities. Several profiles contain a broad, dense layer at 100 km, with a peak density 10^4/cm^3, which can be produced by electron precipitation or SEP events. Several profiles have a potential meteoric layer at altitudes 70-90 km with peak densities from $5 \cdot 10^3$/cm^3 to 10^4/cm^3. This value is smaller than on the dayside. It may be related to data statistics or less efficient mechanisms of ions production on the nightside. The M3 layer as well as the D layer is probably more constant at night than the M2 layer. The peak of the D region during nighttime is assumed to be at the 30 km altitude, with the density ca. 10^2/cm^3 [*Haider et al*., 2007]. It is described in more detail in point 2.4.2.

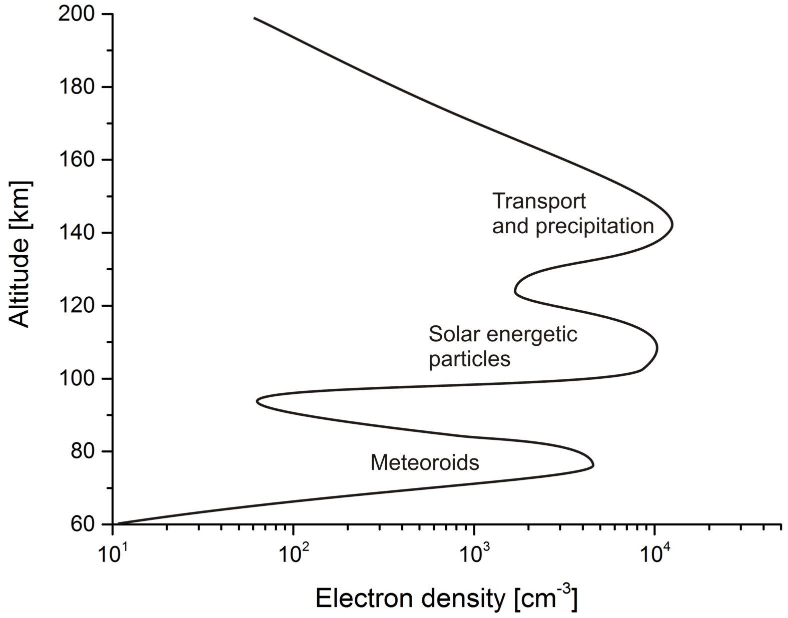

Figure 13. Schematic electron density profile of the nightside ionosphere of Mars.

Electron density profiles are influenced by dust storms. During Mariner 9 mission, the peak altitude was located 20-30 km higher than usually. It was suggested that this anomalous profile resulted from a regional dust storm taking place at that time. The observed temperatures of the atmosphere were higher than usual, leading to an expansion of the atmosphere. An increase in the density of the upper atmosphere provided more material for photoionization but also reduced EUV radiation in the lower altitudes [*Wang and Nielsen*, 2003]. The peak altitude in the ionosphere is also influenced by large zonal variations in the atmospheric density generated by non-migrating thermal tides. Additionally, the migrating thermal tides may drag ionospheric plasma across magnetic field lines, inducing electric fields and currents [*Aplin*, 2006].

In regions above strong crustal magnetic anomalies, dynamic effects are substantial [*Witasse et al*., 2008]. High electron temperatures and density peaks were found at the boundaries of mini-magnetospheres and within them [*Krymskii et al*., 2003; *Nielsen et al*., 2007b; *Withers*, 2009]. However, due to still small statistics, these anomalous data may be related to other sources. In the MARSIS observations, some oblique echoes were found, which are probably related to an upward bulge in the ionosphere above regions with the vertical orientation of the magnetic field [*Gurnett et al*., 2008]. The influence of the remanent magnetic field on the nighttime ionosphere has not been studied because of insufficient data [*Withers et al*., 2012b]. The difference in the peak density between cusp and void regions may be as large as two orders of magnitude [*Fillingim et al*., 2010].

The altitude at which the collision frequency is equal to the gyrofrequnecy is ca. 110 km for electrons, and ca. 160 km for ions. Between these two altitudes the electric dynamo region is located [*Fillingim et al.*, 2010]. Distribution and intensity of perpendicular conductivities in the ionosphere is coupled to the solar wind. Therefore, changes in the IMF have an immediate effect on the current systems in the ionosphere. In the dayside ionosphere, *Opgenoorth et al.*, [2010] indicated that there is a high altitude Pedersen peak, located between 180 and 200 km. In addition, a second and typically much stronger region of Pedersen conductivity is located between 120 and 130 km, which is below the Hall conductivity peak at about 130–140 km. This profile of perpendicular conductivities is similar to those found on Titan, yet stronger. Nonetheless, above Martian magnetic anomalies, the perpendicular conductivities are one or two orders of magnitude smaller than above the rest of the planet. *Opgenoorth et al*. [2010] concluded that in terms of ionospheric conductivities the ionosphere of Mars, over the regions of strong magnetic anomalies, behaves like terrestrial ionosphere, and in other regions, like Titan's ionosphere.

The lower layers of the ionosphere are the most important for ELF wave propagation as the main electromagnetic sources in the spherics band are related to the near surface phenomena. Therefore, in the next point the electrical properties of the Martian atmosphere below the main ionospheric layers are described in detail.

2.4.2 Electrical properties of the lower atmosphere

The permittivity of the Martian atmosphere can be assumed as constant and equal to free space permittivity ε_0. As shown in point 1.2.4.2, the conductivity of the atmosphere depends on the electron and ion density, which in turn depends on sources of ionization and sinks of charged particles.

GCR is the main source of ionization below 70 km altitude [*Molina-Cuberos et al*., 2002]. It is not deflected significantly by the crustal magnetic field [*Dartnell et al.*, 2007]. The GCR flux decreases exponentially with decreasing altitude. However, due to the thin atmosphere, the maximum production rate by GCR is at the surface [*Molina-Cuberos et al*., 2002]. The seasonal variations in the atmospheric density lead to modifications in the GCR penetration [*Aplin*, 2006]. Since there is no ozonosphere also a significant fraction of UV solar photons reaches the planetary surface. The ionization related to solar Lyman α is not efficient in the ionosphere of Mars due to low density of NO [*Haider et al*., 2009]. As photons of energy greater that 6 eV are absorbed in the upper atmosphere, photoelectrons are produced only by lower energy solar photons. Such photons are unable to ionize any gaseous medium, yet when their energy is greater than 4 eV, they generate photoelectron emission from solid materials at the ground and aerosols in the atmosphere [*Grard*, 1995].

The atmosphere electricity, beside the solar and cosmic radiation, is additionally influenced by the planetary boundary layer. The thickness of the PBL on Mars displays a diurnal variation. It is typically 10 km thick during daytime, and very shallow during nighttime [*Petrosyan et al*, 2011]. Exogenic sources are almost entirely responsible for ionization in the PBL [see *Hassler et al*., 2014] as the Martian basaltic crust is characterized by smaller amount of radon, thorium or uranium [*Surkov et al*., 1980] and the surface density of the Martian atmosphere is 70 times smaller than on Earth. The PBL impact on the atmospheric conductivity is related especially to aerosols, generated by dusty phenomena as well as meteoroid fluxes. *Michael et al*. [2007] showed that concentration of charged aerosols in the Martian atmosphere decreases with increasing altitude, and in addition, at lower altitudes aerosols have larger charges. More than 80% of neutral aerosols are charged close to the surface. *Michael et al*. [2008] stated that more than 60% of ions and 95% of electrons get attached to aerosols near the ground, which makes them almost immobile.

2.4.2.1 Electron densities

As there are no electron density measurements for altitudes below 70 km, only some theoretical predictions are possible. The first models of ionization in the lower atmosphere were presented in the work of *Whitten et al*. [1971]. Later, *Molina-Cuberos et al*. [2001, 2002] developed an ion-neutral model on the basis of more exact atmospheric composition, obtained from the Viking landers and Mars Pathfinder rover data. The results indicate that negative ions below 30 km are more abundant than electrons. The maximum ion concentration occurs at the surface. Electrons dominate above ca. 40 km. The most abundant positive ions below 60 km are hydrated hydronium ions $H_3O^+(H_2O)_n$, where n varies from 1 to 4, and above this altitude are O_2^+ ions. The most abundant negative ion was found to be $CO_3^-(H_2O)_2$. For the nighttime ionosphere (χ = 105°), *Haider et al*. [2007] obtained similar to the dayside ionosphere values. The hydrated hydronium ions dominate below 60 km, while O_2^+ and NO^+ above this altitude. The most abundant negative ions, below 40 km, is $CO^-{}_3(H_2O)_n$, for n = 1,2, and above this altitude electrons are dominant. The most recent publications by *Haider et al*. [2009] and *Sheel et al.* [2012] confirmed the results obtained previously. In the latter work, the authors also showed that electron densities below the 100 km altitude can be enhanced up to 2 orders of magnitude due to SEP events. The density profiles of electrons and ions under the normal conditions in the dayside atmosphere are presented in Figure 14.

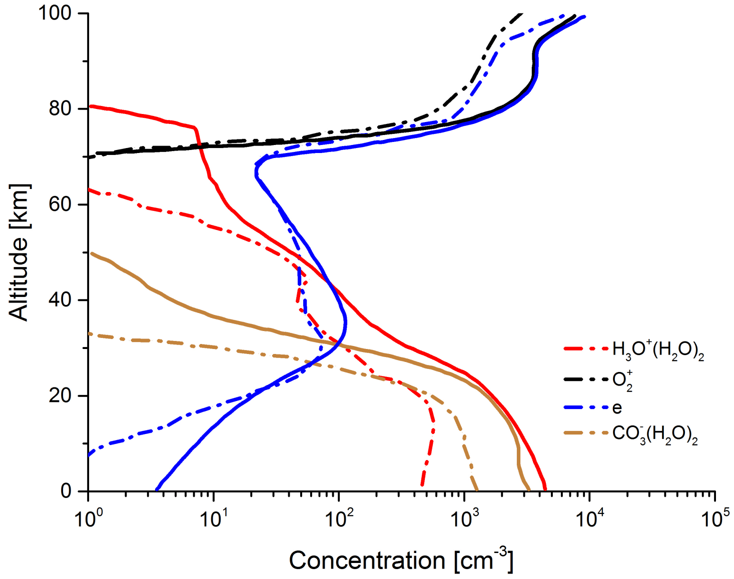

Figure 14. The density profiles of major ions, and electrons in the Martian lower dayside atmosphere.

On the basis of *Molina-Cuberos et al.* [2002] (solid line), *Haider et al.* [2009] (dashed line).

Ions are three orders of magnitude less mobile than electrons [*Michael et al.*, 2008]. As a result, widespread electrons control the conductivity of the Martian atmosphere though close to the surface, where the concentration of electrons is more than two orders of magnitude lesser, the conductivity depends also on ions [*Molina-Cuberos et al.*, 2002; *Aplin*, 2006; *Molina-Cuberos et al.*, 2006; *Michael et al.*, 2008]. As water clusters are the most abundant ions in the lower atmosphere, the concentration of these species depends on the amount of water vapor, which varies during the Martian year [*Molina-Cuberos et al.*, 2002] and dust activity.

Whitten et al. [1971] found that the D layer is located ca. 25-35 km above the Martian surface and has a density approaching $10^3/cm^3$. *Molina-Cuberos et al.* [2002] calculated that this peak is at the 35 km altitude and has smaller density, ca. $10^2/cm^3$. Recently, *Haider et al.* [2008] determined its density as ca. $0.5 \cdot 10^2/cm^3$. This is a permanent layer (Figure 14), distinct especially at night [*Whitten et al.*, 1971; *Haider et al.*, 2010]. It was probably observed, using the occultation method, during Mars 4 and 5 missions, for χ = 127° and 106°, respectively, [*Savich and Samovol*, 1976; *Haider et al.*, 2010]. These observations, however, were not very accurate for these altitudes. In the work of *Haider et al.* [2008], the authors calculated that the D layer altitude changes during the year. It is 30 km in summer, and 25 km in winter. Also in winter its concentrations are lower. In addition, during dust storms a hole in the bottom of the D region may occur [*Haider et al.*, 2010].

2.4.2.2 Conductivity profiles

The conductivity of the Martian lower atmosphere varies spatially and temporally. The most significant is the diurnal variation related to solar radiation. Seasonal oscillations of the daytime ionosphere are related to solar flux variations, due to changes in the distance to the Sun. Other factors are related to solar activity, as during its maximum GCR flux is limited, and SEP flux is enhanced. The conductivity depends also on aerosol concentration, surface morphology, and magnetic anomalies.

Since the average Martian atmospheric pressure at the planetary surface (ca. 7 mb) is similar to this in the terrestrial stratosphere, it is commonly assumed that the Martian atmospheric conductivity at the ground level should be equivalent to that in the terrestrial stratosphere (ca. 10^{-11} S/m) [*Berthelier et al*., 2000]. This assumption has been confirmed by numerical calculations [*Michael et al*., 2008]. Therefore, on Mars at the ground level, the atmospheric conductivity is 2-3 magnitudes larger than on Earth.

The conductivity profiles of the nighttime and daytime lower atmosphere proposed in literature are based on electron densities and collisions frequencies data [*Sukhorukov*, 1991; *Pechony and Price*, 2004]. More recently those profiles were developed, taking into consideration ion and aerosol concentrations [*Michael et al*., 2007; 2008], influence of high ($F_{10.7}$ = 166) and low ($F_{10.7}$ = 69) solar activity, and precipitation of meteoroids [*Molina-Cuberos et al*., 2006]. At the 80 km altitude, the atmospheric conductivity reaches ca. 10^{-5} S/m during daytime, and 10^{-7} S/m during nighttime (Figure 15).

The distance between the surface and the ionosphere is not constant. It is substantially reduced for the Tharsis region and Olympus Mons (see point 2.5), influencing a local conductivity profile [*Aplin*, 2006]. Aerosols existing in the atmosphere reduce conductivity about a factor of 2 [*Michael et al*., 2008], however that effect becomes negligible above 50 km altitude. During dust storms, the conductivity is reduced by 2 orders of magnitude [*Michael and Tripathi*, 2008].

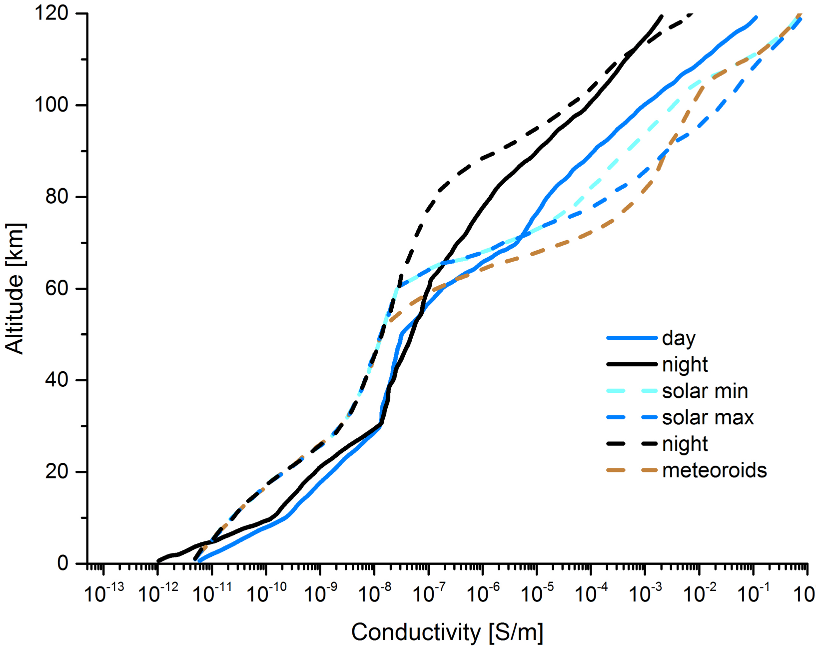

Figure 15. Conductivity profiles of the Martian ionosphere.

On the basis of: *Pechony and Price* [2004] (solid lines), *Molina-Cuberos et al*. [2006] (dashed lines).

As seen in Figure 15, the independently obtained conductivity profiles by *Pechony and Price* [2004] and *Molina-Cuberos et al*. [2006] are similar. Due to these small differences and in order to compare results with those obtained from previously analytical modeling, the conductivity profiles calculated by *Pechony and Price* [2004] are employed in this work. These profiles were established on the basis of electron density and electron collision frequency data given by *Cummer and Farrell* [1999] (Figure 16). The electron-neutral collision frequency was calculated from the theory of *Banks and Kockarts* [1973] and the electro-CO_2 cross-section was taken from *Hake and Phelps* [1967]. The atmospheric pressure and temperature were used from the Viking Landers data [*MacElroy et al*., 1977]. The conductivity profiles below 80 km were calculated on the basis of *Whitten et al*. [1971]. Above 110 km by *Zhang et al*. [1990] and *Hanson et al*. [1977] for nighttime and daytime, respectively.

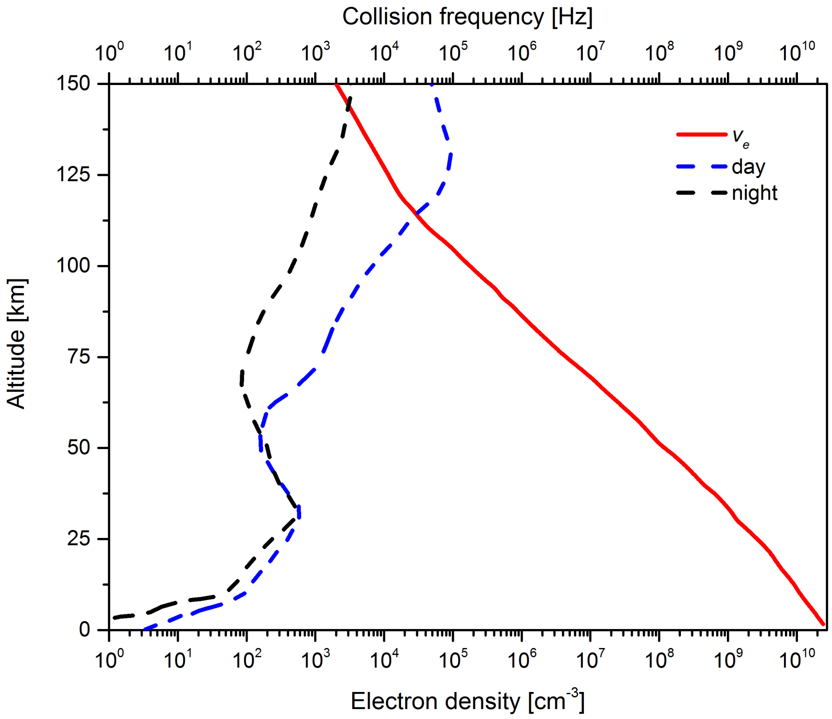

Figure 16. Profiles of electron collision frequency (solid line) and electron density (dashed lines) on Mars.

On the basis of *Cummer and Farrell* [1999].

On the basis of these conductivity profiles, the atmospheric resistance, R_A, can be calculated from (1.48a). It is ~10 Ω, a much smaller value than the terrestrial atmosphere resistance (~250 Ω). Due to this high value, the electric relaxation time at the surface, given by (1.49), is ca. 0.1 min. The characteristic time of discharging of the Martian electric circuit is therefore 400 times shorter than on Earth and more frequent sources are required to maintain the circuit.

2.4.3 ELF sources in the atmosphere

It is possible that some natural EM sources of the magnetospheric or atmospheric origin exist on Mars and can be employed to investigate the subsurface of the planet. The magnetospheric group is related most probably with magnetic pulsations, and transient magnetic variations, described in point 2.3, whereas the atmospheric group to electrical discharges, which are presented in this point.

Fossils informed us that lightning activity on Earth has existed for at last 250 million years. Its abundance and longevity suggests that it might have played a significant role in the origin of life [*Rakov and Uman*, 2006; *Harrison et al.*, 2008; *Yair et al.*, 2012]. Remote observations have allowed for detection of lightning activity on Jupiter, Saturn, and probably Venus. Uranus and Neptune yielded possible signals of lightning discharges as well. Electricity in the Solar System can also be related to charging of planetary rings, volcanism on Io, and charges carried by asteroids [*Harrison et al.*, 2008].

Electrical discharges are transient events that take place when electric field reaches the breakdown value. The energy gained by electrons in this field becomes larger than the energy threshold for ionization. The medium is ionized, and current can flow, neutralizing the field. The return stroke current may be given by [*Jones*, 1970; *Cummer and Farrell*, 1999]:

$$I(t) = I_0 (e^{-t/\tau_\alpha} - e^{-t/\tau_\beta}) \tag{2.1}$$

where: I_0, τ_α, and τ_β are constants. For discharges similar to terrestrial ones, we may assume: I_0 ~20 kA, τ_α ~50 μs, and τ_β ~5 μs [*Cummer and Farrell*, 1999; *Rakov and Uman*, 2006], implying that the stroke duration, $\tau = \tau_\alpha - \tau_\beta$, is ca. 45 μs. Radio emission is produced in broad spectrum, peaking at about $1/\tau$, i.e. in the VLF range [*Zarka et al.*, 2008].

For comparative purposes, we can assume that on Mars, there are vertical electric discharges characterized by the current given by (2.1). A waveform related to such an electric discharge is presented in Figure 17. This source generates a peak current ca. 14 kA. The charge transported by the discharge, q_c, can be obtained by integrating (2.1):

$$q_c = \int_0^\infty I(t)dt = I_0(\tau_\alpha - \tau_\beta) = I_0 \tau ,$$

and it is 0.9 C.

I assumed that the current propagates similar as on Earth with exponentially decreasing velocity *v*, given by [*Cummer*, 1997]:

$$v(t) = v_0 e^{-t/\tau_\lambda} ,$$

where: τ_γ ~33 μs, and $v_0 = 8 \cdot 10^7$ m/s [*Cummer*, 1997]. Therefore, the total length of the discharge channel is:

$$\ell_0 = \int_0^\infty v(t)dt ,$$

which gives ℓ_0 = 2.6 km, and the channel length can be given by:

$$\ell(t) = \ell_0 (1 - e^{-t/\tau_\gamma}) . \tag{2.2}$$

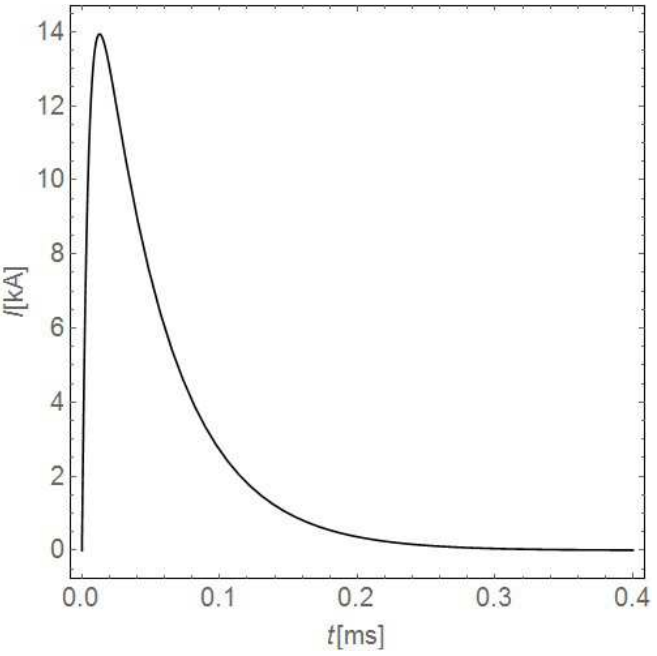

Figure 17. Electric discharge current waveform.

The current moment *s*(*t*), can be calculated using (2.1) and (2.2):

$$s(t) = I(t)\ell(t) = I_0\ell_0\left(e^{-t/\tau_\alpha} - e^{-t/\tau_\beta}\right)\left(1 - e^{-t/\tau_\gamma}\right). \tag{2.3}$$

By the Fourier transform of (2.3), we get the spectral source current moment *s*(*f*). For low frequencies (below 3 kHz), the spectrum is almost flat and equals to the electric dipole moment (charge moment) of the return stroke, which can be defined as [*Kulak et al.*, 2010]:

$$\tilde{p} = \int_0^\infty s(t)dt = I_o\ell_0\left(\tau_\alpha - \tau_\beta - \frac{\tau_\alpha\tau_\gamma}{\tau_\alpha + \tau_\gamma} + \frac{\tau_\beta\tau_\gamma}{\tau_\beta + \tau_\gamma}\right). \tag{2.4}$$

This means that the return stroke can be described in the ELF range as a very short impulse of amplitude given by (2.4). Using (2.4), we get that the studied discharge is characterized by a charge moment: ca. 1 C·km. Since ELF propagation is a linear problem, the obtained values could be rescaled easily for other sources [*Cummer and Farrell*, 1999]. On Earth, a typical discharge has a charge moment ca. 6.2 C·km [*Kulak et al.*, 2010].

The electric field value necessary for the electric breakdown depends on the atmospheric pressure and composition and can be described using Paschen’s law [*Raizer*, 1991]:

$$E_{br} = \frac{\tilde{B}p}{\tilde{G} + \ln(pd)}, \tag{2.5}$$

where: $\tilde{G} = \ln[\tilde{A}/\ln(1/\tilde{\gamma}+1)]$, $\tilde{G}$ and $\tilde{B}$ are constants, depending on the composition, $\tilde{\gamma}$ is the Townsend ionization coefficient, *p* is the atmospheric pressure, and *d* is the distance between charges.

On Mars, due to low atmospheric pressure, the electric breakdown (for *d* = 1 m) is ca. 20-25 kV/m, whereas on Earth, it is ca. 3 MV/m at sea level, and in clouds can be less than $5 \cdot 10^2$ kV/m [*Melnik and Parrot*, 1998]. Energetic electrons, which trigger the breakdown process are generated by cosmic radiation, but on Mars they can also be related to additional sources, such as: solar energetic particles. Since energetic electrons can penetrate to low altitudes, e.g. within magnetic cusps, they may interact with aloft dust and generate also secondary electrons [*Pavlu et al.*, 2014].

Electrical discharges in the Martian atmosphere are not associated with *Cb* clouds as they do not occur on Mars. However, many theoretical and experimental studies indicate that the most widespread cloudy phenomena, dust storms and dust devils, can generate electrical discharges, and they are assumed to be sources of ELF radiation on Mars [*Farrell and Desch*, 2001; *Krauss et al.,* 2006; *Zhai et al.*, 2006]. Nonetheless, there is no strong evidence of such electric activity [*Ruf et al.*, 2009; *Gurnett et al.* 2010; *Anderson et al.*, 2012].

2.4.3.1 Martian dust

Dust has significant impact on the global Martian atmospheric structure and circulation. Energetic electrons produced by wind-blown sand are responsible for generation of hydrogen peroxide [*Atreya et al.*, 2006], a strong oxidant hostile to life, and dissociation of methane [*Farrell et al.*, 2006]. Martian dust particles are 1-2.5 μm in diameter, and their size can vary with altitude [*Clancy et al.*, 2003]. Dust can acquire electrostatic charges, which is manifested by dust-covered wheels and solar panels of the rovers and landers [*Ferguson et al.*, 1999]. Dust also has strong magnetic properties, which were measured by magnet arrays onboard the *in situ* missions, such as Viking, Pathfinder or Mars Exploration Rovers (MER) [*Hviid et al.*, 1997; *Goetz et al.*, 2008]. As there is always huge amount of suspended dust in the atmosphere, the Martian sky is pink in color. Some observations indicate presence of two temporal dusty layers, located ca. 20-30 km and ca. 45-65 km above the surface [*Guzewich et al.*, 2013].

The omnipresence of dust in the atmosphere cannot be explained easily. Under the Martian gravity and atmospheric density, the most susceptible to move by wind are not dust grains but sand grains, which are ca. 120 microns in diameter [*Greeley and Iversen*, 1985]. Dust grains are more difficult to be lifted off, mainly due to strong interparticle forces. The threshold wind velocity near the surface necessary to set such grains in motion is ca. 200 m/s, which is unrealistic. Therefore, a mechanism, which allows carrying them into the atmosphere, must be related to other phenomena. The most probable ones are saltation and dust devils.

Saltation is a primary mode of aeolian transport. In this mode particles are lifted off the ground and accelerated downwind. During transport they collide with the surface, ejecting new grains into the atmosphere. On Mars, saltation, due to lower atmospheric density and gravity, is characterized by longer and higher trajectories. Their height may be up to 10 m and their length up to 100 m, whereas on Earth, it is 1 m and 10 m, respectively [*Almeida et al.*, 2008]. As the velocity of saltating grains on Mars is higher than on Earth, their impact on smaller grains can be more important.

Dust devils are thermally driven vortices. They are associated with high-speed winds and low pressures, which facilitate dust lifting from the surface. Their role can be very significant. Since global dust storms take place every few years and dust deposition rate is much shorter, frequent dust devils are probably responsible for the existence of constant dust haze in the Martian atmosphere [*Basu et al.*, 2004].

2.4.3.2 Charging mechanism

There are three processes that can be related to charging of dust and sand grains: triboelectricity, fracto-emission, and photoemission. All of those processes are present on Mars and the former is the most important. Triboelectricity (“tribo“ from *gr*. ‘to rub’) is a transient contact electrification process that occurs between similar as well as dissimilar materials. Materials have been arranged into triboelectric series based upon their tendency to become charged and the polarity of charging. Particle-particle electrical interactions depend on many factors, such as: composition, size, roughness of particles, coatings, collision frequency, and contact time between colliding grains. Triboelectric potential is related to a surface workfunction, which measures the ability of a surface to retain free electrons. Materials with a low workfunction have a positive charge [*Yair*, 2008]. In laboratory tests, bigger grains become more often positively charged, whereas the smaller ones tend to be charged negatively [*Stow*, 1969; *Ette* 1971]. This is also true for a Martian regolith simulant called JSC-Mars-1 (see point 2.5) [*Forward et al.*, 2009]. Triboelectric charging does not occur when materials are characterized by unimodal size distribution. Charge transfer during collisions depends on the pre-collision charges, radii of particles, and difference in contact potential [*Desch and Cuzzi*, 2000; *Kok and Renno*, 2008]. It has been experimentally measured that charges of up to $\pm 52 \cdot 10^4$ e are associated with a single Martian regolith simulant (JSC-Mars-1) particle [*Sickafoose et al.*, 2001], and effective workfunction of this material is 5.6 eV [*Yair*, 2008].

Fracto-emission is related to separation of charges due to the fracture of material. Fracto-emission plays an important role in the generation of charged materials during fragmentation of volcanic ejecta, and therefore in volcanic lightning activity [*Gilbert et al.*, 1991]. On Mars, it can be of some importance, especially in polar regions, where dust storm particles collide with ice particles, and collision-based processes can play a more significant role [*Yair et al.*, 2008].

Photoemission is related to emission of free electrons from a material surface due to external radiation of energy higher than the material workfunction (see point 2.4.2). Photoemission charging of a JSC-Mars-1 simulant is much lower than the triboelectric charging [*Sickafoose et al.*, 2001].

Many experimental and theoretical works have studied occurrence of electric discharges and generation of electric fields on Mars due to triboelectricity of dust-sand material. In an idealized model, charge generation in dusty phenomena is related to triboelectricity among saltating sand particles and the ground, and between sand particles and dust particles. During a dust phenomenon smaller particles, negatively charged, are carried by wind to higher altitudes, whereas heavier grains are concentrated near the ground. This leads to charge separation.

Eden and Vonnegut [1973] observed sparks and glow discharges from agitated dry sand in a glass flask. In the similar study, *Mills* [1977] also observed such phenomena. *Krauss et al*. [2006] conducted analogous research using a glass tube, a JSC-Mars-1 simulant, and glass micro-balloons. High intensive discharges were much less common than smaller ones. The number of discharges increased with decreasing pressure, and it was concluded that a large number of collisions is necessary to build up a significant amount of charge. On the other hand, the study by *Aplin et al*. [2012] displayed that electrical discharges occurred only if glass micro-balloons were added into sand particles. Therefore, the Martian simulant may not generate discharges, and the previous studies may be irrelevant as the glass containers, in which the experiments were conducted, affected the observed results by wall-dust interactions.

2.4.3.3 Electric field generation in saltation

Some measurements showed that the height of saltating trajectories does not change as wind speed increases [*Greeley et al.*, 1996]. This can be explained by a numerical model of *Kok and Renno* [2008]. The saltation layer is electrically active. Having included electric forces into the model, the authors found two effects. The saltation height does not increase linearly with wind friction velocity and can be constant along some values of shear velocity. In addition, electric forces facilitate lifting off particles from the surface, which results in a higher particle flux. The authors indicated that electric fields increase sharply towards the surface, as there is more particles, and with increasing wind velocity.

Experimental studies on Earth showed that electrification in saltation increases with wind velocity, as well as depends on grain size, and water content. When small amounts of water were added to a sand sample, the electrical field increased [*Qu et al.*, 2004]. On the contrary, large amount of water (over 2%) reduced these values, probably because the particles became less mobile. Electricity caused by fine sand is larger than that of coarse sand by 1-2 orders of magnitude [*Qu et al.*, 2004; *Zhang et al.*, 2004]. *Schmidt et al.* [1998] found that the trajectories of positive and negative charged particles were, respectively, 163% and 57% longer than the trajectories of particles without charge. They also found that strong upward-pointing electric fields, even up to many tens of kilovolts per meter, are related to saltating grains. Wind tunnels simulations have indicated similar values [*Qu et al.*, 2004; *Zhang et al.*, 2004]. Measurements indicated that electric fields above ~80kV/m reduce the threshold friction velocity necessary to lift sand grains by wind, resulting in doubling the flux of sand particles [*Kok and Renno*, 2006].

The electric breakdown increases with decreasing distance between electrodes (see (2.5)). In saltation, this distance is ca. 30 cm, which leads to a higher value [*Kok and Renno*, 2009]. In addition, in saltation, electric fields exceeding 5 kV/m accelerate free electrons to energies sufficient to ionize CO_2 molecules [*Delory et al.*, 2006]. The increase in ion and electron concentrations enhances the atmospheric conductivity, neutralizing the charges and limiting further increase in the electric field. This negative feedback limits the electric field to 15-20 kV/m and rules out the initiation of electric discharges [*Kok and Renno*, 2009]. Yet these findings do not limit discharges in dust devils and dust storms, where electric discharges are associated not solely with saltation but also suspension, and in which charge separation is not limited to small distances.

2.4.3.4 Electric field generation in dust storms

Processes leading to initiate a dust storm on Mars are various, complex, and still not fully understood although such phenomena occur every day. Only in 1999, from March 9 to December 31, were observed 783 dust storms. The majority of them, 771, were local events (area > 10^2 km^2), and 12 were of regional scale (area > $1.6 \cdot 10^6$ km^2). Statistically, the dust storm occurrence rate during that time was 2-3 per sol [*Cantor et al.*, 2001]. Over the period from 1999 to 2011, 65 large storms were identified. Two of them, in 2001 and 2007, were global, planet-encircling events (Figure 18), and the rest of them were regional in scale, with only a few slightly smaller [*Wang and Richardson*, 2013]. Martian dust storms form especially in two periods, for solar areocentric longitudes (Ls) from 150° to 270° and from 300° to 360°. On the basis of ground-based telescopic data, which have been acquiring over more than 100 years, it is possible to establish that global dust storms occur every few years [*Martin and Zurek*, 1993]. Local storms last a day, regional several days, global many weeks. Large dust storms most frequently originate in Acidalia. The second most popular region is Utopia, however initiation of large storms is 3 times less frequent there. Other areas are Arcadia and Hellas, Syria-Solis, Cimmeria-Sirenum, Chryse, Argyre, Noachis, Margaritifier, and the southern edge of Arabia. The 2001 global storm resulted from merging of several dust storms, originated in Hellas and Syria-Solis, whereas the 2007 dust storm, of somewhat tentative Chryse origin, grew between Hellas and Noachis [*Wang and Richardson*, 2013]. During the 2001 planet-encircling event, it was found that atmospheric dust was lofted to altitudes as high as 80 km [*Clancy et al.*, 2010]. Also, the polar caps zones are areas where many small dust storms initiate. Wind velocity associated with large dust storms was measured during Vikings' missions. The Viking Lander 1 (VL1) experienced gusts of wind ca. 26 m/s at 1.6-m altitude during the arrival of two global dust storms in 1977. The MGS observations acquired between 1997 and 2001 revealed that several local-scale dust storms reoccur annually at nearly the same locations and the same time of year [*Cantor et al.*, 2002].

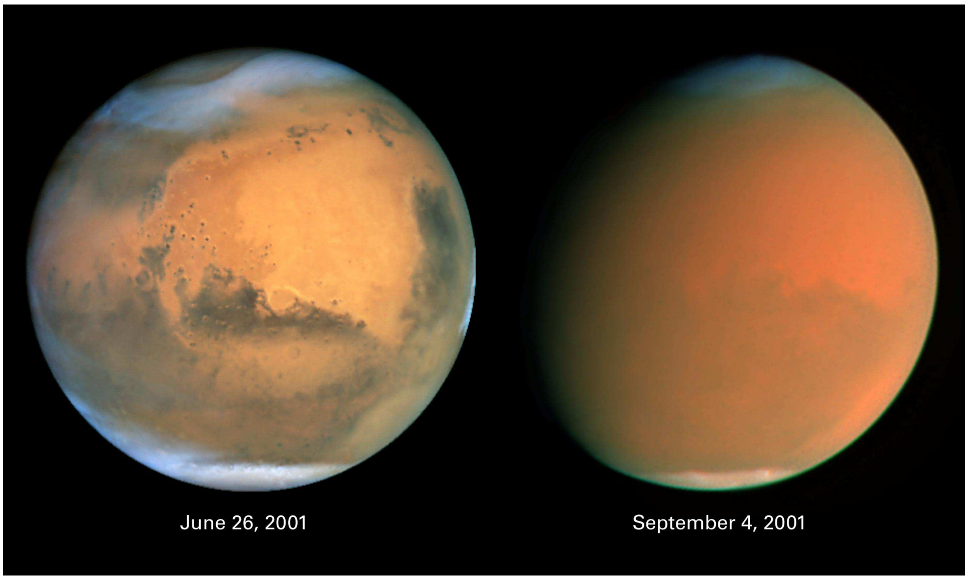

Figure 18. 2001 global dust storm on Mars. The image on the left shows a situation priori to the global storm, on the right during planet-encircling storm.

Source: JPL/NASA/STScI.

As there are no measurements on Mars, we can only approximate the electric activity from dust storms and dust devils on the basis of studied cases in the terrestrial environment. Several works have been conducted especially in Africa, Asia, and North America [*Stow*, 1969; *Kamra* 1972; *Williams et al*., 2008; *Zhang et al*., 2004]. *Stow* [1969] observed upward-pointing electric fields up to 200 kV/m at the ground level during dust storms in the Sahara desert. In work of *Zhang et al.* [2004], the authors observed sand storms in China at the Tengeli desert area. During fine weather the observed electric field was of positive values, increased with altitude, and weakly depended on wind speed. The maximum value 5 kV/m was observed at 16 m altitude. During sandstorm, however, the fields varied with wind speed, transportation rate, and electric conditions preceding the storm. When the wind speed was larger than 9 m/s, the electric field was at all heights negative. During slower winds positive and negative fields were observed. The maximum value of the field -200 kV/m was observed at 16 m. Also over West Africa, in the Sahel region, violent dust storms called ‘haboobs’ were investigated. They were found as highly electrified. Electrification was the strongest during large mass loading. The magnitude of the field perturbation related to those gust fronts was up to 10 kV/m [*Williams et al*., 2008].

2.4.3.5 Electric field generation in dust devils

Martian dust devils are larger and more frequent than those observed on Earth. They can reach more than 10 km in height and a kilometer in diameter (Figure 19). Terrestrial ones are not higher than 2.5 km and not wider than 150 m [*Fisher et al*., 2005; *Cantor et al*., 2006; *Greeley et al*., 2006]. On Mars, they were firstly identified from the Viking Orbiter images [*Thomas and Gierasch*, 1985]. As calculated from *in situ* observations in Gusev Crater, such phenomena have a typical lifetime of several minutes, with a mean value ca. 170 s. Dust devils do not play a major role in the initiation of major storms. However, they are important in the Martian dust cycle. Throughout the Mars Pathfinder (MPF) mission atmospheric opacity was increasing despite the fact that there was no global dust storm. Calculations made by *Ferri et al*. [2003] showed that dust devils can produce dust flux an order of magnitude larger than mean deposition rate observed by the MPF. The dust devils registered in the MPF images were interpreted to be tens of meter wide, and hundreds of meters tall. The wind speed about 5 m/s was responsible for the development of those structures [*Schofield et al*., 1997; *Metzger et al.*, 1999]. Dust devils are present in all latitudes and elevations. The images acquired during the MGS mission from 1997 to 2006 showed that northern Amazonis Planitia between 14:00 and 15:00 local solar time (LST) is the most active dust devil region in terms of occurrence, frequency, and size. Dust devils tend to arise during local spring and summer, with a peak in midsummer. The largest dust devils, aside from Amazonis, occur also in Syria-Claritas or Meridiani [*Cantor et al*., 2006] often in large groups [*Fisher et al.*, 2005]. Dust devil tracks give us additional information on these phenomena. These linear structures can be easily recognized in images. They are of various lengths and typically tens of meters across. *In situ* observations of dust devils have also been conducted. The Spirit rover, in Gusev Crater, imaged 533 dust devils in 270 sols during a spring-summer season. They occurred from 09:30 to 16:30 LST, with the maximum around 13:00 hours [*Greeley et al*., 2006]. In the Martian arctic, dust devils were captured by the Phoenix mission instruments. During the 151-sol mission, 502 vortices, with a peak around noon, were observed in pressure data [*Ellehoj et al*., 2010]. The VL instruments measured wind velocity exceeding 25 m/s during dust devils passages. Three vortices were assumed to have produced gusts of 36-44 m/s. These values correspond to a strong gale on Earth, though as the Martian atmospheric density is ca. 60 times smaller than the terrestrial atmosphere density, such phenomena have 10 times weaker wind influence [*Read and Lewis*, 2004].

Figure 19. A 20 km high dust devil captured by the High Resolution Imaging Science Experiment (HiRISE) camera on the Mars Reconnaissance Orbiter. The diameter of the plume is 70 m.

Source: NASA/JPL-Caltech/UA.

The evidence for electrification of dust devils is various and related to experiments, computer simulations, and analytical studies. The electric and magnetic observation on Earth indicate that with dust devils are related: quasi-static DC electric fields of the order of 1-100 kV/m, [*Freier*, 1960; *Crozier*, 1964; *Farrell et al*., 2004; *Renno et al.,* 2004; *Zhai et al*., 2006], AC currents [*Houser at al*., 2003], and ELF emission.

Studies of *Freier* [1960] and *Crozier* [1964] showed that in a dust devil negative charges are located above positive ones. Charge concentration in terrestrial dust devils is ~10^6 e/cm^3. Such values are comparable to the charge particle density in the F region of the ionosphere [*Farrell and Desch*, 2001]. In the work of *Houser et al*. [2003], the authors measured static discharges in the range 30-300 Hz, when a magnetic sensor was immersed within a 10-m wide, and hundred-meter tall structure. They observed also continuous ELF emission (with a peak at ca. 10 Hz) during its approaching and receding. They proposed that this continuous radiation is related to cyclonic motion of charge dust particles within the dust devil. Such motion leads to forming a solenoid-type structure, which evolution results in the magnetic field changes. The similar results were found during the major experiment of the MATADOR (Martian ATmosphere And Dust in the Optical and Radio) program [*Farrell et al*., 2004]. The MATADOR program studied the electromagnetic nature of dust devils in Nevada and Arizona. In an observed dust devil, the electric field measurement exceeded -4.3 kV/m and saturated the field mill, used in the investigation. The fair weather electric field measured during that time indicated 70 V/m. In addition, ELF detection correlated with DC detection. The magnetic emission in the ELF range, measured when the dust devil was active, was 100 times stronger than the background level [*Farrell et al*., 2004].

Such high values of the electric field in dust devils have also been obtained from simulations. *Renno et al.* [2004] found that in a 7 m wide dust devil, the electric field exceeds 10 kV/m. *Zhai et al*. [2006] simulated a dust devil with the diameter of 10 m, and 100 m high. In this structure, the maximum electric field of 150 kV/m was reached after 10 min.

Melnik and Parrot [1998] developed a 2D numerical model, which indicated that Martian dust devils are capable of generating discharges, when there was sufficiently high dust particle density, and wind velocity. Their results showed that the electric fields associated with these events can reach the atmospheric breakdown level.

In the work of *Farrell et al*. [2003], the analytical method was employed. It was indicated that Martian dust devils, due to higher atmospheric conductivity, do not reach the same values of electric field as terrestrial ones. However, they found that the electric fields quickly rise to the breakdown level for some specific triboelectric potential of smaller and larger grains. More robust model was presented by *Farrell et al*. [2006]. In this work, the authors included not only electrostatic modeling and charge exchange between particles, but also fluid dynamics. This allowed establishing the relationship between wind velocity, particle flux, and electric field generation. The model did not employ saturation mechanisms, such as corona effect or grains separation. In this model, the electric field increased linearly with wind velocity. The field grew exponentially and reached the breakdown level in about 15 s after initiation of vertical winds. In addition, the electric field decreased sharply as the grain radii became comparable.

2.4.3.6 Global atmospheric electric circuit

If there is a global circuit on Mars, its current will flow in the opposite direction than on Earth, due to the character of the sources (Figure 20). *Farrell and Desch* [2001] presented a simplified model in which current from a single small dust was ~1 A. For a small dust devil of 1 km height, current was assumed to be only 2 μA. In contrast, current from a regional storm was established to be very large, of the order of 10^5 A, but distributed over the 500x500 km system. As one large dust storm may exist, along with numerous smaller storms, during storm season, the electric field in the fair-weather regions was estimated to be 475 V/m. During quiescent season, dust devils were believed to be most significant in the process. The anticipated total electric field in fair-weather regions related to them was calculated to be about 0.1 V/m. The authors, therefore, proposed two different seasons with a 10^3 variation in the Martian electric field value, much greater than that on Earth, which varies by a factor of ~2 [*Farrell and Desch*, 2001].

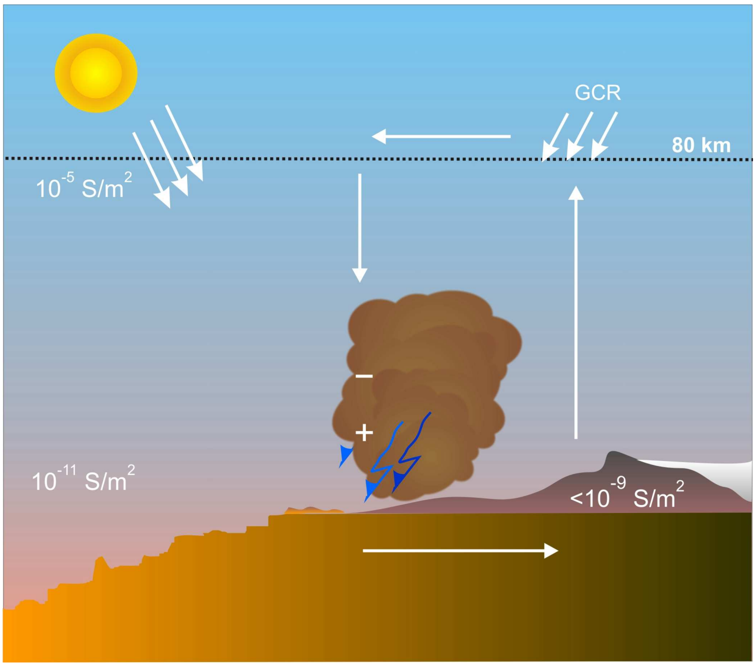

Figure 20. Martian global electric circuit. The dashed line indicates the ionosphere boundary.

If a global circuit exists on Mars, it might display a “Carnegie” curve variations [*Aplin*, 2006]. A morning peak could result from dust storms in the Utopia and Hellas regions at 60-120°E, and an afternoon peak would start around 13:00 at 0°E as dust storms occur most frequently in regions at ca. 300°E, and the maximum of dust devil activity is at about 13:00 LST. This peak is supposed to extend till late evening owing to relatively high dust storm activity in regions between 200 and 300°E. The curve minimum could occur during nighttime at 0°E as there is small number of dust storms in the longitudinal range 150°-200°E and no dust devil activity during night. Due to seasonal changes of the sources, the curve is expected to vary during the year.

2.4.3.7 Radio emission from the Martian sources

Emission associated with the Martian EM sources should be different from that observed in the terrestrial environment, and their changeable character should lead to diurnal and seasonal variations in ELF field.

In the work of *Farrell et al*. [1999], two different types of radio emission from dusty phenomena on Mars were speculated. The first, with a peak in the VLF range, was associated with charge separation within a cloud. The second, with a peak in the high frequency range (HF, 3-30 MHz), was assumed to be generated by short glow discharges as microscopic charges from grains are removed to the air. Such phenomena will take place only if the time rate of tribocharging is faster than the local charge relaxation determined by the atmospheric conductivity [*Desch and Cuzzi*, 2000].

The calculations and observations made by *Renno et al*. [2003], based on the suggestion that HF radio emission could be generated by glow discharges [*Farrell et al*., 1999], led to possible detection of such events on Mars in the microwave range. *Renno et al*. [2003] concluded that ground-based radio observations, at 22 GHz with the Very Large Array (VLA) telescope, made in 1995, displayed a correlation between high microwave emission and dust devil activity. The highest discrepancy between the observations of the microwave emission and the modeled values was found to be between 12:00 and 16:00 LST, in the period of the dust devil activity peak. In 2006, *Ruf et al*. [2009] conducted some observation also in the microwave range using a 34 m parabolic antenna of the Deep Space Network. They observed unusual pattern of radiation, emitted in minutes-long bursts, when a regional dust storm was present on Mars. They also observed ELF peaks at approximately 10 Hz, which were explained as detection of Schumann resonance induced by discharges within the dust storm [*Ondraskova et al*., 2008]. *Anderson et al*. [2012] performed similar observation using the Allen Telescope Array in 2010. They found similar variations. However, this variability spread across a broad spectrum and was driven by narrowband radio frequency interferences. The spectral peaks with a periodic 10 Hz structure were common, appearing one or two per hour, and despite the fact that there was no dust storm on Mars during observations. The authors did not concluded whether observed signal had its source on Mars or on Earth. Also *Gurnett et al*. [2010] stated that during five-year search for radio signals associated with discharges, no signal was discovered although during this period two major and several regional storms occurred. It is worth mentioning that the MARSIS instrument, used in this research, would be capable of the detection of terrestrial lightning activity.

Mills [1977] anticipated that it is necessary to conduct radio observations and electrostatic field measurements at the Martian surface to establish whether electrical discharges are present on Mars. *Delory* [2010] also stated that a relatively simple experiment to measure radio waves in the spherics band would provide a similar confirmation, as would the detection of Schumann resonance, and that among all possible measurements, observations from instruments on the future *in situ* network platforms are most likely to produce a significant step in our understanding of the true nature of the atmospheric electricity on Mars. They will enable to study the entire electro-meteorological system, including AC and DC fields, wind velocity, temperature, pressure, and dust properties.

2.5 Ground

The subsurface layers as well as the planetary interior are unknown variables of the Martian environment. Our knowledge of this vast region is based mainly on theoretical models, Martian meteorites planetary surface structure and composition or gravimetric and magnetic data.

The initial stage of Mars' evolution went through a phase of differentiation. When the planet was still very hot, heavier components fell to the center, and lighter became building blocks of the outer layers of the globe. As a result, separated spheres were formed. Due to the currently limited knowledge, the interior of the planet is divided into three spheres: a core, a mantle, and a crust. We do not know how these layers are separated from each other, and what their physical and chemical properties are. Since the planet never accreted much beyond a protoplanet stage, the differentiation of Mars was complete some 20-50 Myr after its formation. The planet had not been changed much during the periods of heavy impacts [*Taylor and McLennan*, 2009]. In comparison to Earth, the bulk Mars composition is enriched in volatile elements [*Dreibus and Wanke*, 1985].

The most important sources of our knowledge of the interior of Mars are SNC meteorites, named after places: Shergotty (S), Nakhla (N), and Chassigny (C), where the first specimens of these meteorites were found. These rare meteorites are basaltic achondrites. Shergotites are mainly composed of pigeonite and augite. They crystallized several hundred millions years ago. Nakhlites mainly composed of augite, and Chassignites of olivine, crystallized ca. 1.3 Gya. There is also one Martian meteorite, ALH84001, which cannot be included in those groups; it is orthopyroxenite, which was formed 4.5 Gya [*Taylor and McLennan*, 2009].

The Martian core constitutes 20-25% of the planetary mass, as it was estimated from the moment of inertia (MOI) measurements [*Taylor and McLennan*, 2009]. The core composition, phase and size are not well defined. It is proposed that the core is partially or fully liquid, with an average density 7 g/cm^3 for the liquid outer core, and 8 g/cm^3 for the solid inner core [*Taylor and McLennan*, 2009], composed mainly of iron, nickel, and a considerable amount (ca. 15%) of lighter elements, probably sulfur [*Stevenson*, 2001]. This high amount of sulfur allows for a decrease in the melting point temperature, and for the presence of the liquid outer core. In the past, the core magnetic dynamo was active as Mars had an intrinsic magnetic field even at about 500 million years after the formation [*Arkani-Hamed and Olson*, 2010]. The presence of the dynamo is confirmed by the residual magnetization of rocks [*Acuna et al*., 2001], but also by remanent magnetization in ALH84001 meteorite [*Taylor and McLennan*, 2009]. The dynamo termination could occur, for example, due to partial core solidification or modifications in the mantle convection. After the dynamo cessation, the magnetic field decay period related to the magnetic diffusivity was of the order of 10^4 years [*Barlow*, 2008]. The inner core radius is proposed to be ca. 700 km [*Taylor and McLennan*, 2009]. The radius of the outer core is not well determined. As the Martian MOI factor is large (0.36), the core is probably much smaller than the terrestrial one (MOI factor 0.33), and is assumed to be in the range of 1400-1800 km [*Taylor and McLennan*, 2009]. Due to these approximations, the boundary between the mantle and the core is not well established and can be located at depths from 1600 to 2000 km.

The mantle can be divided into two or three regions of various compositions. It contains significantly higher amounts of iron and volatiles than the terrestrial mantle. The upper mantle, to the depth of ca. 1000 km, with a density ca. 3.5 g/cm^3, is probably composed of olivine, orthopyroxene, clinopyroxene, and garnet, and can be described as a peridotite mantle [*Bertka and Fei*, 1998; *Fei and Bertka*, 2005]. The subsequent region is dominated by γ-spinel and majorite. The lower mantle, from the depth ca. 1850 km is composed mostly of Fe-Mg perovskite, which is formed under 225 kbar pressure transformation of γ-spinel [*Taylor and McLennan*, 2009]. The Fe-Mg perovskite will not be present in the mantle if the depth of this boundary is less than 1850 km. Its presence is an important factor in geological evolution of Mars as it may lead to development of long-lived large flow plumes [*Breuer et al*., 1998].

The Martian crust is poorly known. It is very homogenous, composed primarily of basaltic materials and has a mean density of ca. 2.9 g/cm^3 [*McGovern et al*., 2004]. The bulk composition of the Martian crust is presented in Table 5.

Table 5. The chemistry of the regolith, the JSC Mars-1 simulant, and the bulk composition of the Martian crust (na – not analyzed).

Oxide [wt.%]	Viking 1	Spirit	Opportunity	Pathfinder	JSC	Bulk
Na_2O	na	3.25	2.32	2.1	2.4	2.97
MgO	6	9.14	8.16	7.0	3.4	9.06
Al_2O_3	7.3	11.0	10.0	7.5	23.3	10.5
SiO_2	43	49.7	49.3	44.0	43.5	49.3
P_2O_5	na	1.09	0.91	na	0.9	0.90
K_2O	<0.15	0.49	0.51	0.3	0.6	0.45
CaO	5.9	6.85	7.63	5.6	6.2	6.92
TiO_2	0.66	1.02	1.03	1.1	3.8	0.98
MnO	na	0.33	0.40	na	0.3	0.36
FeO	18.5	16.8	19.2	16.5	15.6	18.2

On the basis of: *Allen et al*. [1998], *Bruckner et al*. [2008], *Taylor and McLennan* [2009].

Thermal inertia measurements provide maps of the surface particle size distribution. Regions of low thermal inertia, covered by dust, generate so-called thermal continents. These areas quickly heat up during daytime and also quickly cool down during nighttime. High thermal inertia regions are abundant in larger rock fragments or outcrops. The characteristic areas of high albedo (Figure 8) are commonly associated with dust, while the darker areas, with hard rocks layers, blocks of rocks, and their fragments. The brighter areas are mainly in the northern hemisphere and darker on the south. There is almost no lithological diversity of the Martian surface as the source of the secondary products is almost everywhere the same [*Taylor and McLennan*, 2009]. In the low albedo regions, two types of the crust have been determined. The first type is dominant on the southern hemisphere and is made of clionpiroxene-plagioclase basaltic rocks. The latter type is probably composed of altered basalts and is present mostly in the Acidalia region [*Bandfield et al*., 2000; *Rogers et al.*, 2007; *Taylor and McLennan*, 2009]. The Martian crust is mainly a primary crust, formed short after the accretion from the magma ocean. Later magmatic activity, related to the partial melting of the mantle, formed the secondary crust, which comprises ca. 20% of the entire crust [*Taylor and McLennan*, 2009]. The thickness of the crust was estimated to be about 50 km, using the Airy isostasy and variations in the Martian topography [*Spohn et al*., 2001; *Wieczorek and Zuber*, 2004]. However, this value may vary from 5 km to 100 km [*Carr*, 2008]. Several profiles of the crust thickness were presented in the work of *Neumann et al*. [2004] (Figure 21).

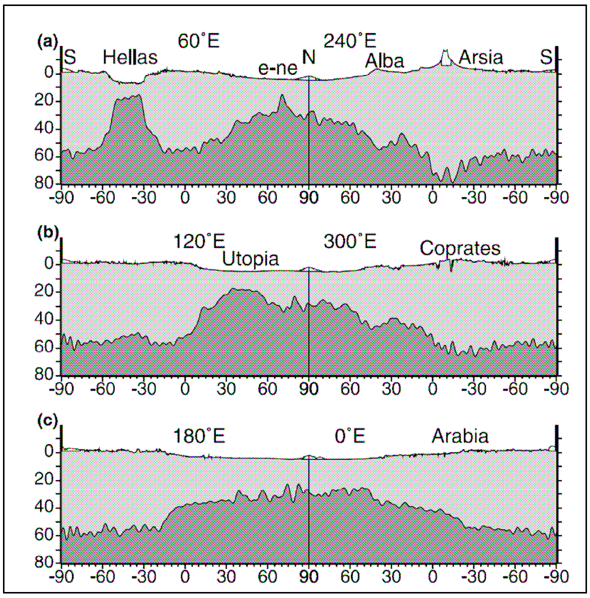

Figure 21. Crustal thickness from pole-to-pole along different longitudes: (A) 60-240°, (B) 120-300°, and (C) 180-360°.

Source: *Neumann et al*. [2004].

Currently, Mars is composed of one plate, and in this stagnant-lid regime, the interior of the planet cannot cool down as efficiently as in a case of tectonic plates. On the surface of the planet, there are some tectonic faults, but otherwise there are no actual signs of tectonic activity. The present models of the Martian evolution do not include even early plate tectonics [*Breuer and Spohn*, 2003], which had been proposed previously [*Sleep*, 1994].

Three periods in the geologic history of Mars have been distinguished (Table 6). The earliest, up to 3.7 Gya is called the Noachian, and was followed by the Hesperian, which ended 3.3-2.9 Gya. The last period is called the Amazonian. Most areas derived from the Noachian period are located in the southern highlands. The northern lowlands were mostly created in the youngest period [*Tanaka et al*., 2014].

Table 6. Geological periods of Mars.

Geological Period	Age [Gyr]	Major Endogenic Activity	Major Exogenic Activity	Minerals	Atmosphere
Late Amazonian	0.4-0.0	Very low volcanic activity	Glaciations, PLD formation, aeolian activity, mass movements	Iron oxides (ferric oxide-rich)	Thin, dry
Middle Amazonian	1.5-0.4	Low volcanic activity	Mass movements		

Early Amazonian	3.1-1.5	Elysium volcanism	Mass movements		Thin, cold, dry with wetter periods
Late Hesperian	3.4-3.1	Limited volcanism	Marine processes (?), fluvial processes	Sulfates (sulfate-rich)	
Early Hesperian	3.7-3.4	Tharsis volcanism, tectonic activity, seismic activity	Fluvial processes, lacustrine processes		
Late Noachian	3.8-3.7	Tharsis volcanism, tectonic activity, seismic activity	Fluvial processes, lacustrine processes	Phyllosilicates (clay-rich)	Dense, warm, wet
Middle Noachian	4.0-3.8	Volcanism, formation of Hellas, cessation of the dynamo	Late heavy bombardment		
Early Noachian	4.6-4.0	Magma ocean, differentiation, magnetic dynamo	Crustal dichotomy formation, heavy bombardment		Loss of primary atmosphere

Data taken from: *Bibring et al*. [2006], *Barlow* [2008], *Taylor and McLennan* [2009], and *Cabrol and Grin* [2010].

Due to the fact that on Mars there is no sea level, the reference elevation is determined by the average radius surface (3396 km). The Martian surface is characterized by a bimodal hypsographic curve, with the maxima at: ca. 1500 m for the southern hemisphere and ca. -4000 m for the northern hemisphere. The planet therefore can be divided into the northern lowlands and the southern highlands (Figure 22). The average width of this Martian dichotomy boundary is several hundred kilometers. Yet, the transition between the lowlands and the highlands is not significant, for example in the Isidis area, the elevation changes by 4 km over a distance of 2500 km [*Carr*, 2008]. That dichotomy leads to unequal pole radius values, which in the northern hemisphere is 3376 km and in the southern: 3382 km. The dichotomy is also evident in terms of the aforementioned thickness of the crust. In the southern hemisphere the average thickness of the crust is 58 km, while in the northern hemisphere only 32 km. There are also differences in composition between those two regions. The northern plains are 2-3% FeO_T enriched. The Amazonian crust is depleted in incompatible elements, similarly to the SNC meteorites [*Taylor and McLennan*, 2009]. A hypsometric difference on Mars is much larger than on Earth and reaches 29,429 m. The lowest place, 8200 m deep, is located in the Hellas Basin, and the highest point, 21,229 m high, is the peak of the Olympus Mons volcano [*Carr*, 2008].

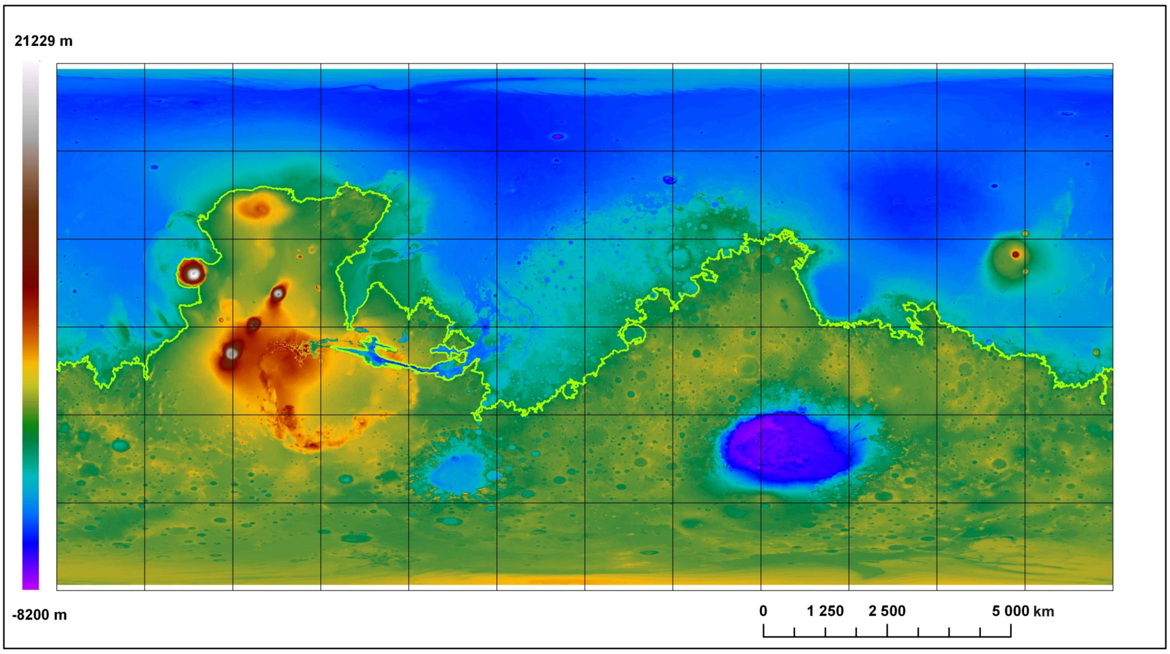

Figure 22. The Martian surface hypsometric map with the clearly visible dichotomy. The yellow line describes the zero elevation.

The surface of Mars is covered by loose regolith (Figure 23), which is homogenous across the planet (Table 5), probably due to global dust storms and almost uniform crust composition. It mainly consists of SiO_2 and iron oxides [*Bruckner et al*., 2008], from which magnetite is probably responsible for the magnetic properties of dust [*Geotz et al*., 2005]. The regolith is derived from impact ejecta, aeolian transport, weathering processes, and volcanic pyroclastics. Widespread sulfates and chlorines are of volcanic origin. To analysis the regolith properties in laboratories, Mars regolith simulants have been produced. The most popular of them are JSC Mars-1 simulants (Table 5).

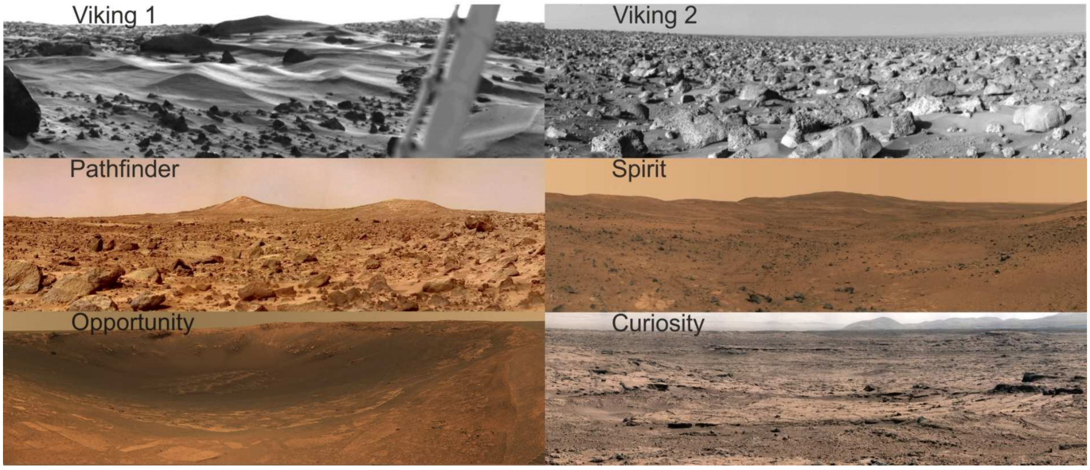

Figure 23. Martian surface as seen by six *in situ* missions.

All images by NASA.

The subsurface layers are more or less lithified sediments of various origin (volcanic, impacting, weathering), lava flows mixed with various fragmented and porous types of basaltic rocks. These layers may also contain ice deposits as some features of the surface morphology indicate permafrost processes and landforms. Under this cryosphere, where temperature is high enough, the presence of liquid water has been suggested [*Clifford*, 1993; *Clifford et al*., 2010]. The lowest layer of the crust is a basaltic basement. At this level, rocks are compressed and impermeable. The crust compositional variations with depth are probably insignificant.

Minerals found on the surface of Mars are mostly plagioclases and pyroxenes with a complement of olivines, layered silicates, oxides and hydroxides (magnetite, ilmenite, chromite, hematite, goetyt), sulfates (jarosite, gypsum), and salts (chlorides, bromides) [*Bandfield*, 2002]. In general, the planet is rich in mafic minerals. The entire surface of Mars is covered with iron oxides with varying degrees of oxidation. Quite commonly, especially in the older parts of the planet, clay minerals are observed. There are regions rich in hematite, primarily in Meridani Planum. The presence of olivine on Mars clearly indicates that an aquatic environment, in which they would be quickly destroyed, has not been present on Mars for some long time.

Most of the rocks on the surface of Mars are of volcanic origin, but there are also sedimentary rocks: evaporites and sandstones. Metamorphic rocks are not very common on Mars, and little is known about their occurrence. Sand covering large areas has composition similar to dark basaltic rocks. However, in many places sand layers have high salt content. Partial melting of the crust by intrusions of basaltic magma could form a small amount of silicate rocks [*Taylor et al*., 2008].

Since on Mars the average atmospheric pressure is very low, water does not occur in liquid state at the planetary surface (Figure 24). It sublimates in hot seasons and deposits as ice under cold conditions. In liquid state, it can exist only as an unstable form; in areas situated in depressions and exposed to strong sunlight. It has been proposed that such conditions may exist for several days in a year in Amazonis, Arabia, Hellas, Argyre, and Elysium [*Barlow*, 2008]. Liquid water may also occur during volcanic activity. Volcanic activity on Mars was present some 160-10 Mya [*Taylor and McLennan*, 2009]. Water in the largest concentrations is located in the polar regions in the form of ice.

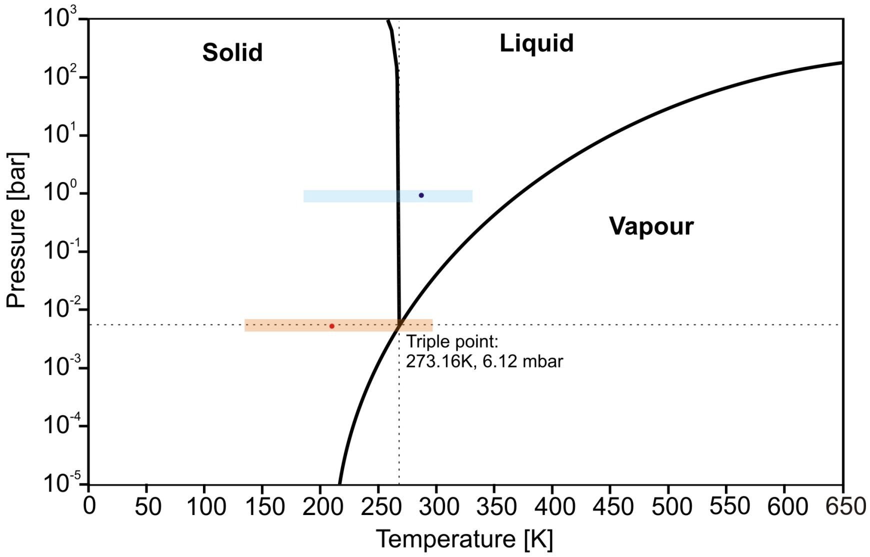

Figure 24. Water phase diagram. The orange area shows possible temperatures and pressures at the Martian surface, the blue – at the Earth surface. The dots indicate the mean values of those parameters.

Adapted from *Faure and Mensing* [2007].

Boynton et al. [2002], using the Gamma-Ray Spectrometer on the Mars Odyssey, identified two regions near the poles enriched in hydrogen. As these regions correlate with the areas of ice stability, the authors suggested that the hydrogen is related to subsurface ice. Also, the neutron mapping indicated that on average the top 1 m of the surface contains 14% of water [*Feldman et al*., 2004]. In greater part, it can be associated with ground ice, but also the presence of hydrated minerals can influence the outcome. In addition, those data indicate high amounts of water (up to 11%) even at latitudes <30° [*Feldman et al*., 2011]. This is difficult to interpret since there are no visible permafrost forms, and ice at these latitudes is unstable [*Mellon and Jakosky*, 1995]. In view of the fact that Mars undergoes from a period of higher obliquity to a period of lower obliquity, ice can occur beneath the surface even in areas where is presently unstable, but not at such low latitudes. The hydrated minerals cannot explain this either, because they are not present in so great amounts [*Carr*, 2008]. It is possible that other mechanisms, related to ice and water distributions within the crust, play a role, yet this must be verified [*Travis et al*., 2013].

Phyllosilicate and evaporite sediments found on Mars suggest that there was liquid medium on Mars [*Poulet et al*., 2005]. The presence of ground ice as well as observed extensive aqueous alteration indicates that this medium was water [*Craddock and Howard*, 2002]. In favor of this argument is also the fact that no other fluid has appropriate viscosity and stability properties to erode common surface features, such as outflow channels and valley networks [*Carr*, 2008].

Outflow channels, commonly 10–100 km across and 1 km deep, formed mainly during the Hesperian by floods occurring on the planet. Their origin is probably related to eruptions of groundwater, triggered by impact, volcanic or tectonic events or catastrophic drainage of paleolakes. These processes were associated with gigantic release of meltwater [*Carr*, 2008]. In addition, near the polar caps, events similar to Icelandic jökulhlaups might have taken place.

Valley networks, associated with fluvial erosive activity, were formed especially during the Naochian. These are very diverse structures with sizes ranging up to 2000 km in length, 200 m deep, and a few km wide [*Carr*, 2008]. The observed morphological characteristics indicate the existence of seeping or running water. Seeping water is probable even under cold conditions, for example under the cryosphere [*Gaidos and Marion*, 2003]. However, water had to be replenished to erode such features. On Earth, rainfall is responsible for recharging. On Mars, under cold conditions, rainfall was not possible over long periods. Therefore, a global water cycle of different origin was proposed. It is related to water deposition in the polar caps, resulting in melting of their basal layer under increasing pressure, infiltration to the underground, then seepage and sublimation to the atmosphere [*Clifford*, 1993]. Such phenomena were observed today at the south pole deposits probably rich in ground ice [*Milkovich and Pratt*, 2002]. However, it cannot explain all the visible forms as the length of some is too large and their elevation is higher than the polar caps [*Carr*, 2008].

Fluvial processes can most easily explain high erosion rate of the Noachian terrains, where almost all larger and older craters are highly eroded. This erosion decreased of 3-6 orders of magnitude from the Late Noachian to Hesperian [*Golombek and Bridges*, 2000]. The possible explanation is a climate change.

As at the Martian surface are some features that can be related to lacustrine or marine deposition, such as terraces, fan deposits (deltas), and layered sediments, the existence of paleolakes and oceans has been proposed [*Malin and Edgett*, 2003; *Cabrol and Grin*, 2010]. The large Noachian depressions such as Hellas and Argyre as well as lowlands of the northern hemisphere could be flooded during the Hesperian flooding periods. The existence of the Post-Noachian floods can be explained by changes in the atmospheric composition, due to releasing of CO_2, SO_2 or CH_4 by impact or volcanic activity. Such reservoirs would have left ice deposits. Such a deposit is probably the Vesitas Borealis Formation (VBF), which is roughly 100 m thick, and Late Hesperian in age [*Carr*, 2008]. Several recent works have found evidence supporting a subaqueous origin of the VBF [*Cooke et al*., 2011; *Moscardelli et al*., 2012; *Allen et al*., 2013]. The very low VBF dielectric constant, measured by the MARSIS, can be explained by the widespread deposition of desiccated aqueous sediments or sediments mixed with massive ice [*Mouginot et al*., 2012].

On the basis of the abovementioned landforms' morphology the volume of water that was necessary for their creation has been estimated. The results obtained in various works are given in a depth of a water layer spread over the entire surface of the planet (global equivalent layer, GEL) and range from 100 to 1000 m [*Parker et al.,* 1989; *Clifford and Parker*, 2001; *Carr*, 2008]. The loss of this amount of water is not completely explained. Probably 15-50 m GEL has been lost to space, and 10 m GEL is in the ice caps. The rest might sublimate to the atmosphere and then be cold-trapped in the cryosphere elsewhere on the planet. Some part of water was consumed by the formation of hydrated minerals [*Carr*, 2008, *Clifford et al*., 2010; *Valeille et al*., 2010].

Another aspect related to water reservoirs is the presence of methane. The release or production of methane, which has to take place continually, in order to explain its abundance, most probably involves the existence of liquid water under the surface, at least in the past [*Wray and Ehlmann*, 2011].

Bibring et al. [2006] suggested that pyllosilicates could be formed in the Early Noachian only in water-rich and pH-neutral conditions, whereas low-pH conditions characterized the Late Noachian to Early Hesperian period. In turn, the Late Hesperian and the Amazonian were water limited (Table 6). If this thesis is correct, weathering and subaqueous diagenesis took place in acidic environment. Also *Hurowitz and McLennan* [2007] suggested that chemical weathering on Mars was related to a sulfuric acid-rich environment with relatively low water-to-rock ratio. Therefore, olivine, apatite and Fe–Ti oxides were soluble, and other less soluble silicates (plagioclase, pyroxene) did not contribute. Under such conditions, Al-mobilization (which is very high on Earth) was limited, and the formation of significant Al-bearing products (clays) was inhibited. Evidence for chemical weathering processes in acidic conditions on Mars is: vast amounts of sulfates in the regolith, absence of carbonates, high iron and low aluminum mobility [*Taylor and McLennan*, 2009].

Water ice reservoirs are within the polar layered deposits (PLD). In winter, they are covered by seasonal CO_2 ice caps, which changes during a Martian year, presenting the most dynamic process on Mars [*Titus et al.*, 2008]. The largest part of PLD is concentrated up to the 80° latitude, but thin remnants are present even at 70° latitude [*Carr*, 2008]. They might be more extensive in the past as Mars probably is emerging from an ice age. These permanent forms are 3 km thick. They have spiral structures and are built mostly of water ice, with some debris and dust. The deposits are well stratified and cut by numerous valleys. Their volume is $\sim 10^6$ km^3 [*Carr*, 2008]. It is also assumed that some observed morphological structures located in the polar regions, and even at lower latitudes, are postglacial. Other features in these areas are interpreted as permafrost landforms, such as thermokarst and ice polygons [*Barlow*, 2008].

Another reservoir of water can be related to the cryosphere. As the temperature at the surface is lower than the freezing point of water, the upper limit of the cryosphere could be located just below the surface, beneath the daily fluctuations region. Below the cryosphere, liquid water can be present as radiogenic heating is expected to increase temperature above the freezing point [*Clifford*, 1993]. Unfortunately, we do not have information to verify this thesis. Also, we are not able to determine the properties of such reservoir of water. Aquifers can occur only if the total inventory of the Martian H_2O exceeds the amount of water consolidated within the cryosphere. The amount of water, therefore, is related to the pore volume of the subsurface and the cryosphere size (see point 3.1).

The composition and structure of the surface and subsurface affect the ground electrical properties, which are still unknown parameters in the global electric circuit. In the next chapter, some theoretical estimations of the subsurface structure of Mars are presented, providing information necessary to create hypothetical Martian EM waveguides and to find the relationship between various ground properties and the ELF propagation parameters.

3 Modeling of ELF propagation in the Martian waveguide

3.1 Modeling of the ground electrical properties

The electrical properties of the Martian subsurface can be solely estimated using theoretical models or studying terrestrial and lunar analogs [*Olhoeft and Strangway*, 1974]. The Martian ground conductivity is expected to be very low as water in liquid state cannot exist at the surface. In the work of *Grimm* [2002], some electrical models of the ground were proposed, but their parameters were not presented in detail. Also some laboratory experiments on analogous geological models of the Martian ground have been conducted, but solely regarding near surface layers and a 1-20 MHz frequency range [*Heggy et al.*, 2003]. Almost all other experimental works were only related to the electrical properties of the regolith [*Iben et al.*, 1996; *Morris et al.*, 1997; *Pettinelli et al.*, 2005; *Stillman and Olhoeft*, 2008], most frequently using JSC Mars-1 simulant [*Williams and Greeley*, 2004; *Stillman and Olhoeft*, 2008]. Therefore, in this point, in order to find whether ELF propagation can be employed to study the subsurface of Mars some theoretical models of the Martian ground are constructed on the basis of the present knowledge of the Martian surface petrology and available results of experimental studies on electrical properties of rocks.

Studies related to the Martian ground conductivity are limited. VHF radar investigation indicated that the conductivity of the Martian regolith in the first few centimeters is lower than 10^{-8} S/m [*Farell and Desch*, 2001]. Locally some contributions of iron deposits can significantly increase this value. The conductivity of the upper part of the crust, by comparison with lunar analogs, has been estimated to be less than 10^{-12} S/m [*Olhoeft and Strangway*, 1974]. In the work of *Cummer and Farrell* [1999], it was proposed to be 10^{-7} S/m, as a transitional value between terrestrial and lunar ground. In the work of *Berthelier et al.* [2000], both approaches were presented, however, the authors were more inclined to accept values between 10^{-10} and 10^{-12} S/m. If there are aquifers under the surface, they will considerably raise the ground conductivity.

Rock conductivity is a dry electrolytic conduction. Electrolysis takes place due to the presence of imperfections in crystals: such as Schottky and Frenkel defects [*Zhdanov and Keller*, 1994]. Rock resistivity is primarily a function of temperature, water content, and composition. The influence of the latter is significant only at lower temperatures, with acidic rocks (e.g. granite) having lower conductivities than basic rocks (e.g. basalt). Conductivity of rocks containing water (aqueous electrolytes) depends on amount of water, temperature, way in which water is distributed inside rocks, and its salinity. Pressure from overburden layers is important, because the vaporized point is never reached. Brines lower the freezing point. In addition, the presence of various intrusions can be important. Dendritic hematite causes a significant reduction in rock resistivity. Graphite intrusions rise the conductivity. On the other hand, metal sulfides, which are very common on Mars, must have several tens of the weight percentage to influence the resistivity [*Zhdanov and Keller*, 1994].

Depending on temperature, pressure, composition, and water content, the conductivity of rocks changes gradually with depth. The effect of pressure on rocks conductivity is much smaller than the effect of other factors [*Schon*, 2004] and is neglected in this study. The conductivity of rocks, σ_R, exhibiting dry electrolytic conduction can be approximated by the Arrhenius-type equation [*Zhdanov and Keller*, 1994]:

$$\sigma_R(T) = A_1 \exp\left(\frac{-U_1}{kT}\right) + A_2 \exp\left(\frac{-U_2}{kT}\right), \tag{3.1}$$

where: $A_{1,2}$ are the reference conductivities related to the number of ions that can be activated, $U_{1,2}$ are the activation energies of these ions. Basalt rocks are characterized by: $A_1 = 0.7$ S/m, $A_2 = 10^7$ S/m, $U_1 = 0.57$ eV, $U_2 = 2.0$ eV and peridotite rocks by: $A_1 = 4$ S/m, $A_2 = 10^7$ S/m, $U_1 = 0.81$ eV, $U_2 = 2.3$ eV.

The conductivity of rocks increases also with increasing frequency. All materials have a low and high frequency limit. At the low frequency limit charge transfer dominates, and the dielectric constant term in the complex conductivity (1.31) may be neglected. At the high frequency limit, the dielectric polarization is dominant. Therefore, for low frequencies, the conductivity is frequency independent, and for higher frequencies, it is frequency dependent. The frequency at which this transmission takes place depends on water content and temperature [*Lastovickova and*

Bochnicek, 1992]. In most situations, it can be placed at ca. 100 Hz [*Olhoeft*, 1981; *Lastovickova and Bochnicek*, 1992].

To calculate the conductivity profiles of the Martian ground, I used the average depth of the basaltic crust (50 km), and beneath it, I assumed a homogenous peridotite upper mantle. Computing the conductivity inside the ground requires determining the temperature as a function of depth. The one-dimensional Fourier Law allows establishing the temperature at a given depth under the surface. In solid material, such as the lithosphere, the main transport process is conduction. Fourier's Law presents the relationship between the thermal conductivity, heat flow, and thermal gradient [*Lowrie*, 2007]:

$$Q_g = -\kappa \Delta T = -\kappa \frac{\partial T}{\partial z} \tag{3.2}$$

where: z – is the depth, ΔT – is the areothermal gradient. As Mars has a stagnant lid regime, homogenous composition of the crust, and we still do not know the exact value of heat production in the planet, a constant value of the heat flow and thermal conductivity must be assumed. The thermal conductivity mainly depends on the crust composition, structure, and temperature. The heat flux is related to the thermal conductivity of the crust, the convection in the mantle, and the crustal abundance of heat producing elements, such as: K, Th, U. *McGovern et al*. [2002] concluded that heat flow decreased rapidly during the Noachian from 50 mW/m^2, and was reduced more slowly to the present value <20 mW/m^2 during the Amazonian. In the work of *Li and Kiefer* [2007], the heat flux value was proposed to be between 15-25 mW/m^2.

From (3.2) we can obtain the value of the temperature at a given point under the Martian surface ($z < 0$):

$$T(z, \varphi_a) = T_{ms}(\varphi_a) + \Delta T \cdot z\,, \tag{3.3}$$

where: φ_a – is the aerographic latitude. The mean annual surface temperature depends on latitude, but also changes in time. It can be calculated using the equilibrium between the insolation and radiation from the surface. The mean annual insolation depends on latitude and orbital parameters. The radiation depends strongly on albedo and emissivity [*Schorghofer,* 2008]. The latitude dependency of the mean annual temperature can be derived from observations, such as those obtained by the MGS [*Read and Lewis*, 2004]. In this work, the present mean annual surface temperature is estimated on the basis of data given by *Clifford* [1993] and presented in Figure 25. The data may be described by a function:

$$T_{ms}(\varphi_a) = T_1 + \frac{T_2 - T_1}{1 + \exp(\frac{\varphi_a - \varphi_{a0}}{d\varphi_a})}, \tag{3.4}$$

where: T_1 = 154 K and T_2 = 218 K are the mean annual temperature at the pole and at the equator, respectively, φ_{a0} = 56.7° is the latitude at which the temperature reaches the median, and $d\varphi_a$ = 11.6°. The underground temperature depends on the mean surface temperature only to some depth.

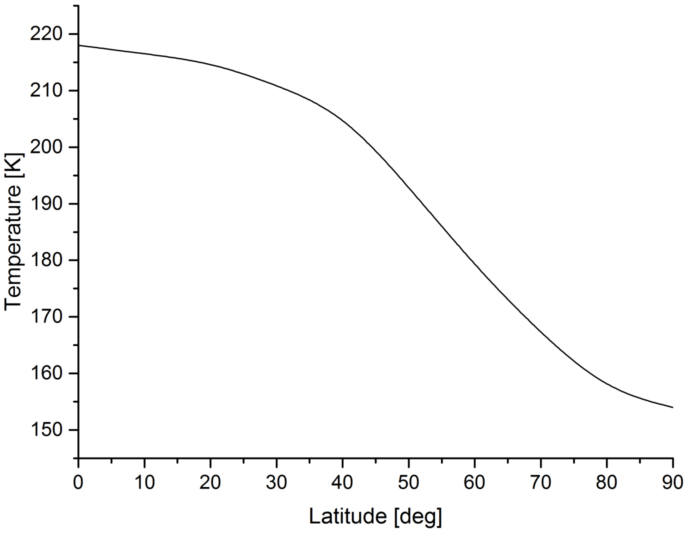

Figure 25. The mean annual surface temperature.

As it was mentioned, the subsurface rocks may contain some ice or liquid water. The volume of those components depends on rocks porosity and the depth of the cryosphere, which in turn depends on the thermal gradient. First, I considered the most favorable conditions for water existence. Hence, I assumed the mean global lithospheric heat flow is Q_g = 30 mW/m^2 and the constant thermal conductivity of rocks and rocks with ice is κ = 2 W/m/K [*Clifford*, 1993; *Grimm*, 2002; *Clifford et al.*, 2010]. Therefore, the crustal areothermal gradient: ΔT = 15 K/km. Pores in igneous rocks are mainly fractures, joints, and microcracks in crystalline. The porosity of the Martian subsurface rocks φ, was established in the works of Clifford [*Clifford*, 1993]. At the given depth, it can be calculated from:

$$\varphi = \varphi_0 \exp\left(-z / K_p\right), \tag{3.5}$$

where: φ_0 is the surface rock porosity, z is the depth, and K_p is the porosity decay constant, which for Mars is: K_p = 2820 m. The surface rock porosity may be as high as 0.35 [*Clifford et al.*, 2010].

To study the influence of water on the SR parameters, I considered two geological models of the Martian ground containing aquifers. In both cases, the upper part of the Martian crust is composed of porous basaltic rocks containing ice. Beneath this layer, there are water-bearing basalts. I assumed that ice and water contain some NaCl impurities or solutions. In the first case, called the Water model, I regarded that the salinity of ice S_L is low and equals to 0.5 ppt (1 ppt = 1 g/L) and the salinity of water S_W is 3 ppt. In the second case, called the Brine model, I presumed some high-impurity ice (S_L = 50 ppt) and brines (S_W = 100 ppt). Since high salinity will lower the freezing point of water, in the Brine model, the water-bearing layer is presumed to be larger than in the Water model. As the Martian crust is characterized by the existence of various salts, and the underground water reservoirs has not been supplied with considerable amounts of infiltrating water for very long time, the salinity of water and ice is expected to be high. Therefore, if any water is present under the surface, the Brine model is more probable than the Water model. To compare the results of the Water and Brine cases with the situation, in which there is no water under the Martian surface, I introduced the Dry model, in which the crust is composed only of dry basaltic rocks. The schematic geologic profiles of those models are presented in Figure 26.

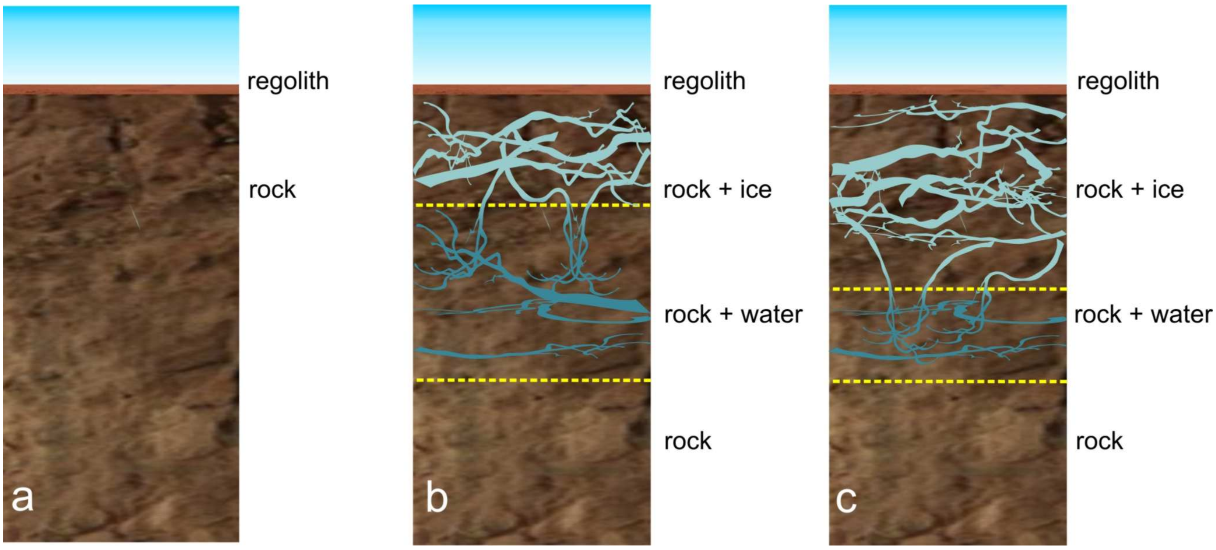

Figure 26. Three geological models of the Martian ground: (A) the Dry model, (B) the Brine model, and (C) the Water model.

The conductivity and permittivity of water and ice depend on temperature, frequency, and impurities [*Evans*, 1965; *Keller*, 1988; *Grimm et al.*, 2008; *Angulo-Sherman and Mercado-Uribe*; 2011].

The conductivity of ice can be derived from the work of *Grimm et al.* [2008], in which the authors conducted some experimental studies on the electrical properties of ice with various impurities given in molarity. As the molar mass of NaCl is 58.44 g/mol, the Water model corresponds to 0.01 M and the Brine model to 0.85 M. Therefore, those two cases are used in this study (Figure 27). As the measured relationship between temperature and ice conductivity is almost linear, we can fit those data to a linear function without losing any important information for this study.

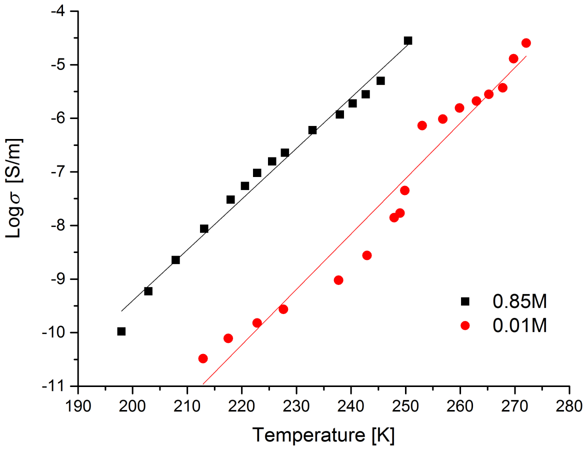

Figure 27. The conductivity of ice with NaCl impurities given in molar concentration of liquid state, along with the fitted lines.

On the basis of *Grimm et al*. [2008].

The ice conductivity, σ_L, in the Water model, can be approximated up to 273 K by a function:

$$\log\sigma_L = 0.100T - 33.0\,, \tag{3.6a}$$

and in the Brine model, up to 252 K by:

$$\log\sigma_L = 0.095T - 28.4\,. \tag{3.6b}$$

To calculate the conductivity of rocks with ice σ_{RL}, I used the parallel-plate model:

$$\sigma_{RL} = \sigma_R(1-\varphi) + \sigma_L\varphi\,. \tag{3.7}$$

Water can be present at depths where the temperature is high enough. The conductivity of rocks with some water content σ_{RW}, can be given by Archie's law: $\sigma_{RW} = a_w^{-1}\sigma_W\varphi^{\Sigma}\psi^{\varpi}$, where: σ_W – the conductivity of the water present in the pore structure, φ – the porosity, ψ – the fraction of the pore space saturated with water, a_w and Σ, ϖ are empirical quantities. For dense igneous rocks a = 1.4, Σ = 1.58, and ϖ normally is ca. 2 [*Zhdanov and Keller*, 1994]. Archie's law does not reflect a situation in which the conductivity of rocks is high and their porosity is low. This situation can be found on Mars at depths greater than ca. 25 km. In such a case the major contribution to the conductivity comes from rocks not from water. Therefore, to calculate the conductivity profiles of rocks with water to the depth of 50 km, I used the modified Archie Law [*Glover*, 2010].

$$\sigma_{RW} = \sigma_R (1-\varphi)^{\upsilon} + \sigma_W \varphi^{\Sigma} \tag{3.8}$$

where: $\upsilon = \mathrm{Log}[1-\varphi^{\Sigma}]/\mathrm{Log}[1-\varphi]$. The conductivity of water with dissolved NaCl, for both studied cases, can be approximated as follows [*Grimm*, 2002]:

$$\log\sigma_w = \log S_W - 1 + (T-273)/150, \tag{3.9}$$

where: S_W – the salinity of water [g/L]. I assumed that in the models, all available pores are filled with either water or ice. The amount of underground water depends not only on rock porosity but also on the depth of the cryosphere. Therefore, the conductivity of the ground σ_{RWL}, can be given by:

$$\sigma_{RLW} = \begin{cases} \sigma_{RL}, & 0 < z < z_d \\ \sigma_{RW}, & z \geq z_d \end{cases}, \tag{3.10}$$

where: z_d – is the depth of the cryosphere. This lower boundary of the cryosphere can be computed by integrating (3.2) [*Clifford et al.*, 1993; 2010]:

$$z_d(T_{ms}) = \kappa \frac{T_{mp} - T_{ms}}{Q_g}, \tag{3.11}$$

where: T_{ms} – the annual average surface temperature and T_{mp} – the temperature of the subsurface ice melting. The average annual temperature at the surface varies with latitude from 154 to 218 K [*Clifford,* 1993]. The temperature of the subsurface ice melting depends on ice properties, which are unknown and can be only predicted on the basis of some theoretical considerations.

In the Dry model, the first term in (3.3) has much smaller impact than the second term, and to calculate the conductivity in this case, I used (3.1), with the mean value of the surface temperature computed from (3.4). I also assumed that the conductivity of the Martian surface is everywhere the same. I considered two values of the surface conductivity: low, 10^{-10} S/m, and high, 10^{-7} S/m. In cases with aquifers, the temperature of the subsurface ice melting is also necessary to establish. In the work of *Clifford et al.* [2010], the authors proposed several geological models of the Martian crust and calculated the cryosphere depth using numerical modeling to determine its evolution during past epochs. The authors proposed three different models of water salinity: pure water, NaCl and $Mg(ClO_4)_2$ (perchlorate) brines, with the freezing point temperatures: 273K, ~252K, and ~203K, respectively. They also assumed two values of the heat flow: low, $Q_g = 15$ mW/m^2, and high $Q_g = 30$ mW/m^2. Their results indicated that the depth of the cryosphere for the low-heat flow model is more than doubled in comparison to the high-heat flow models. On the other hand, for the $Mg(ClO_4)_2$ brines, this value is almost two times smaller than for the NaCl brines.

I employed from these models the groundwater freezing temperature, which in the Brine case is $T_{mp} = 252$ K and in the Water case $T_{mp} = 273$ K. For both models the cryosphere depth was calculated using (3.11), and is presented in Figure 28. For the low-salinity model, it is ~3.7 km at the equator and ~7.7 km at the poles. For the high-salinity model, it is ~2.2 km at the equator and ~6.3 km at the poles.

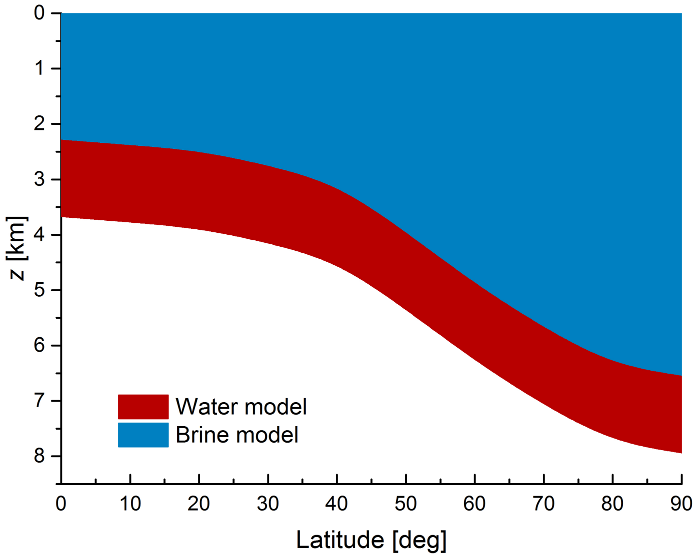

Figure 28. The depth of the Martian cryosphere for two models, presented for one hemisphere from the equator to the pole.

The conductivities for the models with aquifers were calculated using (3.10), with σ_{RL} given by (3.7), σ_{RW} by (3.8), σ_R given by (3.1), φ by (3.5), σ_L by (3.6), σ_W by (3.9), T by (3.3), and T_{ms} by (3.4). The calculated conductivity profiles of the Martian crust for the Water model and Brine model with the high (10^{-10} S/m) and low (10^{-7} S/m) surface conductivity are presented in Figure 29-32.

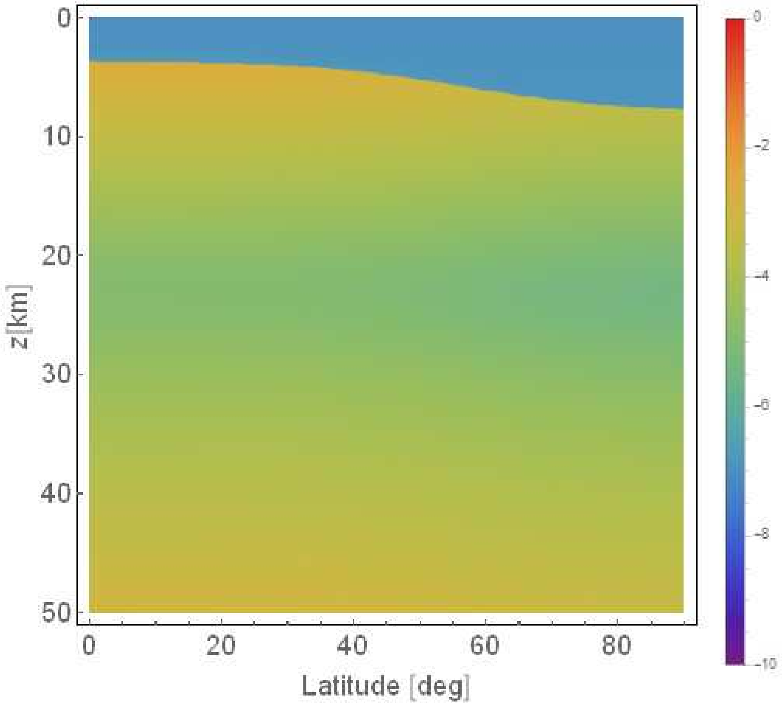

Figure 29. The conductivity in Log(S/m) in the Water model with the high-conductivity Martian surface.

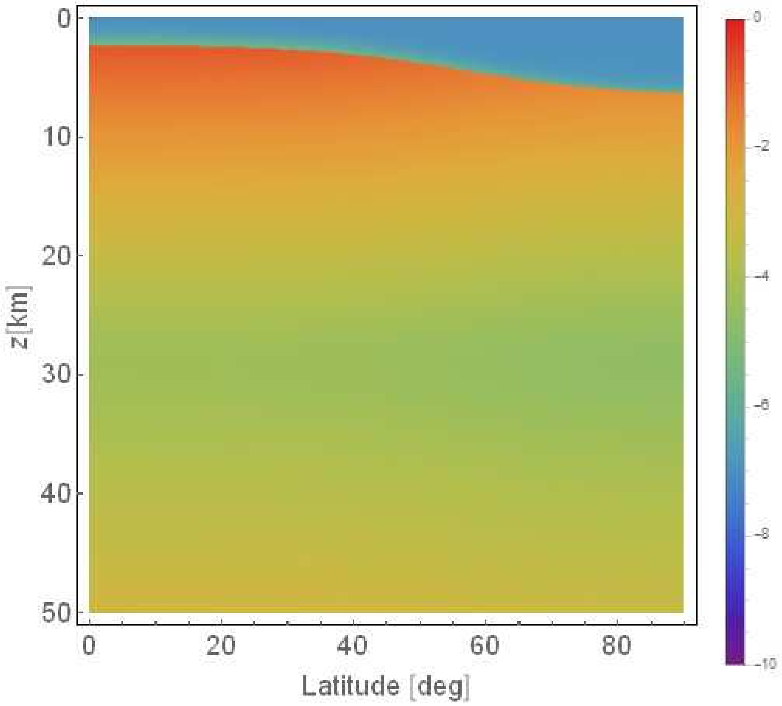

Figure 30. The conductivity in Log(S/m) in the Brine model with the high-conductivity Martian surface.

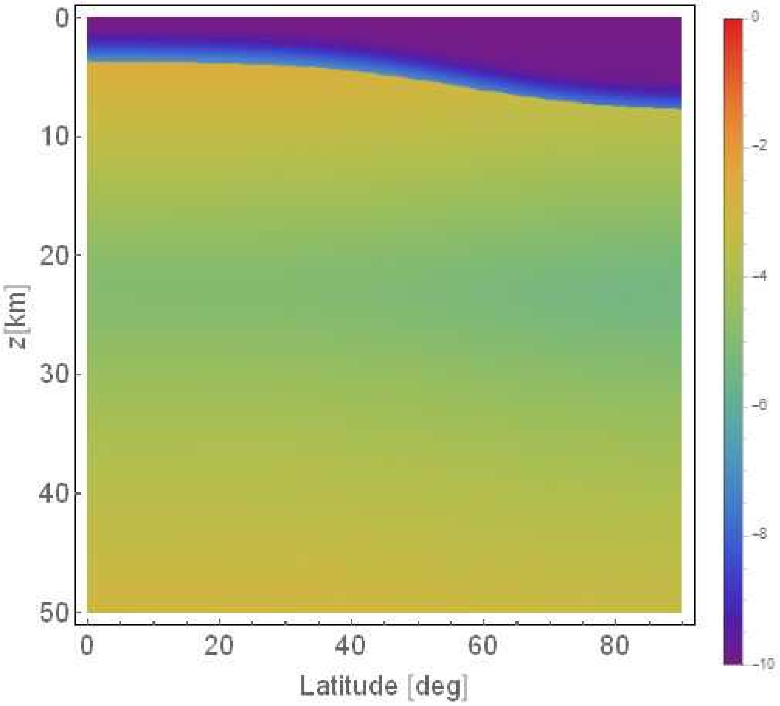

Figure 31. The conductivity in Log(S/m) in the Water model with the low-conductivity Martian surface.

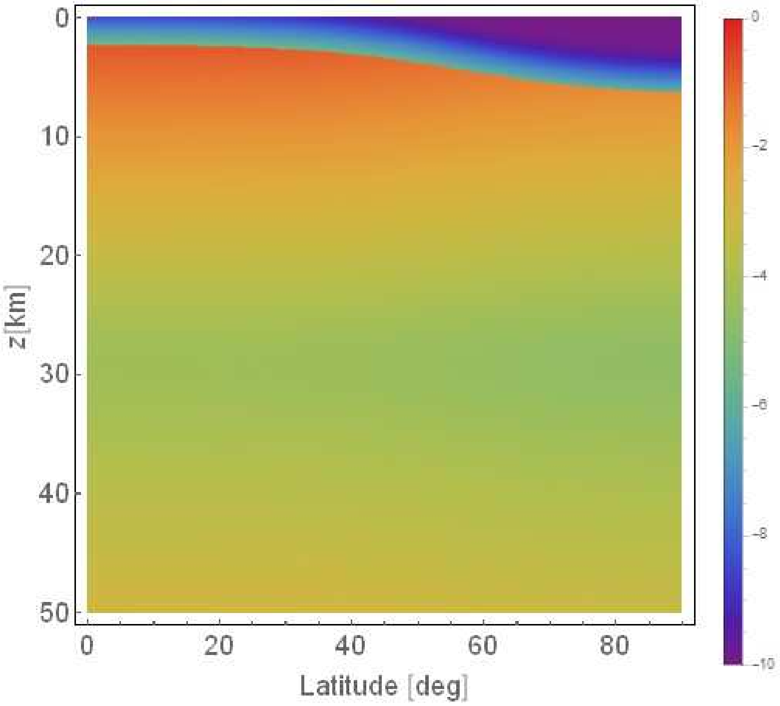

Figure 32. The conductivity in Log(S/m) in the Brine model with the low-conductivity Martian surface.

As seen in Figures 29-32, the presence of water highly increases the conductivity values. The ice may also influence its values. It is especially visible in the cases with the low-conductivity surface.

In the Brine model, the conductivity is higher, and this higher conductivity occurs at shallower depths than in the Water model. The highest values occur at the equatorial region. The influence of water and the surface electromagnetic properties on the ground conductivity is negligible at depths lower than ca. 35 km. The influence of the latitude-dependent component is only important down to ca. 20 km.

The average depth of the cryosphere is 5.3 km and 3.9 km, in the Water model and Brine model, correspondingly. Using theses values, I calculated the averaged over the entire planet profiles of the crustal conductivity (Figure 33). The models with the low surface conductivity are assumed to be more realistic. However, the models with the high surface conductivity are presented for comparison purposes.

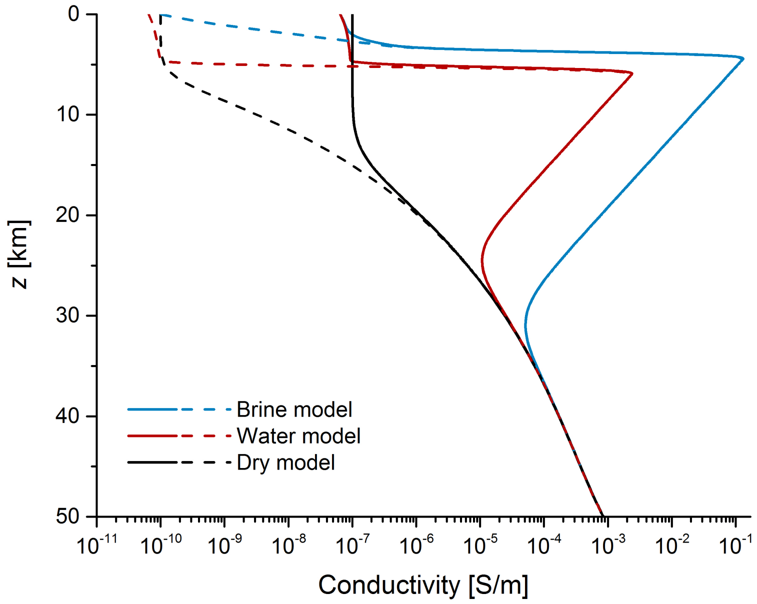

Figure 33. The conductivity profiles of the Martian crust for the averaged Water, Brine and the Dry model, for two values of the surface rock conductivity: 10^{-7} S/m (solid lines) and 10^{-10} S/m (dashed lines).

Crustal conductivity anomalies can be expected on Mars; on Earth they are related to various sources: extensional tectonics, shallow occurrence of molten rocks, ores deposits, graphotype layers of rocks, and sedimentary basins of marine sediment [*Zhdanov and Keller*, 1994]. Especially important may be magnetite and hematite concretions.

The ground-atmosphere conductivity ratio must be at least ≥ 1 for a global circuit existence [*Aplin*, 2006]. On Earth, this ratio is very high ~10^{12}, whereas on Mars, it can be very low. As the atmospheric conductivity can be probably as high as 10^{-11} S/m and the surface conductivity is as low as 10^{-10} S/m this condition may be met not at the surface but at some depth. This does not rule out the global circuit existence, but rather influences its properties, as the distance between the boundaries of the waveguide is in such a case much larger.

The greatest resistance of the ground is in the Dry model with the low surface conductivity. Using (1.48b), it is ca. 0.5 Ω. Therefore, it is one order of magnitude lower than the atmospheric resistance. Even for models with the thermal gradient as low as 5 K/km, the ground resistance is still lower than the resistance of the atmosphere.

On the basis of VHF radar exploration, the relative permittivity of the Martian ground ε_R, was determined to be 5 [*Tyler et al.*, 1976; *Olhoeft and Strangeway*, 1974]. Experimental studies on dry rocks indicate that the relative permittivity of minerals composing basaltic rocks lies between 5 and 9 [*Zhdanov and Keller*, 1994]. In the work of *Grimm* [2002], the relative permittivity for basalt and peridotite is assumed to be 7. In the work of *Simoes et al*. [2008a,b], this value is proposed to fall in the range of 5 to 10. The maps of dielectric constant recently obtained by the MARSIS instrument in the HF range show that the real dielectric constant of rocks can be assumed to be 7, a typical value for the Martian surface (Figure 34) [*Mouginot et al*., 2010]. Low values of the dielectric constant are present at high latitudes due to ice in the polar caps and at mid-latitudes due to subsurface ice. In tropics, especially in the Medusae Fossae Formation region, low dielectric constant may be related to low-density sedimentary rocks. Since for dry rocks the relative permittivity does not change significantly with frequency [*Singh et al*., 1980], we can use this typical value to study ELF propagation.

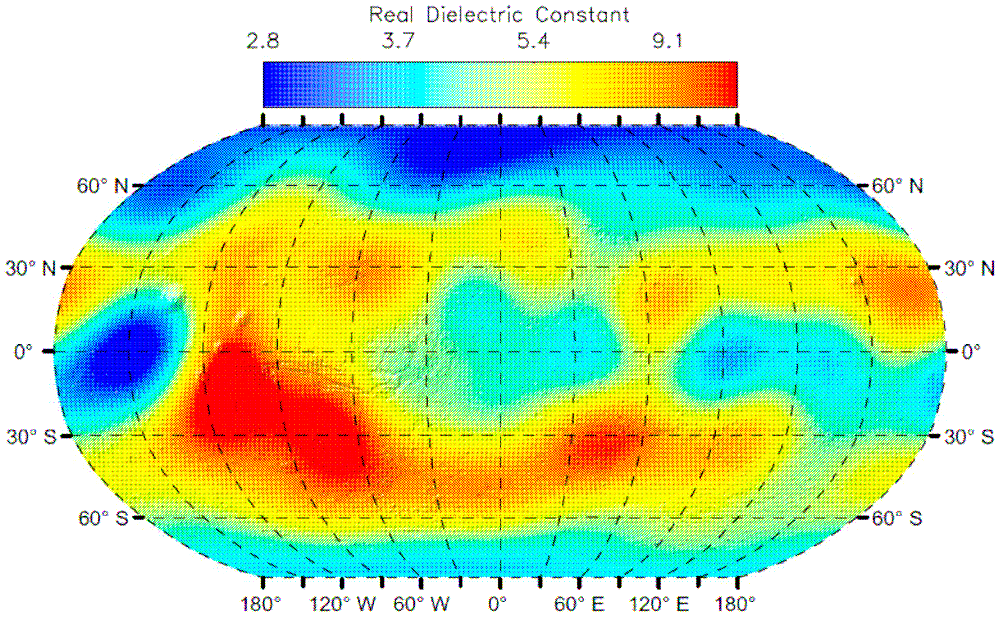

Source: *Mouginot et al.*, [2010].

Figure 34. The map of the real dielectric constant obtained from the interpolation of the MARSIS data.

I assumed that the relative permittivity of ice in the Brine and Water models is ε_L = 110, and it is temperature-independent. As the content of ice decreases with increasing depth, the permittivity of ice and rock mixtures decreases toward the lower boundary of the cryosphere. As the permittivity has smaller impact on the SR parameters than the conductivity [*Kozakiewicz et al.*, 2015], I considered the averaged (over depth) relative permittivity for such rocks, assuming the parallel plate model formula: $\varepsilon_{RL} = \varepsilon_R(1-\varphi)+\varepsilon_L\varphi$, where: ε_{RL} – the relative permittivity of rocks with ice, ε_R – the relative permittivity of basaltic rocks, and ε_L – the relative permittivity of ice. In both models, this value is: ε_{RL} = 25. I concluded that for low frequencies the dielectric constant of rocks with some water content in the Water model is $\varepsilon_{RW} = 10^3$ and in the Brine model: $\varepsilon_{RW} = 10^4$ [*Chelidze et al.*, 1999].

Magnetic properties are only important for magnetite. Magnetite has very high conductivity and unusual for rocks minerals permeability, much larger than 1 (2.5 to 16) [*Zhdanov and Keller*, 1994]. Although it occurrence on Mars is very probable in the regolith and dust [*Yen et al.*, 2005], it is not a main constituent of the crust. Therefore, for the Martian ground, it is possible to assume that the magnetic permeability $\mu = \mu_0$. However, locally it may not be true.

3.2 Modeling of the Martian waveguide

The Martian waveguide is characterized by several parameters: the conductivity of the atmosphere $\sigma_i(z)$, its permittivity ε_i equals to the free space value ε_0, the permittivity of the ground $\varepsilon_g(z)$, its conductivity $\sigma_g(z)$, and the planetary radius (Figure 35). Calculating the propagation parameters requires establishing the electric and magnetic altitudes of the ionosphere and ground.

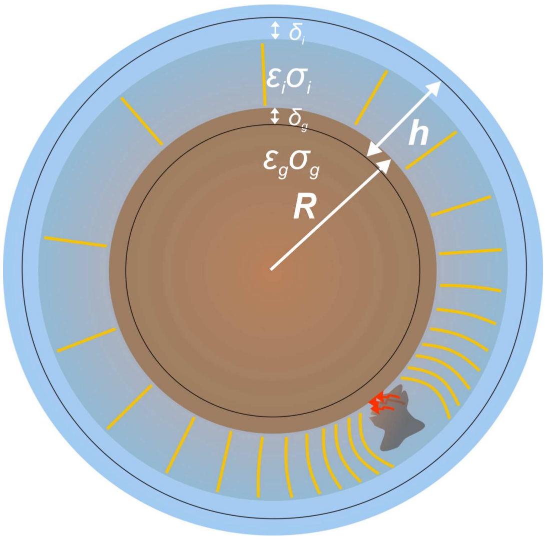

Figure 35. The Martian cavity. A dust storm as a source of ELF waves (yellow), propagating in the Martian waveguide. h – the distance between the boundaries, $\delta_{i,g}$ – the skin depth of the ionosphere and ground, respectively.

3.2.1 Electric models of the atmosphere

The profiles calculated in the work by *Pechony and Price* [2004], and presented in point 2.4.2.2 (Figure 15), can be approximated by exponential functions. Such fitting is called the "multi-knee" model and can be used even with highly structured profiles by introducing many "knees". The Martian atmospheric conductivity profiles $\sigma_i(z)$ can be fitted by a "double-knee" model given by [*Pechony and Price*, 2004]:

$$\sigma_i(z)=\begin{cases}\sigma_1\exp\left(\dfrac{z-h_1}{\varsigma_1}\right),\ z<h_1\\[2ex] \exp\left[\dfrac{z(\ln\sigma_1-\ln\sigma_2)+(h_1\ln\sigma_2-h_2\ln\sigma_1)}{h_1-h_2}\right],\ \ h_1\le z<\ h_2,\\[2ex] \sigma_1\exp\left(\dfrac{z-h_2}{\varsigma_2}\right),z\ge h_2\end{cases}\tag{3.12}$$

where: σ_1, σ_2 are the conductivities at a first and second “knee” altitudes h_1 and h_2, ζ_1 and ζ_2 are the scale heights of two exponential function: the first below the first “knee”, and the second above the second “knee”. Those parameters for the daytime and nighttime profiles are presented in Table 7.

Table 7. Parameters for the daytime and nighttime conductivity profiles of the Martian atmosphere.

	σ_1[10^{-9} S/m]	σ_2[10^{-9} S/m]	h_1 [km]	h_2 [km]	ζ_1 [km]	ζ_2 [km]
daytime	8.3	55.6	28.0	53.0	3.5	4.6
nighttime	8.3	55.6	30.0	58.0	3.5	6.1

The approximated profiles are shown in Figure 36. These two profiles describe the atmospheric conductivity model called the partially uniform knee model (PUK). We can easily notice that ELF waves propagating in the waveguide are reflected from high-conductive upper layers of the atmosphere. Therefore, the atmospheric regions located above the boundary altitude, for which the real part of the reflection coefficient R_{coeff} is almost equal -1, can be ignored in the study. This reflection coefficient can be given by [*Molina-Cuberos et al*., 2006]:

$$R_{coeff}(z) = \frac{\sqrt{i\omega\varepsilon_0 / \sigma_i(z)} - 1}{\sqrt{i\omega\varepsilon_0 / \sigma_i(z)} + 1} \ , \tag{3.13}$$

and is also presented in Figure 36. At a 10 Hz frequency, the real part of the reflection coefficient reaches -0.99 at ca. 80 km altitude for the daytime profile and ca. 90 km for the nighttime profile. A similar boundary altitude was obtained by *Molina-Cuberos et al*. [2006] with their daytime conductivity profile for minimum solar activity. Therefore, I assumed that ELF waves propagate in the atmospheric region extending from the surface to 100 km altitude.

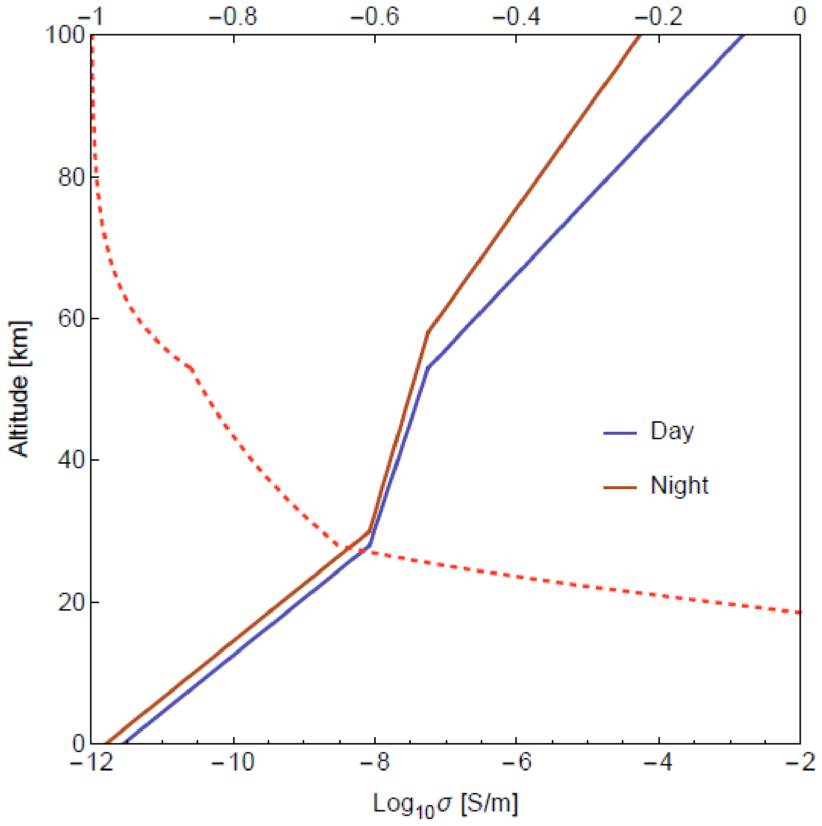

Figure 36. The approximated conductivity profiles of the lower Martian atmosphere. The dashed red line shows the real part of the reflection coefficient calculated from (3.13) for the daytime profile and at a 10 Hz frequency.

On Earth, the impact of magnetic fields on ELF radio wave propagation is negligible. Consequently, the Martian induced magnetic field, which is much weaker than the intrinsic terrestrial magnetic field is insignificant in this research. Relatively strong Martian magnetic anomalies, related to the remanent magnetization of the crust, are very rare and on the global scale they have a small effect. On Mars, as shown in Chapter 2, the Hall and Pedersen conductivities are important solely above 100 km. Therefore, the influence of magnetic fields is not included in this study.

The electric altitude for the profiles given by (3.12) is [*Pechony and Price*, 2004]:

$$\mathrm{Re}\,\bar{h}_e = h_2 - \zeta_2 \ln\left(\frac{f_2}{f}\right) + \frac{1}{2}\zeta_2 \ln\left(1+\left(\frac{f_2}{f}\right)^2\right) - \frac{1}{2}\zeta_1 \ln\left(1+\left(\frac{f_1}{f}\right)^2\right) + \frac{1}{2}\frac{(h_1-h_2)}{\ln(f_1/f_2)} \ln\left(\frac{1+(f_1/f)^2}{1+(f_2/f)^2}\right), \quad (3.14a)$$

$$\mathrm{Im}\,\bar{h}_e = -\zeta_2 \frac{\pi}{2} + \zeta_2 \arctan\left(\frac{f_2}{f}\right) - \zeta_1 \arctan\left(\frac{f_1}{f}\right) + \frac{(h_1-h_2)}{\ln(f_1/f_2)}\left(\arctan\left(\frac{f_1}{f}\right) - \arctan\left(\frac{f_2}{f}\right)\right), \quad (3.14b)$$

where: $f_{1,2} = \sigma_{1,2}/2\pi\varepsilon_0$, and all the other parameters are given in Table 7.

The magnetic altitude of the atmosphere is described by the phenomenological approximation [*Mushtak and Williams*, 2002; *Pechony and Price*, 2004]:

$$\mathrm{Re}\,\overline{h}_m = h_b - \zeta_b \ln\left(\frac{f}{f_b}\right), \tag{3.15a}$$

$$\mathrm{Im}\,\overline{h}_m = \zeta_b \frac{\pi}{2}, \tag{3.15b}$$

where:

$$\zeta_b = \zeta_b^* + b\left(\frac{1}{f} - \frac{1}{f_b}\right), \tag{3.15c}$$

and the magnetic altitude parameters are given in Table 8.

Table 8. Magnetic altitude parameters for the daytime and nighttime conductivity profiles of the Martian atmosphere.

	h_b [km]	f_b [Hz]	ζ^*_b [km]	b [km]
daytime	78	150	7.0	10
nighttime	86	150	7.3	10

3.2.2 Electrical models of the ground

I used two simplified approaches to establish the electrical models of the Martian ground. In the first approach, I employed the conductivity values averaged over the entire planet. In the cases with aquifers, it is possible to distinguish three layers of almost constant conductivity in the upper part of the crust (Figure 33). The first one is of low, the second of high, and the third of medium conductivity. For the low-surface conductivity (10^{-10} S/m), the first layer is 5 km deep in the Water model and 1 km thick in the Brine model. For both models, its conductivity is 10^{-10} S/m. For the high-surface conductivity (10^{-7} S/m), these values are respectively: for the Water case, 5 km and 10^{-7} S/m, and for the Brine case, 2 km and 10^{-7} S/m. The lower layers are not affected by the surface conductivity. The second layer ranges, in the Water model to the depth of ca. 24 km, in the Brine model to ca. 30 km. The average conductivity of the layer is: $5{\cdot}10^{-4}$ S/m and 10^{-2}S/m, respectively in these two models. The skin depths for such conductivities are: 6.8 km and 1.2 km, correspondingly. Therefore, in both situations ELF waves do not penetrate into consecutive layers and the two-layer model can be easily used in these cases. In the Dry model, the conductivity changes continually with depth and a multi-layer model should be used. However, the three-layer model can be applied as a helpful approximation for comparison purposes. In this case, the first as well as the second layer of the crust has low conductivities. A conductivity for which the skin depth is small enough to not allow for wave penetration to underlying layers (σ = 10^{-4} S/m) is present only at the depth of ca. 40 km (Figure 37). I assumed that in the low-conductive surface case, the first layer has a conductivity of 10^{-10} S/m and is 5 km deep. The second layer is 20 km thick, and is characterized by the conductivity $5 \cdot 10^{-7}$ S/m, and the third layer has the conductivity 10^{-4} S/m. In the high-conductivity surface model, the first layer conductivity is 10^{-7} S/m, and it is 15 km deep, the second layer is 10 km thick and its conductivity is 10^{-6} S/m, and the third layer conductivity is 10^{-4} S/m.

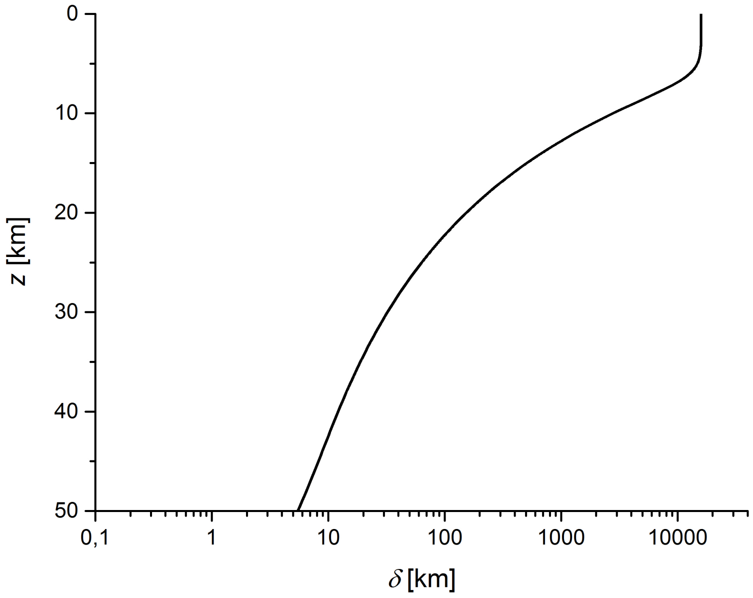

Figure 37. The skin depth for the Dry model of the Martian ground with the low surface conductivity at 10 Hz.

The reflective coefficients for such profiles were calculated using (3.13) and they are presented in Figure 38. At a 10 Hz frequency, the real part of the reflection coefficient reach -0.99 at ca. 4 km altitude for the Brine profile, ca. 6 km for the Water profile, and ca. 35 km for the Dry profile.

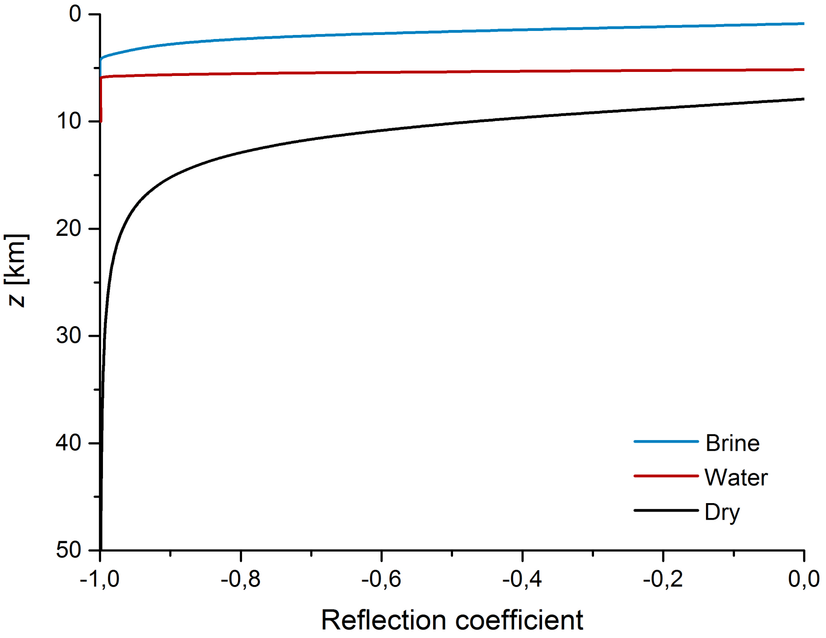

Figure 38. Reflection coefficient at a 10 Hz frequency for the different models of the ground with the low surface conductivity.

In the second approach, five temperature zones on each hemisphere were distinguished: the tropical region (0-30°), the low-latitude region (30-40°), the mid-latitude region (40-50°), the high-latitude region (50-75°), and the polar region (75-90°). For each zone, I employed the approximated mean depth of the cryosphere and the mean annual value of the surface temperature. The depth of the cryosphere was averaged using (3.11) and the temperature by (3.4). Two layers in each zone were distinguished. All the values are presented in Table 9.

Table 9. The mean value of the surface annual temperature, cryosphere depth, and electric models of the ground in the different zones.

	Tropical	**Low-latitude**	**Mid-latitude**	**High-latitude**	**Polar**
T [K]	215	209	200	179	160
Brine z_d [km]	2.4	2.8	3.4	4.9	6.1
Water z_d [km]	3.8	4.2	4.8	6.3	7.5
	Water model with the low-conductivity surface				
σ_1 [S/m]	$1 \cdot 10^{-10}$	$1 \cdot 10^{-10}$	$1 \cdot 10^{-10}$	$1 \cdot 10^{-10}$	$1 \cdot 10^{-10}$
h_1 [km]	1.5	2.0	2.5	4.0	5.5
σ_2 [S/m]	$1 \cdot 10^{-3}$	$1 \cdot 10^{-3}$	$5 \cdot 10^{-4}$	$5 \cdot 10^{-4}$	$1 \cdot 10^{-4}$

	Brine model with the low-conductivity surface				
σ_1 [S/m]	$1{\cdot}10^{-8}$	$5{\cdot}10^{-9}$	$5{\cdot}10^{-9}$	$1{\cdot}10^{-10}$	$1{\cdot}10^{-10}$
h_1 [km]	0.5	1.0	1.5	2.0	3.5
σ_2 [S/m]	$5{\cdot}10^{-2}$	$5{\cdot}10^{-2}$	$1{\cdot}10^{-2}$	$1{\cdot}10^{-2}$	$5{\cdot}10^{-3}$
	Water model with the high-conductivity surface				
σ_1 [S/m]	$1{\cdot}10^{-7}$	$1{\cdot}10^{-7}$	$1{\cdot}10^{-7}$	$1{\cdot}10^{-7}$	$1{\cdot}10^{-7}$
h_1 [km]	3.5	4.0	4.5	6.0	7.5
σ_2 [S/m]	$1{\cdot}10^{-3}$	$1{\cdot}10^{-3}$	$5{\cdot}10^{-4}$	$5{\cdot}10^{-4}$	$1{\cdot}10^{-4}$
	Brine model with the high-conductivity surface				
σ_1 [S/m]	$1{\cdot}10^{-7}$	$1{\cdot}10^{-7}$	$1{\cdot}10^{-7}$	$1{\cdot}10^{-7}$	$1{\cdot}10^{-7}$
h_1 [km]	1.5	2.0	2.5	4.0	5.5
σ_2 [S/m]	$5{\cdot}10^{-2}$	$5{\cdot}10^{-2}$	$1{\cdot}10^{-2}$	$1{\cdot}10^{-2}$	$5{\cdot}10^{-3}$

Higher ground conductivities at tropical to mid-latitude regions in the Brine model with the low-conductivity surface are related to stronger influence of ice.

To study Schumann resonance and ELF propagation on Mars, the analytical method presented in point 1.2.3 must allow including finite conductivity models of the ground. Therefore, in the next point this method is developed to enable studying the influence of a multi-layered ground on the ELF propagation.

3.3 Analytical modeling with a multi-layer ground

We can approximate the structure of the Martian ground by multi-layer models with layers of constant conductivity and permittivity. In such a situation, the magnetic and electric altitudes of the ground can be determined using (1.47). To calculate those altitudes, we can consider a TEM wave, described by a wave vector $\mathbf{k_0}$, propagating along the x-axis parallel to the surface ($z = 0$). If there is free space above the ground ($z < 0$), inside the ground the wave, according to Snell's law, propagates at angle given by the relation: $\sin\phi_1 = 1/\eta_1$, where η_1 is the refractive index of the first layer of the ground. The x-component of the wave vector $\mathbf{k_0}$ within the ground does not change, but the second component $\mathbf{u}$, associated with the z-axis, appears [*Kulak and Mlynarczyk*, 2013]. Therefore, the wave vector within the ground is $\mathbf{k} = k_0\hat{\mathbf{x}} + u\hat{\mathbf{z}}$, and $k^2 = k_0^2 + u^2$. The characteristic altitudes of the ground $\overline{h}_{eg}$, $\overline{h}_{mg}$ depend on $\mathbf{u}$, which is a $\mathbf{k}$ projection on the z-axis (Figure 39).

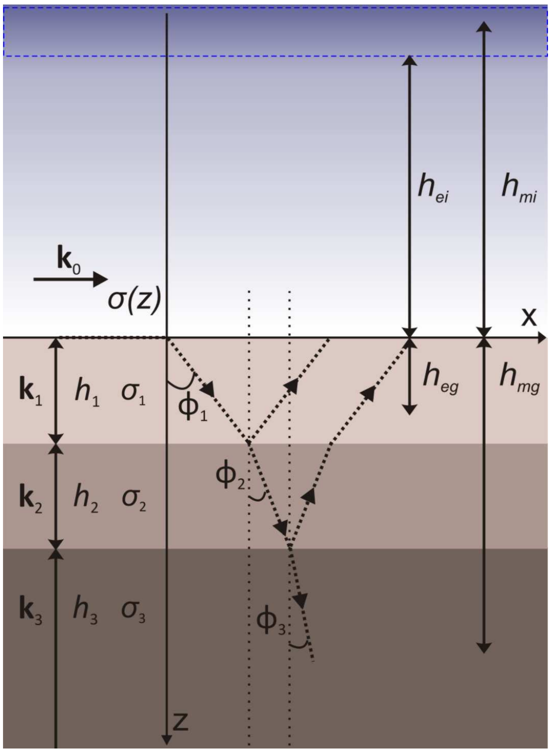

Figure 39. ELF wave penetration into the ground: k_0 – the wave vector above the ground, k_i – the wave vector within the i^{th} layer, h_i – the thickness of the i^{th} layer, σ_i – the conductivity of the i^{th} layer, h_e and h_m are the real parts of the electric and magnetic altitudes. At the boundary, the wave is partly reflected and partly transmitted to the consecutive layer.

Adapted from *Kozakiewicz et al.* [2015].

3.3.1 Three-layer modeling

Firstly, I considered the three-layer models of the ground such as those obtained in the previous point. Figure 39 shows a ground structure composed of three layers, each having a thickness h_i, a permittivity ε_i, and a complex conductivity $\overline{\sigma}_i$. Calculating the equivalent altitudes of the ground requires finding field distribution inside the ground. The magnetic component of the wave in the i^{th} layer can be given by [*Kulak et al.*, 2013]: $H_y = H_{iy} e^{iu_i z} e^{ik_0 x}$, where: H_{iy} is the amplitude of the H_y component in the i^{th} layer. Hence, using (1.37b,c), the electric components are:

$$E_x = -\frac{iu_i}{\overline{\sigma}_i} H_y , \tag{3.16a}$$

$$E_z = \frac{ik_0}{\overline{\sigma}_i} H_y , \tag{3.16b}$$

where from (1.34a) and (1.32b):

$$u_i^2 = k_0^2\left(\overline{\eta}_i^2 - 1\right) = \overline{k}_i^2 - k_0^2 = i\mu_i \overline{\sigma}_i \omega - k_0^2 \ . \tag{3.16c}$$

The H_y and E_x components form transverse waves propagating in the subsurface layers. These components projected onto the plane $x = 0$ can be given by:

$$H_y = H_{iy} e^{iu_i z} \tag{3.17a}$$

$$E_x = -\frac{iu_i}{\bar{\sigma}_i} H_y = K_i H_y , \tag{3.17b}$$

The waves given by (3.17) propagate into the ground and reflect from the boundary between the first and the second layer. Using the boundary conditions between these layers, I determined the coefficients describing amplitude of the forward and reflected waves in the first layer, C_1 and D_1, and the forward and reflected waves in the second layer, C_2 and D_2:

$$C_1 e^{iu_1 h_1} - D_1 e^{-iu_1 h_1} = C_2 e^{iu_2 h_1} - D_2 e^{-iu_2 h_1} , \tag{3.18a}$$

$$K_1 \left(C_1 e^{iu_1 h_1} + D_1 e^{-iu_1 h_1} \right) = K_2 \left(C_2 e^{iu_2 h_1} + D_2 e^{-iu_2 h_1} \right). \tag{3.18b}$$

The relationship between the forward and reflected wave amplitudes is met also in the consecutive layers:

$$F e^{iu_3 (h_1 + h_2)} = C_2 e^{iu_2 (h_1 + h_2)} - D_2 e^{-iu_2 (h_1 + h_2)} , \tag{3.19a}$$

$$K_3 F e^{iu_3 (h_1 + h_2)} = K_2 \left(C_2 e^{iu_2 (h_1 + h_2)} + D_2 e^{-iu_2 (h_1 + h_2)} \right), \tag{3.19b}$$

where: F is the coefficient describing the amplitude of the forward waves in the third layer. Using (3.18)-(3.19), we can obtain:

$$D_1 = A \left(R_1 + R_2 e^{i2u_2 h_2} \right) e^{i2u_1 h_1} , \tag{3.20a}$$

$$C_2 = A T_1 e^{i(u_1 - u_2) h_1} , \tag{3.20b}$$

$$D_2 = A T_1 R_2 e^{i(u_1 - u_2) h_1 + i2u_2 (h_1 + h_2)} , \tag{3.20c}$$

$$F = A T_1 T_2 e^{i(u_1 - u_2) h_1 + i(u_2 - u_3)(h_1 + h_2)} , \tag{3.20d}$$

where:

$$R_1 = \frac{K_2 - K_1}{K_2 + K_1} , \; T_1 = \frac{2K_1}{K_2 + K_1} , \; R_2 = \frac{K_3 - K_2}{K_3 + K_2} , \; T_2 = \frac{2K_2}{K_3 + K_2} , \tag{3.21a,b,c,d}$$

and

$$A = \frac{C_1}{1 + R_1 R_2 e^{i2u_2 h_2}} . \tag{3.21e}$$

Using (3.19), (3.20), and (3.21), we can calculate the magnetic component in the first layer [*Kozakiewicz et al*, 2015]:

$$H_y = H_{1y} C_1 \left(e^{iu_1 z} - \frac{\left(R_1 + R_2 e^{i2u_2 h_2} \right) e^{i2u_1 h_1} e^{-iu_1 z}}{1 + R_1 R_2 e^{i2u_2 h_2}} \right), \tag{3.22}$$

in the second layer:

$$H_y = H_{1y} A T_1 \left(e^{i(u_1-u_2)h_1} e^{iu_2 z} - R_2 e^{i(u_1-u_2)h_1 + i2u_2(h_1+h_2)} e^{-iu_2 z} \right), \tag{3.23}$$

and in the third layer:

$$H_y = H_{1y} A T_1 T_2 \left(e^{i(u_1-u_2)h_1 + i(u_2-u_3)(h_1+h_2)} e^{iu_3 z} \right). \tag{3.24}$$

The C_1 coefficient can be determined from the boundary condition (1.36) that requires the continuity of the magnetic field component on the surface (z = 0), $H_{0y} = H_{1y}$, then:

$$C_1 = \frac{1 + R_1 R_2 e^{i2u_2h_2}}{1 - \left(R_1 + R_2 e^{i2u_2h_2}\right) e^{i2u_1h_1} + R_1 R_2 e^{i2u_2h_2}}\,. \tag{3.25}$$

The magnetic altitude (1.47b) of a three-layer ground can be calculated using (3.22), (3.23), and (3.24), with the C_1 coefficient given by (3.25). Hence, the magnetic altitude is:

$$\overline{h}_m = \int_0^{h_1} \chi_1(z)dz + \int_{h_1}^{h_1+h_2} \chi_2(z)dz + \int_{h_1+h_2}^{\infty} \chi_3(z)dz\,, \tag{3.26}$$

where:

$$\chi_1(z) = \frac{\left(1 + R_1 R_2 e^{i2u_2h_2}\right) e^{iu_1 z} - \left(R_1 + R_2 e^{i2u_2h_2}\right) e^{i2u_1h_1} e^{-iu_1 z}}{1 - e^{i2u_1h_1}\left(R_1 + R_2 e^{i2u_2h_2}\right) + R_1 R_2 e^{i2u_2h_2}}\,, \tag{3.27a}$$

$$\chi_2(z) = \frac{T_1\left(e^{i(u_1-u_2)h_1} e^{iu_2 z} - R_2 e^{i(u_1-u_2)h_1 + i2u_2(h_1+h_2)} e^{-iu_2 z}\right)}{1 - e^{i2u_1h_1}\left(R_1 + R_2 e^{i2u_2h_2}\right) + R_1 R_2 e^{i2u_2h_2}}\,, \tag{3.27b}$$

$$\chi_3(z) = \frac{T_1 T_2 \left(e^{i(u_1-u_2)h_1 + i(u_2-u_3)(h_1+h_2)} e^{iu_3 z}\right)}{1 - e^{i2u_1h_1}\left(R_1 + R_2 e^{i2u_2h_2}\right) + R_1 R_2 e^{i2u_2h_2}}\,. \tag{3.27c}$$

The electric altitude (1.47a) can be calculated easily, as according to (3.16b), the z component of the electric field E_z, in each layer is related to the corresponding magnetic field component (3.22), (3.23), and (3.24). Hence, the electric component in the first layer is:

$$E_z = \frac{ik_0}{\overline{\sigma}_1} H_{0y} \frac{\left(1 + R_1 R_2 e^{i2u_2h_2}\right) e^{iu_1 z} - \left(R_1 + R_2 e^{i2u_2h_2}\right) e^{i2u_1h_1} e^{-iu_1 z}}{1 - e^{i2u_1h_1}\left(R_1 + R_2 e^{i2u_2h_2}\right) + R_1 R_2 e^{i2u_2h_2}}\,, \tag{3.28}$$

in the second layer:

$$E_z = \frac{ik_0}{\overline{\sigma}_2} H_{0y} A T_1 \left(e^{i(u_1-u_2)h_1} e^{iu_2 z} - R_2 e^{i(u_1-u_2)h_1 + i2u_2(h_1+h_2)} e^{-iu_2 z} \right), \tag{3.29}$$

and in the third layer:

$$E_z = \frac{ik_0}{\overline{\sigma}_3} H_{0y} A T_1 T_2 \left(e^{i(u_1-u_2)h_1 + i(u_2-u_3)(h_1+h_2)} e^{iu_3 z} \right). \tag{3.30}$$

Using the relation: η_0 = $E_{0z}/H_{0y} = \sqrt{\mu_0/\varepsilon_0}$ with (3.28)-(3.30), we get the electric altitude in the three-layer model:

$$\bar{h}_e = \int_0^{h_1} \xi_1(z)dz + \int_{h_1}^{h_1+h_2} \xi_2(z)dz + \int_{h_1+h_2}^{\infty} \xi_3(z)dz\,, \tag{3.31}$$

where:

$$\xi_1(z) = \frac{\varepsilon_0\omega}{i\bar{\sigma}_1}\chi_1(z) = \frac{1}{\bar{\eta}_1^2}\chi_1(z) \tag{3.32a}$$

$$\xi_2(z) = \frac{1}{\bar{\eta}_2^2}\chi_2(z)\,, \tag{3.32b}$$

$$\xi_3(z) = \frac{1}{\bar{\eta}_3^2}\chi_3(z)\,. \tag{3.32c}$$

Employing the obtained expressions, it is possible to establish analytical formulas for a two-layer and a one-layer ground.

3.3.2 Two-layer modeling

In a two-layer model, we have: $h_1 = 0$, $\sigma_1 = \sigma_2$, and $\varepsilon_1 = \varepsilon_2$. Therefore, from (3.16c) and (3.21): $u_1 = u_2$, $K_1 = K_2$, $R_1 = 0$, and $T_1 = 1$. Hence, the magnetic altitude in a two-layer model is given by:

$$\bar{h}_m = \int_0^{h_2} \chi_2(z)dz + \int_{h_2}^{\infty} \chi_3(z)dz \tag{3.33}$$

where:

$$\chi_2(z) = \frac{e^{iu_2z} - R_2 e^{i2u_2h_2} e^{-iu_2z}}{1 - R_2 e^{i2u_2h_2}}\,, \tag{3.34a}$$

$$\chi_3(z) = \frac{T_2 e^{i(u_2-u_3)h_2} e^{iu_3z}}{1 - R_2 e^{i2u_2h_2}}\,. \tag{3.34b}$$

The electric altitude in a two-layer model is:

$$\bar{h}_e = \int_0^{h_2} \xi_2(z)dz + \int_{h_2}^{\infty} \xi_3(z)dz\,, \tag{3.35}$$

where: ξ_2 and ξ_3 are given by (3.32b,c).

3.3.3 One-layer modeling

In a one-layer model, we have: $h_1 = h_2 = 0$, $\sigma_1 = \sigma_2 = \sigma_3$, and $\varepsilon_1 = \varepsilon_2 = \varepsilon_3$. Therefore, $u_1 = u_2 = u_3$, $K_1 = K_2 = K_3$, $R_1 = R_2 = 0$, and $T_1 = T_2 = 1$. Hence, the magnetic altitude in a one-layer model is given by:

$$\bar{h}_m = \int_0^{\infty} \chi_3(z)dz\,, \tag{3.36}$$

where:

$$\chi_3(z) = e^{iu_3 z} \,. \tag{3.37}$$

The electric altitude in a one-layer model is:

$$\overline{h}_e = \int_0^\infty \xi_3(z)dz \,, \tag{3.38}$$

where: ξ_3 is given by (3.32c).

Having developed the analytical method, we can employ it to study the ELF propagation as well as Schumann resonance in the Martian waveguide.

4 Schumann resonance and ELF propagation parameters on Mars

4.1 Previous studies on Schumann resonance on Mars

In previous publications, the possibility of studying the Martian environment using ELF waves was considered, and exemplified by studies on Schumann resonance on Mars [*Sukhorukov*, 1991, *Simoes et al.*, 2008a,b] and employment of natural and artificial sources of ELF waves for geophysical prospecting [*Grimm*, 2002]. *Sukhorukov* [1991] calculated the first three modes of SR and their Q factors using a semi-analytic method and a two-layer model of the ionosphere. *Pechony and Price* [2004] obtained these parameters using an analytical method based on the TDTE technique, however they did not consider the influence of the ground. The subsequent calculations were based on numerical modeling. In the work of *Molina-Cuberos et al.* [2006], several profiles of the Martian ionosphere were employed though the transmission line modeling (TLM) does not allow separating the peaks of SR. *Yang et al.* [2006] obtained results from the finite-difference time-domain (FDTD) method with the PUK profiles used by *Pechony and Price* [2004]. This is also the first work that considered a finite conductivity of the Martian ground. It was proposed that the crust is composed of a basaltic layer of the conductivity 10^{-7} S/m, extending to the depth of 40 km. *Soriano et al.* [2007] used the FDTD method with the same profiles as *Molina-Cuberos et al*. [2006] and did not include a finite conductivity of the ground. In the works of *Simoes et al.* [2008a,b], the finite element method (FEM) was used with the PUK model in the lower part of the atmosphere and with one of the atmospheric profiles proposed by *Molina-Cuberos et al*. [2006] in the upper part. In that work, the ground was also considered. The SR parameters were estimated for two types of ground. The first type conductivity was 10^{-7} S/m, the second: 10^{-10} S/m. The authors also considered two values of the basaltic layer's depth: 5 and 10 km, under which the authors assumed a perfectly conducting medium. In the more recent publication, *Kozakiewicz et al*. [2015] presented the Schumann resonance and propagation parameters with several multi-layer models of the Martian ground. All the results are presented in Table 10.

Table 10. The Schumann resonance frequencies on Mars.

Author(s)	**Method**	**Ionosphere**	**Ground**	***n* = 1**	***n* = 2**	***n* = 3**
					f [Hz]	
Sukhorukov [1991]	semi-analytic	two-layer	-	13-14	24-26	35-38
Pechony and Price [2004]	TDTE	PUK	-	8.6	16.3	24.4
Molina-Cuberos et al. [2006]	TLM	daytime, solar minimum	-	11.3	24.5	24.5
		daytime, solar maximum	-	11.6	23.9	23.9
		meteoroids, solar minimum	-	12.0	24.9	24.9
		nighttime	-	11.0	21.7	21.7
Yang et al. [2006]	FDTD	PUK	-	8.8	16.1	23.6
			$\sigma = 10^{-7}$ S/m, d = 40 km	7.3	13.1	19.2
Soriano et al. [2007]	FDTD	daytime, solar minimum	-	11.0	20.3	30.2
		daytime, solar maximum	-	11.2	20.7	30.6
		meteoroids, solar minimum	-	11.6	21.4	31.7
		nighttime	-	9.7	17.9	26.5
Simoes et al. [2008]	FEM	PUK + daytime, solar maximum	-	8.3	15.6	23.5
			$\varepsilon = [5, 10]$, $\sigma = 10^{-7}$ S/m, d = 5 km	8.3	15.5	22.8
			$\varepsilon = 5$, $\sigma = 10^{-10}$ S/m, d = 5 km	8.6	15.9	23.4
			$\varepsilon = 10$, $\sigma = 10^{-10}$ S/m, d = 5 km	8.4	15.7	23.1
			$\varepsilon = [5, 10]$, $\sigma = 10^{-7}$ S/m, d = 10 km	7.9	14.9	22.4
			$\varepsilon = 5$, $\sigma = 10^{-10}$ S/m, d = 10 km	8.5	15.9	23.7
			$\varepsilon = 10$, $\sigma = 10^{-10}$ S/m, d = 10 km	8.2	15.4	23.1
Kozakiewicz et al. [2015]	TDTE	PUK	-	8.5	16.0	23.7
			$\sigma_1 = 5 \cdot 10^{-10}$ S/m, h_1 = 2.6 km, $\sigma_2 = 10^{-2}$ S/m	8.4	15.7	23.3
			$\sigma_1 = 10^{-10}$ S/m, h_1 = 4.2 km, $\sigma_2 = 5 \cdot 10^{-4}$ S/m	8.2	15.4	22.9
			$\sigma_1 = 5 \cdot 10^{-10}$ S/m, h_1 = 10 km, $\sigma_2 = 10^{-8}$ S/m, h_2 = 30 km, $\sigma_3 = 10^{-4}$ S/m	7.2	13.7	20.5

4.2 Schumann resonance parameters with a multi-layer ground

From the Schumann formula (1.28), the first three normal modes for Mars can be calculated: f_{01} = 19.9 Hz, f_{02} = 34.5 Hz, and f_{03} = 48.8 Hz. For cases including the ground of finite conductivity, the SR frequencies and Q factors can be computed employing the methodology presented in the previous chapter, using (1.30) and (1.39c). With the non-uniform profile of the atmosphere, Q^{-1} values, computed under different part of the cavity, can be averaged to give the whole waveguide parameters [*Galejs*, 1972; *Pechony and Price*, 2004]. The same method can be applied to the zonal models of the ground. The phase velocities and attenuation coefficients at specified resonant frequencies for various models of the ground can be calculated using (1.39a,b). The geometric mean of the attenuation coefficients for different zones and atmospheric profiles can be calculated to get the global value.

In the modeling, the daytime and nighttime hemispheres were divided into equal parts [*Galejs*, 1972] with the electric and magnetic altitudes of the ionosphere given by (3.14) and (3.15), respectively. The ground characteristic altitudes were calculated using (3.36)-(3.38) for one-layer models, (3.33)-(3.35) two-layer models, and (3.26)-(3.27) as well as (3.31)-(3.32) for three-layer models. To calculate the SR frequencies using (1.30), with (1.39), (1.45) and the characteristic altitudes, I implemented a simple algorithm into Wolfram *Mathematica*.

Firstly, to examine the influence of a low-conductivity ground on the SR parameters, I considered three models of a one-layer ground: wet, transitional, and dry basaltic. In the first case, I assumed that the conductivity of the ground is $\sigma_g = 10^{-2}$ S/m, in the second: $\sigma_g = 10^{-4}$ S/m, and in the third: $\sigma_g = 10^{-7}$ S/m. In all the cases, the relative permittivity of rocks ε_R was 7. In the wet and transitional cases, the skin depth, given by (1.35b), is low, and a one-layer ground is a good approximation. In case of the dry basaltic crust, the skin depth is of the order of 10^2 km (Figure 40). In such a situation ELF waves could penetrate the crust and even the planetary upper mantle. Therefore, at least a two-layer model of the ground must be used to study the subsurface of Mars. The results for the wet and transitional cases are presented in Table 11.

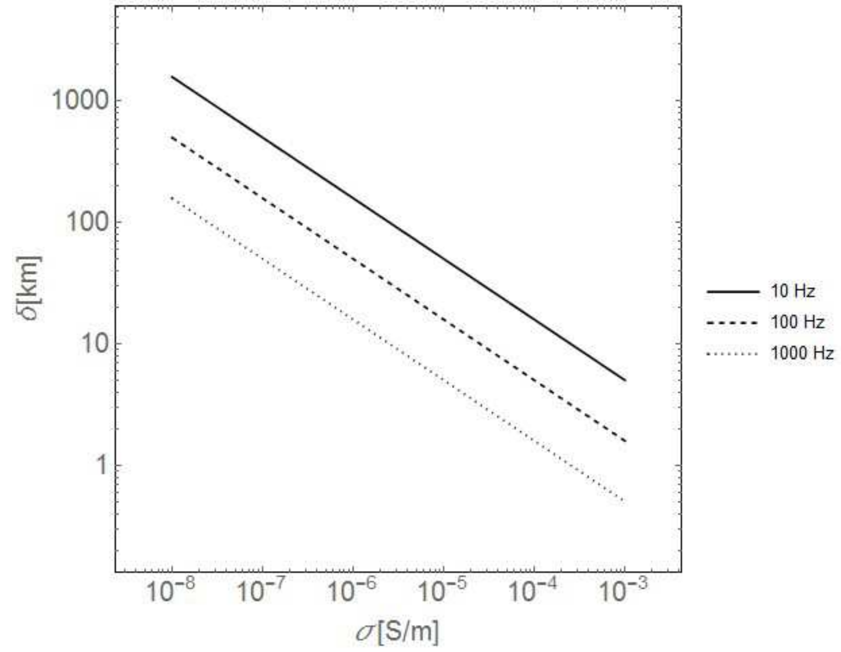

Figure 40. The skin depth as a function of conductivity for three frequency values.

Next, with the intention to test the results from numerical models, I considered cases presented in the previous publications. In the Case_1, I used a model from the work by *Simoes et al*. [2008a,b] and in the Case_2 a model presented in the work of *Yang et al.* [2006]. The obtained results (Table 11) confirmed the calculations obtained by those numerical methods. The difference between the obtained results and the numerical ones does not exceed 3%. In case of the work by *Simoes et al*. [2008a,b], they are also related to the differences with the ionospheric profiles.

Table 11. The resonant frequencies and Q factors for the first three modes of SR on Mars (*R* = 3390 km). All the presented results, except those of *Simoes et al.* [2008a,b], were modeled using the ionospheric profiles calculated by *Pechony and Price* [2004]. L – low surface conductivity, H – high surface conductivity, A – global averaged, Z – zonal averaged model.

	***n* = 1**		***n* = 2**		***n* = 3**	
	***f* [Hz]**	***Q***	***f* [Hz]**	***Q***	***f* [Hz]**	***Q***
Perfectly conducting ground						
Ideal Conductor Case TDTE	8.5	2.3	16.0	2.4	23.7	2.3
***Pechony and Price* [2004] TDTE**	8.5	2.3	16.3	2.4	24.4	2.4
***Yang et al.* [2006] FDTD**	8.8	2.3	16.1	2.4	23.6	2.4
***Simoes et al.* [2008a] FEM**	8.3	1.9	15.6	1.8	23.5	1.8
One-layer ground						
Wet Case: $\sigma_g = 10^{-2}$S/m	8.5	2.2	15.9	2.3	23.6	2.3
Transitional Case: $\sigma_g = 10^{-4}$S/m	8.0	1.9	15.2	2.1	22.8	2.1

Two-layer ground						
Water case LA: $\sigma_1 = 10^{-10}$S/m, h_1 = 5km, $\sigma_2 = 5\cdot10^{-4}$S/m	8.1	2.1	15.3	2.1	22.8	2.3
Water case HA: $\sigma_1 = 10^{-7}$S/m, h_1 = 5km, $\sigma_2 = 5\cdot10^{-4}$S/m	8.1	2.1	15.2	2.2	22.7	2.3
Brine case LA: $\sigma_1 = 10^{-10}$S/m, h_1 = 1km, $\sigma_2 = 10^{-2}$S/m	8.4	2.2	15.8	2.2	23.5	2.3
Brine case HA: $\sigma_1 = 10^{-7}$S/m, h_1 = 2km, $\sigma_2 = 10^{-2}$S/m	8.4	2.2	15.7	2.2	23.4	2.3
Water case LZ: *zonal distribution*	8.2	2.1	15.4	2.2	22.9	2.3
Water case HZ: *zonal distribution*	8.1	2.1	15.2	2.2	22.6	2.2
Brine case LZ: *zonal distribution*	8.4	2.2	15.8	2.3	23.5	2.3
Brine case HZ: *zonal distribution*	8.4	2.2	15.7	2.3	23.2	2.3
Case_1: $\sigma_1 = 10^{-7}$S/m, h_1 = 10km, σ_2 = inf	8.1	2.3	15.2	2.4	22.5	2.4
Case_2: $\sigma_1 = 10^{-7}$S/m, h_1 = 40km, σ_2 = inf	7.1	2.4	13.3	2.5	19.6	2.4
Numerical modeling with ground						
***Simoes et al.* [2008a]**: $\sigma = 10^{-7}$S/m, h = 10km	7.9	1.9	14.9	1.9	22.4	1.9
***Yang et al.* [2006]:** $\sigma = 10^{-7}$S/m, h = 40km	7.3	2.5	13.1	2.5	19.2	2.8
Three-layer ground						
Dry case LA: $\sigma_1 = 10^{-10}$S/m, h_1 = 5km, $\sigma_2 = 5\cdot10^{-7}$S/m, h_2 = 20km, $\sigma_3 = 10^{-4}$S/m	7.3	2.1	13.8	2.3	20.6	2.3
Dry case HA: $\sigma_1 = 10^{-7}$S/m, h_1 = 15km, $\sigma_2 = 10^{-6}$S/m, h_2 = 10km, $\sigma_3 = 10^{-4}$S/m	7.2	2.0	13.6	2.2	20.2	2.2

Finally, I studied the models of the ground, presented in Chapter 3. The obtained results are also shown in Table 11.

The spectra of ELF waves in the Martian cavity were calculated (Figure 41, 42) using the amplitudes of the magnetic field component $H(\vartheta,f)$ in a spherical cavity given by [*Mushtak and Williams,* 2002]:

$$H_\varphi(\vartheta,f) = -\frac{s(f)}{4h_mR}\frac{P_{\overline{\nu}}^1[\cos(\pi-\vartheta)]}{\sin[\pi\overline{\nu}_S(f)]}, \tag{4.1}$$

where: $P_{\overline{\nu}}^1$ is the Legendre function of complex order, h_m is the real part of the magnetic altitude, $s(f)$ is the spectral current moment of the source, ϑ is the distance from the source, $\overline{\nu}_S$ is the complex propagation parameter for a spherical cavity, associated with $\overline{S}$ through the relation [*Galejs*, 1972]: $\overline{S}^2 = \overline{\nu}_S(f)[\overline{\nu}_S(f)+1]/(k_0R)^2$. The spectra were obtained for a source that has the form of the Dirac delta function and amplitude 1 C·km (see point 2.4.3). Seeing that on Mars higher modes of SR are weak, the spectra were presented for $\vartheta = \pi/2$, as this distance provides the best visibility of the first mode. Therefore, only the first and third mode can be seen in the figures. All spectra were normalized to the amplitude of the Ideal case.

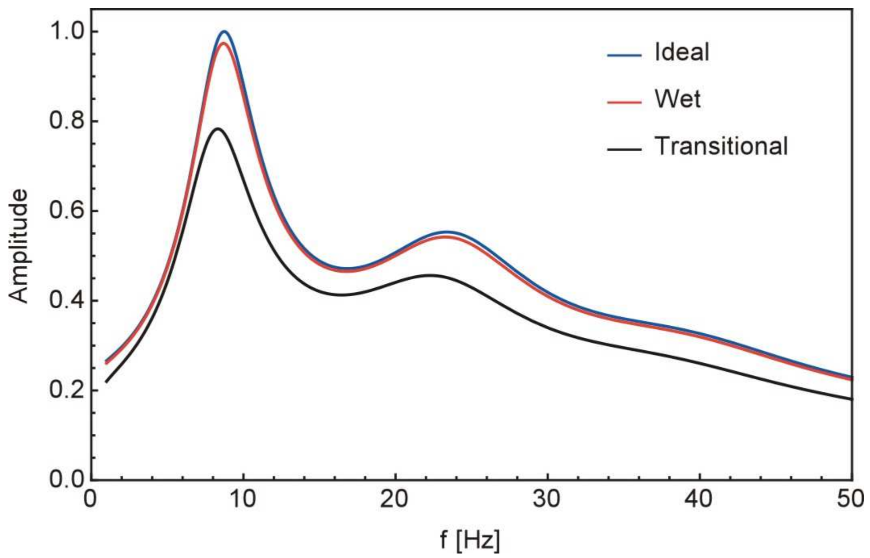

Figure 41. The spectra of SR for the one-layer ground cases, calculated using (4.1) and normalized to the Ideal case.

Source: *Kozakiewicz et al*. [2015].

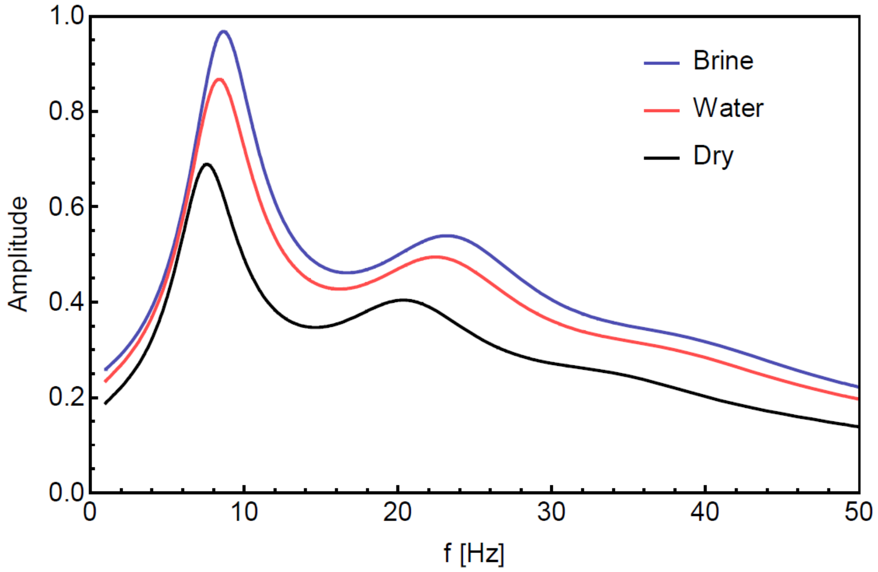

Figure 42.The spectra of SR for the situations in which there is some groundwater of high and low salinity under the Martian surface or there is no groundwater. All the spectra are with low surface conductivity and normalized to the amplitude of the Ideal case.

The amplitude spectral density of the magnetic field component at the first resonant frequency expressed in physical units is: $3.3 \cdot 10^{-4}$ $\mathrm{pT}/\sqrt{\mathrm{Hz}}$ in the Dry model, $4.1 \cdot 10^{-4}$ $\mathrm{pT}/\sqrt{\mathrm{Hz}}$ in the Water model, $4.6 \cdot 10^{-4}$ $\mathrm{pT}/\sqrt{\mathrm{Hz}}$ in the Brine model.

4.3 Propagation parameters with a multi-layer ground

The phase velocities and attenuation coefficients for the Ideal, Brine, Water and Dry models are shown in Table 12. The cutoff frequency f_c for the Martian waveguide, given by $c/(2h)$ is also presented.

Table 12. The attenuation coefficients, the ratio between the phase velocity to the velocity of light in free space, and cutoff frequency for the different ground models at 10 Hz and 100 Hz. L – low surface conductivity, H – high surface conductivity, A – global averaged, Z – zonal averaged model.

	f_c [Hz]	f = 10 Hz		f = 100 Hz	
		v_{ph}/c	α [dB/Mm]	v_{ph}/c	α [dB/Mm]
Ideal Conductor Case	1500	0.46	0.9	0.62	7.2
Wet Case: $\sigma_g = 10^{-2}$S/m		0.46	0.9	0.62	7.2
Transitional Case: $\sigma_g = 10^{-4}$S/m		0.44	1.1	0.62	7.7
Brine case LA: $\sigma_1 = 10^{-10}$S/m, h_1 = 1km, $\sigma_2 = 10^{-2}$S/m	1450	0.45	0.9	0.62	7.3
Brine case HA: $\sigma_1 = 10^{-7}$S/m, h_1 = 2km, $\sigma_2 = 10^{-2}$S/m		0.45	0.9	0.62	7.3
Water case LA: $\sigma_1 = 10^{-10}$S/m, h_1 = 5km, $\sigma_2 = 5\cdot10^{-4}$S/m	1400	0.44	0.9	0.60	7.5
Water case HA: $\sigma_1 = 10^{-7}$S/m, h_1 = 5km, $\sigma_2 = 5\cdot10^{-4}$S/m		0.44	0.9	0.60	7.5
Dry case LA $\sigma_1 = 10^{-10}$S/m, h_1 = 5km, $\sigma_2 = 5\cdot10^{-7}$S/m, h_2 = 20km, $\sigma_3 = 10^{-4}$S/m	1110	0.41	1.0	0.55	8.2
Dry case HA: $\sigma_1 = 10^{-7}$S/m, h_1 = 15km, $\sigma_2 = 10^{-6}$S/m, h_2 =10km, $\sigma_3 = 10^{-4}$S/m		0.40	1.1	0.55	8.5

The values in Table 12 indicate that the propagation parameters are only slightly influenced by the surface conductivity, therefore the ratio between the phase velocity to the velocity of light in free space and the attenuation coefficients in the function of frequency were calculated only for the low surface conductivity models (Figure 43-44).

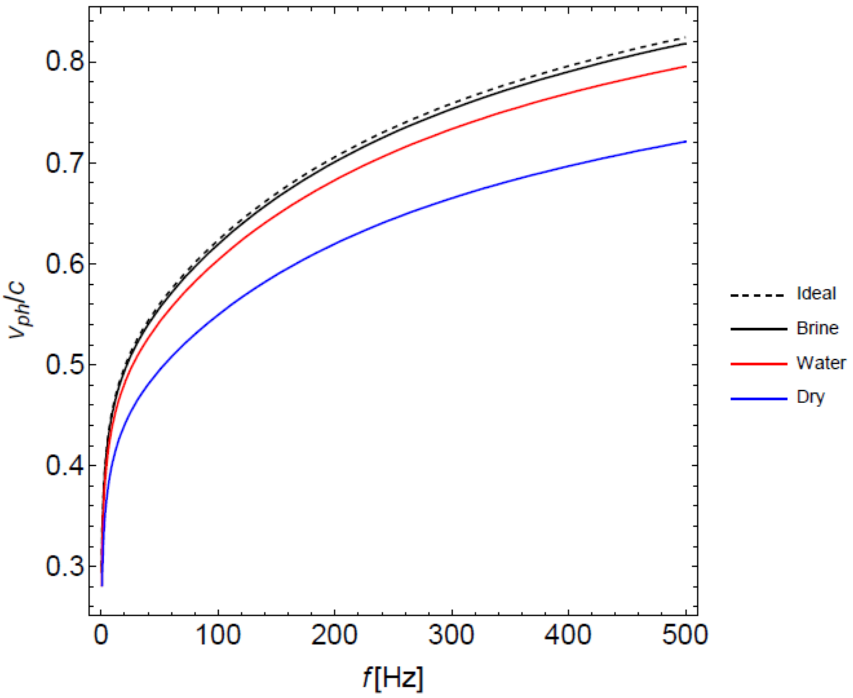

Figure 43. The ratio between the waveguide phase velocity to the velocity of light in free space for various models of the ground with the low surface conductivity.

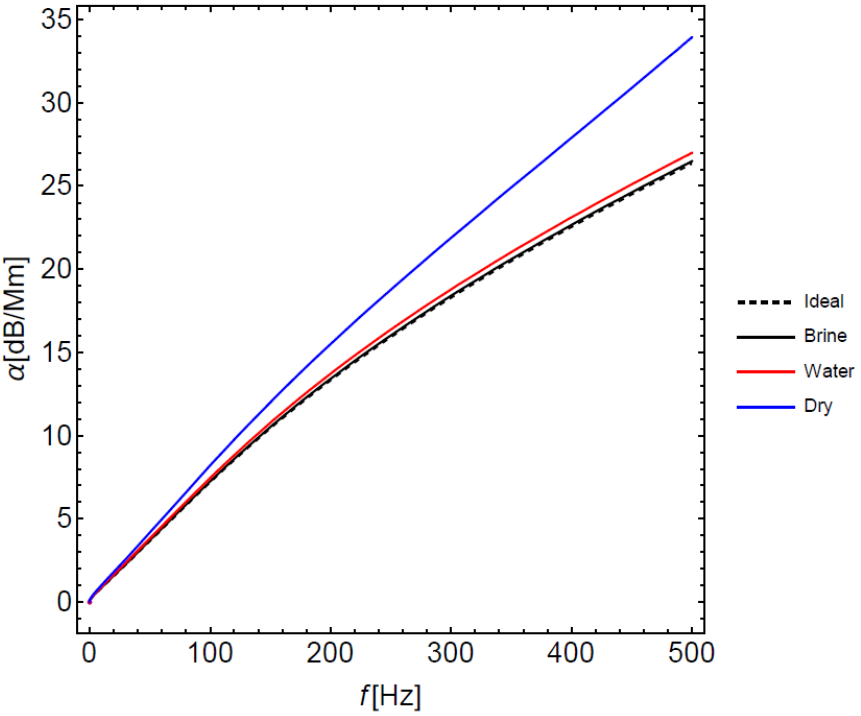

Figure 44. The attenuation coefficients for various models of the ground with the low surface conductivity.

4.4 Discussion of the results

In the analysis of the impact of the environmental properties on the SR parameters, the influence of the permittivity, which is quite small, was omitted.

As the propagation parameters and the Schumann resonance frequencies are related to the magnetic and electric altitudes, the relationship between the ground conductivity, wave frequency and characteristic altitudes for the Martian waveguides is presented in Figures 45 and 46.

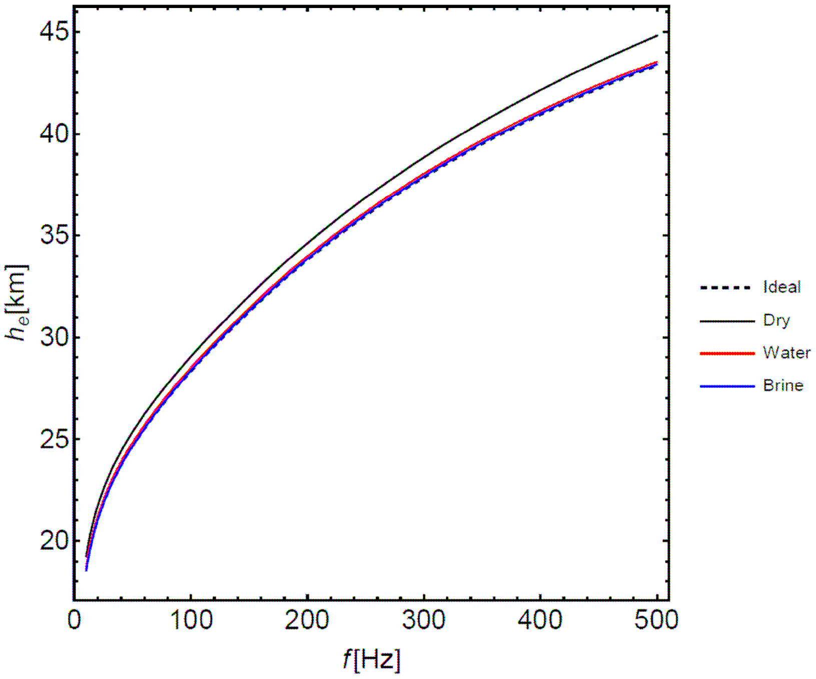

Figure 45. The real part of the electric altitude of the waveguide made of the ideal ground and the low surface conductivity models as a function of frequency.

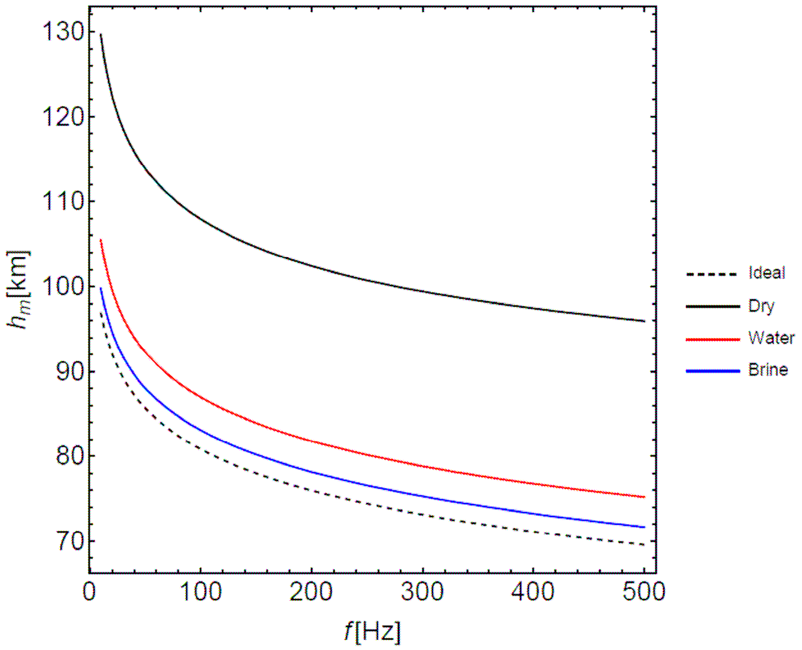

Figure 46. The real part of the magnetic altitude of the waveguide made of the ideal ground and the low surface conductivity models as a function of frequency.

The magnetic altitude is always larger than the electric altitude, and as the former increases with frequency, the latter decreases. The electric altitude is not as much influenced by the electric properties of the ground as the magnetic altitude. This can be explained by the fact that the magnetic altitude describes the distance between currents generated within the boundary mediums by the magnetic field component, whereas the electric altitude between charges collected at the boundaries. Therefore, the magnetic altitude variability in terms of frequency and ground properties determines to a greater extent the Schumann resonance and ELF propagation parameters. The magnetic altitude is larger for lower frequencies due to the fact that such low frequency waves penetrate the boundaries to greater depths than high frequency waves. The same is true in terms of conductivity. The higher is the ground or atmospheric resistivity, the higher is the magnetic altitude of the waveguide. The electric altitude is also larger for the lower conductivities of the waveguide boundaries. The values of the electric and magnetic altitude at a 10 Hz frequency are presented in Table 13.

Table 13. The magnetic and electric altitude at a 10 Hz frequency for the various ground models and the daytime ionosphere profile.

	h_e [km]	h_m [km]
Ideal Ground	18.5	97.0
Brine case LA: $\sigma_1 = 10^{-10}$S/m, h_1 = 1km, $\sigma_2 = 10^{-2}$S/m	18.5	99.8
Water case LA: $\sigma_1 = 10^{-10}$S/m, h_1 = 5km, $\sigma_2 = 5{\cdot}10^{-4}$S/m	18.7	105.5
Dry case LA: $\sigma_1 = 10^{-10}$S/m, h_1 = 5km, $\sigma_2 = 5{\cdot}10^{-7}$S/m, h_2 = 20km, $\sigma_3 = 10^{-4}$S/m	19.3	129.7

From the calculated spectra (Figure 41, 42), we can see that the SR frequencies (frequencies at which ELF field amplitude reaches the local maxima) and the SR amplitudes depend strongly on the thickness and conductivities of the ground layers. In the one-layer model (Figure 41), with decreasing conductivity of the ground the SR frequencies and amplitudes decrease. This is expected due to the fact that the magnetic altitude also increases in such situations. In the two-layer model, the resonant frequencies and amplitudes decrease with increasing thickness of the upper layer and decreasing conductivity of the lower layer. To show this dependence, four examples of two-layer cases are presented in Figure 47.

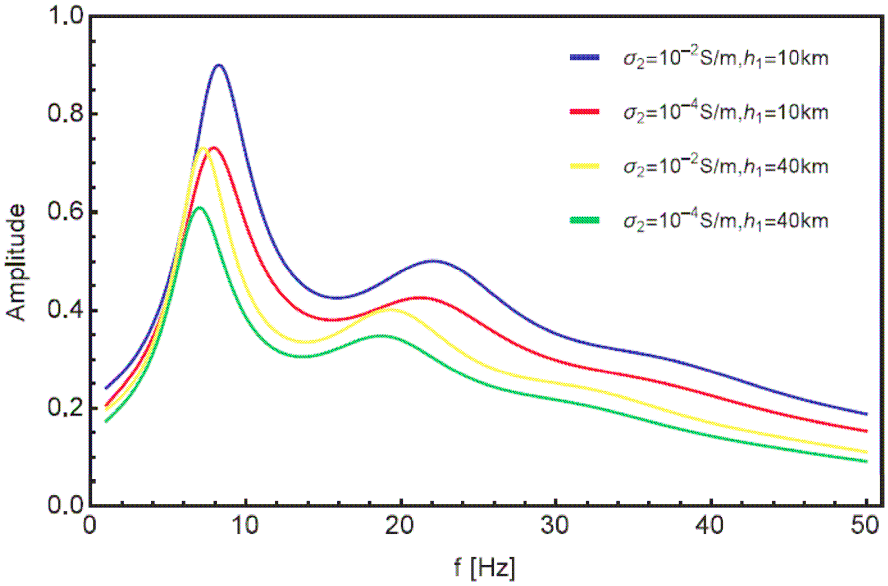

Figure 47. The influence of the conductivity of the second layer and thickness of the first layer on the SR parameters for some examples of the two-layer ground. The conductivity of the first layer in all cases is $\sigma_1 = 10^{-7}$ S/m. All the spectra were normalized to the amplitude of the Ideal case.

Source: *Kozakiewicz et al.* [2015].

There are clear differences in the SR parameters for the different models of the Martian ground (Figure 42). The SR frequencies are lower about 14% in the Dry model as compared to the Ideal case. For the Water and Brine models these values are only 4% and 1%, respectively. The SR frequencies for the Water and Brine models are also larger than those for the Dry model by 13% and 10%, correspondingly. The same applies to the SR amplitudes. In the Dry model, they are 41% lower than in the Ideal case, 39% than in the Brine case, and 34% in the Water case. The Q factors are similar for all the models, and they are much lower than those on Earth, indicating that the Martian waveguide is more damped than the terrestrial one.

The difference between the zonal and averaged over the entire planet results indicates that the influence of the regional scale variations cannot be easily distinguished. This result is expected due to the global nature of the Schumann resonance phenomenon.

In two-layer models of the ground, the influence of the top layer on the SR parameters is most interesting and can be easily analyzed using the analytical method. Figures 48 and 49 illustrate the relationship between the first mode of the SR frequencies and the properties of the ground. Figure 48 displays that high-conductivity upper layers barely influence the SR parameters since ELF waves reflect from them. For conductivities lower than 10^{-4} S/m, the influence of the ground on the SR parameters is obvious. If the upper layer thickness is larger than the skin depth, ELF waves penetrate only into this layer and the underlying region does not influence the SR parameters. If the conductivity of the upper layer is low or its thickness is small, the waves reach the underlying region. If the conductivity of this region is high, the waves reflect from it. In the opposite situation, they penetrate into it, and the SR frequencies are additionally reduced. Along with the increase of the thickness of the low-conductivity upper layer (Figure 49), the influence of its conductivity on the SR frequencies increases. The strongest impact on the SR frequencies can be observed for conductivities ca. 10^{-7} S/m. The influence rapidly declines for conductivities lower than 10^{-9} S/m as the upper layer becomes transparent for ELF waves. In this situation, the upper layer behaves as an insulator, and as a result, the SR parameters depend more on the properties of the underlying region.

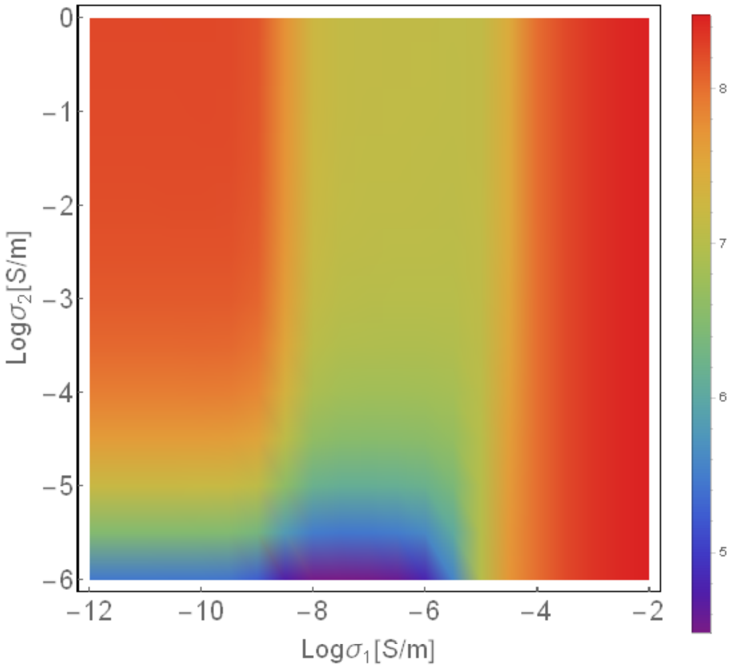

Figure 48. The SR first mode frequency as a function of the conductivity of the first and second layer in the two-layer model. The depth of the first layer is 40 km. At the conductivity Log σ_1 = -4.8, the skin depth is larger than 40 km and the second layer starts to contribute to changes in the SR frequency.

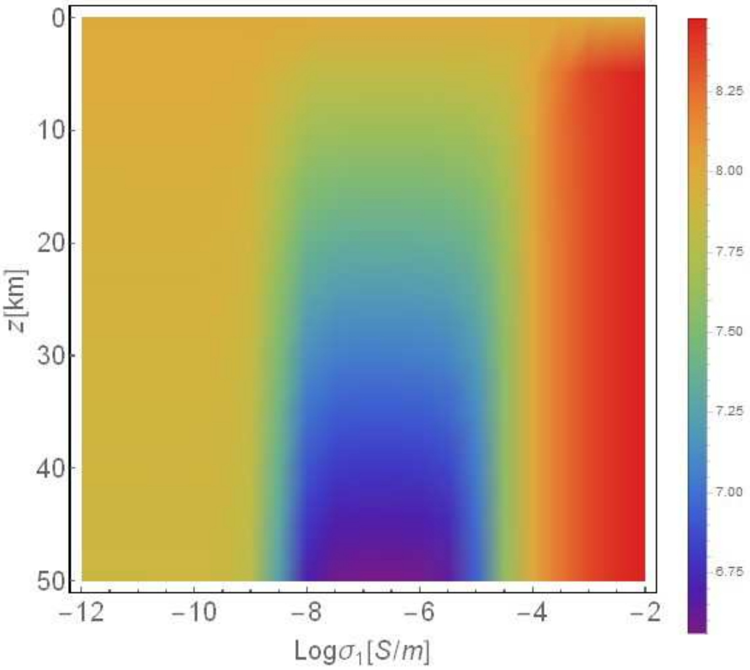

Figure 49.The SR first mode frequency as a function of the depth and conductivity of the first layer in the two-layer model. The conductivity of the second layer is 10^{-4} S/m.

The differences between the low and high surface conductivity models are not well visible in the SR parameter (Table 11). The higher results of the SR frequencies in the Dry LA model than in the

Dry HA model can be explained by the less significant influence of the top layer in the former model. To indicate this influence, the first mode frequency as a function of depth and conductivity of the first (Figure 50) and the second layer (Figure 51) in the three-layer model were calculated.

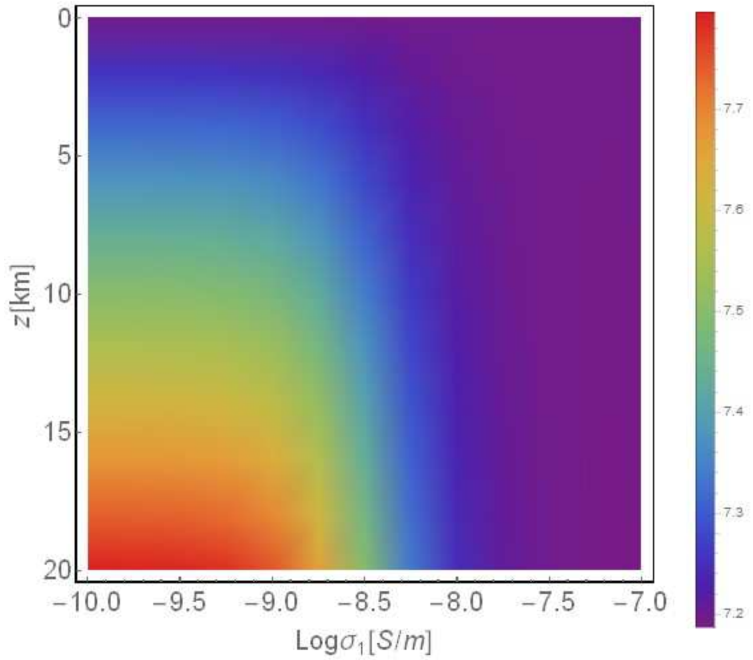

Figure 50. The SR fundamental mode frequency as a function of depth and conductivity of the first layer in the three-layer model. The conductivity of the second layer is 10^{-6} S/m and this layer stretches to the depth of 25 km. The conductivity of the third layer is 10^{-4} S/m.

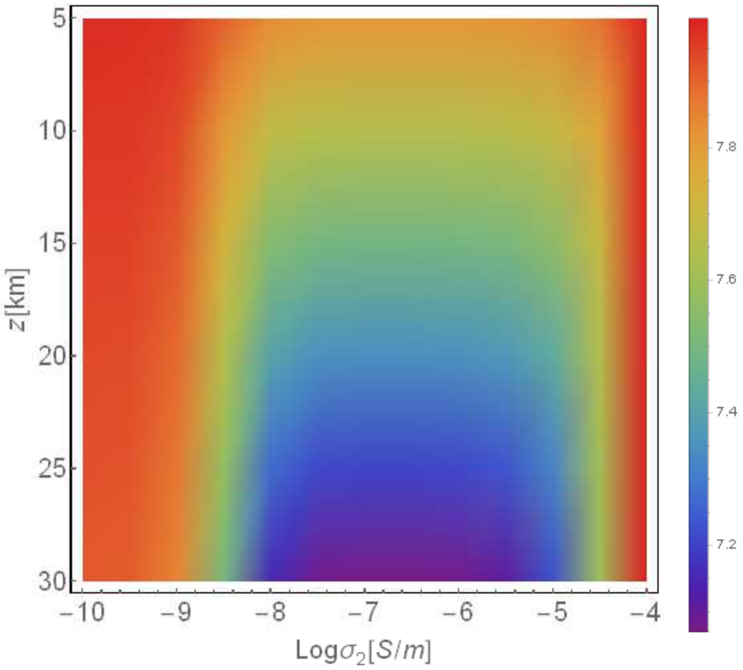

Figure 51. The SR fundamental mode frequency as a function of depth and conductivity of the second layer in the three-layer model. The conductivity of the first layer is 10^{-10} S/m and it is 5 km deep. The conductivity of the third layer is 10^{-4} S/m.

Figures 50 displays that the SR first mode reduction by the top layer takes place especially for surface conductivities larger than 10^{-8} S/m. Conductivities of the order of 10^{-10} S/m barely influence the SR parameters, since then the ground is almost transparent to ELF waves. In these calculations, when the top layer thickness increases the second layer thickness decreases. The reduction is less significant as the contribution of the second layer becomes small. The most important is the second layer, which can have conductivities of the order of 10^{-8} to 10^{-5} S/m (Figure 33). These values have the strongest impact on the SR frequencies. Also with the increase of the thickness of the second layer (Figure 51), the influence of its conductivity on the SR frequencies increases. In addition, in this range of conductivities, the reduction is almost constant for a given thickness. Only if this layer thickness is greater than 25 km then some differences in the outcome for various conductivities are visible. The greatest reduction takes place for conductivities ca. 10^{-7} S/m. Similarly, as in the two-layer model, this layer influence rapidly declines for conductivities lower than 10^{-9} S/m. It also does not contribute when its conductivity becomes close to 10^{-4} S/m.

The propagation parameters depend on the ground properties (Table 12, Figures 43-44). The phase velocities are reduced in the Dry model by more than 10% in compare to the Ideal case. In the Brine and Water models, this reduction is 2% and 4%, respectively. The phase velocities increase with increasing frequency as higher frequency waves penetrate the boundaries of the waveguide to shallower depths (Figure 40). The value of the reduction does not depend on frequency. The attenuation is larger in the Dry model than in the cases with water or brines beneath the Martian surface. In the Schumann resonance frequency range (5-50 Hz), the increase in the attenuation coefficient is ca. 15% for the Dry model, 5% for the Water model, and 1% for the Brine model as compare to the Ideal case.

As the ELF propagation and Schumann resonance parameters depend on the ground structure, it is possible to acquire some information about the properties of the Martian subsurface from measurements made by an ELF station located on the Martian surface. Such a station is described in the next chapter.

5 The ELF experiment on Mars

In this chapter, an experiment, which enables to investigate some of the major aspects of electrical environment of Mars, such as electrical discharges in the atmosphere and the structure of the planetary subsurface, is proposed. First, the previous and ongoing *in situ* electromagnetic experiments on Mars are described. Next, our ELF station on Earth and information about the terrestrial environment it provides is displayed. Finally, the objectives and the preliminary description of the ELF experiment on Mars are presented and two examples of such research are proposed: ELF source investigation and underground water detection.

5.1 Electrical activity investigation on Mars

5.1.1 Remote sensing measurements

There are several different techniques for detection of electric discharges. Optical measurements are the easiest, however as it was described in Chapter 2, they are not possible on Mars as dusty phenomena do not allow for such investigation. Another important technique is related to remote sensing radio observations. Yet, as shown in Chapter 2, the previous studies employing this technique did not provide sufficient data to indicate any presence of electrical activity on Mars. In future, intensive electric discharges on Mars may be detected by large terrestrial radio interferometers such as the LOFAR (Low Frequency ARray) or the Square Kilometer Array. The LOFAR with arcseconds resolution in the range 30-240 MHz is capable of resolve such phenomena on the planetary disk of Mars (18”) [*Zarka et al.*, 2008]. Also chemical analysis can provide some evidence of discharges. When a lightning channel passes through a planetary atmosphere, it generates compounds that can be remotely detected. For example *Krasnopolsky* [2006], from ground-based observations using a spectrograph, detected NO lines in the Venusian spectrum, suggesting that electrical discharges may play a role in the atmosphere of Venus. This approach however, in the case of Mars has been inconclusive.

5.1.2 *In situ* measurements

Although some experiments and instruments were proposed to study electromagnetic properties of the Martian environment many years ago [*Bertherlier et al.*, 2000], the only up-to-date experimental evidence for electrical activity on Mars is related to electrostatic adhesion of dust to the wheels of rovers [*Ferguson et al.*, 1999; *Aplin*, 2006]. For instance, the Mars Pathfinder rover was equipped with a metal strips attached to the wheels and with dissipation points which prevented from any possibility of electrical discharging [*Ferguson et al.*, 1999]. The amount of dust accumulated in the wheels suggested that dust takes place in triboelectric processes.

The planned DREAMS payload in the ExoMars 2016 program will function for few days after landing as an environmental station. DREAMS will provide new insights into the role of electric forces on dust lifting and its impact on dust storms initiation. The MicroARES sensor will be responsible for measurements of electric fields. It consists of a 27 cm high antenna mounted on the top of the lander. At the top of the antenna a spherical electrode is placed. The signal will be measured between this electrode and chassis of the lander [*Deprez et al.*, 2014]. In addition, another instrument will complement MicroARES measurements with data on humidity enabling to understand dust electrification processes. However, the payload will not allow studying distant low-intensity electromagnetic sources or the electromagnetic properties of the ground.

From all the techniques the Schumann resonance investigation is identified as the most informative single measurement and should be a priority when proposing future planetary electrical instrumentation [*Berthelier et al.*, 2000; *Aplin et al.*, 2008, *Harrison et al.*, 2008]. The Schumann resonance phenomenon can be a very useful tool to detect electrical discharges, to study the electromagnetic properties of the planetary cavity or the influence of space weather on the planetary environment. The electromagnetic sounding in the low frequency range is favorable for detection of deep subsurface water layers, which cannot be done using radar or seismic methods [*Delory et al.*, 2007; *Grimm et al.*, 2009]. Using this technique the presence of groundwater at depths up to several kilometers below the surface can be investigated.

It is possible to study SR from the planetary surface and probably also from a planetary orbit as proposed by *Simoes et al*. [2011]. In this second approach, the measurements are possible due to wave leakage from the atmosphere to the ionosphere [*Grimalsky et al.*, 2005]. But this technique can be used only with planets which have intrinsic magnetic field, therefore, not on Mars.

5.2 ELF measurements on Earth

There are several ELF stations on Earth. One of them, the Hylaty station, is located in the southeastern part of Poland in a very low electromagnetic noise environment. The station has been measuring the magnetic field components of ELF since 1994. Research projects based on the data obtained from this station comprise studying the Schumann resonance phenomenon, global lighting activity along with TLE, and mapping of strong discharges. The recorded signals include fields generated in the magnetosphere, lower atmosphere, and ionosphere. Various phenomena hidden in the data can be extracted using suitable signal analysis methods.

At present, the station consists of two orthogonal magnetic antennas, and receivers, equipped with a power supply, which enables few months of continuous operation without recharging. The antennas with their preamplifiers are placed in hermetic boxes at a shallow depth below the ground level. They can measure the B_x and B_y (NS and EW) ELF field components [*Kulak et al*., 2014].

Schumann resonance has a noise-like characteristic with coherence time of about 1 s [*Kulak et al*. 2014]. The amplitude spectral density of the magnetic field component at the first resonant frequency is ca. 3 pT/$\sqrt{\text{Hz}}$.

The self-noise of the magnetic antennas is ca. 0.02 pT/$\sqrt{\text{Hz}}$ at 10 Hz. The receiver has a 300 Hz bandwidth and a 900 Hz sampling frequency. Neglecting fields originating from local thunderstorms, the dynamics of natural field amplitudes does not exceed 80 dB, thus it allows using 16 bit (96 dB) analog-to-digital converters (ADCs). The data stream in the ELF range is small, so it is reasonable to record raw data. The Hylaty receiver produces 300 Mb per day [*Kulak et al*., 2014]. The detailed parameters and description of the antennas and receivers are given in the work of *Kulak et al*. [2014].

The accuracy of the noise-like-spectra measurements increases with the recording time. As the signal level in the Earth-ionosphere cavity does not decrease below 0.1 pT/$\sqrt{\text{Hz}}$ at 10 Hz, the signal-to-noise ratio of a recorded spectrum during 300 s with the Hylaty sensors is about 26dB (see point 5.3).

In addition to spectral measurements, waveform measurements are also possible. Waveforms measured at relatively short distances (not exceeding about 10 Mm) can be separated from around the globe wave. Their waveforms take a form of short impulses and their shapes depend on the transfer functions of the Earth-ionosphere waveguide and a receiver. As the propagation properties of the Earth-ionosphere waveguide are fairly well known, it is possible to reconstruct the parameters of a source generating pulses. It is possible to collect statistical data on individual discharges and measure activity of the lightning centers [*Kulak et al*., 2014].

The antennas allow calculating the direction of a wave arrival. A single station however is not sufficient to determine precisely location of individual discharges. This can be done using a network of a few ELF stations located far enough from each other to triangulate the signal.

5.3 Objectives and description of the Martian experiment

To study electromagnetic properties of a planet, passive and active electromagnetic exploration can be employed. The passive sensors can be used when natural EM source are present in the cavity. The active ones when those sources are of insufficient intensity.

It is not possible to locate at the surface of Mars any transmitter in the ELF range due to its large dimensions and high power consumption. However, the Martian environment probably possesses natural sources of electromagnetic waves in the ULF-ELF range. These include electrical discharges connected to dust storms and dust devils as well as emission generated by interactions among the solar wind, magnetosphere, ionosphere, and crustal magnetization, as discussed in point 2.3. The risk related with the assumption on the existence of natural sources of ULF-ELF waves on Mars is probably smaller than this connected with life detection. In addition, lack of detection of any of those sources during the experiment also carries important information on the Martian environment. Consequently, placing an ELF platform on the Martian surface can be justified.

When an ELF wave is propagating from its source to a receiver, the environmental properties influence its propagation parameters. As shown in Chapter 4, it is possible to investigate the waveguide properties on the basis of the measured Schumann resonance parameters or ELF propagations parameters. Since the method presented in Chapter 3 is fully analytical, it is computationally efficient and can be very useful to find inverse solutions. It takes minutes to acquire results for different environmental models, which with numerical modeling takes weeks. This method can be use as a tool to study the depth and thickness of subsurface conductive layers, such as aquifers and investigate ELF sources.

5.3.1 Objectives

The main objectives of the experiment are associated with studying natural electromagnetic sources. The importance of the atmospheric electricity can be summarized with the role it plays in chemistry of the atmosphere, aeolian transport, production and destruction of organic compounds, which indirectly influences global climate and the presence of life. The natural electromagnetic sources are of great importance as they may influence radio communication on the planet during the future more robust missions and can be a treat to their safety. In addition, they produce electromagnetic fields, which can be employed to investigate the structure of the planetary subsurface or studying the lower layer of the atmosphere.

5.3.2 Description of the measuring system

As the considered phenomena are mainly of low intensity, I proposed a high-sensitive and low-noise system for the Martian exploration. As any electromagnetic instrument placed near the system would interfere with its measurements, therefore, it is necessary to consider it as an autonomous platform. This measuring station is designed to detect weak Schumann resonance and ELF sources. The continuous raw data will be recorded to allow spectral and waveform investigation. The receiver bandwidth is proposed to be 0.03 to 1500 Hz to cover also the cutoff frequency region.

The sounding system consists of two orthogonal horizontal magnetic antennas, with built-in preamplifiers, an active vertical electric antenna, and a receiver. The receiver has a basic function of auto-calibration and self-diagnosis. It is also possible to disconnect power from unused (or damaged) measuring circuits. The electric antenna is 400 mm long and is deployable. This short electric dipole is a wire ended at the top with a metal sphere. Each magnetic antenna is 700 mm long and is 60 mm in diameter. Their design is based on a wire-wound induction coil with a core of high-permeability material.

The magnetic antennas were selected in a way to maximize the signal-to-noise ratio and minimize their weight and size. To find the best ratio between the size and mass of the antenna and its sensitivity, I used as a parameter the lower threshold of the amplitude spectral density at the first Schumann resonance frequency, which a given antenna enables to measure. This in turn depends on the antenna noise. The relationship between the antenna noise for a unit bandwidth B_n and its size can be given by [*Kulak*, 2010]:

$$B_n = 0.028\frac{\sqrt{F_a}}{d_c^{2.5} r_c^{2.2} f}\text{, } r_c = l_a/d_c\text{, } D_a \cong \alpha_a\, d_c \tag{5.1a,b,c}$$

where: d_c – the diameter of the antenna core, D_a – the diameter of the antenna, α_a = 3 is the constructional parameter, l_a – the length of the antenna, F_a = 1.6 is the noise factor of the amplifier at 10 Hz, and r_c is the slenderness ratio of the antenna core. From (5.1), the antenna of the size proposed above has a noise level ca. 0.02 pT/$\sqrt{\text{Hz}}$.

The mass of the antenna depends on the antenna size, the mass of the antenna core, and the coil density:

$$m_a = m_c\left[\left(\alpha_a^2 - 1\right)\frac{\rho_a}{\rho_c} + 1\right], m_c = \frac{\pi d_c^2}{4} l_a \rho_c , \tag{5.2a,b}$$

where: m_a – the mass of the antenna, m_c – the mass of the antenna core, ρ_a – the density of the antenna coil, ρ_c – the density of the antenna core. Using (5.2) with an iron core of density ca. 7874 kg/m^3 and an aluminum coil of density 2700 kg/m^3, the mass of the proposed antenna is ca. 6.5 kg.

The minimum fluctuation of spectral intensity $\Delta|B_s|^2$ that the magnetic antenna is enabled to detect can be given by [*Kulak et al.*, 2014]:

$$\Delta|B_s|^2 = |B_n|^2 \frac{1}{\sqrt{\Delta f \tau_R}}, \tag{5.3}$$

where: $|B_n|^2$ is the spectral density of the magnetic antenna self-noise, Δf is the frequency range, and τ_R is the recording time. The power spectrum of the Schumann resonance signal on Mars can be given by [*Nickolaenko and Hayakawa*, 2002]:

$$|H(f)|^2 = \lambda_p \left\langle \tilde{p}^2 \right\rangle \left\langle \left(\frac{1}{4h_m R} \frac{P_{\overline{\nu}}^1[\cos(\pi - \vartheta)]}{\sin[\pi \overline{\nu}_S(f)]} \right)^2 \right\rangle, \tag{5.4}$$

where: λ_p is the discharge rate, and the angular brackets express avarged values over the independent amplitudes and spectra of pulses. From (5.3) and (5.4), with Δf = 1 Hz, τ_R = 300 s, and the amplitude of the magnetic component calculated in the Dry model of the ground (see point 4.2), we find that the platform should easily detect Schumann resonance if the intensity of discharges on the planet, described by $\lambda_p\left\langle \tilde{p}^2 \right\rangle$, is of order of 10^2 C^2·km^2/s. On Earth, the observed discharge intensity is of order of 10^3 C^2·km^2/s (see the values in points 1.2.4 and 2.4.3).

With the vertical electric antenna weaker sources can be detected. This fact is simple to explain, as both type of the antennas sensitivity is proportional to their volumes and for a similar size and equal energy density, as $\mathbf{E} = c\mathbf{B}$, the electric antenna sensitivity is better [*Gurnett*, 1998]. However, the electric antenna does not allow for estimation of the source position. Using an amplifier characterized by small input capacitance (in comparison to the self-capacitance of the antenna), high impendence ~10^9 Ω, and with input noise level U_n: 2 nV/$\sqrt{\text{Hz}}$ at 10 Hz, we can calculate that the antenna can detect electric fields of intensity E_n, given by:

$$E_n = \frac{U_n}{h_{eff}}, \tag{5.5}$$

where: h_{eff} – is the effective height of the antenna [*Bem*, 1973; *Nickolaenko,* 2014]. From (5.5), assuming that $h_{eff} \approx h_a$ = 400 mm, the detectable electric field limit is 5 nV/m$\sqrt{\text{Hz}}$. As a result, this antenna enables to study a single discharge described in point (2.4.3).

5.3.3 Martian platform description

Apart from the scientific payload, the platform consists of a general processing unit (GPU), communication unit (CU) with a UHF (ultra high frequency) deployable antenna, power management unit (PMU), solar panel (SP), and a lithium-ion battery (BAT). The block diagram of the scientific payload within the platform is presented in Figure 52, and the conceptual 3D visualization of the station in Figures 53 and 54.

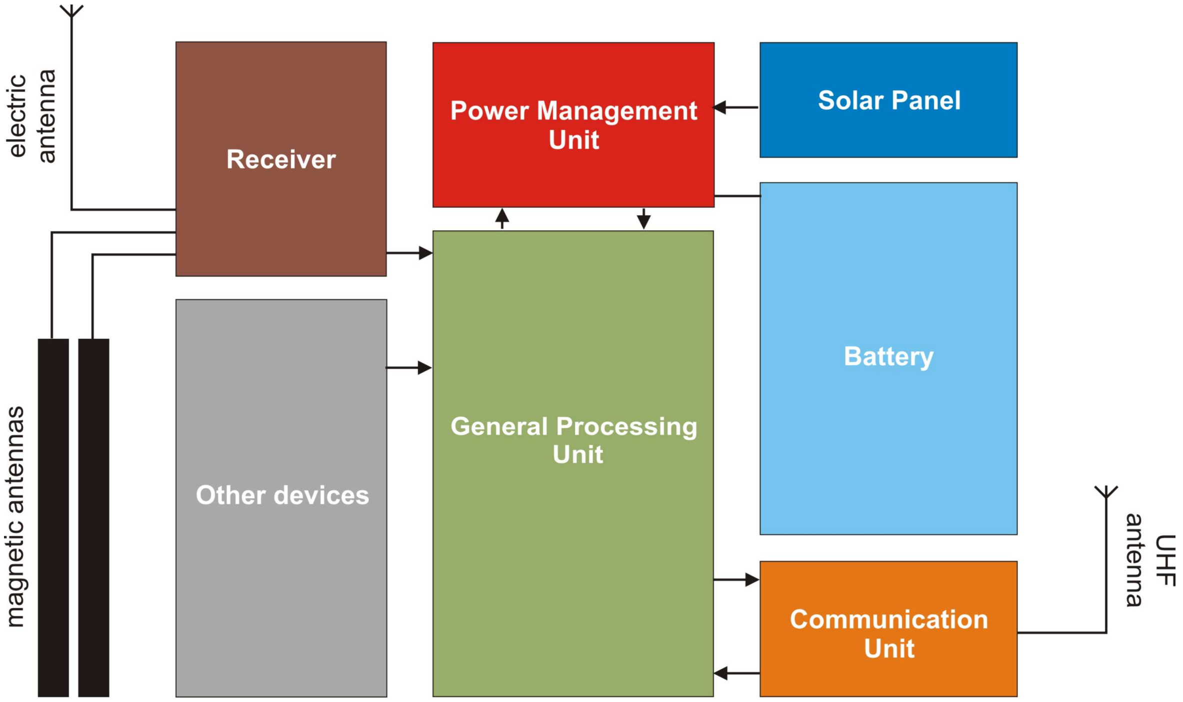

Figure 52. Block diagram of the ELF station.

On the basis of *Kozakiewicz et al*. [2014].

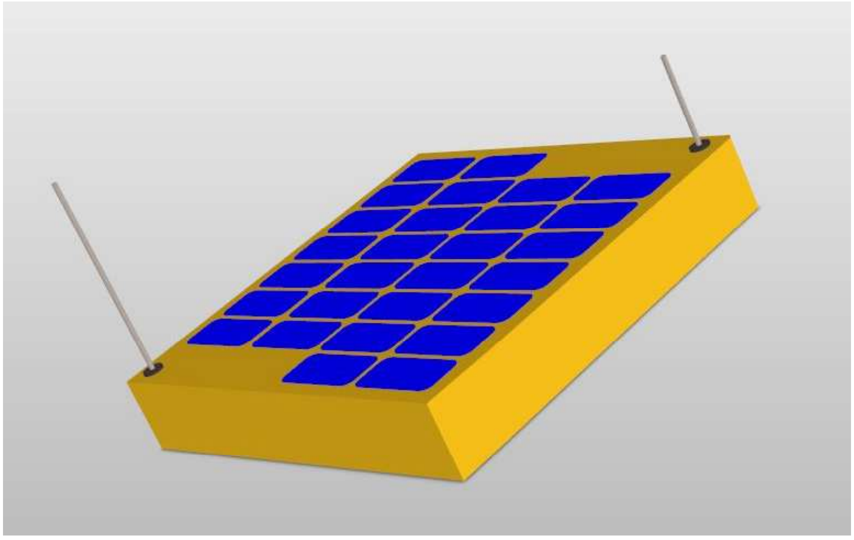

Figure 53. The 3D visualization of the platform.

Source: *Kozakiewicz et al*. [2014].

Figure 54. The 3D visualization of the platform inside part.

Source: *Kozakiewicz et al*. [2014].

The magnetic antennas, which are placed in cylindrical hermetic boxes, are supported by the receiver. It consists of multiple input channels, an analog-integrating circuit (AIC), and ADCs, which are connected to a data acquisition unit (DAU) in the CPU. The role of an analog circuit, containing amplifiers and antialiasing filters, is to strengthen and reduce the bandwidth of measured signals before they reach working synchronously ADCs. It is hard to establish the dynamic range of ELF fields on Mars though probably 16-bit ADCs are sufficient to achieve suitable measurements. The ability to switch antennas and input measurement channels increases reliability and enables conducting additional tests after landing on Mars.

The GPU controls all measuring devices, performs the measurement task schedules, and data acquisition by a field programmable gate array (FPGA) controller with a time control circuit, and by the data acquisition unit, respectively. It prepares, pre-analyzes, and compresses data from the receiver. In the absence of communication with Earth or other technical problems, it performs special scenarios. During normal operation, the GPU collects reports on the status of individual modules, which analyzes and periodically sends to Earth. The GPU has a memory of adequate capacity for buffering data during communication.

The principal role of the power management unit is to control energy, especially necessary for the GPU. In case of emergency, it can cut off the energy supply to other modules. The main tasks of the PMU are supervision of the battery and solar panels, forecasting time at a given load, and handling emergency situations. As this unit is the heaviest part of the platform, aside from the magnetic antennas, this unit and the magnetic antennas are placed at the opposite sides of the platform (Figure 54).

The primary function of the communication unit is to provide a radio connection with a Martian orbiter, testing the current link quality, and adjustment of transmitted power to propagation conditions. Although it is possible to use direct communication with Earth, the uplink to orbiters allows sending much more data for much longer time periods, therefore, the surface-to-orbit communication is considered to be more convenient than the direct Earth link.

The antennas configuration and position within the platform, as well as low electromagnetic noise of the rest of the instrumentation will not provide significant interferences [personal communications with A. Kulak].

The constraints on power supply and temperature were decisive factors to locate the platform in a tropical region. The temperature at the surface can vary significantly during the Martian sol. During daytime, it can reach +20°C, and at night can drop to –80°C. In cold Martian conditions, electronics must be well protected. In this design, the platform is equipped with the external and internal electronic warm boxes. The external electronic warm box (EEWB) has dimensions 850 mm x 850 mm x 150 mm. Inside the EEWB are the magnetic antennas and internal electronic warm box (IEWB). On the EEWB surface are mounted both electric and UHF antennas. The EEWB is made of a composite thermally insulated with aerogel and its wall is 20 mm thick. The interior space dimensions are 810 mm x 810 mm x 110 mm. The IEWB has dimensions 645 mm x 645 mm x 100 mm. It is made of the same composite as the EEWB. It provides a support structure for the entire electronics and additional thermal insulation. Its internal dimensions are 625 mm x 625 mm x 80 mm [*Kozakiewicz et al.*, 2015]. Heat generated by the electronics is sufficient to support suitable operation of the station, and due the fact that only small amount of heat is produced a heat rejection system is not necessary [personal communication with K. Zietara].

The measuring system is low in power consumption. The whole station including all units requires not more than 120 Wh per sol. The solar panel covers almost the whole surface of the EEWB and provide minimum 350 Wh per sol. As within the platform is enough room and the amount of energy provided by the panels is larger than necessary, other measuring instruments, characterized by low electromagnetic noise can be located within the platform to extend scientific payload.

All instruments inside the EEWB are insulated from sand, dust, and UV emission. Only the electric antenna is affected by both photoemission and impacts of charged dust particles. The mass of the platform, ca. 18 kg, enables steady operation even during strong gusts of wind. As the station must be place in an appropriate position, it is therefore consider as a deployable part of a rover or as a lander. The proposed station can operate at least one Martian year.

Although a single station allows some basic research, the network of platforms is favorable. Such a network may consist of three or four stations located at different parts of Mars, with a baseline larger than 1Mm.

5.3.4 Measuring impulses of ELF sources

The station will be observing waveforms associated with electric discharges, if any exist on Mars [*Kulak et al.*, 2013]. A discharge described in point 2.4.3 would be visible in measurements by an ELF station on Mars even if located in the opposite hemisphere of the planet. The shape and amplitude of an observed waveform would be lower than on Earth and would depend on the ground properties. In the Dry model, the ELF pulse associated with a discharge would arrive later to the station and its amplitude would be lower as compared to a situation with aquifers beneath the Martian surface [*Kulak et al.*, 2013].

5.3.5 Detection of underground water

Ice is difficult to distinguish from dry rocks in the ELF range as it has almost the same conductivity as rocks. However, liquid water can be easily detected even if it is present in small amounts sparsely distributed within rocks.

Since the amount of underground water depends on the rock surface porosity and the thermal gradient, it is proposed to establish the relationship between those parameters and the average crustal conductivity. Lower values of the heat flow than those considered in the previous points seems very likely [*Li and Kiefer*, 2007], and lead to lower thermal gradients. In this point, I assumed that the heat flow values are between 10 and 30 mW/m^2 and the thermal conductivity value is still 2 W/m/K. Also the surface rock porosity can be lower and may be either fully or partially filled with water. I studied the influence of those less favorable parameters on groundwater inventory and ELF propagation employing the most probable case: the low surface conductivity and high water salinity.

Amount of water, as its fraction inside rocks, for different values of the thermal gradient and porosity is presented in Figures 55 and 56. The depth at which the water is present increases with decreasing thermal gradient, and therefore with increasing thickness of the cryosphere.

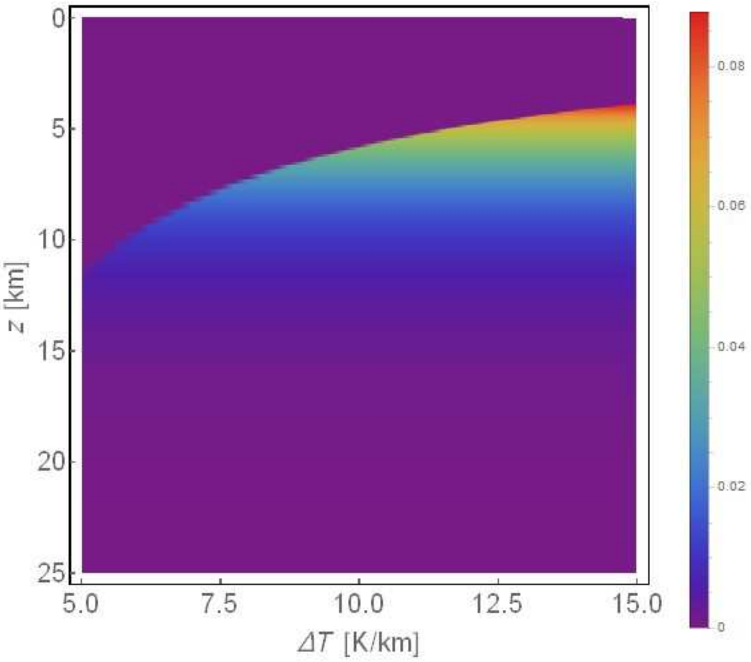

Figure 55. Amount of water under the Martian surface as the fraction of the entire rock basement at a given depth for the rock surface porosity $\varphi_0 = 0.35$ and various thermal gradients. Pores are entirely filled with water.

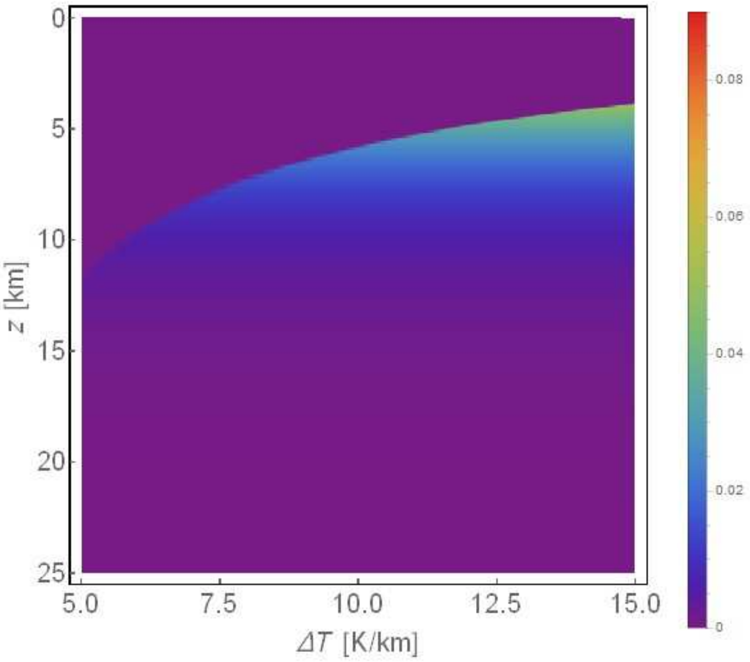

Figure 56. Amount of water under the Martian surface as the fraction of the entire rock basement at a given depth for the rock surface porosity $\varphi_0 = 0.20$ and various thermal gradients. Pores are entirely filled with water.

The profiles presented in Figures 55 and 56 integrated to the depth of 26 km, the self-compaction depth, provide the amount of water expressed in Global Equivalent Layer (Table 14). Multiplying those values by the area of the planet, we can obtain that the expected volume of underground water is $1.4 \cdot 10^6$ km^3 for the lowest thermal gradient and low surface porosity ($\varphi_0 = 0.20$), and $3.6 \cdot 10^7$ km^3 for the highest thermal gradient and high surface porosity ($\varphi_0 = 0.35$). The former value may correspond to the amount of water in the PDL. The latter seems rather improbable as it is commonly assumed that the Martian water inventory is lower than 150 m.

Table 14. Water inventory in Global Equivalent Layer for the different models. All pores are filled with water.

	$\varphi_0 = 0.20$	$\varphi_0 = 0.35$
ΔT = 5.0 K/km	10 m	15 m
ΔT = 7.5 K/km	40 m	65 m
ΔT = 10.0 K/km	70 m	125 m
ΔT = 12.5 K/km	110 m	190 m
ΔT = 15.0 K/km	140 m	250 m

The relationship between the crustal thermal gradient, surface rock porosity, and its conductivity is shown in Figure 57.

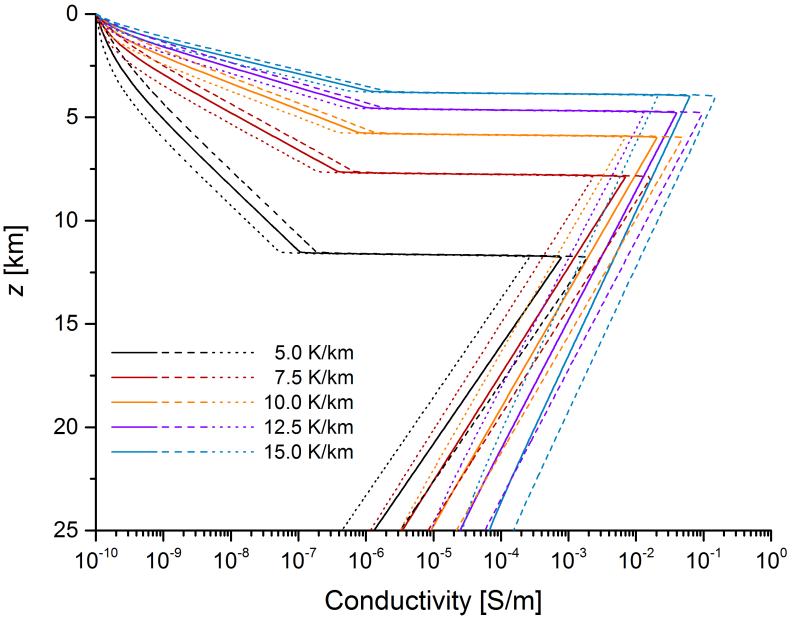

Figure 57. The conductivity profiles for the saline water and the low surface conductivity cases with different values of the heat flow and surface rock porosity. The dashed lines represent models with the 35% surface porosity, the solid lines with the 20% porosity and with pores entirely filled with water, and the dotted lines with the 20% porosity and with 50% pores filled with water.

In the upper part of the crust, the most significant is the influence of ice. As temperature or porosity increases, the ground conductivity increases as well, due to higher conductivity of ice. The greatest influence on waves propagation has the bottom part of this layer as the conductivity ca. 10^{-7} S/m reduces strongly the Schumann resonance frequency (see Figure 48). The top part of this layer is almost invisible to ELF waves. In the lower layer, water is a dominant factor. The upper part of this region is more important as here the conductivity is high enough for ELF wave reflection. Consequently, to establish a general theoretical relationship between amount of water and the first SR frequency, I used, as the representative conductivities, the values of the lower part of the first layer, and the upper part of the second layer. Such a choice of parameters gives us the lower limit on the SR frequency (Table 15).

Table 15. The ground models with the pores filled entirely (100%) or partially with water (50%).

	Depth of the 2nd layer [km]	Conductivity of the layers [S/m]					
		$\varphi_0 = 0.20$				$\varphi_0 = 0.35$	
		(50%)		(100%)		(100%)	
		1st	2nd	1st	2nd	1st	2nd
ΔT = 5.0 K/km	12	$3.2\cdot10^{-8}$	$1.8\cdot10^{-4}$	$1.0\cdot10^{-7}$	$5.6\cdot10^{-4}$	$1.8\cdot10^{-7}$	$1.0\cdot10^{-3}$
ΔT = 7.5 K/km	8	$1.8\cdot10^{-7}$	$1.8\cdot10^{-3}$	$1.8\cdot10^{-7}$	$5.6\cdot10^{-3}$	$5.6\cdot10^{-7}$	$1.0\cdot10^{-2}$
ΔT = 10.0 K/km	6	$3.2\cdot10^{-7}$	$5.6\cdot10^{-3}$	$5.6\cdot10^{-7}$	$1.8\cdot10^{-2}$	$1.0\cdot10^{-6}$	$3.2\cdot10^{-2}$
ΔT = 12.5 K/km	5	$5.6\cdot10^{-7}$	$1.0\cdot10^{-2}$	$1.0\cdot10^{-6}$	$3.2\cdot10^{-2}$	$1.8\cdot10^{-6}$	$5.6\cdot10^{-2}$
ΔT = 15.0 K/km	4	$5.6\cdot10^{-7}$	$1.8\cdot10^{-2}$	$1.0\cdot10^{-6}$	$5.6\cdot10^{-2}$	$1.8\cdot10^{-6}$	$1.0\cdot10^{-1}$

The relationship between the amount of water and the fundamental mode of Schumann resonance for the low surface rock porosity and pores filled partially with water (50%) is presented in Figure 58. To establish whether on the basis of SR measurements, it is possible to distinguish between the situations with and without water under the Martian surface, I compared those results with the value calculated in the Dry model. This model is characterized by the high thermal gradient, thus the fundamental frequency in this case is much higher than for the models with lower gradients. For example, ELF waves would penetrate into the Martian mantle if the Mars subsurface was described by the thermal gradient of 5 K/km and rocks without water. Since the peridotite mantle at a given temperature is less conductive than the basaltic crust (see relation (3.1)), the 10^{-4} S/m conductivity value would not be reached to the depth of 150 km. In such a situation, the first mode frequency would be as low as 5.1 Hz.

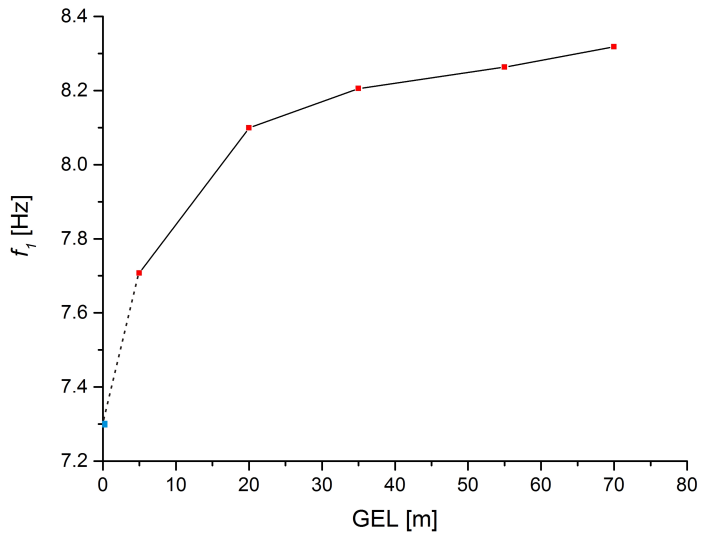

Figure 58. The relationship between the inventory of the underground water and the first mode of Schumann resonance frequency for the models with various thermal gradients, the low surface porosity (φ_0 = 0.20), and the pores filled by water in 50%. The blue dot indicates a value for the Dry model with 15 K/km temperature gradient.

Figure 58 displays that the first Schumann resonance frequency depends on the amount of underground water. When there is no water on Mars, the frequency is low, but even small amount of water can significantly increase its value. For higher amounts of water, this frequency steady approaches the value of the ideal ground case, ca. 8.5 Hz.

Water-sensitive magnetotelluric instruments, which have been proposed for the future Martian missions [*Delory et al.*, 2007] as well as an active electromagnetic sounder [*Grimm et al.*, 2009] enable to investigate regional properties of the surface and subsurface of the planet. The presented methodology is also very sensitive to any presence of water and is capable of studying the entire planet.

If it was possible to place three or more stations on the Martian surface, the better resolution of the presented methodology would allow studying the location of water reservoirs on the planet.

6 Conclusions

In this study, I showed that the Schumann resonance parameters depend significantly on the electrical properties of the Martian ground, and that it is possible to study the subsurface of Mars using a single Martian ELF station.

In Chapter 2 and 3, I described and modeled, on the basis of the actual knowledge of the Martian environment, the factors that are important for the SR studies, such as electrical discharges, atmospheric electrical properties, magnetic fields, and subsurface ground structure. In Chapter 3, I developed the analytical method in order to study ELF propagation in the cavities made of multi-layered infinite-conductivity grounds. In Chapter 4, having employed this methodology, I found that the Martian ground has a very important influence on the SR parameters. In Chapter 5, I indicated that it is possible to manufacture an ELF station enabling detection of SR from the Martian surface.

ELF propagation issues are related to several aspects of the Martian environment, such as:

- atmospheric composition and structure, its global circulation, solar and cosmic radiation, and changes in the orbital parameters, which influence the atmospheric and hydrospheric conditions, and in turn the planetary waveguide;
- surface morphology and ground properties, which determine the shape of the planetary cavity and influence on the ELF propagation parameters;
- character of low-frequency EM sources, which are necessary for the global electric circuit existence.

The ionosphere is affected by periodical variations associated with solar activity, and occasional phenomena, such as higher flux of meteoroids, which have an impact on Schumann resonance. However, regardless of the ionospheric conductivity profiles, which will certainly be developed in the future, due to *in situ* measurements, the factors associated with the ground cannot be disregarded in any model of the Martian resonant cavity. The results obtained from the various ionospheric models (Table 11) display that the differences in the conductivity profiles of the atmosphere will probably have smaller impact on the ELF propagation parameters than the differences related to the presence or absence of liquid water within the Martian ground. The influence of such atmospheric events, which lead to an increase in the atmospheric conductivity, results in the increase of the SR parameters, whereas the ground reduces their values, and the extent of this reduction will depend on the presence of liquid water under the Martian surface. The planned *in situ* measurements on Mars will take into account the electrical properties of the planet as well as the lithospheric heat flow. This will allow estimating more precise models of the Martian ground and their influence on ELF propagation.

Only in cases of a high-conductivity planetary surface, like on Earth, the ground has very little influence on the SR parameters. However, even for conductivities slightly lower than 10^{-4} S/m, the SR frequencies are reduced by more than 10%. We do not know the exact value of the Martian surface conductivity, however, for the value of ca. 10^{-7} S/m, the SR frequencies reach the lowest values. If the models with liquid water under the Martian surface are valid, the presence of such underground aquifers will influence the cavity properties on a global scale, and result in higher SR frequencies and amplitudes.

Sources of ELF waves are probably present on Mars, and the proposed ELF station enables detection of Schumann resonance even if the electrical discharge intensity is one order of magnitude weaker than that observed on Earth. If Schumann resonance is present on Mars, it will probably be subject to seasonal variations. It is even possible that this phenomenon exists only in certain periods.

Schumann resonace measurements would facilitate further study of the atmosphere and lithosphere of Mars. They would simultaneously confirm the existence of the global electrical circuit.

The physical phenomenon is a manifestation of some processes in some environment. Processes based on the laws of physics are probably everywhere the same and consequently can be studied by analogy. Although the environment is also made as a result of the physical processes, their multiplicity and complexity as well as our lack of knowledge of the initial conditions, makes different environments difficult to compare. The number of unexpected discoveries, made during exploration of Mars, confirms that statement. With regard to the study of other worlds, we cannot act under the influence of "automaticity". Using the analytical approach, we can study the influence of various ground layers on the SR parameters. Knowing this relationship, it should be possible to estimate approximated properties of the Martian ground. Yet, as we measure the described phenomenon solely on Earth, on Mars, some physical processes or environmental properties, which we have not predicted nor expected, may affect the acquired ELF measurements. However, any observed ELF signals in the Martian cavity will indicate the existence of ELF sources. In addition, if the measured parameters were much lower than those estimated on the basis of the exact profiles of the atmospheric conductivity, then we would be able to say that there is no liquid water in the subsurface down to several kilometers.

The presented methodology may be employed also to study other bodies in the Solar System, having a planetary cavity. Although Schumann resonance was discovered more than 60 years ago, there still remains a number of unresolved issues, and certainly, research performed on other planets will help us to achieve a more complete understanding of this phenomenon.

List of Figures

List of Tables

References

1. Acuna, M. H., J. E. P. Connerney, N. F. Ness, R. P. Lin, D. Mitchell, C. W. Carlson, J. McFadden, K. A. Anderson, H. Reme, C. Mazelle, D. Vignes, P. Wasilewski, P. Cloutier (1999), Global Distribution of Crustal Magnetization Discovered by the Mars Global Surveyor MAG/ER Experiment, *Science,* 284, 790-793.

2. Acuna, M. H., J. E. P. Connerney, P. Wasilewski, R. P. Lin, D. Mitchell, K. A. Anderson, C., W. Carlson, J. McFadden, H. Rème, C. Mazelle, D. Vignes, S. J. Bauer, P. Cloutier, N. F. Ness. (2001), Magnetic field of Mars: Summary of results from the aerobraking and mapping orbits*, J. Geophys. Res.*, 106(E10), 23403–23417, doi:10.1029/2000JE001404.

3. Allen, C. C., K. M. Jager, R. V. Morris, D. J. Lindstrom, M. M. Lindtsrom, and J. P. Lockwood (1998), Martian soil simulant available for scientific, educational study, *Eos Trans. AGU*, 79(34), 405–409, doi:10.1029/98EO00309.

4. Allen, C. C., D. Z. Oehler, G. Etiope, P. Van Rensbergen, C. Baciu, A. Feyzullayev, G. Martinelli, K. Tanaka, and D. Van Rooij (2013), Fluid expulsion in terrestrial sedimentary basins: A process providing potential analogs for giant polygons and mounds in the martian lowlands: *Icarus*, v. 224, p. 424–432.

5. Almeida, M. P., E. J. R. Parteli, J. S. Andrade, H. J. Herrmann (2008), Giant saltation on Mars Proc. *Natl. Acad. Sci*., 105, 6222-6.

6. Alperovich, L. S., E. N. Fedorov (2007), *Hydromagnetic Waves in the Magnetosphere and the Ionosphere*, Astrophysics and Space Science Library, Springer, pp. 426.

7. Anderson, M. M., A. P. V. Siemion, W. C. Barrot, G. C. Bower, G.T. Delory, I. De Pater, D. Werthimer (2012), The allen telescope array search for electrostatic discharges on mars, *The Astrophsical Journal*, 744, 15, 1-13.

8. Angulo-Sherman, A. and H. Mercado Uribe (2011), Dielectric spectroscopy of water at low frequencies: The existence of an isopermitive point, *Chemical Physics Letters*, Vol. 503, Issue 4, p. 327-330.

9. Aplin K. L. (2006), Atmospheric Electrification In The Solar System, *Surveys in Geophysics*, 27, 63–108.

10. Aplin K. L., R. G. Harrison, M. J. Rycroft (2008), Investigating Earth's Atmospheric Electricity: a Role Model for Planetary Studies, *Space Sci. Rev.*, 137, 11–27.

11. Aplin, K. L., T.Goodman, K. L. Herpoldt, C. J. Davis (2012), Laboratory analogues of Martian electrostatic discharges, *Planetary and Space Science,* 69, 100–104.

12. Appleton, E. V., and M. A. F. Barnett (1925), On some direct evidence for downward atmospheric reflection of electric rays, *Proc. R. Soc. London, Ser. A*, 109, 621–641.

13. Arkani-Hamed, J., P. Olson (2010), Giant impact stratification of the Martian core, *Geophysical Research Letters*, Vol. 37, L02201, doi:10.1029/2009GL041417.

14. Atreya, S. K., Ah-San Wong, Nilton O. Renno, William M. Farrell, Gregory T. Delory, Davis D. Sentman, Steven A. Cummer, John R. Marshall, Scot C. R. Rafkin, and David C. Catling (2006), Oxidant enhancement in martian dust devils and storms: implications for life and habitability, *Astrobiology*, 6(3), 439-450, doi:10.1089.

15. Baker, W. G., D. F. Martyn (1953), Electric Currents in the Ionosphere. I. The Conductivity, *Philosophical Transactions of the Royal Society of London. Series A,* Vol. 246, No. 913, 281-294.

16. Balser M. and C. Wagner (1960), Observations of Earth–ionosphere cavity resonances, *Nature*, 188, 4751, 638–641.

17. Bandfield, J. L. (2002), Global mineral distributions on Mars, *J. Geophys. Res*. 107, doi:10.1029/2001JE001510.

18. Bandfield, J. L., V. E. Hamilton, and P. R. Christensen (2000), A global view of Martian surface compositions from MGS-TES, *Science*, 287(5458), pp. 1626–1630.

19. Banks, P. M., and G. Kockarts, (1973), *Aeronomy* (*Part A*)*,* Academic, San Diego, Calif., pp. 355.

20. Barlow, N. G. (2008), *Mars. An Introduction to its Interior, Surface and Atmosphere,* Cambridge University Press, UK, pp. 264.

21. Basu, S., M. I. Richardson, R. J. Wilson (2004), Simulation of the martian dust cycle with the DFDL Mars GCM, *Journal of Geophysical Research*, 109, E11006, doi:10.1029/2004JE002243.

22. Bazilevskaya, G. A., I. G. Usoskin, E. O. Flückiger, R. G. Harrison, L. Desorgher, R. Bütikofer, M. B. Krainev, V. S. Makhmutov, Y. I. Stozhkov, A. K. Svirzhevskaya, N. S. Svirzhevsky, G. A. Kovaltsov (2008), Cosmic Ray Induced Ion Production in the Atmosphere, *Space Sci. Rev*., 137, 149–173.

23. Belyaev, P. P., S. V Polyakov, V. O. Rapoport, V. Yu Trakhtengerts (1990), The ionospheric Alfven resonator, *Journal of Atmospheric and Terrestrial Physics*, Volume 52, Issue 9, 781-788.

24. Bem, Daniel Józef (1973), *Anteny i rozchodzenie się fal radiowych*, Wydawnictwa Naukowo-Techniczne, Warszawa, pp.475.

25. Bertaux, J. L., F. Leblanc, O. Witasse, E. Quemerais, J. Lilensten, S.A. Stern, B. Sandel, O. Korablev (2005), Discovery of an aurora on Mars, *Nature,* 435, 790–794.

26. Berthelier, J. J., R. Grard, H. Laakso, M. Parrot (2000), ARES, atmospheric relaxation and electric field sensor, the electric field experiment on NETLANDER, *Planetary and Space Sci*., 48, 1193-1200, doi:10.1016/S0032-0633(00)00103-3.

27. Bertka, C. M., and Y. Fei (1998), Density profile of an SNC model Martian interior and the moment-of-inertia factor of Mars, *Earth and Planetary Science Letters*, 157, 79-88, doi: 10.1016/S0012-821X(98)00030-2.

28. Besser, B. P., (2007), Synopsis of the historical development of Schumann resonances, *Radio Sci.,* 42, RS2S02, doi:10.1029/2006RS003495.

29. Bibring, J. P. et al (2006), Global mineralogical and aqueous Mars history derived from OMEGA/Mars Express data, *Science*, 312, 400-404.

30. Blamont, J. E. and E. Chassefiere (1993), First detection of ozone in the middle atmosphere of Mars from solar occultation measurements, *Icarus*, 104, 324-336.

31. Bliokh, P. V., A. P. Nickolaenko, and Y. F. Fillippov (1980), *Schumann Resonances in the Earth-Ionosphere Cavity*, *IEE Electromagn. Wave Ser*., vol. 9, Peter Peregrinus, pp. 166.

32. Bougher, S., S. Engel, R. G. Roble, B. Foster (1999), Comparative terrestrial planet thermospheres, 2. Solar cycle variation of global structure and winds at equinox. *J. Geophys. Res.* 104, 16591–16611.

33. Bougher, S. W., T. E. Cravens, J. Grebowsky, J. Luhmann (2014), The Aeronomy of Mars: Characterization by MAVEN of the Upper Atmosphere Reservoir That Regulates Volatile Escape, *Space Science Reviews*, doi:10.1007/s11214-014-0053-7.

34. Boynton, W. V., *et al*. (2002), Surface of Mars: Evidence for Subsurface Ice Deposits, *Science*, 297, 81–85.

35. Brain, D. A., F. Bagenal, M. H. Acuna and J. E. P. Connerney (2003), Martian magnetic morphology: Contributions from the solar wind and crust, *Journal of Geophysical Research*, 108, No. A12, 1424.

36. Brain, D. A., J. S. Halekas, L. M. Peticolas, R. P. Lin, J. G. Luhmann, D. L. Mitchell, G. T. Delory, S. W. Bougher, M. H. Acuna, and H. Reme (2006), On the origin of aurorae on Mars, *Geophysical Research Letters*, 33, L01201, doi:10.1029/2005GL024782.

37. Brain, D. A., R. J. Lillis, D. L. Mitchell, J. S. Halekas, and R. P. Lin (2007), Electron pitch angle distributions as indicators of magnetic field topology near Mars, *Journal of Geophysical Research*, 112, A09201, doi:10.1029/2007JA012435.

38. Breuer, D., Dave A. Yuene, T. $pohn, S. Zhang (1998), Three dimensional models of Martian mantle convect ion with phase transit ions, *Geophysical Research Letters*, vol. 25, no. 3, pages 229-232.

39. Breuer, D., and T. Spohn (2003), Early plate tectonics versus single-plate tectonics on Mars: Evidence from magnetic field history and crust evolution, *J. Geophys. Res*., 108(E7), 5072, doi:10.1029/2002JE001999.

40. Bruckner, J., G. Dreibus, R. Gellert, S. W. Squyres, H. Wänke, A. Yen, and J. Zipfel (2008), Mars Exploration Rovers: chemical composition by the APXS, [in]: *The Martian Surface - Composition, Mineralogy, and Physical Properties*, (eds.) J. Bell, III, Cambridge University Press, Cambridge, pp. 58-101.

41. Cabrol, N., and E. Grin (2010), *Lakes on Mars*, Elsevier, pp. 410.

42. Cahoy, K. L., D. P. Hinson, and G. L. Tyler (2006), Radio science measurements of atmospheric refractivity with Mars Global Surveyor, *J. Geophys. Res*., 111, E05003, doi:10.1029/2005JE002634.

43. Campbell, W. H. (2003), *Introduction to Geomagnetic Fields*, Cambridge University Press, New York, pp. 337.

44. Cantor, B. A., P. B. James, M. Caplinger, and M. J. Wolff (2001), Martian dust storms: 1999 Mars Orbiter Camera observations, *J. Geophys. Res*., 106(E10), 23653–23687, doi:10.1029/2000JE001310.

45. Cantor, B., M. Malin, and K. S. Edgett (2002), Multiyear Mars Orbiter Camera (MOC) observations of repeated Martian weather phenomena during the northern summer season, *J. Geophys. Res*., 107(E3), doi:10.1029/2001JE001588.

46. Cantor, B. A., K. M. Kanak, and K. S. Edgett (2006), Mars Orbiter Camera observations of Martian dust devils and their tracks (September 1997 to January 2006) and evaluation of theoretical vortex models, *J. Geophys. Res*., 111, E12002, doi:10.1029/2006JE002700.

47. Carr, M. H., (2008), *The Surface of Mars*, Cambridge University Press, pp. 322.

48. Chapman, F. W. and D. L. Jones (1964), Observation of earth-ionosphere cavity resonances and their interpretation in terms of a two-layer ionosphere model, *Radio Sci. J. Res. NBS* 68D, 11, 1177-1185.

49. Chassefiere, F., F. Le Blanc (2004), Mars atmospheric escape and evolution; interaction with the solar wind, *Planetary and Space Science*, Volume 52, Issue 11, p. 1039-1058.

50. Chelidze, T. L., Y. Gueguen, and C. Ruffet (1999), Electrical spectroscopy of porous rocks: a review-II. Experimental results and interpretation, *Geophysical Journal International*, Volume 137, Issue 1, pp. 16-34.

51. Christian, H. J., Richard J. Blakeslee, Dennis J. Boccippio, William L. Boeck, Dennis E. Buechler, Kevin T. Driscoll, Steven J. Goodman, John M. Hall, William J. Koshak, Douglas M. Mach, and Michael F. Stewart (2003), Global frequency and distribution of lightning as observed from space by the Optical Transient Detector, *Journal of Geophysical Research*, Vol. 108, No. D1, 400.

52. Clancy, R. T., M. J. Wolff, and P. R. Christensen (2003), Mars aerosol studies with the MGS TES emission phase function observations: Optical depths, particle sizes, and ice cloud types versus latitude and solar longitude, *J. Geophys. Res*., 108, doi:10.1029/2003JE002058.

53. Clancy, R. Todd, Michael J. Wolff, Barbara A. Whitney, Bruce A. Cantor, Michael D. Smith, Timothy H. McConnochie (2010), Extension of atmospheric dust loading to high altitudes during the 2001 Mars dust storm: MGS TES limb observations, *Icarus*, Volume 207, Issue 1, pp. 98-109.

54. Clifford, S. M. (1993), A model for the hydrologic and climatic behavior of water on Mars*, J. Geophys. Res.,* 98 (E6), 10973–11016, doi:10.1029/93JE00225.

55. Clifford, S. M., T.J. Parker (2001), The evolution of the martian hydrosphere: implications for the fate of a primordial ocean and the current state of the northern plains, *Icarus,* 154, 40–79.

56. Clifford, S. M., J. Lasue, E. Heggy, J. Boisson, P. McGovern, M. D. Max (2010), The Depth of the Martian Cryosphere: Revised Estimates and Implications for the Existence and Detection of Subpermafrost Groundwater, *J. Geophys. Res.*, doi:10.1029/2009JE003462.

57. Cole, Jr., R. K. (1965), The Schumann Resonances, *Radio Science Journal of Research,* 69D, No. 10, 1345-1349.

58. Connerney, J. E. P., M. H. Acuña, P. J. Wasilewski, G, Kletetschka, N. F. Ness, H. Reme, R. P. Lin, and D. L. Mitchell (2001), The Global Magnetic Field of Mars and Implications for Crustal Evolution, *Geophysical Research Letters*, Vol. 28, No. 21, 4015-4018.

59. Connerney, J. E. P., M. H. Acuna, N. F. Ness, T. Spohn, G. Schubert (2004), Mars crustal magnetism, *Space Science Reviews*, 111, 1-32.

60. Cooke, M., Islam, F., and G. McGill (2011), Basement controls on the scale of giant polygons in Utopia Planitia, Mars: *Journal of Geophysical Research–Planets*, v. 116, E09003, doi: 10.1029/2011JE003812.

61. Craddock, R. A., A. D. Howard (2002), The case for rainfall on a warm wet early Mars, *J. Geophys. Res*., 107, doi:10.1029/2001JE001505.

62. Crozier, W. D. (1964), The electric field of a New Mexico dust devil, *J. Geophys. Res.* 69, 5427–5429.

63. Cummer, S. A. (1997), *Lightning and ionospheric remote sensing using VLF/ELF radio atmospherics*, PHD Thesis, Stanford University, pp. 137.

64. Cummer, S. A. (2000), Current moment in sprite-producing lightning, *Journal of Atmospheric and Solar-Terrestrial Physics*, Volume 65, Issue 5, Pages 499-508.

65. Cummer, S. A., W. M. Farrell (1999), Radio atmospheric propagation on Mars and potential remote sensing application, *J. Geophys. Res*.,104, E6, 14149-14157, doi:10.1029/1998JE000622.

66. Dartnell, L. R., L. Desorgher, J. M. Ward, and A. J. Coates (2007), Martian sub-surface ionising radiation: Biosignatures and geology, *Biogeosciences*, 4(4), 545–558.

67. Delory, Gregory T. (2010), Electrical Phenomena on the Moon and Mars, *Proc. ESA Annual Meeting on Electrostatics*, Paper A1.

68. Delory, G., *et al*. (2006), Oxidant enhancement in martian dust devils and storms: Storm electric fields and electron dissociative attachment, *Astrobiology*, 6(3), 451– 462.

69. Delory, T. R. E. Grimm, T. Nielsen, and W. M. Farrell (2007), Prospecting For Subsurface Liquid Water Using Magnetotellurics On Mars, *LPI Contribution*, No. 1353, 3293.

70. Deprez, G., F. Montmessin, O. Witasse, L. Lapauw, F. Vivat, S. Abbaki, D. Moirin, R. Trautner, R. Hassen-Khodja, E. d'Almeida, L. Charnenal, J-J. Berthelier, F. Esposito, S. Debei, S.Rafkin, E.Barth, P. Granier (2014), Micro-ARES, an electric-field sensor for exomars 2016: Electric fields modelling, sensitivity evaluations and end-to-end tests*, LPI Contributions*, No. 1791, 1290.

71. Desch, S. J., J. N. Cuzzi (2000), The Generation of Lightning in the Solar Nebula, *Icarus*, 143, 87–105.

72. Dreibus, G. and H. Wanke (1985), Mars: A volatile rich planet, *Meteoritics*, 20, 367-382.

73. Duru, F., D. A. Gurnett, R. A. Frahm, J. D. Winningham, D. D. Morgan, and G. G. Howes (2009), Steep, transient density gradients in the Martian ionosphere similar to the ionopause at Venus, *Journal of Geophysical Research*, 114, A12310, doi:10.1029/2009JA014711.

74. Dyrda, M., A. Kulak, J. Mlynarczyk, M. Ostrowski, J. Kubisz, A. Michalec, and Z. Nieckarz (2014), Application of the Schumann resonance spectral decomposition in characterizing the main African thunderstorm center, *J. Geophys. Res. Atmos.*, 119, 13,338–13,349, doi:10.1002/2014JD022613.

75. Eden, H. F., and B. Vonnegut (1973), Electrical breakdown caused by dust motion in low-pressure atmosphere: Consideration of Mars, *Science*, 180, 962-963.

76. Ellehoj, M. D., *et al*. (2010), Convective vortices and dust devils at the Phoenix Mars mission landing site, *J. Geophys. Res*., 115, E00E16, doi:10.1029/2009JE003413.

77. Ette, A. I. I. (1971), The effect of the Harmattan dust on atmospheric electric parameters, *J. Atmos Terr.Phys*., 33, 295-300.

78. Evans, S., (1965), Dielectric properties of ice and snow-a review, *Journal of Glaciology*, vol.5, Issue 42, pp.773-792.

79. Farrell, W. M. and M. D. Desch (2001), Is there a Martian atmospheric electric circuit?, *J. Geophys. Res*., 106 (E4): doi:10.1029/2000JE001271.

80. Farrell, W. M., M. L. Kaiser, M. D. Desch, J. G. Houser, and S. A. Cummer (1999), Detecting electrical activity from Martian dust storms, *Journal of Geophysical Research*, Vol. 104, No. 2, Pages 3795–3801.

81. Farrell, W. M., G. T. Delory, S. A. Cummer, and J. Marshall (2003), A simple electrodynamic model of a dust devil, *Geophys. Res. Lett*., 30(20), 2050, doi:10.1029/2003GL017606.

82. Farrell, W. M., *et al*. (2004), Electric and magnetic signatures of dust devils from the 2000–2001 MATADOR desert tests, *J. Geophys. Res*., 109, E03004, doi:10.1029/2003JE002088.

83. Farrell, W. M., N. O. Renno, G. Delory, S. Cummer, and J. R. Marshall (2006), Integration of electrostatic and fluid dynamics within a dust devil, *J. Geophys. Res*., 111, E01006, doi:10.1029/2005JE002527.

84. Faure, G., T. M. Mensing (2007), *Introduction to Planetary Science*. *The Geological Perspective*, Springer, The Netherlands, pp. 526.

85. Fei Y., C. Bertka (2005), The interior of Mars, *Science*, Vol. 308 no. 5725 pp. 1120-1121, doi: 10.1126.

86. Feldman, W. C., et al. (2004), Global distribution of near-surface hydrogen on Mars, *J. Geophys. Res*., 109, E09006, doi:10.1029/2003JE002160.

87. Feldman, W. C., A. Pathare, S. Maurice, T. H. Prettyman, D. J. Lawrence, R. E. Milliken, and B. J. Travis (2011), Mars Odyssey neutron data: 2. Search for buried excess water ice deposits at non-polar latitudes of Mars, *J. Geophys. Res*., 116, E11009.

88. Ferguson, D. C., J. C. Kolecki, M. W. Siebert, D. M. Wilt, and J. R. Matijevic (1999), Evidence for Martian electrostatic charging and abrasive wheel wear from the Wheel Abrasion Experiment on the Pathfinder Sojourner rover, *J. Geophys. Res*., 104(E4), 8747–8759, doi:10.1029/98JE02249.

89. Ferri, F., P. H. Smith, M. Lemmon, and N. O. Renno (2003), Dust devils as observed by Mars Pathfinder, *J. Geophys. Res*., 108(E12), 5133, doi:10.1029/2000JE001421.

90. Feynman, R. P., R. B. Leighton, M. Sands, (2005), *Feynmana wykłady z fizyki.* Vol II, Part II, Państwowe Wydawnictwo Naukowe, Warszawa, pp. 451.

91. Fillingim, M. O., L. M. Peticolas, R. J. Lillis, D. A. Brain, J. S. Halekas, D. Lummerzheim, S.W. Bougher (2010), Localized ionization patches in the nighttime ionosphere of Mars and their electrodynamic consequences, *Icarus*, 206, 1, 112-119.

92. Fisher, J. A., M. I. Richardson, C. E. Newman, M. A. Szwast, C. Graf, S. Basu, S. P. Ewald, A. D. Toigo, and R. J. Wilson (2005), A survey of Martian dust devil activity using Mars Global Surveyor Mars Orbiter Camera images, *J. Geophys. Res*., 110, E03004, doi:10.1029/2003JE002165.

93. Formisano, V., S. K. Atreya, T. Encrenaz, N. Ignatiev, M. Giuranna, (2004), Detection of methane in the atmosphere of Mars. *Science*, 306, 1758–1761.

94. Forward, K. M., D. J. Lacks, and R. M. Sankaran (2009), Particle-size dependent bipolar charging of Martian regolith simulant, *Geophys. Res. Lett*., 36, L13201, doi:10.1029/2009GL038589.

95. Frank-Kamieniecki, D. A. (1968), *Plazma czwarty stan materii*, PWN, Warszawa, pp. 188.

96. Freier, G .D. (1960), The electric field of a large dust devil, *J. Geophys Res*., 65, 3504.

97. Gaidos, E. G. Marion (2003), Geologic and geochemical legacy of a cold early Mars, *J. Geophys. Res*., 108, doi:10.1029/2002JE002000.

98. Galejs, J. (1965), On the terrestrial propagation on ELF and VLF waves in the presence of the radial magnetic fields, *Radio Sci. J. Res*. *NBS* 69D, 5, 705-720.

99. Galejs, J. (1972), *Terrestrial Propagation of Long Electromagnetic Waves*, Pergamon, New York, pp. 362.

100. Gilbert, J. S., S. J. Lane, R. S. J. Sparks, and T. Koyaguchi (1991), Charge measurements on particle fallout from a volcanic plume, *Nature*, 349, 598-600.

101. Glover, P. W. J. (2010), A generalized Archie's law for n phases, *Geophysics*, 75 (6), 85-91.

102. Goebel, D. M. and I. Katz (2008), Basic Plasma Physics, [in:] *Fundamentals of Electric Propulsion: Ion and Hall Thrusters*, John Wiley & Sons, Inc., Hoboken, NJ, USA, doi: 10.1002/9780470436448.ch3

103. Goetz, W., *et al*. (2008), Search for magnetic minerals in Martian rocks: Overview of the Rock Abrasion Tool (RAT) magnet investigation on Spirit and Opportunity, *J. Geophys. Res*., 113, E05S90, doi:10.1029/2006JE002819.

104. Golombek, M. P., N. T. Bridges (2000), Erosion rates on Mars and implications for climate change: constraints from the Pathfinder landing site, *J. Geophys. Res*., 105, 1841-1853.
105. Grard, R. (1995), Solar Photon Interaction with the Martian Surface and Related Electrical and Chemical Phenomena, *Icarus*, 114, 130-138.

106. Greeley, R., J. D. Iversen (1985), *Wind as a geological process on Earth, Mars, Venus and Titan*, Cambridge University Press, New York, pp. 333.

107. Greeley, R., D. G. Blumberg, and S. H. Williams (1996), Field measurements of the flux and speed of wind-blown sand, *Sedimentology* 43, 41.

108. Greeley, R., et al. (2006), Active dust devils in Gusev crater, Mars: Observations from the Mars Exploration Rover Spirit, *J. Geophys. Res*., 111 , E12S09, doi:10.1029/2006JE002743.

109. Greifinger, C., and P. Greifinger (1978), Approximate method for determining ELF eigenvalues in the Earth-ionosphere waveguide, *Radio Sci.*, 13, 831, doi:10.1029/RS013i005p00831.

110. Greifinger, C., and P. Greifinger (1986), Noniterative procedure for calculating ELF mode constants in the anisotropic earth-ionosphere weaveguide, *Radio Science,* vol. 21, No. 6, 981-990.

111. Greifinger, P. S., V. C. Mushtak, and E. R. Williams (2007), On modeling the lower characteristic ELF altitude from aeronomical data, *Radio Science,* 42, RS2S12.

112. Griffiths, D. J. (2005), *Podstawy Elektrodynamiki*, Wydawnictwo Naukowe PWN, Warszawa, pp. 602.

113. Grimalsky, V., S. Koshevaya, A. Kotsarenko, and R. Perez Enriquez (2005), Penetration of the electric and magnetic field components of Schumann resonances into the ionosphere, *Ann. Geophys*., 23, 2559–2564.

114. Grimm, R. E. (2002), Low-frequency electromagnetic exploration for groundwater on Mars, *J. Geophys. Res*., 107, 0, doi:10.1029/2001JE001504.

115. Grimm, R. E., D. E. Stillman, S. F. Dec, & M. A. Bullock (2008), Low-frequency electrical properties of polycrystalline saline ice and salt hydrates. *J. Phys. Chem.*, B 112, 15382–15390.

116. Grimm, R. E., Barry Berdanier, Robert Warden, James Harrer, Raymond Demara, James Pfeiffer, Richard Blohm (2009), A time–domain electromagnetic sounder for detection and characterization of groundwater on Mars, *Planetary and Space Science*, Volume 57, Issue 11, pp 1268-1281.

117. Gurevich, A. V., K.P. Zybin (2004), High energy cosmic ray particles and the most powerful discharges in thunderstorm atmosphere, *Physics Letters A,* 329, 341–347.

118. Gurevich, A. V., and K. P. Zybin (2005), Runaway breakdown and the mysteries of lightning, *Phys. Today*, 58(5), 37–43, doi:10.1063/1.1995746.

119. Gurnett, D. A. (1998), Principles of Space Plasma Wave Instrument Design, [in:] *Measurement Techniques in Space Plasmas Fields* (eds R. F. Pfaff, J. E. Borovsky and D. T. Young), American Geophysical Union, Washington, D. C., doi: 10.1002/9781118664391.ch14.

120. Gurnett, D. A., R. L. Huff, D. D. Morgan, A. M. Persoon, T. F. Averkamp, D. L. Kirchner, F. Duru, F. Akalin, A. J. Kopf, E. Nielsen, A. Safaeinili, J. J. Plaut, G. Picardi (2008), An overview of radar soundings of the martian ionosphere from the Mars Express spacecraft, *Advances in Space Research*, 41, 9, 1335-1346.

121. Gurnett, D. A., D. D. Morgan, L. J. Granroth, B. A. Cantor, W. M. Farrell, and J. R. Espley (2010), Non-detection of impulsive radio signals from lightning in Martian dust storms using the radar receiver on the Mars Express spacecraft, *Geophys. Res. Lett*., 37(17), doi:10.1029/2010GL044368.

122. Guzewich, S. D., E. R. Talaat, and D. W. Waugh (2012), Observations of planetary waves and nonmigrating tides by the Mars Climate Sounder, *J. Geophys. Res*., 117, E03010, doi:10.1029/2011JE003924.

123. Guzewich, S. D., E. R. Talaat, A. D. Toigo, D. W. Waugh, and T. H. McConnochie (2013), High-altitude dust layers on Mars: Observations with the Thermal Emission Spectrometer, *J. Geophys. Res. Planets*, 118, 1177-1194.

124. Haider, S. A., V. Singh, V. R. Choksi, W. C. Maguire, and M. I. Verigin (2007), Calculated densities of H3O+(H2O)n, NO2 (H2O)n, CO3 (H2O)n and electron in the nighttime ionosphere of Mars: Impact of solar wind electron and galactic cosmic rays, *J. Geophys. Res.,* 112, A12309, doi:10.1029/2007JA012530.

125. Haider, S. A., V. Sheel, V. Singh, W. C. Maguire, and G. J. Molina-Cuberos (2008), Model calculation of production rates, ion and electron densities in the evening troposphere of Mars at latitudes 67°N and 62°S: Seasonal variability, *J. Geophys. Res*., 113, A08320, doi:10.1029/2007JA012980.

126. Haider, S. A., V. Sheel, M. D. Smith, W. C. Maguire, and G. J. Molina Cuberos (2009), Effect of dust storms on the D region of the Martian ionosphere: Atmospheric electricity, *Journal Of Geophysical Research*, Vol. 115, A12336, doi:10.1029/2010JA016125.

127. Haider, S. A., V. Sheel, M. D. Smith, W. C. Maguire, and G. J. Molina-Cuberos (2010), Effect of dust storms on the D region of the Martian ionosphere: Atmospheric electricity, *J. Geophys. Res.*, 115, A12336, doi:10.1029/2010JA016125.

128. Haider, S.A., K.K. Mahajan (2014), Lower and Upper Ionosphere of Mars, *Space Sci. Rev.*, 182, 19–84.

129. Hake, R. D., and A. V. Phelps (1967), Momentum-transfer and inelastic-collision cross sections for electrons in 02, CO, and CO2, *Phys. Rev*., 158, 70.

130. Hanson, W. B., S. Sanatani, and D. R. Zuccaro (1977), The Martian ionosphere as observed by the Viking retarding potential analyzers, *J. Geophys. Res*., 82(28), 4351–4363.

131. Harri, A. M., M. Genzer, O. Kemppinen, H. Kahanpää, J. Gomez-Elvira, J. A. Rodriguez-Manfredi, R. Haberle, J. Polkko, W. Schmidt, H. Savijärvi, J. Kauhanen, E. Atlaskin, M. Richardson, T. Siili, M. Paton, M. de la Torre Juarez, C. Newman, S. Rafkin, M. T. Lemmon, M. Mischna, S. Merikallio, H. Haukka, J. Martin-Torres, M. P. Zorzano, V. Peinado, R. Urqui, A. Lapinette, A. Scodary, T. Mäkinen, L. Vazquez, N. Rennó, and the REMS/MSL Science Team (2014), Pressure observations by the Curiosity rover: Initial results, *Journal Of Geophysical Research*: *Planets*, 119, 82–92.

132. Harrison, R. G. (2005), The global atmospheric electrical circuit and climate, *Surveys in Geophysics*, 25, 5-6, 441-484(44).

133. Harrison, R. G., K. L. Aplin, F. Leblanc, Y. Yair (2008), Planetary Atmospheric Electricity*, Space Sci. Rev*. 137, 5-10.

134. Hassler, D. M., Cary Zeitlin, Robert F. Wimmer-Schweingruber, Bent Ehresmann, Scot Rafkin, Jennifer L. Eigenbrode, David E. Brinza, Gerald Weigle, Stephan Böttcher, Eckart Böhm, Soenke Burmeister, Jingnan Guo, Jan

Köhler, Cesar Martin, Guenther Reitz, Francis A. Cucinotta, Myung-Hee Kim, David Grinspoon, Mark A. Bullock, Arik Posner, Javier Gómez-Elvira, Ashwin Vasavada, John P. Grotzinger, MSL Science Team (2014), Mars' Surface Radiation Environment Measured with the Mars Science Laboratory's Curiosity Rover, *Science,* 343, 1244797-1–1244797-6.

135. Heggy, E., P. Paillou, F. Costard, N. Mangold, G. Ruffie, F. Demontoux, G. Grandjean, and J. M. Malezieux (2003), Local geoelectrical models of the Martian subsurface for shallow groundwater detection using sounding radars, *J. Geophys. Res*., 108(E4), 8030, doi:10.1029/2002JE001871.

136. Hinson, D. P., and R. J. Wilson (2004), Temperature inversions, thermal tides, and water ice clouds in the Martian tropics, *J. Geophys. Res*., 109, E01002, doi:10.1029/2003JE002129.

137. Houser, J. G., W. M. Farrell, and S. M. Metzger (2003), ULF and ELF magnetic activity from a terrestrial dust devil, *Geophys. Res. Lett*., 30, 1027, doi:10.1029/2001GL014144.

138. Hurowitz, Joel A., S. M. McLennan (2007), A ~3.5 Ga record of water-limited, acidic weathering conditions on Mars, *Earth and Planetary Science Letters*, Volume 260, Issues 3–4, Pages 432–443.

139. Hviid, S. F., et al. (1997), Magnetic properties experiments on the Mars Pathfinder Lander: Preliminary results, *Science*, 278, 1768–177.

140. Iben, I. E. T., et al. (1996), *Dielectric Properties of Soil: Application to Radio Frequency Ground Heating*, GE Global Research, Report Number 96CRD150, pp. 35.

141. Jackson, J. D. (1999), *Classical Electrodynamics*, John Wiley and Sons, Hoboken, pp. 808.

142. Jeffrey, A. (2003), *Applied partially differential equations*, Elsevier, USA, pp. 394.

143. Jones, D. L. (1970), Electromagnetic radiation from multiple return strokes of lightning, *Atmos. Terr. Phys.*, 32, 1077.

144. Kamra, A. K. (1972), Measurements of the electrical properties of dust storms, *J. Geophys Res*., 77, 5856-5869.

145. Kamra, A. K., M. Ravichandran, (1993), On the Assumption of the Earth's surface as a Perfect conductor in atmospheric electricity, *Journal of Geophysical Research,* 98, D12, 22.875-22.885.

146. Keller, G. V. (1988), Rock and mineral properties, [in:] *Electromagnetic Methods in Applied Geophysics*, vol. 1, *Theory*, edited by M. N. Nabighian, Soc. Explor. Geophys., Tulsa, Okla., pp. 13– 52.

147. Kirillov, V. V. (1993), Parameters of the Earth-ionosphere waveguide at ELF (in Russian), *Probl. Diffr. Wave Propagat*., 25, 35.

148. Kirillov, V. V. (1996), A two-dimensional theory of propagation of ELF electromagnetic waves within the Earth–ionosphere waveguide (in Russian), *Izv. VUZ Radiofis*., 39(9), 1103–1112.

149. Kirillov, V. V., V. N. Kopeykin, V. C. Mushtak (1997), ELF electromagnetic waves within the Earth–ionosphere waveguide, *Geomagnetizm i Aeronomiya*, 37, 114–120 (in Russian).

150. Kliore, A. J., D. L. Cain, G. Fjeldbo, B. L. Seidel, M. J. Sykes, and S. I. Rasool (1972), The atmosphere of Mars from Mariner 9 radio occultation measurements, *Icarus*, 17, 484–516.

151. Kok J. F., N. O. Renno (2006), Enhancement of the emission of mineral dust aerosols by electric forces *Geophys. Res. Lett*. 33, L19s10, doi:10.1029/2006GL026284.

152. Kok, J. F., N. O. Renno (2008), Electrostatics in Wind-Blown Sand, *Physical Review Letters*, 100(1), 014501. doi: 10.1103.

153. Kok, J. F., N. O. Renno (2009), Electrification of wind-blown sand on Mars and its implications for atmospheric chemistry, *Geophys. Res. Lett*., 36, L05202, doi:10.1029/2008GL036691.

154. Konig, H. (1959), Atmospherics geringster Frequenzen (Atmospherics of lowest frequencies), *Z. Angew. Phys*., 11, 264–274.

155. Kopp, E. (1997), On the abundance of metal ions in the lower ionosphere, *J. Geophys. Res*., 102, 9667-9675.

156. Kozakiewicz, J., A. Kulak, J. Mlynarczyk, K. Zietara, J. Kubisz (2014), Investigation of the Martian Environment by ELF Radio Measurements, *LPI Contribution,* No. 1791, p.1122.

157. Kozakiewicz, Joanna, Andrzej Kulak, Janusz Mlynarczyk (2015), Analytical modeling of Schumann resonance and ELF propagation parameters on Mars with a multi-layered ground, *Planetary and Space Science*, doi:10.1016/j.pss.2015.05.019.

158. Kozuchowski, K. (2004), *Meteorologia i klimatologia*, Wydawnictwo Naukowe PWN, Warszawa, pp. 321.
159. Krakowski, M., (1995), *Elektrotechnika Teoretyczna, Obwody Liniowe i Nieliniowe*, Wydawnictwo Naukowe PWN, Warszawa, pp. 699.

160. Krasnopolsky, V. A. (2004), Jean Pierre Maillard, Tobias C. Owen, Detection of methane in the martian atmosphere: evidence for life?, *Icarus*, Volume 172, Issue 2, Pages 537-547.

161. Krasnopolsky, V. A. (2006), A sensitive search for nitric oxide in the lower atmospheres of Venus and Mars: Detection on Venus and upper limit for Mars, *Icarus* 182, 80–91.

162. Krauss, C. E., M. Horanyi, S. Robertson (2006), Modeling the formation of electrostatic discharges on Mars, *J. Geophys. Res*., 111, E02001, doi:10.1029/2004JE002313.

163. Krymskii, A. M., T. K. Breus, N. F. Ness, M. H. Acuña, J. E. P. Connerney, D. H. Crider, D. L. Mitchell, and S. J. Bauer (2002), Structure of the magnetic field fluxes connected with crustal magnetization and topside ionosphere at Mars, *J. Geophys. Res*., 107(A9), 1245.

164. Krymskii, A. M., T. K. Breus, N. F. Ness, D. P. Hinson, D. I. Bojkov (2003), Effect of crustal magnetic fields on the near terminator ionosphere at Mars: comparison of in situ magnetic field measurements with the data of radio science experiments on board Mars Global Surveyor. *J.Geophys. Res*., 108, 1431, doi:10.1029/2002JA009662.

165. Kulak, A. (2010), Czujniki i system do pomiaru naturalnychpól elektromagnetycznych ekstremalnie niskiej częstotliwości na powierzchni Ziemi, *Elektronika* 01, 106-113.

166. Kulak, A., and J. Mlynarczyk (2013*),* ELF Propagation Parameters for the Ground-Ionosphere Waveguide With Finite Ground Conductivity, *IEEE Transactions on Antennas and Propagations*, Vol. 61, No. 4, doi: 10.1109/TAP.2012.2227445.

167. Kułak, A., Z. Nieckarz, and S. Zięba (2010), Analytical description of ELF transients produced by cloud-to-ground lightning discharges, *J. Geophys. Res*., 115, D19104, doi:10.1029/2009JD013033.

168. Kulak, A., J. Mlynarczyk, J. Kozakiewicz (2013), An Analytical Model of ELF Radiowave Propagation in Ground-Ionosphere Waveguides With a Multilayered Ground, *IEEE Transactions on Antennas and Propagations*, Vol. 61, No. 9, 10.1109/TAP.2013.2268244 .

169. Kulak, A., J. Kubisz, S. Klucjasz, A. Michalec, J. Mlynarczyk, Z. Nieckarz, M. Ostrowski, and S. Zieba (2014), Extremely low frequency electromagnetic field measurements at the Hylaty station and methodology of signal analysis, *Radio Sci*., 49, 361–370, doi:10.1002/2014RS005400.

170. Laskar, Jacques, Benjamin Levrard, John F. Mustard (2002), Orbital forcing of the martian polar layered deposits, *Letters of Nature,* 419, 375-377.

171. Lastovickova, M., J. Bochnicek (1992), A Contribution to the Measurement of Frequency Dependence of Electrical Conductivity of Rocks, *Studia Geoph. et Geod*., 36.

172. Leovy, C. (2001), Weather and climate on Mars, *Nature*, 412, 245-249.

173. Li, Q., and W. S. Kiefer (2007), Mantle convection and magma production on present-day Mars: Effects of temperature-dependent rheology, *Geophys. Res. Lett*., 34, L16203, doi:10.1029/2007GL030544.

174. Lillis, R. J., D. A. Brain, S. L. England, P. Withers, M. O. Fillingim, and A. Safaeinili (2010), Total electron content in the Mars ionosphere: Temporal studies and dependence on solar EUV flux, *J. Geophys. Res*., 115, A11314, doi:10.1029/2010JA015698.

175. Lollo, A., P. Withers, K. Fallows, Z. Girazian, M. Matta, P.C. Chamberlin (2012), Numerical simulations of the ionosphere of Mars during a solar flare, *Journal of Geophysical Research,* 117, A05314, doi:10.1029/2011JA017399.

176. Lowrie, W. (2007), *Fundamentals of Geophysics,* Cambridge University Press, UK, pp. 390.

177. Luhmann, J. G., S. A. Ledvina, C.T. Russell (2004), Induced magnetospheres, *Advances in Space Research,* 33, pp. 1905–1912.

178. Lundin, R., D. Winningham, S. Barabash, R. Frahm, M. Holmstrom, J.-A. Sauvaud, A. Fedorov, K. Asamura, A. J. Coates, Y. Soobiah, K. C. Hsieh, M. Grande, H. Koskinen, E. Kallio, J. Kozyra, J. Woch, M. Fraenz, D. Brain, J. Luhmann, S. McKenna-Lawler, R. S. Orsini, P. Brandt, P. Wurz (2006), Plasma Acceleration Above Martian Magnetic Anomalies, *Science,* 311, 980-983.

179. Lysak, R. L. (1993), *Generalized model of the Ionospheric Alfven Resonator*, [in:] *Auroral Plasma Dynamics*, Geophys. Monogr. Ser., vol. 80, AGU, Washington D. C., pp. 121-128.

180. MacElroy, M. B., T. Y. Kong, and V. L. Yung (1977), Photochemistry and evolution of Mars' atmosphere: A Viking perspective, *Geophys. Res*., 82, 4379.

181. Madden, T., and W. Thompson (1965), Low-frequency electromagnetic oscillations of the Earth-ionosphere cavity, *Rev. of Geophys*., 3(2), pp. 211-254.

182. Malin, M. C. K. S. Edgett (2003), Evidence for persistent flow and aqueous sedimentation on early Mars, *Science*, 302, 1931-1934.

183. Martin, L. J., R. W. Zurek (1993), An analysis of the history of dust storm activity on Mars. *J. Geophys. Res*. 98, 3221–3246.

184. McGovern, P. J., S. S. C. Solomon, D. E. Smith, et al (2002), Localized gravity/topography admittance and correlation spectra on Mars: Implications for regional and global evolution, *J. Geophys. Res*, 107, doi:10.1029/2002JE001854.

185. McGovern, P. J., S. C. Solomon, D. E. Smith, M. T. Zuber, M. Simons, M. A. Wieczorek, R. J. Phillips, G. A. Neumann, O. Aharonson, and J. W. Head (2004), Correction to "Localized gravity/topography admittance and correlation spectra on Mars: Implications for regional and global evolution", *J. Geophys. Res.*, 107, E12, 5136, doi:10.1029/2004JE002286.

186. Mellon, M. T. B. M. Jakosky (1995), The distribution and behavior of martian ground ice during past and present epochs, *Journal of Geophysical Research*, 100, 11781-11799.

187. Melnik, O., and M. Parrot (1998), Electrostatic discharge in Martian dust storms, J. *Geophys. Res*., 103(A12), 29107–29117.

188. Melnik, O., and M. Parrot (1999), Propagation of electromagnetic waves through the Martian ionosphere, *Journal of geophysical research*, Vol. 104, No. A6, 12.705-12.714.

189. Mendillo, M., P. Withers, D. Hinson, H. Rishbeth, and B. Reinisch (2006), Effects of solar flares on the ionosphere of Mars, *Science*, 311, 1135–1138, doi:10.1126/science.1122099.

190. Metzger, S. M., J. R. Johnson, J. R. Carr, T. J. Parker, and M. Lemmon (1999), Dust devil vortices seen by the Mars Pathfinder Camera, *Geophys. Res. Lett*., 26, 2781–2784.

191. Michael, M., M. Barani, and S. N. Tripathi (2007), Numerical predictions of aerosol charging and electrical conductivity of the lower atmosphere of Mars, *Geophys. Res. Lett*., 34, L04201, doi:10.1029/2006GL028434.

192. Michael, M., S. N. Tripathi (2008), Effect of charging of aerosols in the lower atmosphere of Mars during the duststorm of 2001, *Planetary and Space Science*, 56, 1696–1702.

193. Michael, M., S. N. Tripathi, and S. K. Mishra (2008), Dust charging and electrical conductivity in the day and nighttime atmosphere of Mars, *J. Geophys. Res.*, 113, E07010, doi:10.1029/2007JE003047.

194. Milankovitch, M. (1930). Mathematische Klimalehre und Astronomische Theorie der Klimaschwankungen, *Handbuch der Klimalogie Band*, 1 Teil A Borntrager, Berlin.

195. Milkovich, S. M., J.W.S. Pratt (2002), Meltback of Hesperian-aged ice rich deposits near the south pole. Evidence for drainage channels ond lakes. *J. Geophys. Res*., 107, doi: 10.1029/2001JE0018-02.

196. Mills, A. A. (1977), Dust clouds and frictional generation of glow discharges on Mars, *Nature*, 268, 614.

197. Mitchell, D. L., R. P. Lin, C. Mazelle, H. Reme,. A. Cloutier, J. E. P. Connerney, H. Acuna, N. F. (2001), Probing Mars' crustal magnetic field and ionosphere with the MGS Electron Reflectometer, *Journal Of Geophysical Research*, 106, No. El0, 23.419-23.427.

198. Molina-Cuberos, G. J., J. J. Lopez-Moreno, R. Rodrigo, H. Lichtenegger, K. Schwingenschuh (2001), A model of the martian ionosphere below 70 km, *Advances in Space Research*, 27, 1801-1806.

199. Molina-Cuberos, G. J., H. Lichtenegger, K. Schwingenschuh, J. J. López-Moreno, and R. Rodrigo (2002), Ion-neutral chemistry model of the lower ionosphere of Mars, *J. Geophys. Res.*, 107(E5), doi:10.1029/2000JE001447.

200. Molina-Cuberos, Gregorio J., Olivier Witasse, Jean-Pierre Lebreton, Rafael Rodrigo, José J. López-Moreno (2003), Meteoric ions in the atmosphere of Mars, *Planetary and Space Science*, 51, 3, 239-249.

201. Molina-Cuberos, G. J., J. A. Morente, B. P. Besser, J. Porti, H. Lichtenegger, K. Schwingenschuh, A. Salinas, and J. Margineda (2006), Schumann resonances as a tool to study the lower ionospheric structure of Mars, *Radio Sci*., 41, RS1003, doi:10.1029/2004RS003187.

202. Molina-Cuberos, J. G., J. J. López-Moreno, F. Arnold (2008), Meteoric Layers in Planetary Atmospheres, *Space Sci Rev.*, 137, 175–191.

203. Montmessin, F., F. Lefèvre (2013), Transport-driven formation of a polar ozone layer on Mars, *Nature Geoscience*, 6, 930–933.

204. Montmessin, F., *et al.* (2006), Subvisible CO2 ice clouds detected in the mesosphere of Mars, *Icarus*, 183, 403–410.

205. Montmessin, F., B. Gondet, J.-P. Bibring, Y. Langevin, P. Drossart, F. Forget, and T. Fouchet (2007), Hyperspectral imaging of convective CO2 ice clouds in the equatorial mesosphere of Mars, *J. Geophys. Res.*, 112, E11S90, doi:10.1029/2007JE002944.

206. Morente, A. J., Molina-Cuberos, G. J., J. A. Porti, B. P. Besser, A. Salinas, K. Schwingenschuch, H. Lichtenegger (2003), A numerical simulation of Earth's electromagnetic cavity with the Transmission Line Matrix method: Schumann resonances, *Journal of Physical Research,* 108, No. A5, 1195.

207. Morgan, D. D., D. A. Gurnett, D. L. Kirchner, J. L. Fox, E. Nielsen, and J. J. Plaut (2008), Variation of the Martian ionospheric electron density from Mars Express radar soundings, *J. Geophys. Res.*, 113, A09303, doi:10.1029/2008JA013313.

208. Morris, R. V., D. C. Golden, and J. F. Bell III (1997), Low-temperature reflectivity spectra of red hematite and the color of Mars, *J. Geophys. Res.*, 102, 9125– 9133.

209. Moscardelli, L., T. Dooley, D. Dunlap, M. Jackson, and L. Wood (2012), Deep-water polygonal fault systems as terrestrial analogs for large-scale Martian polygonal terrains: *GSA Today*, v. 22, no. 8, p. 4–9.

210. Mouginot, J., A. Pommerol, W. Kofman, P. Beck, B. Schmitt, A. Herique, C. Grima, A. Safaeinili, J. J. Plaut (2010), The 3–5 MHz global reflectivity map of Mars by MARSIS/Mars Express: Implications for the current inventory of subsurface H2O, *Icarus*, 210 (2), 612–625.

211. Mouginot, J., A. Pommerol, P. Beck, W. Kofman, and S. M. Clifford (2012), Dielectric map of the Martian northern hemisphere and the nature of plain filling materials, *Geophys. Res. Lett.,* 39, L02202, doi:10.1029/2011GL050286.

212. Mursula, K., T. Braeysy, K. Kiskala, and C. T. Russel (2001), Pc 1 pearls revisited: structured electromagnetic ion cyclone waves on Polar satellite and on ground, *J. Geophys. Res*, 106, 29543-29553.

213. Mushtak, V. C., and E. R. Williams (2002), ELF propagation parameters for uniform models of the Earth-ionosphere waveguide, *J. Atmos. Sol. Terr. Phys.*, 64, 1989-2001, doi:10.1016/S1364-6826(02)00222-5.

214. Nagy, A. F., D. Winterhalter, K. Sauer, T. E. Cravens, S. Brecht, C. Mazelle, D. Crider, E. Kallio, A. Zakharov, E. Dubinin, M. Verigin, G. Kotova, W. I. Axford, C. Bertucc and J. G. Trotignon (2004), The Plasma Environment Of Mars, *Space Science Reviews,* 111, 33–114.

215. Nemec, F., D. D. Morgan, D. A. Gurnett, F. Duru, and V. Truhlík (2011), Dayside ionosphere of Mars: Empirical model based on data from the MARSIS instrument, *J. Geophys. Res*., 116, E07003, doi:10.1029/2010JE003789.

216. Ness, N. F. (1982), M. H. Acuna, K. W. Behannon, F. M. Neubauer, The induced magnetosphere of Titan. *J. Geophys. Res*., 87, 1369–1381.

217. Neumann, G. A., M. T. Zuber, M. A. Wieczorek, P. J. McGovern, F. G. Lemoine, and D. E. Smith (2004), Crustal structure of Mars from gravity and topography, *J. Geophys. Res.,* 109, E08002, doi:10.1029/2004JE002262.

218. Nickolaenko, A. P., and M. Hayakawa (2002), *Resonances in the Earth-Ionosphere Cavity*, Kluwer, Dordrecht, pp. 380.

219. Nickolaenko, A. P., and M. Hayakawa (2014), *Schumann Resonance for Tyros*, Springer, Tokyo, Heidelberg, New York, Dordrecht, London, pp. 348.

220. Nickolaenko, A. P., A. V. Koloskov, M. Hayakawa, Y. M. Yampolski (2015), 11-year solar cycle in Schumann resonance data as observed in Antarctica, *Sun and Geosphere*, 10, 39-49.

221. Nielsen, E., D. D. Morgan, D. L. Kirchner, J. Plaut, G. Picardi, (2007a), Absorption and reflection of radio waves in the Martian ionosphere, *Planetary and Space Science,* 55, 864–870.

222. Nielsen, E., M. Fraenza, H. Zoua, J.-S. Wanga, D. A. Gurnettb, D. L. Kirchnerb, D. D. Morgan, R. Huff, A. Safaeinili, J. J. Plaut, G. Picardi, J. D. Winningham, R. A. Frahm, R. Lundin (2007b), Local plasma processes and enhanced electron densities in the lower ionosphere in magnetic cusp regions on Mars, *Planetary and Space Science,* 55, 2164–2172.

223. Olhoeft, G. R. (1981), Electrical properties of rocks, [in:] Y. S. Touloukian, W. R. Jadd, R. F. Roy, E., (Eds) *Physical Properties of Rocks and Minerals*, McGraw-Hill, New York, pp. 548.

224. Olhoeft, G. R. and D. W. Strangway (1974), Electrical Properties of the Surface Layers of Mars, *Geophysical Res. Lett*., vol1, no.3.

225. Olsen. N., A. Kuvshinov (2004), Modelling the ocean effect of geomagnetic storms, *Earth Planets Space*, 56, 525-530.

226. Ondraskova, Adriena, Jozsef Bor, Sebastian Sevcık, Pavel Kostecky, Ladislav Rosenberg (2008), Peculiar transient events in the Schumann resonance band and their possible explanation, *Journal of Atmospheric and Solar-Terrestrial Physics,* 70, 937–946.

227. Opgenoorth, H. J., R. S. Dhillon, L. Rosenqvist, M. Lester, N. J. T. Edberg, S. E. Milan, P. Withers, D. Brain (2010), Day-side ionospheric conductivities at Mars, *Planetary and Space Science*, 58, 10, 1139-1151.

228. Pappert, R. A., Moller, W. F. (1974), Propagation theory and Calculations at Lower Ectremely Low Frequencies (ELF), *IEE Transactions on Communications,* vol. Com-22, no. 4, 438-451.

229. Parker, T. J., R. S. Saunders, D. M. Schneeberger (1989), Transitional morphology in west Deuteronilus Mensae, Maars: implications for modification of the lowland/upland boundary, *Icarus*, 82, 111-145.

230. Patzold, M., S. Tellmann, B. Hausler, D. Hinson, R. Schaa, G. L. Tyler (2005), A sporadic third layer in the ionosphere of Mars, *Science*, 310, 837-839, doi:10.1126/science.1117755.

231. Pavlu, J., M. Beránek, J. Vaverka, J. Šafránková, Z. Nemecek, and I. Richterová (2014), Secondary electron emission from Martian soil stimulant *J. Geophys. Res.* Planets, 119, 199–209, doi:10.1002/2013JE004522.

232. Pechony, O., and C. Price (2004), Schumann resonance parameters calculated with a partially uniform knee model on Earth, Venus, Mars, and Titan. *Radio Sci.*, 39, RS5007, doi:10.1029/2004RS003056.

233. Pesnell, W. D., J. Grebowsky (2000), Meteoric magnesium ions in the Martian atmosphere, *J. Geophys. Res*, 105, 1695-1707.

234. Petrenko, V. F. (1993), *Electrical Properties of Ice*, US Army Corps of Engineers, Special Report 93-20, 69.

235. Petrosyan, A., B. Galperin, S. E. Larsen, S. R. Lewis, A. Määttänen, P. L. Read, N. Renno, L. P. H. T. Rogberg, H. Savijärvi, T. Siili, A. Spiga, A. Toigo, and L. Vázquez (2011), The Martian Atmospheric Boundary Layer, *Rev. Geophys*., 49, RG3005, doi:10.1029/2010RG000351.

236. Pettinelli, E., et al. (2005), Laboratory investigations into the electromagnetic properties of magnetite/silica mixtures as Martian soil simulants, *J. Geophys. Res*., 110, E04013, doi:10.1029/2004JE002375.

237. Poulet, F., J.-P. Bibring, J. F. Mustard, A. Gendrin, N. Mangold, Y. Langevin, R. E. Arvidson, B. Gondet1 and C. Gomez (2005), Phyllosilicates on Mars and implications for early martian climate, *Nature* 438, 623-627.

238. Price C., M. Asfur, W. Lyons, T. Nelson (2001), An Improved Elf/Vlf Method For Globally Geolocating Sprite-Producing Lightning*, Geophysical Research Letters,* 29, No. 3, doi: 10.1029/2001GL013519.

239. Price, C., K. Mezuman, E. Galanti (2011), How many thunderstorms are active at any moment? *Geophysical Research Abstracts*, Vol. 13, EGU2011- 9170.

240. Qu, J., Yan Muhong, Dong Guangrong, Zhang Hongfa, Zu Ruiping, Tuo Wanquan, Zhao Aiguo, Xiao Zhenghua, Li Fang & Yang Bao (2004), Wind tunnel simulation experiment and investigation on the electrification of sandstorms, *Science in China Ser. D Earth Sciences* Vol.47, No.6, 529—539.

241. Raizer, Yuri P. (1991), *Gas Discharge Physics*, Springer-Verlag Berlin Heidelberg, pp. 449.

242. Rakov V. A., M. A. Uman (2006), *Lightning*: *Physics and Effects*, Cambridge University Press, New York, pp. 687.

243. Read, P. L., S. R. Lewis (2004), *The Martian Climate Revisited, Atmosphere and Environment of a Desert Planet*, Springer-Praxis, UK, pp. 326.

244. Renno, N. O., A.-S. Wong, S. K. Atreya, I. de Pater, and M. Roos-Serote (2003), Electrical discharges and broadband radio emission by Martian dust devils and dust storms, *Geophys. Res. Lett.*, 30(22), 2140, doi:10.1029/2003GL017879.

245. Renno, N. O., *et al*. (2004), MATADOR 2002: A pilot field experiment on convective plumes and dust devils, *J. Geophys. Res*., 109, E07001, doi:10.1029/2003JE002219.

246. Rishbeth, H., and M. Mendillo (2004), Ionospheric Layers of Mars and Earth, *Planetary and Space Sci.,* 52, 849-852, doi:10.1016/j.pss.2004.02.007.

247. Roble, R. G., I. Tzur (1986), *The global atmospheric-electrical circuit*, [in:] *The Earth's Electrical Environment*, 206-231, Batk Acad Press, Washington D.C., pp. 263.

248. Rogers, A. D., J. L. Bandfield, and P. R. Christensen (2007), Global spectral classification of Martian low-albedo regions with Mars Global Surveyor Thermal Emission Spectrometer (MGS-TES) data, *J. Geophys. Res.,* 112, E02004, doi:10.1029/2006JE002726.

249. Rosenqvist, L., J. Wahlund, K. Ågren, R. Modolo, H. J. Opgenoorth, D. Strobel, I. Müller, Wodarg, P. Garnier, and C. Bertucci (2009), Titan ionospheric conductivities from Cassini measurements, *Planet. Space.Sci.,* 57, 1828-1833.

250. Ruf, C., N. O. Renno, J. F. Kok, E. Bandelier, M. J. Sander, S. Gross, L. Skjerve, and B. Cantor (2009), Emission of non-thermal microwave radiation by a Martian dust storm, *Geophys. Res. Lett*., 36, L13202, doi:10.1029/2009GL038715.

251. Russell, C. T., and O. Vaisberg (1983), *The interaction of the solar wind with Venus,* [in:] *Venus,* (eds.) D. M. Hunten, L. Colin, T. M. Donahue, and V. I. Moroz, Univ. of Ariz. Press, Tuscon, 873–940.

252. Rycroft, M.J., S. Israelsson, C. Price (2000), The global atmospheric electric circuit, solar activity and climate change, *Journal of Atmospheric and Solar-Terrestrial Physics,* 62, 1563-1576.

253. Rycroft, M. J., R. Giles Harrison, Keri A. Nicoll, Evgeny A. Mareev (2008), An Overview of Earth's Global Electric Circuit and Atmospheric Conductivity, *Space Sci Rev*., 137, 83–105.

254. Saito, T. (1969), Geomagnetic Pulsations, *Space Science Reviews*, Volume 10, Issue 3, pp. 319-412.

255. Satori, G., E. Williams, V. Mushtak (2005), Response of the Earth–ionosphere cavity resonator to the 11-year solar cycle in X-radiation, *Journal of Atmospheric and Solar-Terrestrial Physics,* 65, pp. 553-562.

256. Satori,G., E. Williams, I. Lemperger (2009), Variability of global lightning activity on the ENSO time scale, *Atmospheric Research*, 91, pp. 500–507.

257. Saunders, C. (2008), Charge Separation Mechanisms in Clouds, *Space Science Reviews*, vol. 137, Nos 1-4.

258. Savich, N. A., and V. A. Samovol (1976), The night time ionosphere of Mars from Mars 4 and Mars 5 dual frequency radio occultation measurements, *Space Res.,* XVI, 1009–1010.

259. Schlegel, K., Fullekrug, M. (1999), Schumann resonance parameter changes during high-energy particle precipitation, *Journal of Geophysical Research,* vol. 104, No. A5, 10.111-10.118.

260. Schmidt, D. S., R. A. Schmidt, and J. D. Dent (1998), Electrostatic force on saltating sand, *J. Geophys. Res*., 103(D8), 8997–9001.

261. Schofield, J. T., J. R. Barnes, D. Crisp, R. M. Haberle, S. Larsen, J.A. Magalhaes, J. R. Murphy, A. Seiff, G. Wilson (1997), The Mars Pathfinder Atmospheric Structure Investigation/Meteorology (ASI/MET) Experiment*, Science*, 278, 1752-1758.

262. Schon, J. H. (2004*), Physical Properties of Rocks: fundamentals and Principles of Petrophysics,* Vol. 18, Pergamon, UK, pp. 592.

263. Schorghofer, N. (2008), Temperature response of Mars to Milankovitch cycles, *Geophys. Res. Lett*. 35, L18201, doi:10.1029/2008GL034954.

264. Schumann, W. O. (1952), On the radiation free self-oscillations of a conducting sphere which is surrounded by an air layer and an ionospheric shell (in German), *Zeitschrift Naturforschung* Teil A, vol. 7.

265. Seiff, A., D. B. Kirk (1977). Structure of the atmosphere of Mars in summer at mid-latitudes. *J. Geophys. Res*. 82, 4363–4378.

266. Sheel, V., S. A. Haider, P. Withers, K. Kozarev, I. Jun, S. Kang, G. Gronoff, and C. Simon Wedlund (2012), Numerical simulation of the effects of a solar energetic particle event on the ionosphere of Mars, *J. Geophys. Res*., 117, A05312, doi:10.1029/2011JA017455.

267. Sickafoose, A. A., J. E. Colwell, M. Horányi, and S. Robertson (2001), Experimental investigations on photoelectric and triboelectric charging of dust, *J. Geophys. Res*., 106(A5), 8343–8356, doi:10.1029/2000JA000364.

268. Simoes, F., M. Rycroft, N. Renno, Y. Yair, K. L. Aplin, Y. Takahashi (2008a), Schumann Resonances as a Means of Investigating the Electromagnetic Environment in the Solar System, *Space Sci. Rev*., 137, 455–471.

269. Simoes, F., R. Grard, M. Hamelin, J. J. López-Moreno, K. Schwingenschuh, C. Béghin, J.-J. Berthelier, J.-P. Lebreton, G. J. Molina-Cuberos, T. Tokano (2008b), The Schumann resonance: A tool for exploring the atmospheric environment and the subsurface of the planets and their satellites, *Icarus*, 194(1), 30-41.

270. Simoes, F., R. Pfaff, and H. Freudenreich (2011), Satellite observations of Schumann resonances in the Earth's ionosphere, *Geophys. Res. Lett*., 38, L22101, doi:10.1029/2011GL049668.

271. Simoes, F., R. Pfaff, M. Hamelin, J. Klenzing, H. Freudenreich, C. Beghin, J.-J. Berthelier, K. Bromund, R. Grard, J.-P. Lebreton, S. Martin, D. Rowland, D. Sentman, Y. Takahashi, and Y. Yair (2012), Using Schumann Resonance Measurements For Constraining The Water Abundance On The Giant Planets—Implications For The Solar System's Formation, *Astrophys. J.,* 750(1), 85, doi:10.1088/0004-637X/750/1/85.

272. Singh, R. P., M. P. Singh, T. Lal (1980), Laboratory measurement of dielectric constant and loss tangent of Indian rock samples, Annales of Geophysics, Vol. 33, No. 1, 121-140.

273. Sleep, N. H. (1994), Martian plate tectonics*, J. Geophys. Res*., 99(E3), 5639–5655, doi:10.1029/94JE00216.

274. Soriano, A., E. Navarro, D. Paul, J. Port, J. Morente, and I. Craddock (2005), Finite difference time domain simulation of the Earth-ionosphere resonant cavity: Schumann resonances, *IEEE Trans. Antennas Propag*., 53(4), 1535–1541.

275. Soriano, A., E. A. Navarro, J. A. Morente, J. A. Portí (2007), A numerical study of the Schumann resonances in Mars with the FDTD method, *J. Geophys. Res*., 112, A06311, doi:10.1029/2007JA012281.

276. Spohn, T., M. H. Acuña, D. Breuer, M. Golombek, R. Greeley, A. Halliday, E. Hauber, R. Jaumann, F. Sohl (2001), Geophysical Constraints on the Evolution of Mars, *Space Sci. Rev*., 96(1/4), p. 231-262.

277. Stevenson, D. J. (2001), Mars' core and magnetism, *Nature*, 412, 214-219.

278. Stillman, D., and G. Olhoeft (2008), Frequency and temperature dependence in electromagnetic properties of Martian analog minerals, *J. Geophys. Res*., 113, E09005, doi:10.1029/2007JE002977.

279. Stow, C. D. (1969), Dust and sand storm electrification, *Weather*, 24, 134-140.

280. Sukhorukov, A. I. (1991), On the Schumann resonances on Mars, *Planet. Space Sci*., 39(12), 1673, doi:10.1016/0032-0633(91)90028-9.

281. Surkov, Y. A., L. P. Moskaloyoba, O. S. Manveylan, A. T. Basilevsky, V. P. Kharyukova (1980), Geochemical interpretation of the results of measuring gamma-radiation of Mars, *LPI Proceedings*, Volume 1, New York, Pergamon Press, p. 669-676.

282. Tanaka, Kenneth L., James A. Skinner, Jr., James M. Dohm, Rossman P. Irwin, III, Eric J. Kolb, Corey M. Fortezzo, Thomas Platz, Gregory G. Michael and Trent M. Hare (2014), *Geological Map of Mars*.

283. Taylor, G. J. *et al.* (2008), Implications of observed primary lithologies, *The Martian Surface: Composition, Mineralogy, and Physical Properties* (e. J. F. Gell III), Cambridge University Press, pp. 501-518.

284. Taylor, S. T., S. M. McLennan, (2009), *Planetary Crusts, Their Composition, Origin and Evolution*, Cambridge University Press, New York, pp. 378

285. Thomas, P., and P. G. Gierasch (1985), Dust devils on Mars, *Science*, 230, 175-177.

286. Titus, T. N., W. M. Calvin, H. H. Kieffer, Y. Langevin, T. H. Prettyman (2008), Martian polar processes, [in:] *The Martian Surface - Composition, Mineralogy, and Physical Properties*, (edited by) J. Bell, III, Cambridge University Press, Cambridge, pp. 578-598.

287. Tran, A., C. Polk (1979), Schumann resonances and electrical conductivity of the atmosphere and lower ionosphere-I. Effects of conductivity at various altitudes on resonance frequencies and attenuation, *Journal of Atmospheric and Terrestrial Physics,* 41 (12), 1241-1261.

288. Travis, B. J., W. C. Feldman, and S. Maurice (2013), A mechanism for bringing ice and brines to the near surface of Mars, J*. Geophys. Res. Planets*, 118, 877–890, doi:10.1002/jgre.20074.

289. Treumann, R. A., Z. Klos, M. Parrot (2008), Physics off Electric Discharges in Atmospheric Gases: An Informal Introduction, *Space Science Reviews*, vol. 137, nos 1-4.

290. Tyler, G. L., D. B. Campbell, G. S. Downs, R. R. Green, and H. J. Moore (1976), Radar characteristics of Viking 1 landing sites, *Science,* 193, 812.

291. Valeille, A., S. W. Bougher, V. Tenishev, M. R. Combi, A. F. Nagy, (2010), Water loss and evolution of the upper atmosphere and exosphere over martian history, *Icarus*, 206, 28–39.

292. Vasilev, M. B., A. S. Vyshlov, M. A. Kolosov, N. A. Savich, V. A. Samovol, L. N. Samoznaev, A. I. Sidorenko, Iu. N. Aleksandrov, A. I. Danilenko, V. M. Dubrovin (1975), Preliminary results of the two-frequency radio-transillumination of the Martian ionosphere by means of the “Mars” automatic interplanetary stations in 1974, *Cosmic Res*., 13, 41–45.

293. Volland, H. (1984), *Atmospheric Electrodynamics*, Springer-Verlag, New York, pp. 528.

294. Wait, J. R. (1962), On the propagation of ELF pulses in the Earth-ionosphere waveguide, *Canadian J. Phys*., 40, 1360.

295. Wait, J. R. (1970), *Electromagnetic Waves in Stratified Media,* Pergamon Press, Oxford, pp. 372.

296. Wang, H., Mark I. Richardson (2013), The origin, evolution, and trajectory of large dust storms on Mars during Mars years 24–30 (1999–2011), *Icarus*, 251, Pages 112–127.

297. Wang, J.-S., and E. Nielsen (2003), Behavior of the Martian dayside electron density peak during global dust storms, *Planet. Space Sci.*, 51, 329–338.

298. Webster, C. R., P. R. Mahaffy, S. K. Atreya, G. J. Flesch, M. A. Mischna, et al. (2015), Mars methane detection and variability at Gale crater, *Science,* 347, 415-417.

299. Whitten, R. C., I. G. Poppoff, J. S. Sims (1971), The Ionosphere of Mars below 80 km altitude-I quiescent conditions, *Planet. Space Sci.*, 17, 243-250.

300. Wieczorek, M. A., and M. T. Zuber (2004), Thickness of the Martian crust: Improved constraints from geoid-to-topography ratios, *J. Geophys. Res.*, 109, E01009, doi:10.1029/2003je002153.

301. Williams, E. R. (1992), The Schumann resonance: A global tropical thermometer, *Science*, 256, 1184, doi:10.1126/science.256.5060.1184.

302. Williams, K. K., and R. Greeley (2004), Measurements of dielectric loss factors due to a Martian dust analog, *J. Geophys. Res*., 109, E10006, doi:10.1029/2002JE001957.

303. Williams, E. R., and G. Satori (2004), Lightning, thermodynamic and hydrological comparison of the two tropical continental chimneys, *Journal of Atmospheric and Solar-Terrestrial Physics,* 66, 1213–1231.

304. Williams, E., N. Nathou, E. Hicks, C. Pontikis, B. Russell, M. Miller, M. J. Bartholomew (2008), The electrification of dust-lofting gust fronts ('haboobs') in the Sahel, *Atmospheric Research*, vol. 91, issue 2, p. 292-298.

305. Wilson, C. T. R. (1929), Some thundercloud problems, *J. Franklin Inst.*, 208, 1-12.

306. Witasse, O., T. Cravens, M. Mendillo, J. Moses, A. Kliore, A. Nagy, and T. Breus (2008), Solar system ionospheres, *Space Sci. Rev*., 139, 235–265.

307. Withers, P. (2009), A review of observed variability in the dayside ionosphere of Mars, *Advances in Space Research,* 44, 277–307.

308. Withers, P. (2011), Attenuation of radio signals by the ionosphere of Mars: Theoretical development and application to MARSIS observations, *Radio Science*, 46, RS2004, doi:10.1029/2010RS004450.

309. Withers, P., M. Mendillo, H. Rishbeth, D. P. Hinson, and J. Arkani-Hamed (2005), Ionospheric characteristics above Martian crustal magnetic anomalies, *Geophysical Research Letters*, 32, L16204, doi:10.1029/2005GL023483.

310. Withers, P., *et al*. (2012a), A clear view of the multifaceted dayside ionosphere of Mars, *Geophys. Res. Lett*., 39, L18202, doi:10.1029/2012GL053193.

311. Withers, P., M. O. Fillingim, R. J. Lillis, B. Häusler, D. P. Hinson, G. L. Tyler, M. Pätzold, K. Peter, S. Tellmann, and O. Witasse (2012b), Observations of the nightside ionosphere of Mars by the Mars Express Radio Science Experiment (MaRS), *J. Geophys. Res*., 117, A12307, doi:10.1029/2012JA018185.

312. Wray, J. J., Bethany L. Ehlmann (2011), Geology of possible martian methane source regions, *Planetary and Space Science*, 59, 2-3, pp. 196-202.

313. Yair, Y. (2008), Charge Generation and Separation Processes, *Space Sci. Rev.,* 137: 119–131.

314. Yair, Y. (2012), New results on planetary lightning, *Advances in Space Research,* 50, 293–310.

315. Yair, Y., G. Fischer, F. Simões, N. Renno, P. Zarka (2008), Updated Review of Planetary Atmospheric Electricity, *Space Sci. Rev.*, 137, 29–49.

316. Yang, H., V. P. Pasko, Y. Yair (2006), Three-dimensional finite difference time domain modeling of the Schumann resonance parameters on Titan, Venus and Mars. *Radio Sci*., 41, RS2S03, doi:10.1029/2005RS003431.

317. Yen, A. S., *et al*. (2005), An integrated view of the chemistry and mineralogy of Martian soils, *Nature*, 436, 49– 53.

318. Zarka, P., W. Farrell, G. Fischer, A. Konovalenko (2008), Ground-Based and Space-Based Radio Observations of Planetary Lightning, *Space Sci. Rev.*, 137, 257–269.

319. Zhai, Y., S. A. Cummer, and W. M. Farrell (2006), Quasi-electrostatic field analysis and simulation of Martian and terrestrial dust devils, *J. Geophys. Res*., 111, E6, doi:10.1029/2005JE002618.

320. Zhang Hong-Fa, Tao Wang, Jian-Jun Qu, Mu-Hong Yan (2004), An Experimental And Observational Study On The Electric Effect Of Sandstorms, *Chinese Journal Of Geophysics* Vol.47, No.1, pp: 53-60.

321. Zhang, M. H. G., J. G. Luhmann, A. J. Kliore, J. Kim (1990), A post-pioneer Venus reassessment of the Martian dayside ionosphere as observed by radio occultation methods. *J. Geophys. Res*., 95, 14829–14839, doi: 10.1029/JB095iB09p14829.

322. Zhdanov, M. S., and G. V. Keller (1994), *The Geophysical Methods in Geophysical Exploration*, Elsevier, Amsterdam, pp. 873.